NUREG/CR–4671
SAND86–1443

The DF-4 Fuel Damage Experiment in ACRR with a BWR Control Blade and Channel Box

Prepared by R. O. Gauntt, R. D. Gasser, L. J. Ott

Sandia National Laboratories

Prepared for
U.S. Nuclear Regulatory Commission

AVAILABILITY NOTICE

Availability of Reference Materials Cited in NRC Publications

Most documents cited in NRC publications will be available from one of the following sources:

1. The NRC Public Document Room, 2120 L Street, NW, Lower Level, Washington, DC 20555

2. The Superintendent of Documents, U.S. Government Printing Office, P.O. Box 37082, Washington, DC 20013-7082

3. The National Technical Information Service, Springfield, VA 22161

Although the listing that follows represents the majority of documents cited in NRC publications, it is not intended to be exhaustive.

Referenced documents available for inspection and copying for a fee from the NRC Public Document Room include NRC correspondence and internal NRC memoranda; NRC Office of Inspection and Enforcement bulletins, circulars, information notices, inspection and investigation notices; Licensee Event Reports; vendor reports and correspondence; Commission papers; and applicant and licensee documents and correspondence.

The following documents in the NUREG series are available for purchase from the GPO Sales Program: formal NRC staff and contractor reports, NRC-sponsored conference proceedings, and NRC booklets and brochures. Also available are Regulatory Guides, NRC regulations in the *Code of Federal Regulations*, and *Nuclear Regulatory Commission Issuances*.

Documents available from the National Technical Information Service include NUREG series reports and technical reports prepared by other federal agencies and reports prepared by the Atomic Energy Commission, forerunner agency to the Nuclear Regulatory Commission.

Documents available from public and special technical libraries include all open literature items, such as books, journal and periodical articles, and transactions. *Federal Register* notices, federal and state legislation, and congressional reports can usually be obtained from these libraries.

Documents such as theses, dissertations, foreign reports and translations, and non-NRC conference proceedings are available for purchase from the organization sponsoring the publication cited.

Single copies of NRC draft reports are available free, to the extent of supply, upon written request to the Office of Information Resources Management, Distribution Section, U.S. Nuclear Regulatory Commission, Washington, DC 20555.

Copies of industry codes and standards used in a substantive manner in the NRC regulatory process are maintained at the NRC Library, 7920 Norfolk Avenue, Bethesda, Maryland, and are available there for reference use by the public. Codes and standards are usually copyrighted and may be purchased from the originating organization or, if they are American National Standards, from the American National Standards Institute, 1430 Broadway, New York, NY 10018.

NUREG/CR-4671
SAND86-1443
R3

The DF-4 Fuel Damage Experiment in ACRR with a BWR Control Blade and Channel Box

Manuscript Completed: August 1989
Date Published: November 1989

Prepared by
R. O. Gauntt, R. D. Gasser, L. J. Ott*

Sandia National Laboratories
Albuquerque, NM 87185

*Oak Ridge National Laboratory

Prepared for
Division of Systems Research
Office of Nuclear Regulatory Research
U.S. Nuclear Regulatory Commission
Washington, DC 20555
NRC FIN A1335

Abstract

The DF-4 test was an experimental investigation into the melt progression behavior of boiling water reactor (BWR) core components under high temperature severe core damage conditions. In this study 14 zircaloy clad UO_2 fuel rods, and representations of the zircaloy fuel canister and stainless steel/B_4C control blade were assembled into a 0.5 m long test bundle. The test bundle was fission heated in a flowing steam environment, using the Annular Core Research Reactor at Sandia Laboratories, simulating the environmental conditions of an uncovered BWR core experiencing high temperature damage as a result residual fission product decay heating. The experimental results provide information on the thermal response of the test bundle components, the rapid exothermic oxidation of the zircaloy fuel cladding and canister, the production of hydrogen from metal-steam oxidation, and the failure behavior of the progressively melting bundle components. This information is provided in the form of thermocouple data, steam and hydrogen flow rate data, test bundle fission power data and visual observation of the damage progression.

In addition to BWR background information, this document contains a description of the experimental hardware with details on how the experiment was instrumented and diagnosed, a description of the test progression, and a presentation of the on-line measurements. Also in this report are the results of a thermal analysis of the fueled test section of the experiment demonstrating an overall consistency in the measurable quantities from the test. A discussion of the results is provided.

TABLE OF CONTENTS

TABLE OF CONTENTS (Continued)

LIST OF FIGURES

LIST OF FIGURES (Continued)

LIST OF FIGURES (Continued)

LIST OF FIGURES (Continued)

LIST OF TABLES

Preface

This report is the first of several documents that will be issued for the DF-4 BWR Control Blade-Channel Box experiment. At the time that this document was prepared, other test results were available but not included, so that the information contained herein could be released to the technical community. For example, post irradiation destructive examination results were available in part for this report, however, it was decided that this information would be presented in a separate report when the work was completed. Also to appear in a subsequent report is an analysis of the hydrogen production rate determined from interpretation of the copper oxide recombiner bed measurements.

Acknowledgements

The list of participants who contributed to the success of the DF-4 experiment extends far beyond the author list of this document. Many of those involved in this work have been with the DF Program from the beginning, starting with DF-1. Much of the original program definition is attributable to Ken Reil and Paul Pickard, who have actively participated with all of the DF experiments. In an effort to credit all of those who were involved in the DF-4 effort, the following list of participants and activities is offered:

Bob Wright (NRC), Program sponsor and enthusiastic provider of valuable suggestions and guidance.

Al Marshall, Ken Reil, and Paul Pickard, original inception and design of the DF experimental hardware and capsule.

R. O. Gauntt, Project Leader with general oversight of the DF-4 goals and design.

Larry Ott (ORNL), development of an experiment analysis code, MARCON-DF4, which was used for extensive pre-test and post-test analyses.

Ron Gasser, extensive pre and posttest analyses using MARCON-DF4, analysis of high temperature thermocouple data and evaluation of experiment/reactor power coupling.

John Garcia, Paul Helmick, Gerald Naranjo, and Jim Andazola, assembly of the experimental hardware.

Jim Fisk, oversight of the fabrication, assembly and staging of the experiment.

John Wray (deceased), skillful and dedicated operation of motion picture and video recording equipment.

Phil Hargis and Mike Boccabella, assistance in optical diagnostics.

Ken Reil and Kent Richards, computer link to the experiment for experiment control and data collection.

Ray Ostensen participated in the early definition of the DF-4 experiment goals.

The ACRR Operations Division, great assistance in installing the experiment in the ACRR facility and in conducting the nuclear phase of the experiment.

Carol Fryer and Hot Cell Staff, ongoing Postirradiation Examination (PIE).

Ken Murumatsu (JAERI), ongoing consulting on analysis of the hydrogen production in DF-4.

Jay Weingardt, initial neutronics design calculations and ongoing COPOX analysis of DF-4 hydrogen generation.

Rena Yellowrobe, typing and preparation of this document.

To the preceding explicitly mentioned individuals and to any persons who inadvertently were overlooked, congratulations and many thanks for a job well done.

1. INTRODUCTION

1.1 Background

After the accident at the Three Mile Island Unit 2, the United States Nuclear Regulatory Commission (NRC) initiated a severe accident research program,[1,2,3] the general purpose of which was to develop a basis for evaluating reactor core melt progression and ultimately, for assessing the release of fission products from the plant site and the ensuing threat to the public health. An important element of this program has been the development of state-of-the-art computer codes, such as MELPROG,[4] MELCOR,[5] BWRSAR,[6] and SCDAP,[7] which model the physical and chemical processes occurring in a reactor core which has lost cooling capability and become uncovered, and in the generation of a data base by which such codes may be assessed and validated. This data base consists of experimental evidence obtained from several in-pile and out-of-pile phenomenologically oriented programs[3,8,9,10,11] supported by the NRC and other international sponsors.

The Damaged Fuel (DF) experimental program conducted at Sandia National Laboratories (SNL) has made contributions to the severe fuel damage phenomenology data base in the form of results from four in-pile fuel damage experiments carried out in the Annular Core Research Reactor (ACRR) at SNL.[8] These experiments use prototypic materials (UO_2 fuel, zircaloy cladding, control materials) in test configurations that are fission heated in a flowing steam environment, thus simulating the high temperature oxidizing environment of a light water reactor (LWR) undergoing severe damage associated with a loss of coolant accident. These experiments serve to reveal the important physical damage processes so that phenomenological models may be developed and to provide quantitative information for the assessment and validation of these models.

Phenomena known to participate in the severe fuel damage process include rapid zircaloy oxidation with the associated chemical energy release, melting of cladding, UO_2 attack and dissolution by molten zircaloy, relocation of liquefied fuel/cladding mixtures and formation of blockage regions by the refreezing of previously molten components around intact fuel rods in cooler regions. Associated with these damage processes is the production of hydrogen from the steam oxidation of zircaloy and stainless steel, and the release of fission products and aerosol. The core may subsequently collapse to form a rubble geometry which is not coolable and which may melt through the reactor pressure vessel, releasing the core inventory to the containment environment. The chemical and physical state of the reactor core during the time that fission products are being released influences the transport of fission products into the reactor coolant system and ultimately their threat to the environment.

The two principal goals of the DF experimental program are to (1) reveal the dominating physical phenomena that participate in severe reactor core damage processes and (2) to provide well characterized quantitative measurements of the observed phenomena. A successful completion of the first goal insures that the dominating phenomena are identified so that they may be treated in adequately detailed physical models of severe core degradation processes. Attainment of the second goal makes possible the assessment and validation of models of the coupled phenomena.

The DF-4 experiment was conducted to examine and explore the phenomena associated with severe damage of an uncovered boiling water reactor (BWR) core by including structures in the test fuel bundle representative of BWR control blades and fuel canisters. The following sections describe these and other unique aspects of severe BWR core damage that were considered in the design of the experiment.

1.2 Important BWR Features

The major emphasis with the existing experimental data base has been on pressurized water reactor (PWR) geometry, and relatively little attention has been directed towards the boiling water reactor (BWR), although ~31% of nuclear electrical power generation in the United States is derived from BWR's.[12] The large amount of phenomenological information obtained for PWR geometry in the experimental studies conducted to date is applicable to some extent in a generic sense to both PWR's and BWR's. Nevertheless, many important structural differences exist between the two different core designs which necessitates experimental studies of both types of light water reactor (LWR) cores.[13,14]

The substantial differences between the PWR and BWR core lie in the design of the fuel assemblies and in the control rods.[14,15] The PWR core is comprised of numerous open lattice rod bundles, usually in 17 by 17 rod assemblies as shown in Figure 1-1. Control rods containing an alloy of Ag, In, and Cd are distributed within each fuel assembly. In contrast to the open lattice rod geometry of the PWR core, each 8 by 8 fuel rod assembly in the BWR is individually encased in a zircaloy-4 canister, which prevents cross flow of coolant between adjacent fuel assemblies. This feature allows the coolant flow to each of the BWR fuel canisters to be adjusted to accommodate the local core power density, using an orifice at the inlet to the fuel canister.[15,16] Another important difference is in the control assemblies, which in the BWR design is not a single rod, but rather, clusters of rods arranged to form a cruciform-shaped blade, and situated between four adjacent fuel canisters, as shown in Figure 1-2. The individual stainless steel tubes which form the blade are filled with boron carbide (B_4C) powder packed to 70% theoretical density, and are held in the blade configuration by a thin steel sheath. The sheath is perforated at regularly spaced intervals along the length of the blade to allow coolant to enter and remove heat generated by neutron absorptions in the B_4C. Because of the use of zircaloy fuel canisters, the BWR core contains substantially more zirconium in proportion to fuel than a comparably sized PWR core. Table 1-1 summarizes a few notable comparisons in material composition between comparable sized PWR and BWR cores.

1.3 Severe Core Damage In BWR's

As with the PWR, severe core damage in the BWR can result when the coolant level in the pressure vessel falls below the top of the reactor core. Initially the severe damage occurs because of steam oxidation of zircaloy components and the heat released from the exothermic reaction. The driving force for the zircaloy oxidation is the steam boiling rate, as without steam, the reaction ceases. In a BWR, coolant boiling occurs principally within the fuel canisters (channel boxes), because this is where the fuel rods are. For this reason, the major supply of steam for zircaloy oxidation flows within the canister.[13,17] However, steam does flow to a lesser degree in the interstitial regions external to the channel boxes because of direct heating from decay gamma absorption, conduction from the channel box walls, and by coolant flashing when the vessel depressurizes.[6] Thus steam is available in differing

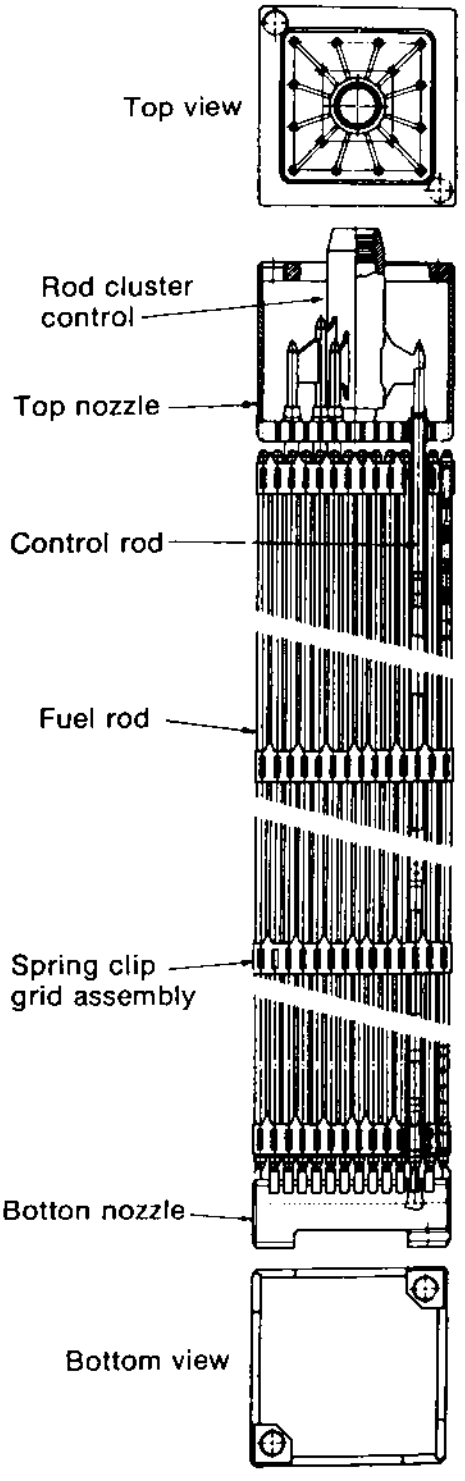

Figure 1-1: Typical open lattice design of 17x17 PWR fuel assembly (taken from Reference 15).

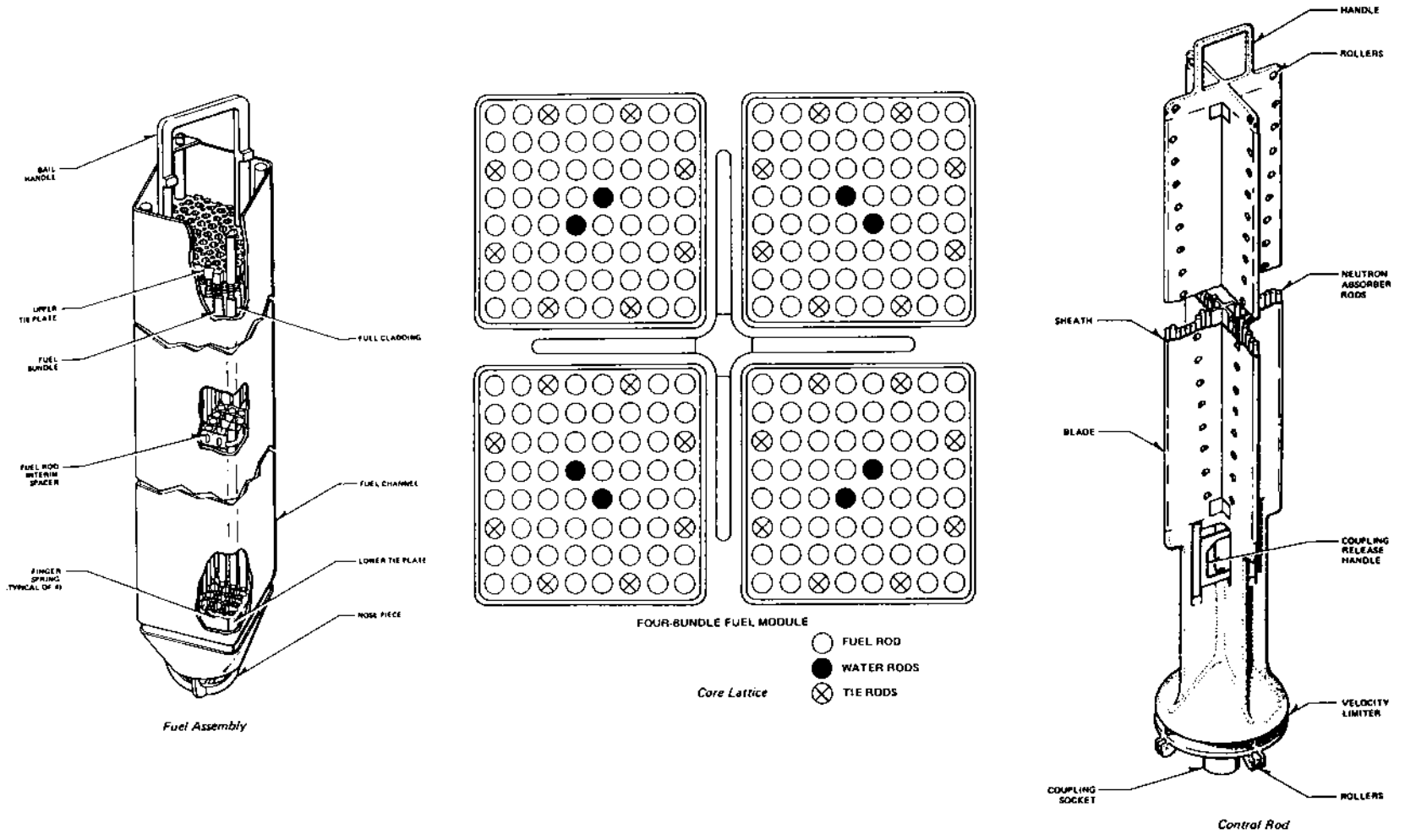

Figure 1-2: BWR core design showing fuel assemblies, control rod geometry, and lattice arrangement (taken from Reference 15).

proportions both to the fuel clad and channel box interior wall as well as to the channel box exterior wall and the stainless steel/B_4C control blade assembly.

Table 1-1

Typical amounts of fuel, zircaloy and other comparisons between comparably sized PWR and BWR reactor cores.**

Component	3411 MWth PWR	3579 MWth BWR
Fuel (UO_2)	118,000 kg	155,000 kg
Cladding	21,000 kg	33,800 kg
Fuel Canisters	N/A	21,600 kg
Total Zircaloy	21,000 kg	55,400 kg
Control Material	1,200 kg Ag/In/Cd	885 kg B_4C
Ratio Zr/UO_2 mass	0.18	0.36
Potential H_2 from Zr oxidation	923 kg or ~10,300 m^3	2435 kg or ~27,300 m^3

** Data compiled from reference 15.

In BWR accident sequences that occur without vessel depressurization, the system pressure is maintained at the safety relief valve (SRV) set point. In such accidents (e.g. Station Blackout), the steam flow in the interstitial region between adjacent channel boxes results in large part from coolant flashing upon automatic actuation of the SRV's.[18] A difference of from 50 to 100 psi exists between the opening pressure and closing pressure of the SRV[14,16] which results in a periodic flashing of steam when the valves are open and a corresponding suppression of steaming in the interstitial region when the valves are closed. Calculations carried out at Oak Ridge National Laboratory[18] indicate that the time between successive depressurization events is on the order of 3 minutes. Under these conditions, oxidation in the interstitial zone occurs in periodic vigorous bursts when the SRV's open to vent steam and relieve pressure, and effectively ceases when the SRV's close. Shown in Figure 1-3 are MARCON2.1B calculations of core steaming rates in the fuel canister and interstitial regions for the Browns Ferry reactor under Station Blackout conditions. Notice the highly transient steaming bursts associated with the SRV actuations.

Under other conditions, the steam generation rate regions can be less transient in nature. Examples of this would include situations where the SRV's are manually opened to depressurize the vessel (as would be required to enable the low pressure emergency core cooling system) or by unintentional means, such as would occur with a stuck open relief valve (SORV). In these events, coolant may continuously flash to steam, and zircaloy oxidation would occur in a more continuous manner (providing core temperatures are sufficiently high).

Another factor which can affect the coolant boiling rate under BWR accident conditions is the operability of the control rod drive hydraulic system (CRDHS). This system, normally used to drive the control blades into the core and provide cooling functions, under accident conditions may be used as a means to inject coolant into the core when other means are not available.[18] Because this system has a relatively low pumping capacity (60 to 112 gal/min or ~7 l/s), the reflooding of a largely uncovered

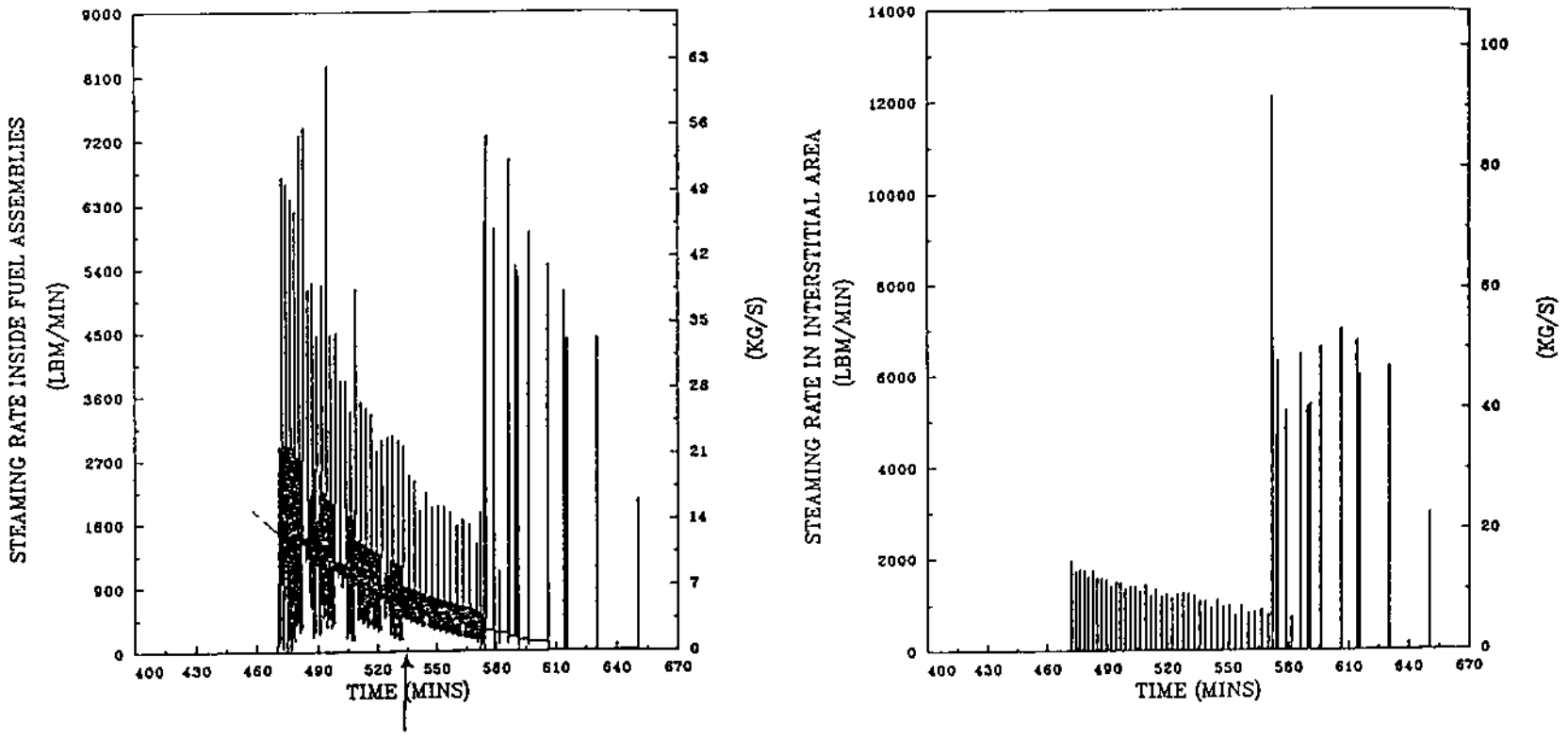

Figure 1-3: MARCON2.1B calculations for Browns Ferry under Station Blackout conditions showing core steaming in fuel assemblies and bypass (interstitial) regions.

core might be slow. If a relief valve is stuck open, the steady steaming period during which severe zircaloy oxidation damage could result could be protracted. Although not a risk dominant BWR accident sequence, the combined events (a) Station Blackout, (b) stuck open relief valve (SORV), and (c) operational CRDHS were analyzed using the MARCON2.1B BWR accident analysis code to evaluate zircaloy oxidation under conditions favoring steady steam production. Figure 1-4 shows predictions of steam production for the Browns Ferry reactor under these conditions.

The results of this calculation together with the results shown in Figure 1-3 for SRV dominated core steaming serve to illustrate the variations possible in BWR core steam generation, that in turn influence the zircaloy oxidation behavior, structural heatup characteristics, and the production of hydrogen.

The thermal and hydraulic behavior of BWRs under severe accidents has been modeled with varying degrees of sophistication in different accident analysis codes (e.g. MELRPI,[13,19] MARCH,[20] MELCOR,[5] MAAP,[21] MARCON,[18] and BWRSAR[6]). However, because of differences in sophistication and level of detail between the models used in these codes, predictions of crucially important quantities, such as hydrogen production, can vary significantly.[13] The production of hydrogen in BWR accidents is especially important in view of the very large zirconium inventory in the BWR core that can lead to potentially huge volumes of hydrogen (see Table 1-1). This potential becomes a significant concern in the evaluation of the integrity of MARK-1 containments. Because of the small volume of the MARK-1 containment (4503 m^3 drywell and 3370 m^3 wetwell),[22] pressurization by hydrogen can be an important factor in the failure of the primary containment, and hydrogen deflagrations subsequently occurring in the secondary containment building play a role in furthering the release of fission products to the environment.[23,24] On the other hand, if the large amount of zircaloy in the core does not react to form hydrogen within the vessel, it will consequently be available later to interact with materials such as water and concrete outside of the vessel if or when failure of the vessel lower head occurs. In this case, the amount of released zirconium metal may be very important in evaluating the subsequent containment performance.[25,26]

These examples were cited to emphasize the importance of accurate modeling of in-vessel BWR core damage phenomena, since events which take place during the in-vessel phase of an accident ultimately determine the initial and boundary conditions for the ex-vessel events that may result in containment failure and releases to the environment.

1.4 The DF-4 Experiment

Because of the significant design differences between the BWR and PWR core designs and because of the lack of any previous experimental investigations of BWR severe core damage phenomena, the DF-4 experiment was designed to investigate the behavior of BWR core geometry under severe reactor accident conditions. The key BWR structural features, including fuel rods, canister, and control blade were included in the DF-4 test section design, shown in cross section in Figure 1-5. The cross section is representative of an approximately .5 m long test bundle.

The chief aim of the DF-4 BWR experiment was to examine the phenomena associated with failures of and interactions between the control blade, fuel canister,

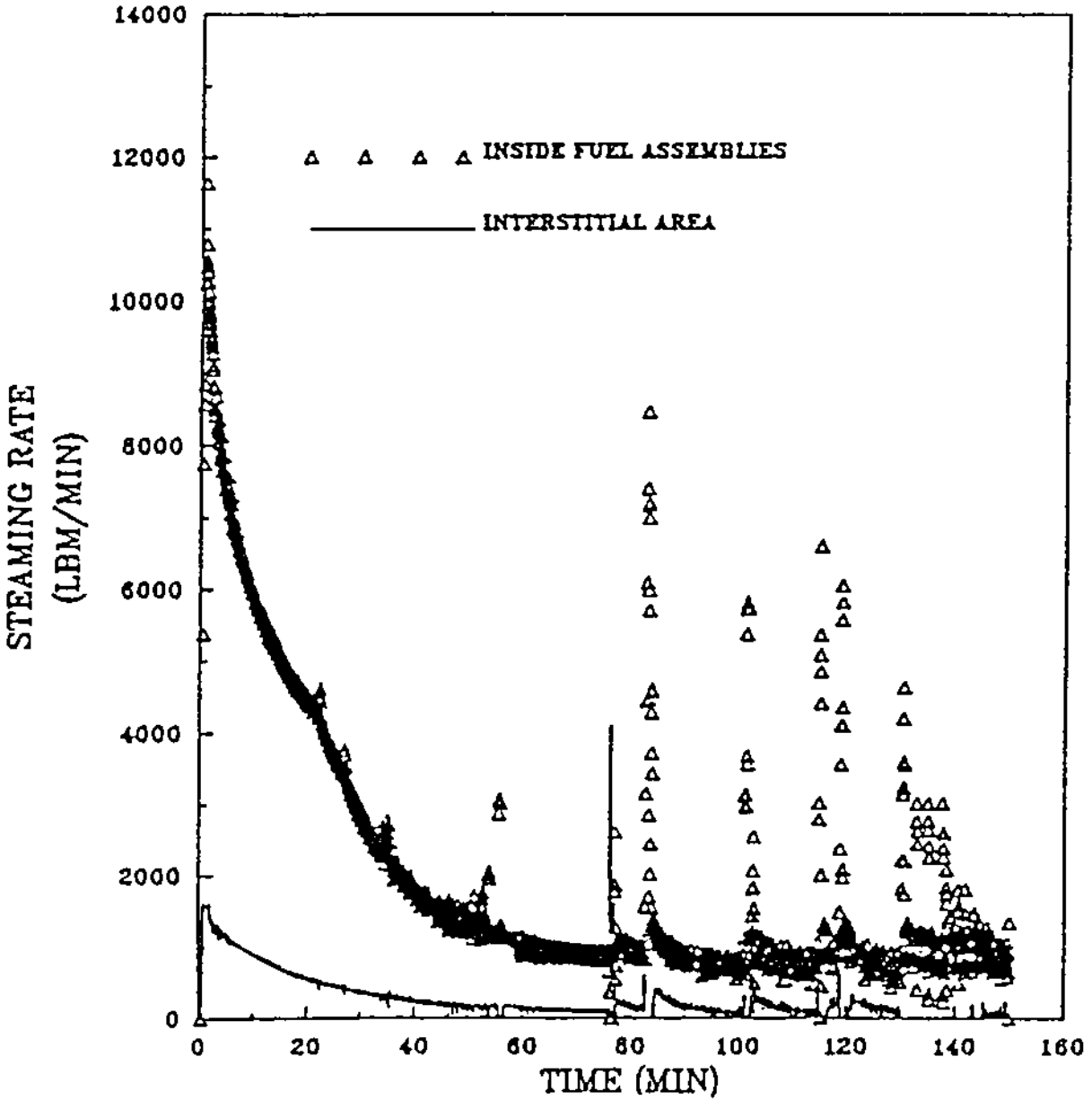

Figure 1-4: MARCON2.1B calculations for Browns Ferry under Station Blackout conditions with stack open relief valve (SORV) and operating control rod drive hydraulic system (CRDHS).

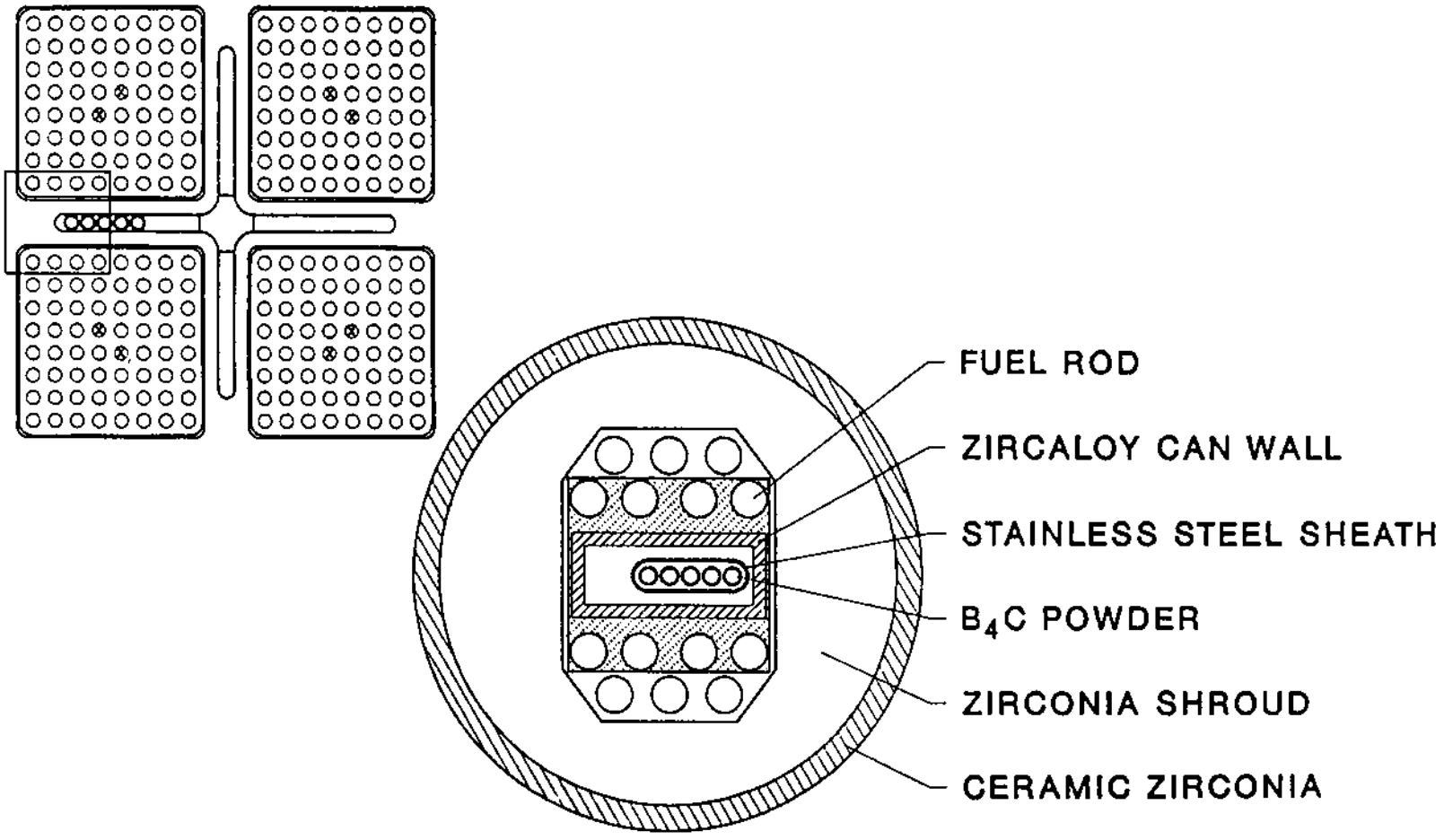

Figure 1-5: Cross section of the DF-4 test bundle showing control blade, channel box (canister walls), and fuel rods. Also shown is location in the BWR core which corresponds to the DF-4 design

and fuel rods in the BWR core. These phenomena were explored by initiating high temperature steam oxidation in the test bundle. In the DF-4 test, fresh fuel rods were used, and fission product decay heat was simulated by fission heating of the 10% enriched (U^{235}) fuel rods, using the ACRR to drive the experiment heatup. Steam was fed through the bundle, supplied by an external steam plant. Important physical processes occurring simultaneously in the damage of the test bundle include: steam oxidation of zircaloy (both fuel cladding and channel box), stainless steel, and possibly B_4C; liquefaction and eutectic interaction between UO_2/zircaloy, stainless steel/B_4C, and stainless steel/channel box zircaloy; and, blockage formation from the refreezing of relocated previously molten components.

As in the BWR core, separate flow regions exist in the DF-4 representation for the fuel rod and the control blade regions. The rectangular channel box in the DF-4 test bundle prevents cross flow of steam between the two zones. (Note that in the DF-4 representation, the region inside the rectangular channel box corresponds to the interstitial/control blade region which is outside the fuel canisters in the actual BWR). Steam flow rates to each zone were established with consideration given to the differences in steaming rates and hydraulic resistance inside the fuel canister and around the control blade tip of the General Electric "D-Lattice" core design, such as is used in the Browns Ferry plant.[14] The "D-Lattice" dimensions are given in Figure 1-6. As discussed in Section 1.3, the steam that flows in the interstitial region may be highly transient in nature in the BWR because of the periodic actuations of the SRV's. In the DF-4 test, however, the steam flowing inside the control blade region was held constant in the interest of simplifying test interpretation. The amount of steam allocated to flow in the fuel rod and control blade zones corresponded roughly to the conditions characteristic of the Station Blackout/SORV/CRDHS calculation described in the previous section, although slightly lower in actual magnitude. These values were considered to be within realistic bounds and therefore suitable for exploring the attendant phenomena.

The progression of the test was characterized thermally by continuous on-line temperature measurements made possible by thermocouple instrumentation located throughout the test bundle. Visual observation of the damage progression was obtained by use of an end-on viewing port located above the test bundle in the experiment capsule which allowed video and film recording of the experiment. Continuous hydrogen production rates are derivable from temperature measurements of a CuO-H_2 reaction bed through which the test section effluent (including hydrogen produced from steam oxidation of the test bundle) flowed. Additional characterizations are obtained post-test through nondestructive and destructive examination of the damaged test bundle, including tomography, metallography, and scanning electron microscopy.

In the following sections, the details of the experimental procedure used in the DF-4 test are reviewed and important features of test instrumentation and conduct are described. The on-line experimental measurements are presented and discussed, including the thermal response of the fuel rods, channel box, control blade, and the hydrogen recombiner tubes. Comparisons are made between the test data and predictions of a numerical model of the DF-4 experiment test section with the purpose of aiding in the interpretation and evaluation of the experimental data. The test results are summarized and discussed from the perspective of highlighting the key phenomena observed in the test that may be important considerations in mechanistic model development and BWR accident analysis.

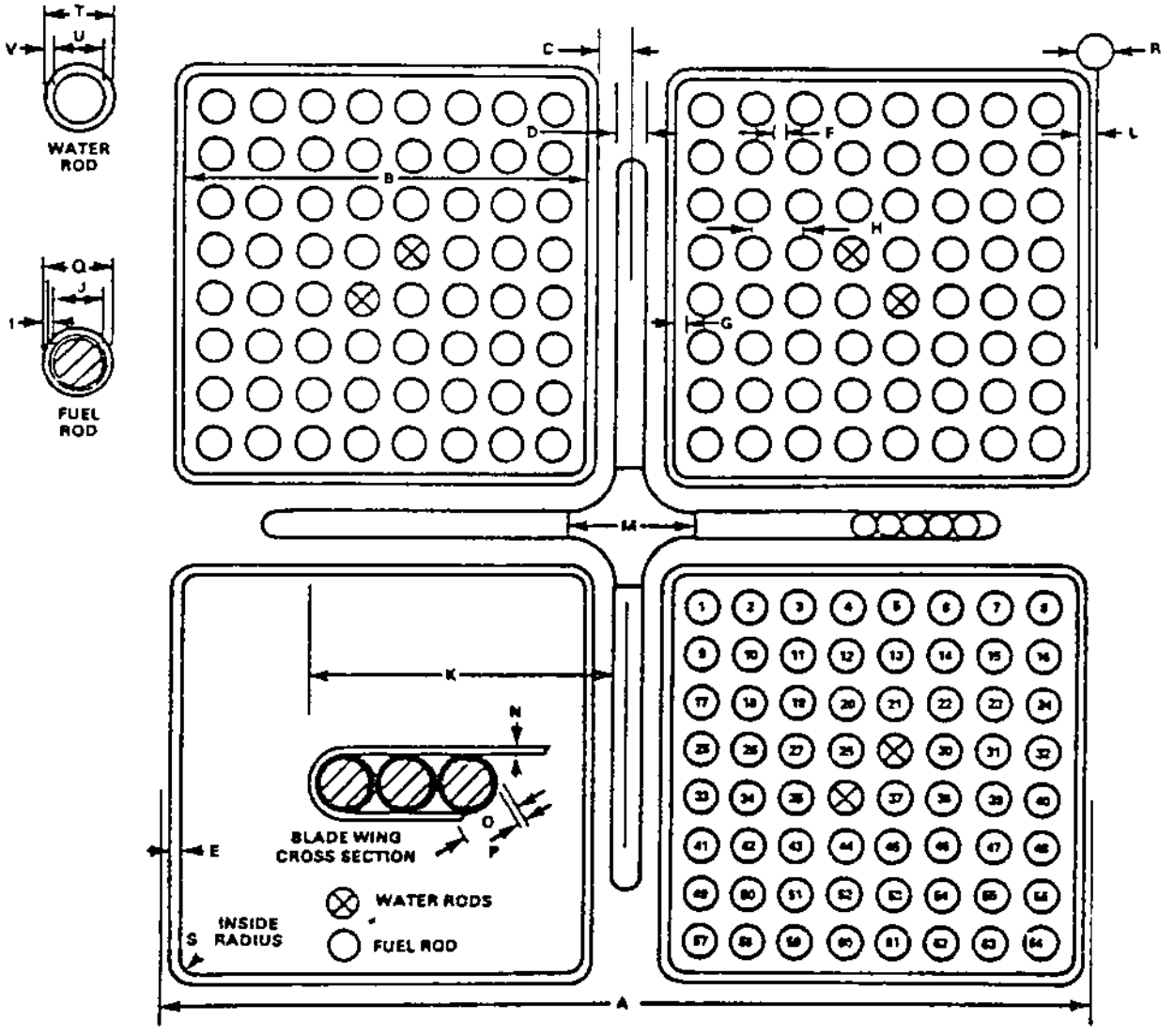

DIM. IDENT	A	B	C	D	E	F	G	H
DIM. INCHES	12.0	5.278	0.356	0.312	0.100	0.157	0.1575	0.840

DIM. IDENT	I	J	K	L	M	N	O	P
DIM. INCHES	0.032	0.410	4.875		1.662	0.056	0.188	0.025

DIM. IDENT	Q	R	S	T	U	V
DIM. INCHES	0.463		0.380	0.581	0.531	0.030

Figure 1-6: Dimensions of the General Electric "D-Lattice" core design.

2. DESCRIPTION OF EXPERIMENT

The experimental apparatus used in the DF-4 test consisted of several major components which will be discussed in detail in the following sections. The first component to be addressed is the experiment test section, which contains the fueled test bundle. Following this, a description of the other major in-pile and out-of-pile ancillary components and instrumentation will be given.

2.1 Test Section

The major feature of the test section is the fueled test bundle, which was made up of fuel rods, a zircaloy-4 channel box structure and an accurate representation of the stainless steel/B_4C control blade. These features are shown in a cross sectional view of the test section in Figure 2-1. Dimensions shown in this figure are in mm.

2.1.1 Stainless Steel/B_4C Control Blade

The control blade structure located in the center of the test bundle was comprised of five B_4C filled stainless steel tubes (SS316). The B_4C powder which filled the tubes was packed to ~70% (1.7 g/cm^3) of theoretical density. Four different B_4C particle sizes were used to obtain this packing density. The mass fraction for each of the particle sizes is given in Table 2-1.

Table 2-1

Size Distribution of B_4C Powder Used in DF-4 Control Blade

mass fraction	size range
.42	20-40 mesh
.31	60-80 mesh
.19	200-325 mesh
.08	< 200 mesh

The B_4C powder was obtained from ESK Engineered Ceramics, New Canaan, CT, a major supplier of boron carbide for nuclear applications. The individual tubes were sealed by welding end caps to the tubes and the backfill gas was ~12 psi (~82 KPa) room air. The five tubes were encased with a thin SS-316 sheath to form a structure resembling the tip region of a BWR control blade. The dimensions used for the individual tubes and the stainless steel sheath were those of the General Electric D-Lattice design used in BWR-4 cores (see Figure 1-6). The blade was situated off center, as shown in Figure 2-1 to create a "tip region" and a "small gap" region through which steam would flow. This was done to assess local oxidation behavior for the blade as it might be influenced by the natural flow patterns of the steam.

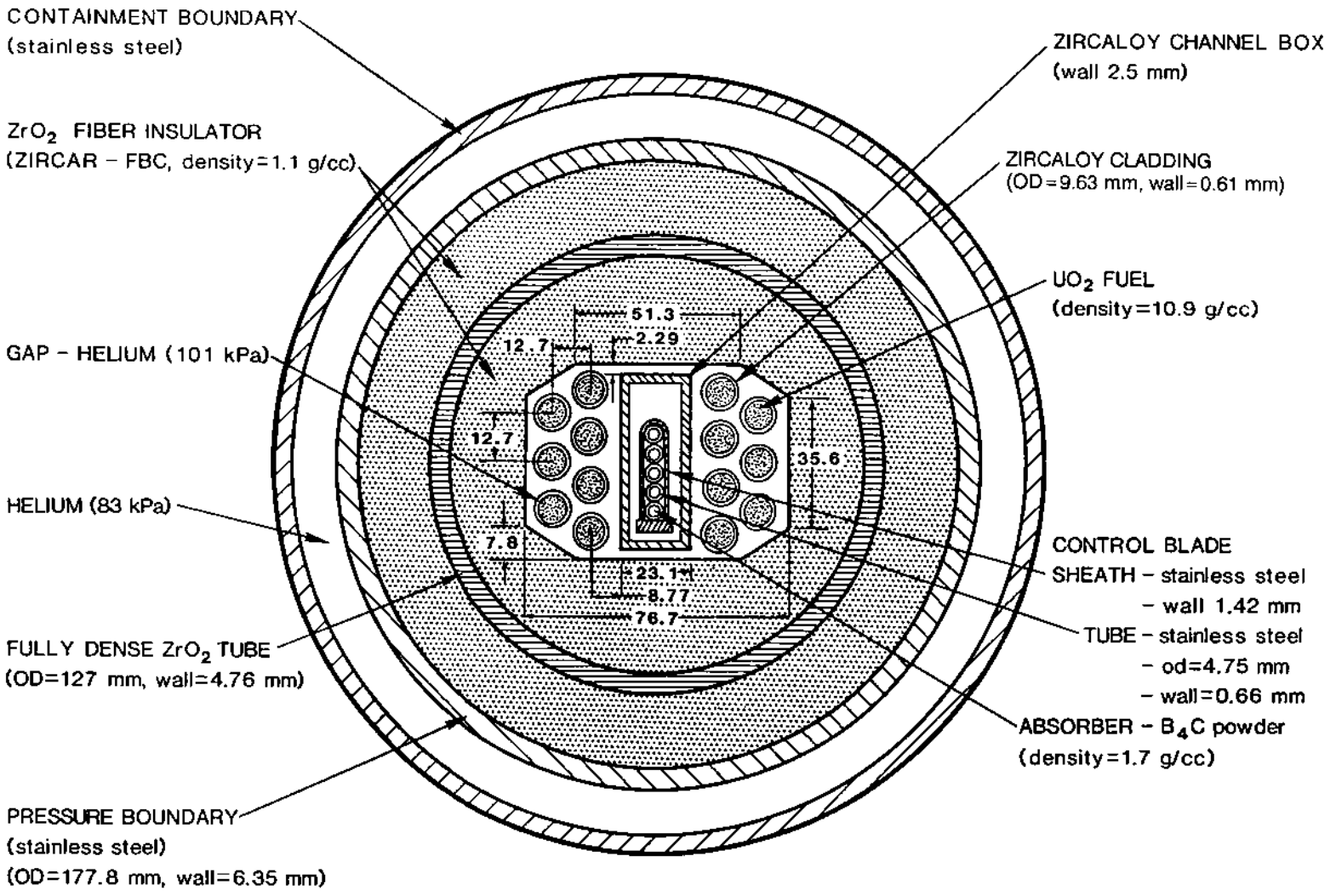

Figure 2-1: Cross section of DF-4 test section showing dimensions of major components

2.1.2 Zircaloy Channel Box

The stainless steel control blade was surrounded on all sides by a Zircaloy-4 channel box which represents the fuel canister walls on either side of the control element in the actual BWR (see Figure 1-5 also). The zircaloy box enclosed the control blade to form two steam flow regions, one associated with the interior box wall and the control blade, and the other associated with the exterior box wall and the surrounding fuel rods. This feature allowed different steam flow rates to be introduced to each region for the reasons discussed in Section 1-3. The Zircaloy-4, obtained from Teledyne Wah Chang, Albany, OR, was BWR fuel canister raw stock having the prototypic 0.1 inch (2.54 mm) wall thickness typical of the GE D-Lattice design. Also prototypic of the D-Lattice configuration is the gap dimension (.205 inch or 5.2 mm) between the channel box surface and the side of the control blade.

2.1.3 Fuel Rods

Seven zircaloy-4 clad fuel rods were situated on either side of the channel box structure. The first row of four fuel rods located nearest to the channel box were spaced on a .5 inch (12.7 mm) pitch which is characteristic of D-Lattice dimensions, and the distance between the cladding surface and the channel box wall was also prototypic; however, the fuel rod diameter was not prototypic. The rods used in DF-4 were "PWR" type rods (which were readily available) and were slightly smaller in diameter than "BWR" rods; 0.379 inch (9.63 mm) for PWR rods vs. 0.483 inch (12.27 mm) for BWR's. The second row of three rods were situated on a triangular .5 inch (12.7 mm) pitch relative to the first row of rods rather than the usual square pitch used in BWR fuel assemblies. This was done to improve the effectiveness of the back row of rods (guard rods) in heating the channel box by increasing the radiative view factor between them, and to decrease the lateral spatial requirements of the bundle.

Each fuel rod contained a fissile section, 20 inches (508 mm) in length, comprised of UO_2 pellets which were enriched in U-235 content to 10%. The pellets were manufactured at Battelle Pacific Northwest Laboratories (PNL) and measure 0.325 inch (8.26 mm) diameter by 0.372 inch (9.45 mm) in height. The ends of each pellet were machined with a dished shape (vol = 1%) and the UO_2 density was 10.9 gm/cm^3. The stoichiometry of the fuel was $UO_{2.002}$.

Both above and below the fissile UO_2 pellets were short non-fissile segments of Al_2O_3 pellets. The length of Al_2O_3 below the fissile zone was 38.1 mm and the length above the fissile section was 47.75 mm. The entire stack of fissile and non-fissile pellets was held in compression by an Inconel-X spring located in the upper fuel rod plenum. Zircaloy-4 end caps closed off both ends of the rod. The backfill gas in the DF-4 fuel rods was helium with a pressure of 14.7 psia (10^5 Pa). The end to end assembled length of the fuel rod was 29 inches (736.6 mm) with a 20 inch (508 mm) fissile length (see also Figure 2-3).

2.1.4 Test Section Insulation

The test bundle, comprised of the control blade, channel box, and 14 fuel rods, was shrouded on all sides by an insulating material whose inner surface conformed to the general shape of the test bundle (Figure 2-1). The insulation material was a low density (1.1 gm/cm^3) fiberous ZrO_2 product (Zircar Products, Florida, NY) which had been stabilized to form a rigid but porous (77% porosity) material. The material was

available in short cylindrical segments (6 inches or 152 mm in length) which were lap jointed on each end and assembled in several segments to form the shroud and the principal heat barrier of the DF-4 test bundle.

The outer diameter of the zirconia shroud was 122 mm. The assembled shroud in turn was enclosed by a high density ceramic zirconia tube, which acted as a barrier to molten materials that in the course of the experiment might penetrate the low density shroud. The high density (98% theoretical) ceramic tube was fabricated from yittria stabilized (8%) ZrO_2 and was purchased from Corning Products (Corning, New York). Although essentially-fully dense, the ceramic tube does not represent a leak tight barrier because of numerous instrumentation penetrations in the side wall of the tube. An additional layer of low density zirconia insulator (Zircar-FBC) was applied between the ceramic tube and the heavy steel wall (0.25 inch or 6.35 mm) of the test section pressure boundary, as shown in Figure 2-1.

Since the test section contained pressurized steam during operation the outer steel pressure boundary was heated to prevent condensation on what would otherwise be a cold surface. This was achieved by covering the outer surface of the pressure boundary with cable type electrical heaters which were firmly attached to the surface by steel shim strips, spot welded in place. To prevent condensation of steam during the DF-4 test, which operated at 100 psi (689 kPa, T_{sat} = 435K), the pressure boundary was heated to approximately 473K.

The pressure boundary formed the outer boundary of the test section. The test section itself and other components were enclosed within a second steel tube which constituted a containment boundary for fission products produced during operation of the test. The test section and containment canister are shown in axial cross section in Figure 2-2, as situated in the ACRR core during operation of the test. The axial positioning of the test section relative to the ACRR core midplane is such that the fissile length of the fuel rods (one rod shown) in centered within the core. The fission heating profile (axial) in the fuel rods was made relatively flat along the length of the bundle by aligning the axial test bundle center with the ACRR midplane and by using an inconel thermal neutron filter (located on the containment canister) to flatten the ACRR midplane flux. An analysis of the axial power distribution and the total bundle power based upon measurements obtained during the experiment is presented in Chapter 4.

2.1.5 Inlet Steam to Test Bundle

The test bundle components (fuel rods, channel box, and control blade) are represented in Figure 2-2 by a single fuel rod. The fuel rods were captured both at the top and at the bottom by stainless steel fixtures which held the rods in the correct lateral arrangement depicted in Figure 2-1. The lower fixture also served the function of distributing steam to the fuel rod/channel box exterior region and to the control blade/channel box interior region. Two steam inlet lines fed a common lower plenum below the lower fuel support grid. The steam was apportioned to the different flow zones by use of several small apertures which fed each flow region. The flow proportions were fixed to feed 40% of the flow to each 7 rod zone on each side of the channel box, and the remaining 20% to the interior of the channel box where the control blade was located. This distribution of flow was selected based upon consideration of the steaming rates for the BWR interstitial and fuel canister zones as discussed in Section 1.3, and upon the flow patterns expected around the tip of the

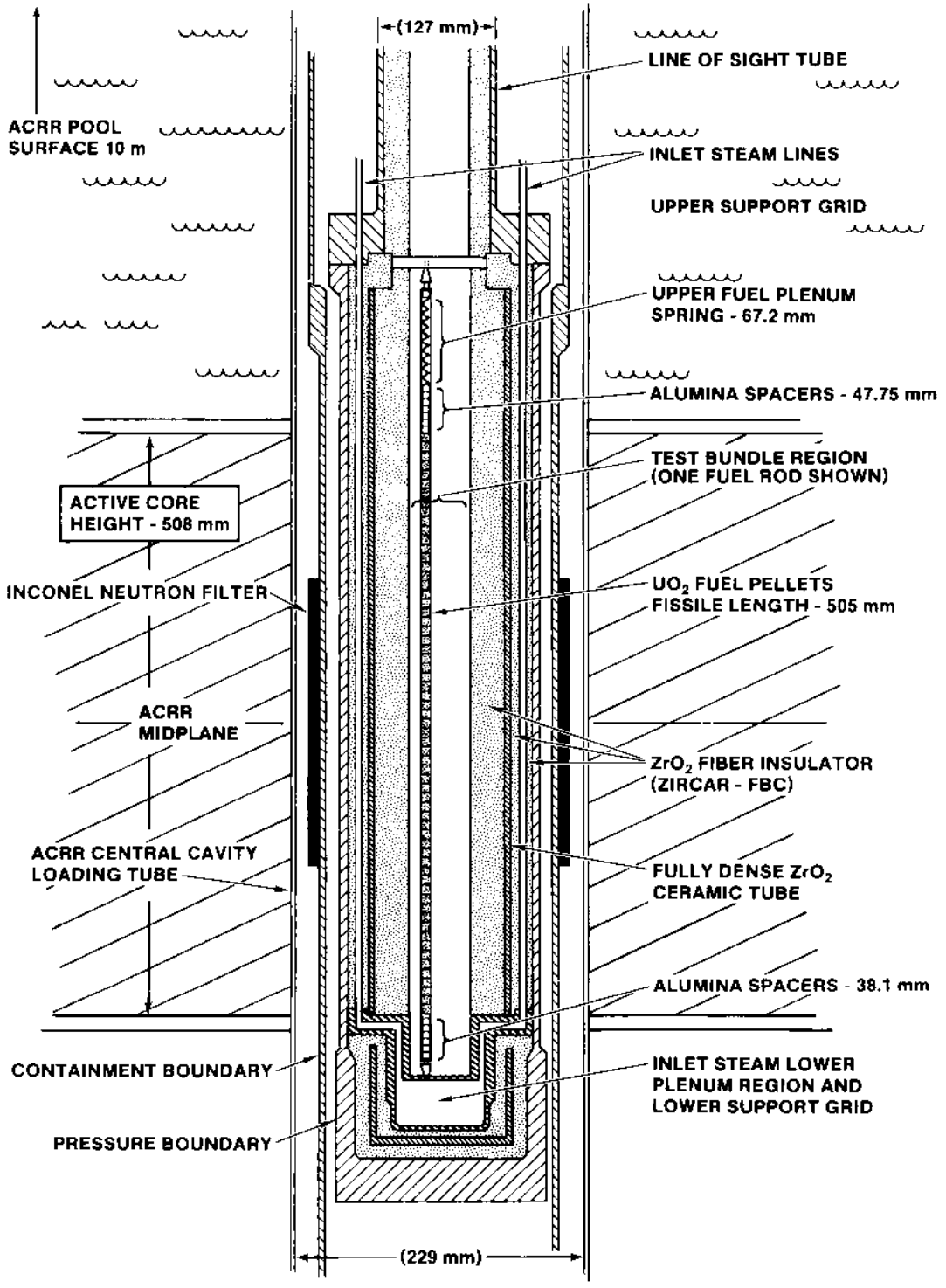

Figure 2-2: Axial section of DF-4 test section showing location of test bundle in the ACRR.

control blade. In this way, steam entered the bundle at the bottom and flowed upwards, and the effluent exited at the top of the bundle, where the two flows freely merged together.

Although the fuel rods were fixtured both at the top and bottom, the channel box and control blade structures were fixed only at the bottom, and the upper end of each structure was allowed to "float" in the axial direction. This allowed each structure to expand in length independently as the temperature of the bundle increased during the test. Lateral support was provided at the upper end of the control blade and channel box by a keyway in the upper steel support grid.

The test bundle was viewed from the top end during the operation of the experiment. This was made possible by the line of sight tube, shown in Figure 2-2. A quartz window was located at the top end of the line of sight tube, providing a transparent viewing port into the test section.

2.1.6 Test Section Instrumentation

The test section was instrumented with numerous thermocouples which tracked not only the temperatures of the test bundle components, but also temperatures within the radial insulating layers and on the boundaries of the pressure vessel.

2.1.6.1 Thermocouple Instrumentation Techniques

The fuel rods were instrumented with two types of thermocouples, type S and type C. The type S thermocouples were Pt/Rh thermocouples housed in a 1/16 inch (1.59 mm) diameter Pt sheath. Installation of the type S thermocouples was as shown in Figure 2-3. The Pt thermocouples were run axially along the inner surface of the dense ZrO_2 ceramic tube, brought radially inward through the low density insulator, and again were run a short axial distance along the fuel rod length (30 mm to 100 mm) to a point where the thermocouple junction was welded to the surface of the cladding. The individual Pt/Rh wires (.01 inch or .254 mm in diameter) were spot welded to the cladding, where the Pt sheath had been striped back by a distance of ~.3 inches (7.6 mm). Strain relief to the delicate junction was achieved by strapping the thermocouple to the fuel rod using Pt wire. The axial run of 3 to 10 cm along the fuel rod near the junction was intended to minimize heat conduction along the Pt wire by running the wire along a region of minimum thermal gradient. This together with the low thermal inertia of the intrinsic welded junction was assumed to provide a measurement with minimal local perturbation.

Because the Pt/Rh thermocouples do not survive the high temperature regime of the experiment, another type of thermocouple instrumentation was developed that would endure the high temperatures associated with the cladding oxidation. This thermocouple is also shown in Figure 2-3. The sensing element itself is a type C W/Re thermocouple manufactured by HEDL (Westinghouse-Hanford, Richland, WA 99352). The thermocouple wires were electrically insulated with HfO_2 and sheathed in a rhenium tube (.071 inches or 1.8 mm in diameter). A stainless steel sheathed extension wire (Type C) was joined to the rhenium tube. Since the rhenium sheath of the thermocouple would oxidize badly in the high temperature steam environment, the thermocouple was encased inside a protective housing containing a helium environment (5 psia or 34 kPa). This assembly is shown in Figure 2-3.

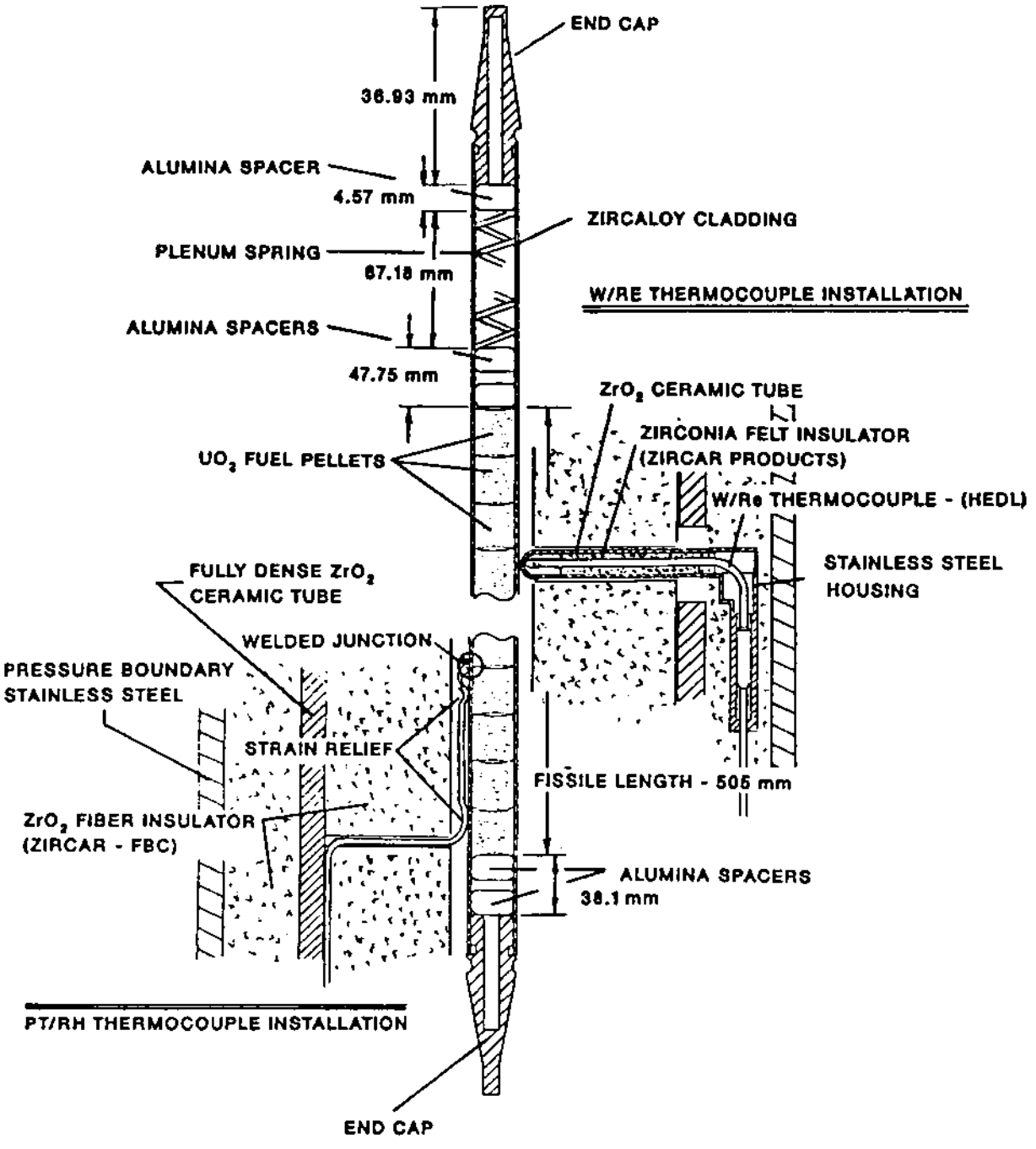

Figure 2-3: Thermocouple installation techniques for type S and type C test bundle thermocouples.

Near the junction of the thermocouple, the protective housing was formed by a closed end ceramic zirconia tube (.25 inch or 6.35 mm diameter by .027 inch or 0.673 mm wall thickness). The ZrO_2 tube, obtained from Corning Glass Works, Corning, NY 14831, was yittria stabilized (8%) and high density (95%). This portion of the thermocouple assembly penetrated through the low density zirconia shroud and contacted the surface of the fuel rod. The protective ceramic tube was brazed to a steel housing near the region where the thermocouple makes a 90° bend (Figure 2-3). The thermocouple extension wire was connected to the rhenium portion of the thermocouple in this region of the assembly and extended out through the steel housing. From there, the extension wire ran axially along the length of the test section to a penetration feedthrough in the bulkhead of the pressure boundary (Figure 2-2).

Although the thermocouple assembly was capable of enduring the high temperature oxidation phase of the test, the temperature sensed at the thermocouple junction lagged significantly the fuel cladding temperature. The major source of the difference between the fuel cladding and thermocouple junction temperatures can be attributed to two factors: (1) the thermal resistance offered by the protective ceramic zirconia housing which lies between the fuel cladding and the thermocouple junction, and (2) the heat conduction along the thermocouple wire itself, which runs normal to the isotherms in the test section insulation. These two factors cause the thermocouple junction temperature to lag the fuel cladding temperature by several hundred degrees K. A detailed thermal analysis of the thermocouple assembly is presented in Section 4.4 of this report.

2.1.6.2 Locations of Test Bundle Thermocouples

Both of the methods described in the previous section were used to instrument the fuel rods of the test bundle, whereas, only W/Re assemblies were used in instrumenting the channel box. For the stainless steel control blade, only the intrinsic junction type S thermocouples were used.

The distribution of the two thermocouple types throughout the bundle is described schematically in Figure 2-4. Shown in this figure are four cross sections through the test bundle for four different axial locations in the test section. The indicated axial plane is relative to the bottom of the 508 mm fissile length of the fuel rods. The two thermocouple types are distinguished both by the schematic representation and by the six character identification label given to each thermocouple. Schematically, the W/Re assemblies are shown as "fingerlike" structures which penetrate through the outer ceramic barrier and the zirconia fiber shroud, and touch either a fuel rod or one end of the channel box. The Pt/Rh intrinsic junction thermocouples, on the other hand, are shown as a dark bump, located on either fuel rods or on the surface of the control blade. The six character label also identifies the thermocouple type and location. To illustrate the label interpretation, the following example is provided:

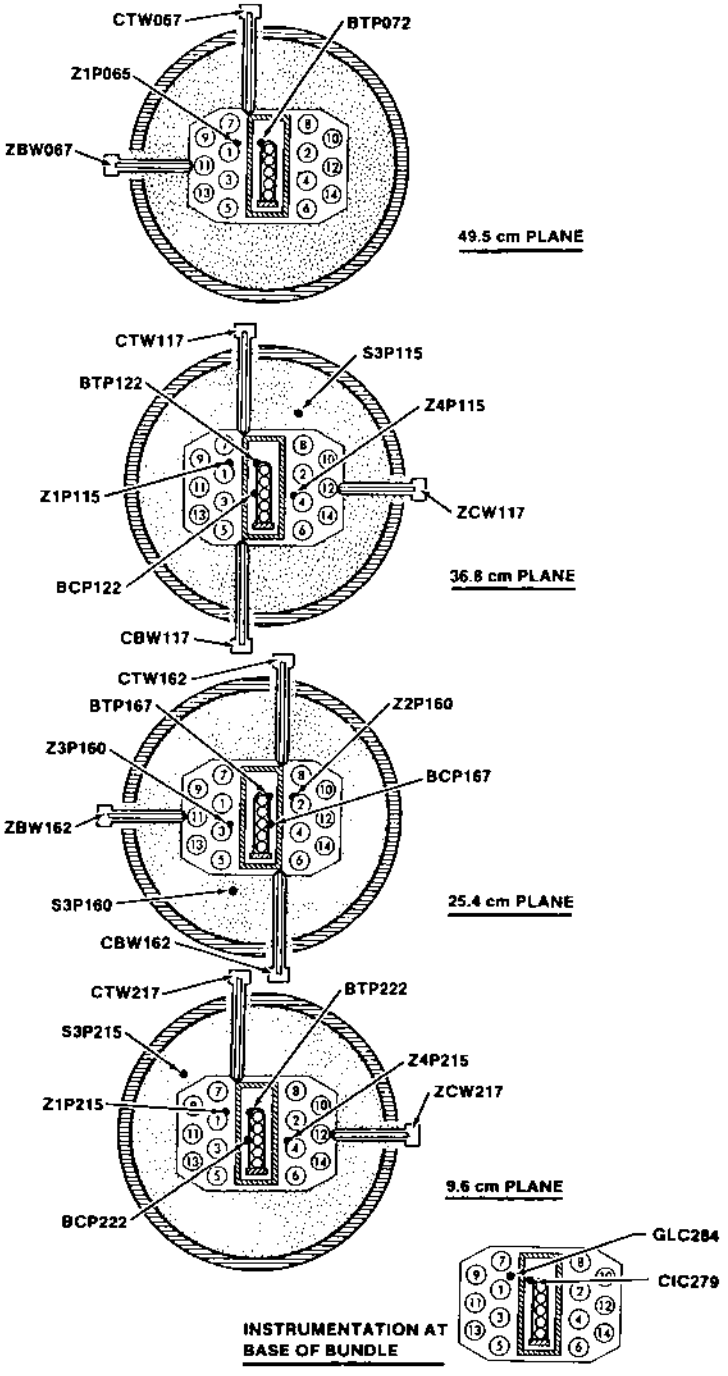

Figure 2-4: Locations of test bundle thermocouples - shown are cross sectional maps at five axial planes.

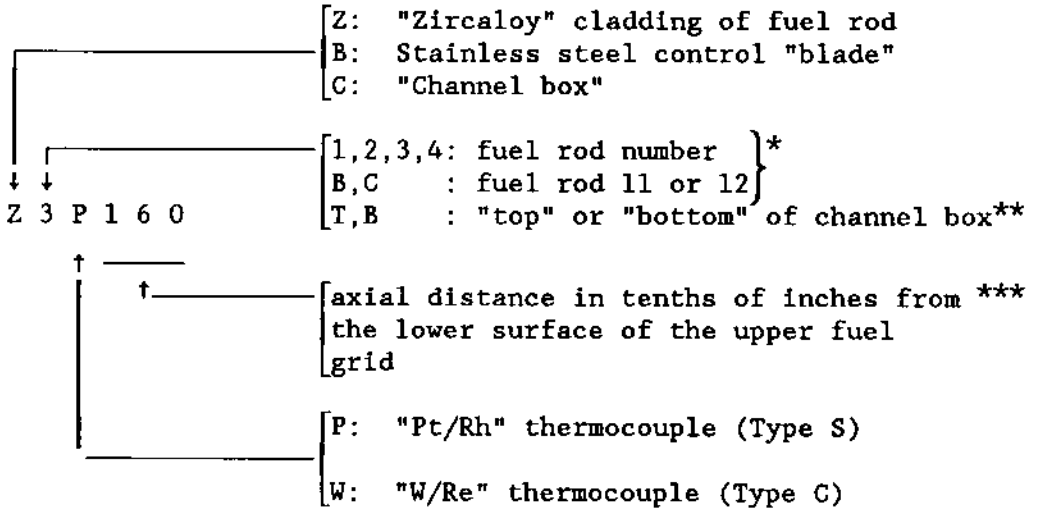

* - this notation used only if the leading prefix is "Z" for zircaloy fuel rod cladding
** - this notation used when the leading prefix is "C" for channel box
*** - this datum is located 26 inches (660 mm) above the bottom of the fuel rod fissile length.

In addition to the type S and type C thermocouples used to instrument the fuel rods, channel box, and control blades, a few other thermocouples are also shown in Figure 2-4. In three of the cross sections, type S thermocouples are shown inside the low density zirconia shroud. These thermocouples are located 0.3 inches (7.62 mm) inside the shroud relative to the inner surface of the shroud boundary. In these cases, the tip of the thermocouple sheath was left intact in variance with the technique applied to the welded junction thermocouples used to instrument the fuel rod cladding and control blade. Note that although the instrumentation is clustered at four principal axial locations which are described nominally as 9.6, 25.4, 36.8, and 49.5 cm relative to the bottom of the fuel rod fissile length, in actuality, small differences in axial location exist for each thermocouple at a given nominal axial location. This difference is greatest for the control blade thermocouples. The slight differences were due to constraints related to assembly. The exact axial location may be found by referring to the coded instrumentation name which reveals the junction location relative to the upper fuel rod support grid (assembly datum point), as described in the above example. The upper fuel rod grid datum was located 26 inches (660 mm) above the bottom of the fuel rod fissile length.

At the base of the test bundle, two additional thermocouples were installed as shown in Figure 2-4. These thermocouples were type K (Cr/Al) 1/16th inch stainless steel sheathed, ungrounded junction thermocouples. One thermocouple was situated at the base of the fuel rod/exterior channel box region near rods 1 and 7, and the other was located at the base of the control blade on the inside of the channel box. This region of the test bundle was initially very near the temperature of the steam that entered the test bundle, being several inches (1.9 to 2.4 inches) below the bottom of the fissile zone. The purpose of the thermocouples in this location was to indicate any sudden arrival of much hotter relocating molten materials which would be evident from a sudden very rapid and large increase in local temperature.

Numerous other type K thermocouples were located on the ceramic zirconia melt barrier which was situated between the two radial zones of low density fiberous insulator, and at various locations on the outer surface of the test section pressure boundary. (A complete descriptive list of the on-line instrumentation is to be found in Appendix A.)

2.2 Associated In-Pile Apparatus

The test section is the principal component of the in-pile test apparatus, which is actually a pressurized flow system. Important aspects of this flow system, including the major control and diagnostic functions will be discussed in the following sections.

2.2.1 Description of the In-Pile Flow System

The in-pile flow system of the DF-4 experiment consisted of the test section and numerous other components through which steam, coolant, or test bundle effluents flow. The various flow circuits are shown schematically in Figure 2-5. Notice that steam flows into the test section at three different points. The inlet steam, which has already been discussed in Section 2.1.5, fed the test bundle and sustained the zircaloy oxidation which caused the high temperature transient of the test. The effluent from the test section flowed upward and was composed principally of high temperature steam or hydrogen produced by oxidation of the metallic bundle components. At the top of the "mixing tube," which is the uppermost region of the test section, another flow of steam entered the flow system. The purpose of this steam flow, referred to as "window steam," was to purge the viewing region below the quartz window of aerosol carried up with the test section effluent. This prevented deposits from forming on the viewing window and improved the image quality. The third flow of steam, labeled "bypass steam," served to further dilute and cool the hot test section effluent as the three flow streams converged prior to exiting the test section. This third flow is referred to "bypass steam" because it bypassed the test section and entered the effluent flow at a location approximately 600 mm above the exit of the test bundle. This flow stream has also on occasion been referred to as "cool steam," since its purpose was to cool down the hot test section effluent.

The test section effluents and dilution steam flows exited the test section assembly and flowed through two identical parallel paths through the remainder of the system. The first component in the remainder of the circuit is the copper oxide/hydrogen recombiners. The CuO/H_2 recombiners will be discussed in greater detail in Section 2.2.5. In the recombiners, any H_2 carried with the flow stream was converted back to steam by the reaction with CuO,

$$CuO + H_2 \rightarrow Cu + H_2O\,(g) + 92.3\ KJ\,.$$

The flow that exited the recombiners was principally steam, which subsequently flowed through a regulating valve (Nupro 4B Series) before entering the steam condenser. The purpose of the valve was to regulate the pressure in the test section and was remotely adjusted to allow more/less flow to enter the low pressure condenser side of the flow system if the test section pressure became too high/low. Furthermore, the valve position was monitored and recorded to facilitate analysis of the steam flow exiting the test section. The steam flow exited the condenser as liquid condensate which drained into a holding tank located at the bottom of the in-pile capsule.

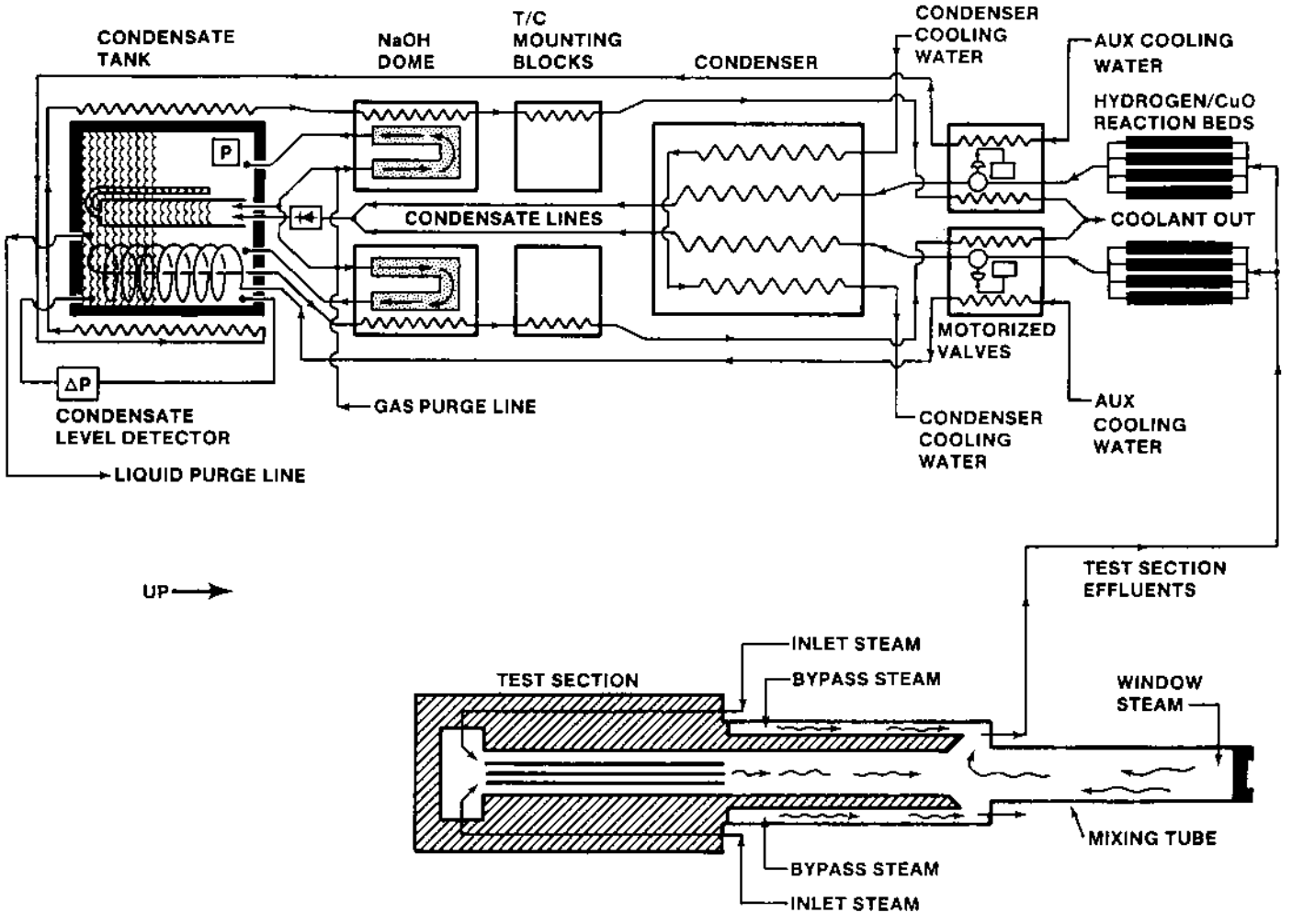

Figure 2-5: Schematic of in-pile experiment flow system

The flow system was also instrumented with pressure transducers at several locations along the flow circuit. Some of these are shown in Figure 2-5. A differential pressure transducer was situated near the condensate tank at the bottom of the in-pile capsule. This transducer measured the weight of the condensate in the tank and thus, provided an indication of the amount of condensate in the tank, and the free volume remaining. The transducer used was a Valydine AP10 Series. An absolute pressure transducer (Kulite Model XTME-100) was located in the condensate tank to measure the absolute pressure in the condensed liquid region of the flow system. In this location, the pressure was approximately equal to the saturation pressure of the condensed liquid in the tank at the start of the test, but increased later, due to the compression of noncondensed gases that accumulated in the tank as the liquid condensate gradually displaced the free volume.

Another absolute pressure transducer, (Kulite Model XTME-100) was located on the inlet steam line just above the in-pile capsule bulkhead. This transducer measured the test section pressure throughout the experiment. This pressure, which was a function of the density of the steam in the heated test section, was held approximately constant at ~100 psia (690 kPa) by balancing the in-flow of steam from the steam plant to the test section with the out-flow of steam through the exit flow motorized valves to the condenser/condensate tank shown in Figure 2-5. In the in-pile flow circuit, the principal pressure drop was across the motorized valves.

2.2.2 NaOH Dome

The NaOH dome is a device which failed to operate as intended. The component was compromised because of an aborted first attempt at running the experiment, which because of moisture uptake by the NaOH caused to pellets to become liquefied thereby blocking the passage of gas through the device. Its purpose was to detect the presence of CO_2 gas carried into the holding tank with the condensate by monitoring for the exothermic reaction with NaOH. A liquid/gas U-tube type separator located in the condensate tank would have caused any non-condensed gas to flow through the NaOH particle bed.

2.2.3 Heat Rejection Circuits

Two water coolant streams entered the in-pile capsule for the purpose of removing heat and cooling certain components, as shown in Figure 2-5. One coolant path was reserved for removing the heat of vaporization released in the condenser when the steam condensed. An auxiliary cooling circuit removed heat from many of the capsule components, including the motor driven regulating valves, the thermocouple mounting block, the NaOH dome, and the liquid condensate holding tank. Since neither of these coolant circuits came into contact with fission products while flowing through the experiment capsule, the coolant and waste heat could be disposed of without special precautions.

2.2.4 Condensate Tank Gas/Liquid Purge

After the initiation of nuclear heating of the test, it was required that the condensate tank (Figure 2-5) be isolated from the outside environment by actuation of explosively actuated closure valves. Prior to this time, however, the accumulated water in the tank could be voided through the liquid purge line shown in Figure 2-5. This was done just

prior to beginning the nuclear heatup phase in order to maximize the length of time the test could operate. This was accomplished by pressurizing the condensate tank with helium using the gas purge line. The condensate was forced out through the liquid purge line and in this way rejected from the experiment capsule. A check valve located in the condensate line connecting the condenser to the condensate tank prevented liquid from being blown from the condenser back into the test section during the tank purging process. The gas purge line was also used to pump noncondensed gases out of the flow system following the liquid purging procedure.

2.2.5 CuO/H_2 Recombiner Tubes

As discussed briefly in Section 2.2.1, the CuO/H_2 recombiner tubes converted any hydrogen produced by metal-water oxidation in the test section back to steam. This was necessary to prevent passage of noncondensible H_2 into the condenser/condensate tank regions. Failure to do this would result in pressurization of the low pressure condensed liquid region of the flow system which would prevent any additional flow of steam into the test section.

The CuO/H_2 recombiners also served another important function, namely as a H_2 production rate diagnostic. By performing a heat balance on the recombiner tube geometry, the chemical energy evolved from the reaction $CuO + H_2 \rightarrow Cu + H_2O$, may be determined, and from this, the hydrogen production rate may be calculated. Since this is a very important diagnostic component, a thorough description of the recombiner tubes, and their function is given.

The eight recombiner tubes were grouped in two banks of four, each bank connected with a common mainfold (4 per manifold) on the tube outlets. The outlet of each tube bank followed identical but separate flow paths until finally converging at the condensate tank, as described previously (Figure 2-5). The eight tube inlets were fed from a single common plenum region in the test section assembly.

Each recombiner tube consisted of a steel tube packed with CuO particles as shown in Figure 2-6. A steel fiber filter was located at the inlet to prevent large amounts of aerosol from entering the CuO bed and coating the particles. The external surface of the steel tube was heated to approximately 750K in order that the copper oxide reduction reaction would proceed spontaneously. The tubes and attached electrical heaters were insulated to decrease heat losses.

In each bank of four recombiner tubes, one of the tubes was specially instrumented with thermocouples (1/16" stainless sheathed type K thermocouples) which penetrated into the CuO particle bed in the tube. These thermocouples measured the heat generated and convected through the CuO bed from the reaction with H_2. The other three tubes in the bank were identical, except that no internal bed thermocouples were used.

A computer code (COPOX) was developed (additional information is included as Appendix B) which models the heat transfer occurring within the tube, using the information provided by: the internal CuO bed thermocouples, the tube heater power, and additional thermocouples placed on the outer surface of the tubes. The result of the heat balance is an estimation of the hydrogen production rate. To aid in the use of this tool, a calibration experiment was conducted prior to the actual experiment where a known volume of hydrogen was injected into the flow system at a metered rate. In

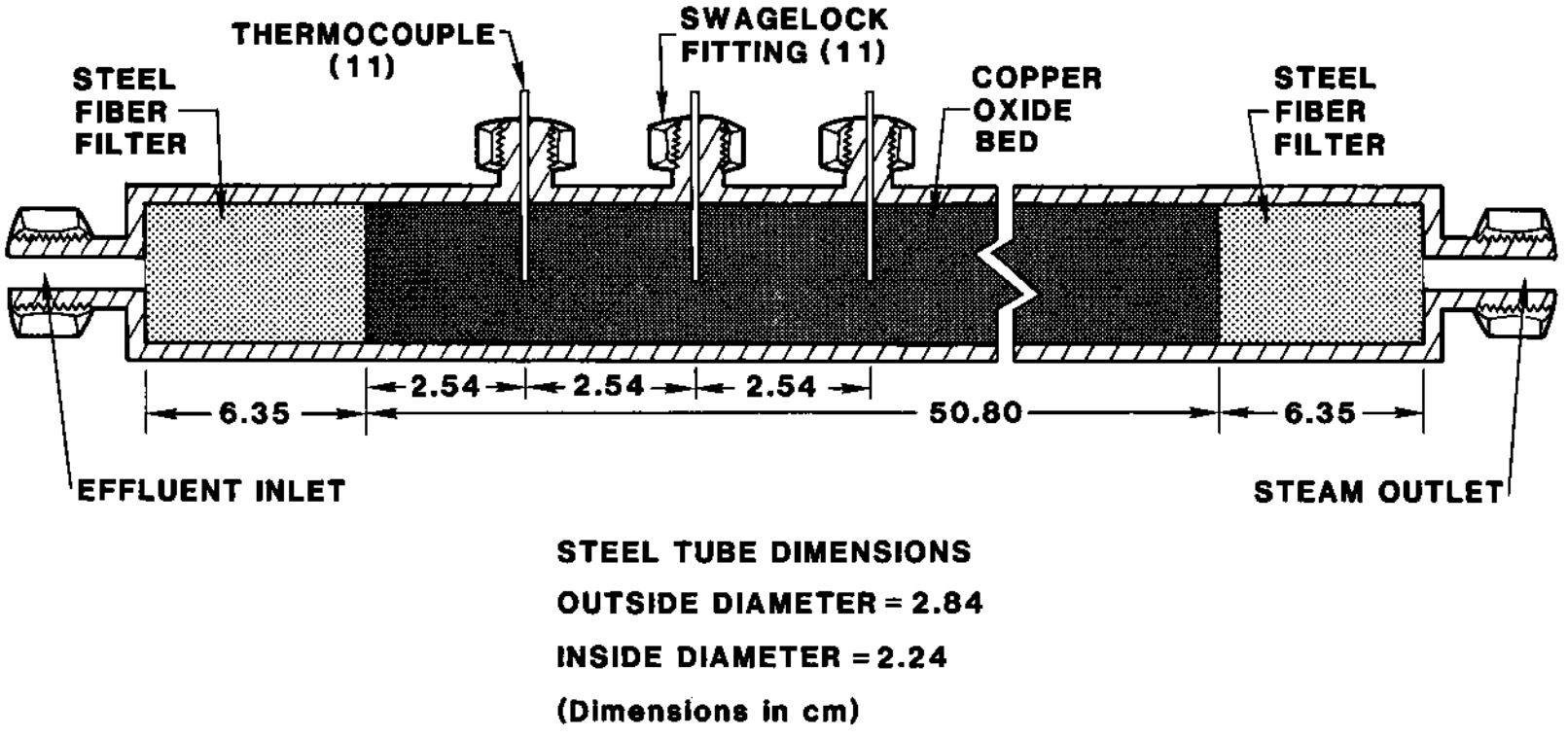

Figure 2-6: Axial section view of instrumented CuO/H_2 recombiner tube

this way the CuO recombiner tube thermal response could be analyzed under known hydrogen flow rate conditions. The thermal response of the CuO recombiners to the calibration H_2 injected and to the actual H_2 produced in the fuel damage phase are both presented in Chapter 3. It should be noted however that the results of the analysis of the hydrogen reaction tubes is not given in this document. Rather, a separate document (currently under preparation) will detail more information on the performance of the hydrogen reaction tubes.

2.3 Associated Out-of-Pile Apparatus

The in-pile components of the experiment, discussed in Section 2.2 were housed in a stainless steel tube, which formed the containment boundary, and located in the central cavity of the ACRR. The in-pile vessel was connected to numerous components which were located out-of-pile on the reactor room floor, approximately 8 M above the ACRR core. A description of these out-of-pile components follows.

2.3.1 Out-of-Pile Flow System

The plumbing connections for the out-of-pile flow system are shown schematically in Figure 2-7. The three steam inlet lines feeding the in-pile test section originate at a boiler system. The boiler provided steam to the flow system at a pressure roughly equal to the desired experiment operating pressure of ~100 psi (690 kPa), (slightly higher to overcome frictional losses in the flow lines). Between the boiler and the in-pile capsule, the steam flow lines were trace heated and insulated to provide some steam superheat (~40 K) and prevent condensation of the flowing steam. The flow in each of the three steam lines was independently regulated and measured with flow controllers (Telledyne Hastings-Raydist Model NALL-50KP). Line pressures were measured at various points in the flow circuit as shown in Figure 2-7.

A system for injecting H_2 into the "bypass steam line" is also shown in this figure. Here a 4 liter bottle was filled with H_2 at 400 psi (2.7 MPa), and allowed to flow into the test section and through the CuO/H_2 recombiner tubes for calibration purposes as described in Section 2.2.5. A flow controller (Matheson Model 8240) maintained the H_2 flow rate at ~30 standard liters per minute for about 2.3 minutes. Also shown are the gas and liquid purge lines, discussed in Section 2.2.4 and the coolant inlet and outlet lines, discussed in Section 2.2.3. The results of the calibration experiment are given in Chapter 3.

The containment technology applied to the DF-4 experiment allowed for steam to enter the in-pile capsule, however, after beginning the nuclear phase of the experiment, no effluents carrying fission products were allowed to emerge from the experiment. (The coolant lines do not come into contact with fissions products, and hence were allowed to leave the experiment capsule.) Several precautions were taken to prevent the possibility of backflow of fission products through the inlet, window, and bypass steam lines. These took the form of both passive systems (redundant check valves) and active systems (pneumatic isolation valves and explosively sealed valves on the two purge lines). A detection of backflow (Δp transducers) or fission products (radiation monitor) would have caused the pneumatic isolation valves to close. After beginning the nuclear phase of the experiment, the explosively closed isolation valves on the gas/liquid purge lines were fired to permanently seal these lines.

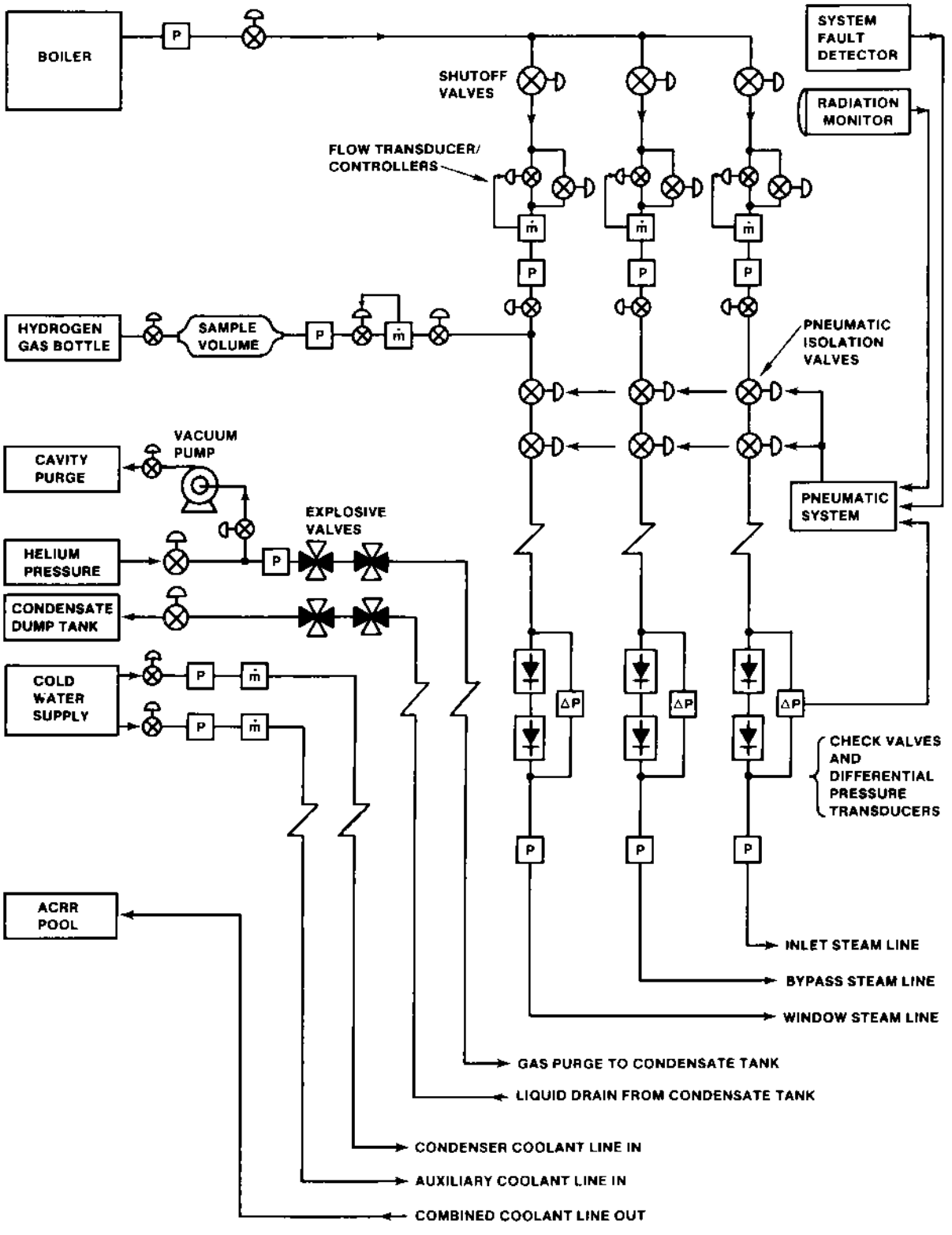

Figure 2-7: Schematic of out-of-pile flow system.

2.3.2 Experiment Control/Data Collection System

In addition to the steam inlet, coolant inlet/outlet and gas purge lines which connected to the in-pile capsule, approximately 250 separate data signals, comprised of thermocouple, pressure transducer, and other signals, emerged from the package. Electrical power to drive the numerous heater circuits within the in-pile capsule also connected to the package. The logging of data signals and control/monitoring of heater circuits, etc., were all managed by a HP1000 computer system using softwares specially developed for these purposes. All diagnostic signals were recorded continuously during the experiment. A complete list of on-line signals which were logged by the system is given in Appendix B, and a microfische is included which contains the data presented graphically. The computer system also displayed many key measurements on continously updated video monitors providing the operators of the experiment with information necessary to both control the test and to verify safe operational limits of the experiment.

2.3.3 Visual Diagnostic System

The optical viewing port in the test section assembly (Figure 2-5) allowed for a visual record of the damage progression (from an end on perspective) to be obtained. Figure 2-8 illustrates how the optical image was directed from the axis of the ACRR central cavity (also the axis of the test bundle) to an optical instrumentation table located on the floor of the ACRR. A large front surface mirror situated directly above the ACRR central cavity performed this function. On the optical table, beam splitters and pellicles directed the image into telescopes, behind which were mounted motion picture and video cameras.

The motion picture cameras were advanced with framing rates of 1 per second and 1 per 4 seconds. (Because of problems with focusing the film cameras, these records are of low quality.) The color video recording of the damage progression however was of excellent quality, and reveals the timing of important damage phenomena such as aerosol release and control blade failure.

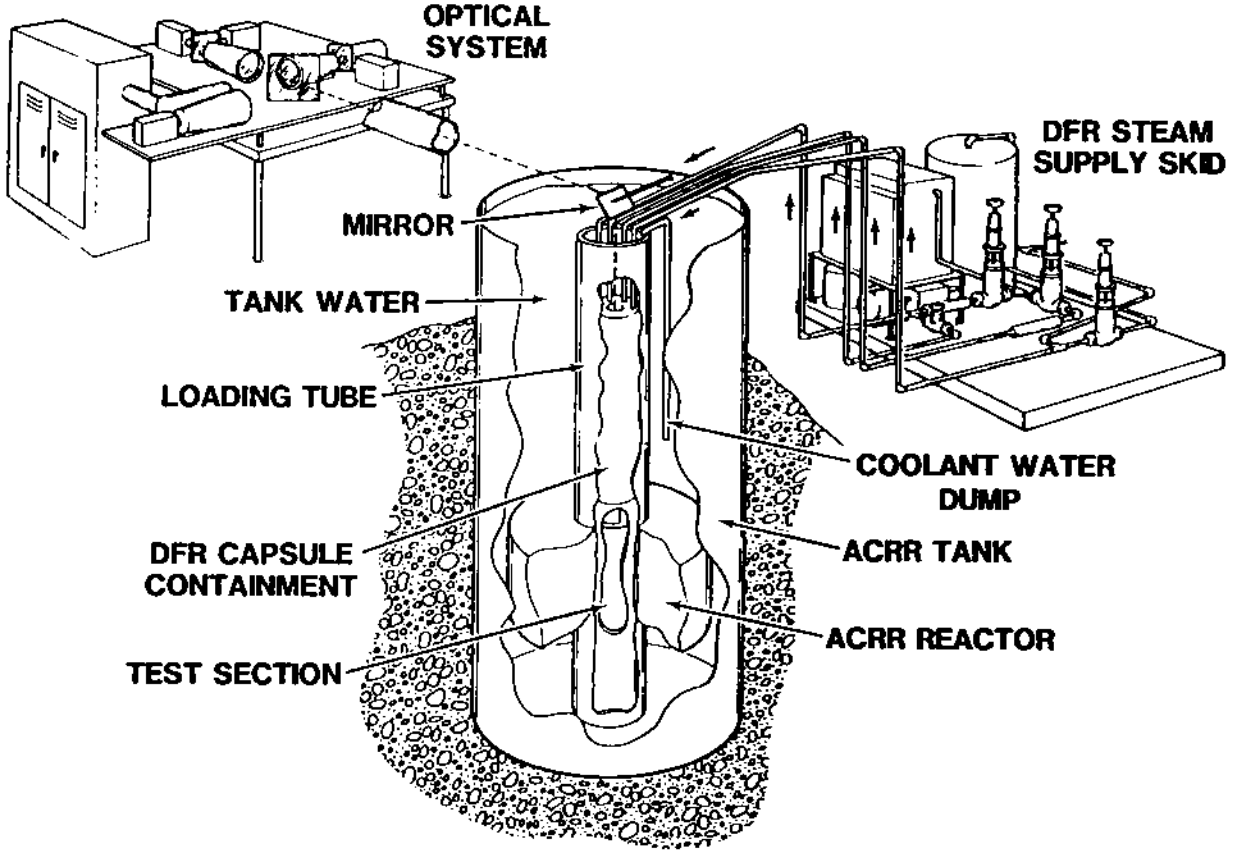

Figure 2-8: Installation of DF-4 in the ACRR, showing out-of-pile components located on the reactor room floor.

3. EXPERIMENTAL RESULTS

The DF-4 test was successfully conducted roughly one month after an aborted initial attempt at running the test. (It was during the initial attempt to run the test that the NaOH dome was unknowingly destroyed by moisture uptake.) The conduct of the DF-4 test occurred over a period of ~6 hours. During this period a number of phases of the test execution may be identified which facilitate the discussion of the results. Briefly, in chronological order, the stages of the experiment were (1) a startup phase during which time the experiment flow system was electrically heated and pressurized with steam; (2) a H_2 calibration phase where the response of the CuO/H_2 recombiners was calibrated; and (3) the nuclear heatup and oxidation transient phase of the experiment. It is the last phase of the experiment in which the primary fuel damage phenomenological information was obtained; however, each phase will be described in some detail in the following sections.

3.1 Startup Phase

Prior to introducing a flow of steam into the experiment, the entire flow system was heated using electric heaters to prevent condensation with cold surfaces. Typically the preheat temperature was on the order of 473 K, which provided ~40 K superheat above the saturation temperature for the nominal operating pressure of 100 psi (690 kPa). The duration of the electrical heatup period was around 4 hours. During this time the flow system trace heating was brought up one heating circuit at a time. Helium was passed through the flow system to facilitate the transfer of heat from the heated boundaries of the test section to the nonheated test bundle components (fuel rods, etc.).

After heating the bulk of the experiment flow system to above the steam saturation temperature for 100 psia (some cold spots remained due to an inability to trace heat all locations), the flow of helium was terminated, and the inlet lines to the experiment were attached to a vacuum pump via the gas purge line (Figure 2-7). The helium and any other noncondensed gases then were purged from the heated system. At this point, the time base for the on-line data collection system was initialized to time=0 and the flow of steam into the experiment was commenced.

Steam was introduced to the experiment after the heated flow system had been evacuated. The steam flows into the experiment are shown in Figure 3-1. The motorized exit flow valves described in Section 2.2.1 were only slightly opened (5 to 8%) when the steam flow was begun at about 250 s, as shown in Figure 3.2. (Note that at the start the valves were fully closed but that the indicated valve positions for the two valves actually indicate positions a few percent different from zero.) By restricting the outflow of steam from the test section, the system pressure was caused to increase, as may be seen in Figure 3-3. When the desired operating pressure of ~100 psia had been reached at approximately 500 s, the exit valves were opened an additional amount (8 to 10%) to balance the test section steam outflow with the inflow, and stabilize the flow system pressure level.

3.2 Hydrogen Calibration Phase

After initiating steam flow into the experiment and stabilizing the flow system pressure at ~100 psia, a calibration of the CuO/H_2 recombiner response was performed. This

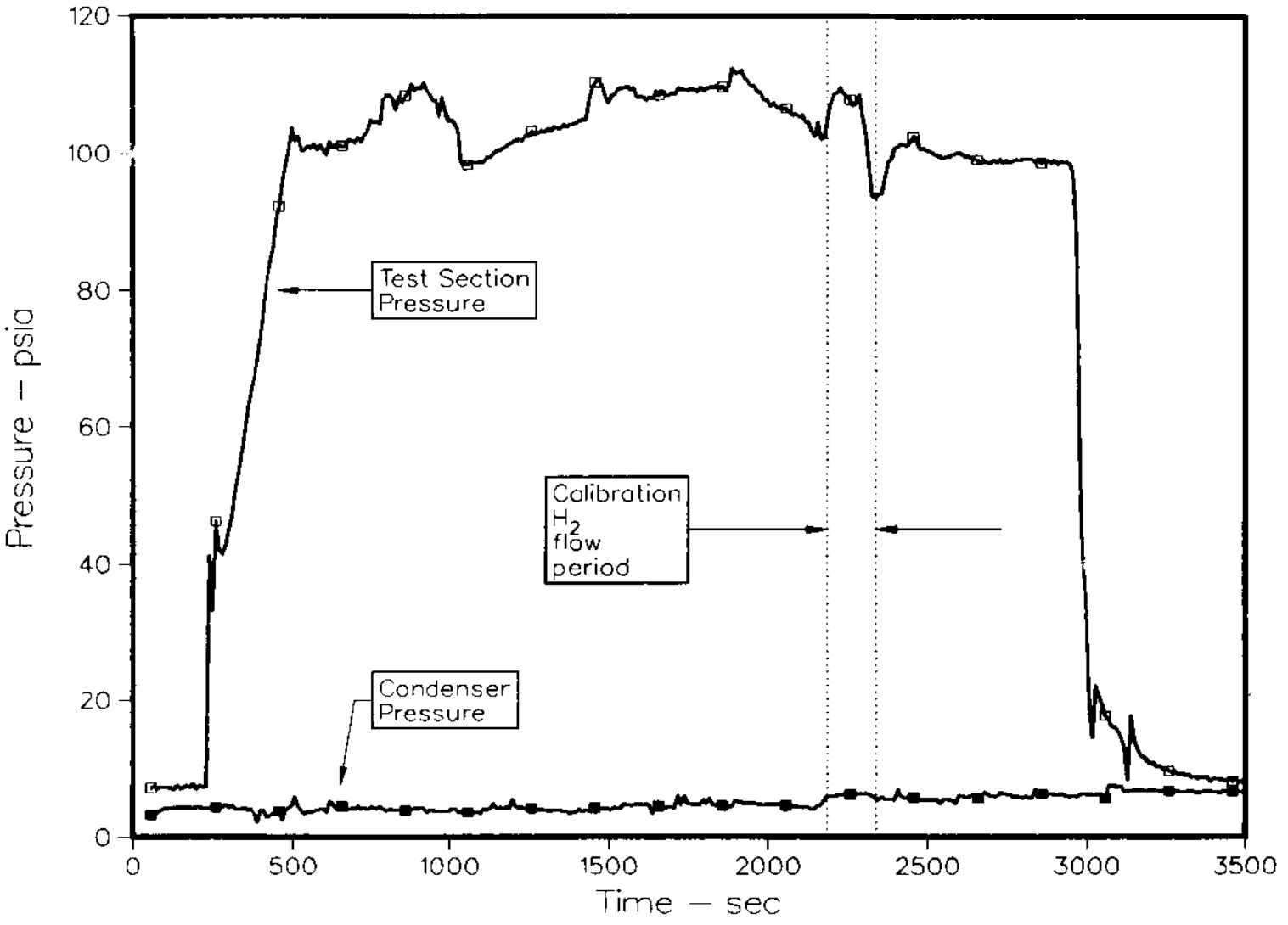

Figure 3-3: Test section pressure and condensate tank/condenser pressure. The difference in the two pressures is the pressure drop across the exit flow valves (see Figure 3-2 and 2-5).

was accomplished by injecting a known volume of hydrogen into the "bypass steam" flow, as described in Section 2.3 (see also Figure 2-7). The hydrogen subsequently was carried into the CuO recombiners where conversion to steam took place and the heat of reaction was released ($CuO + H_2 \rightarrow Cu + H_2O(g) + 92.3$ KJ @ 500 C). The H_2 injection rate into the window steam flow is shown in Figure 3-4. The hydrogen, having been converted to steam in the CuO recombiners, was condensed with the total steam flow after passing into the condenser. Figure 3-5 shows a comparison between the total steam injection rate, the equivalent steam flow for the reacted H_2 and a calculated outlet flow which is based upon a valve flow equation that accounts for valve pressure drop and valve position (flow coefficient, C_v - this flow calculation is discussed in greater detail in Chapter 4). The outlet flow curve shows an increase over the steam inlet flow rate during the time hydrogen was being injected that is due to the H_2 conversion to steam. Note also the pressurization and depressurization effects on the outlet flow due to mass storage in the flow volume at ~250 s, and mass depletion at ~3000 s.

The reaction of H_2 in the recombiners was detected by the CuO internal bed thermocouples described in Section 2.2.5 (see also Figure 2-6). This thermal response is shown in Figures 3-6 and 3-7 for the two instrumented recombiner tubes. Before the H_2 was introduced, the entrance of the CuO bed is seen to be cooler than regions further into the bed axially. This is because the steam cooled the electrically heated bed as it entered and gradually acquired the bed temperature as it flowed through. When the H_2 flow was injected just prior to 2200 s, the bed thermocouples indicated a very sudden large temperature increase in the entrance region of the recombiners where the reaction between CuO and H_2 occurred. Smaller temperature increases were detected further in the bed as heat from the entrance region was convected downstream by the flowing steam. At 3000 s the inlet steam to the experiment was terminated, the outlet valves were opened fully and the experiment package was quickly depressurized. This caused a sudden large flow of steam to pass through the H_2 reaction tubes (see Figure 3-5, outflow steam curve) that led to a sudden cooling of the CuO bed, as seen in Figures 3-6 and 3-7. Notice that between 3000 and 3500 s during which time no steam flowed through the CuO beds, that the bed thermocouples began to approach a common value. This was due to the absence of steam convection and a corresponding diminishing axial thermal gradient.

The COPOX computer code, referred to in Section 2.2.5, models the effects of steam convection, electrical heat input, and radial/axial heat conduction, based on the measurements obtained, and performs a time dependent heat balance for the reaction bed. The heat not accounted for as being due to electrical heat input or heat losses, is assumed to be the heat of the CuO/H_2 reaction, from which the H_2 flow rate into the recombiners may be determined. The calibration data will ultimately be used to adjust the COPOX modeling parameters (heat transfer coefficients) so that the correct known H_2 input rate is predicted for the calibration data. These calculations however are not currently completed and will be presented in a subsequent report.

3.3 The Fuel Damage Phase

The phase of the experiment in which the fuel bundle damage phenomena were investigated spans the time period between 5000 s and 8500 s. At the end of this period, the steam flow and ACRR power were terminated. The cooldown of the damaged test bundle followed this period, where data continued to be taken until

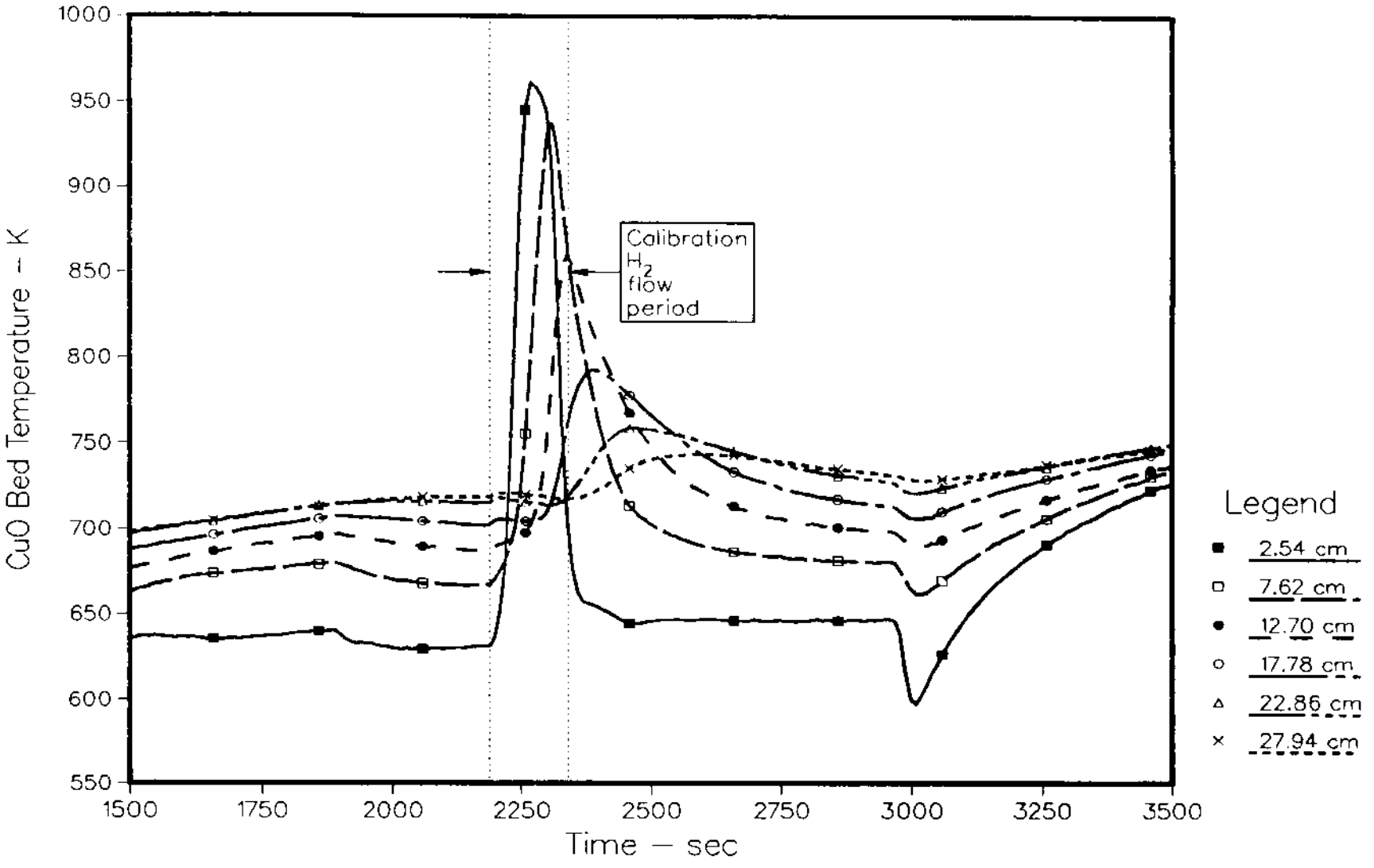

Figure 3-6: Response of CuO internal bed thermocouples to calibration H_2 flows for tube bank 5.

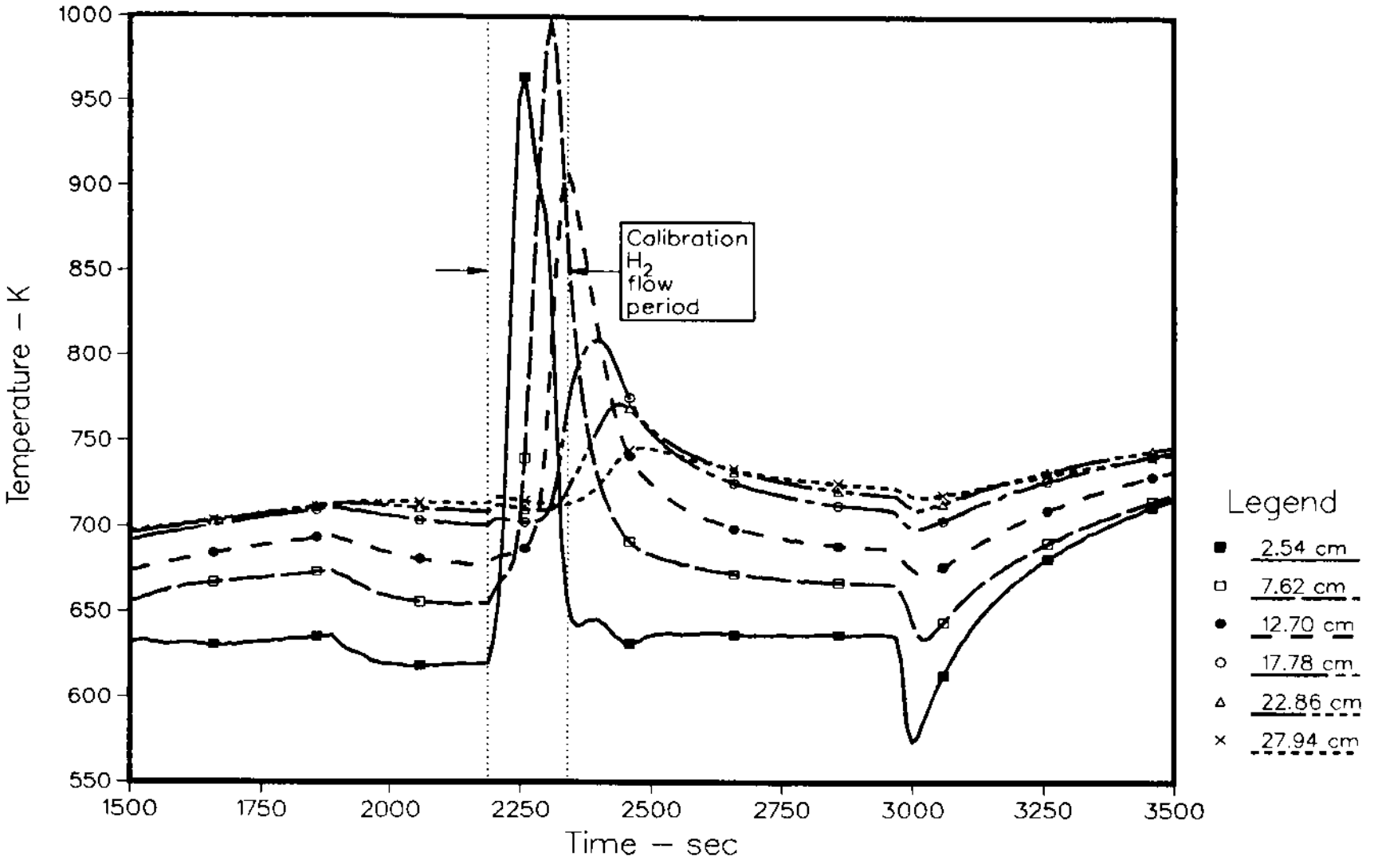

Figure 3-7: Response of CuO internal bed thermocouples to calibration H_2 flow for tube bank 10.

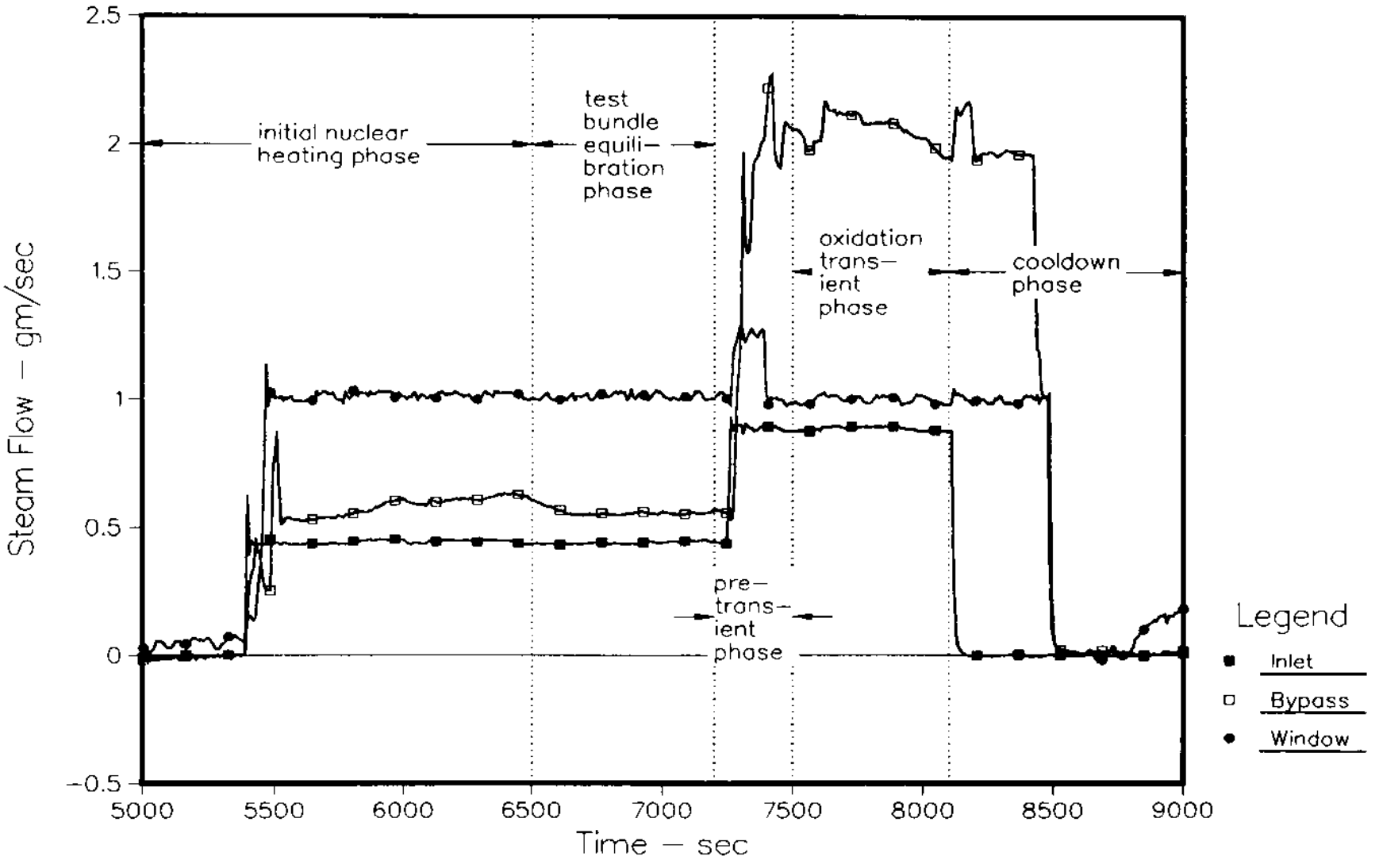

Figure 3-9: Steam flow rates for the test during the Fuel Damage Phases, showing the duration of the five substages of this phase. Steam flows are as measured at the steam plant or the reactor room floor - see Figure 2-7.

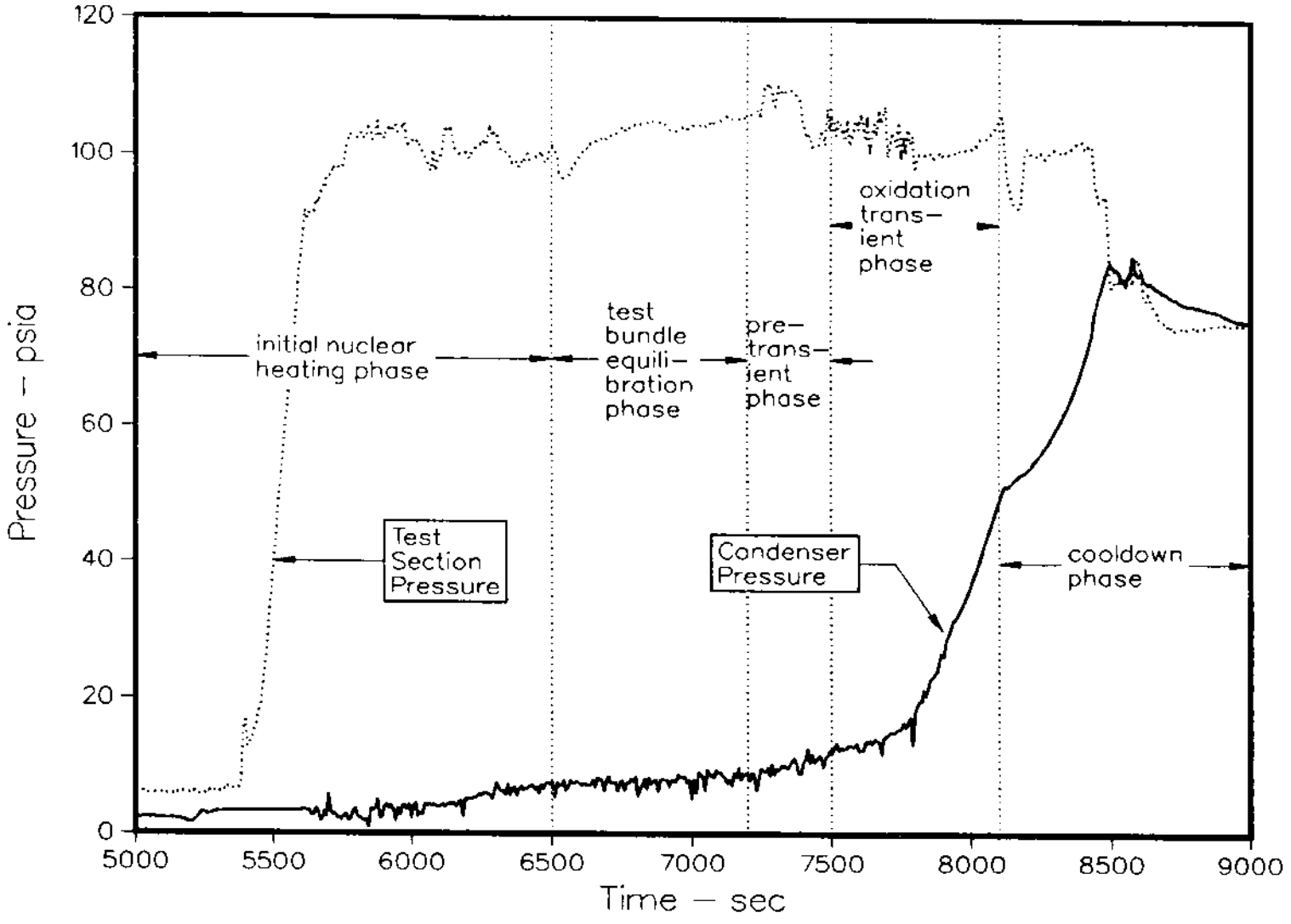

Figure 3-10: Test section pressure and condenser/condensate tank pressure during the Fuel Damage Phase.

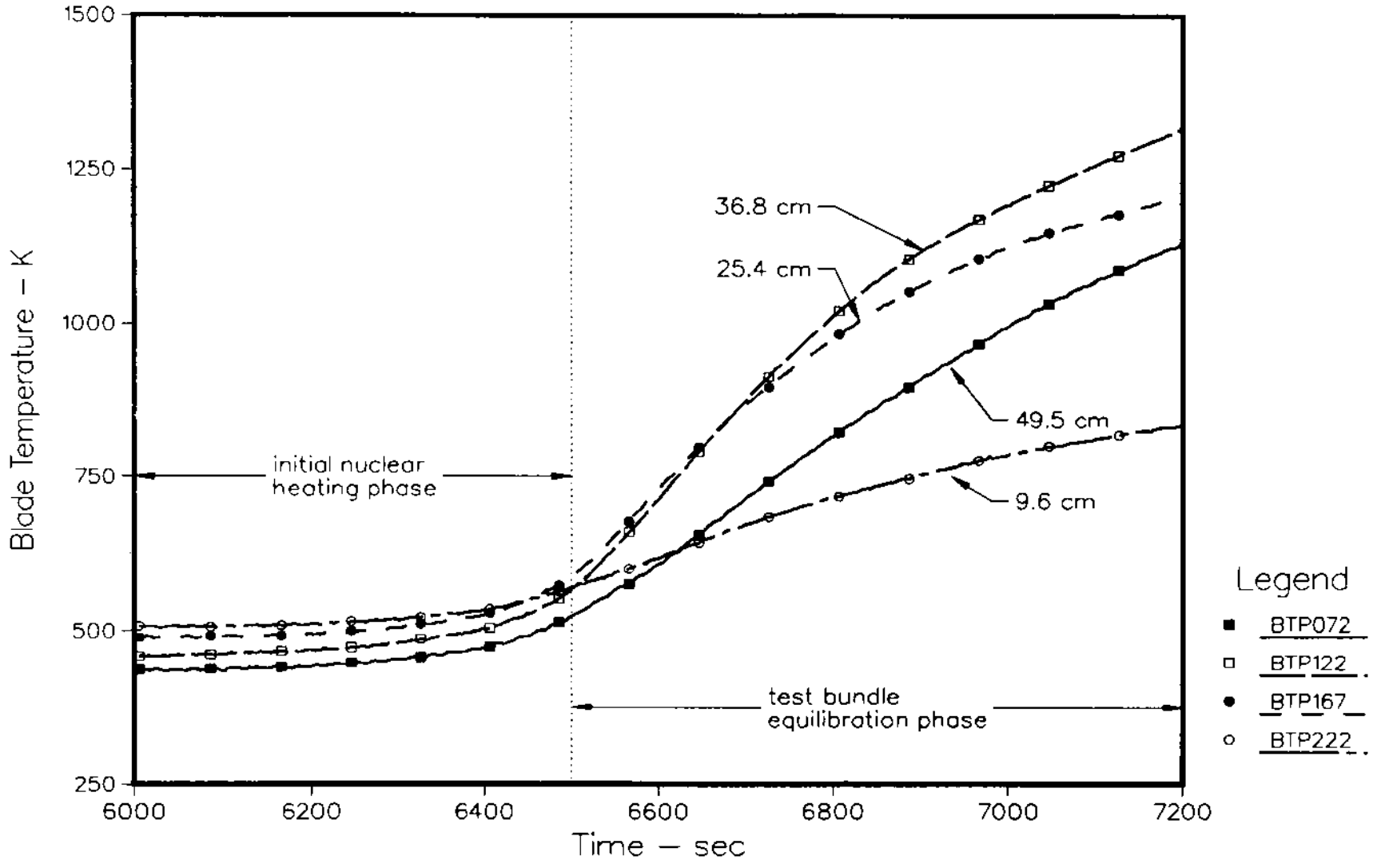

Figure 3-12: Thermal response of the control blade during the "test bundle equilibration" phase as measured by intrinsic junction type S thermocouples.

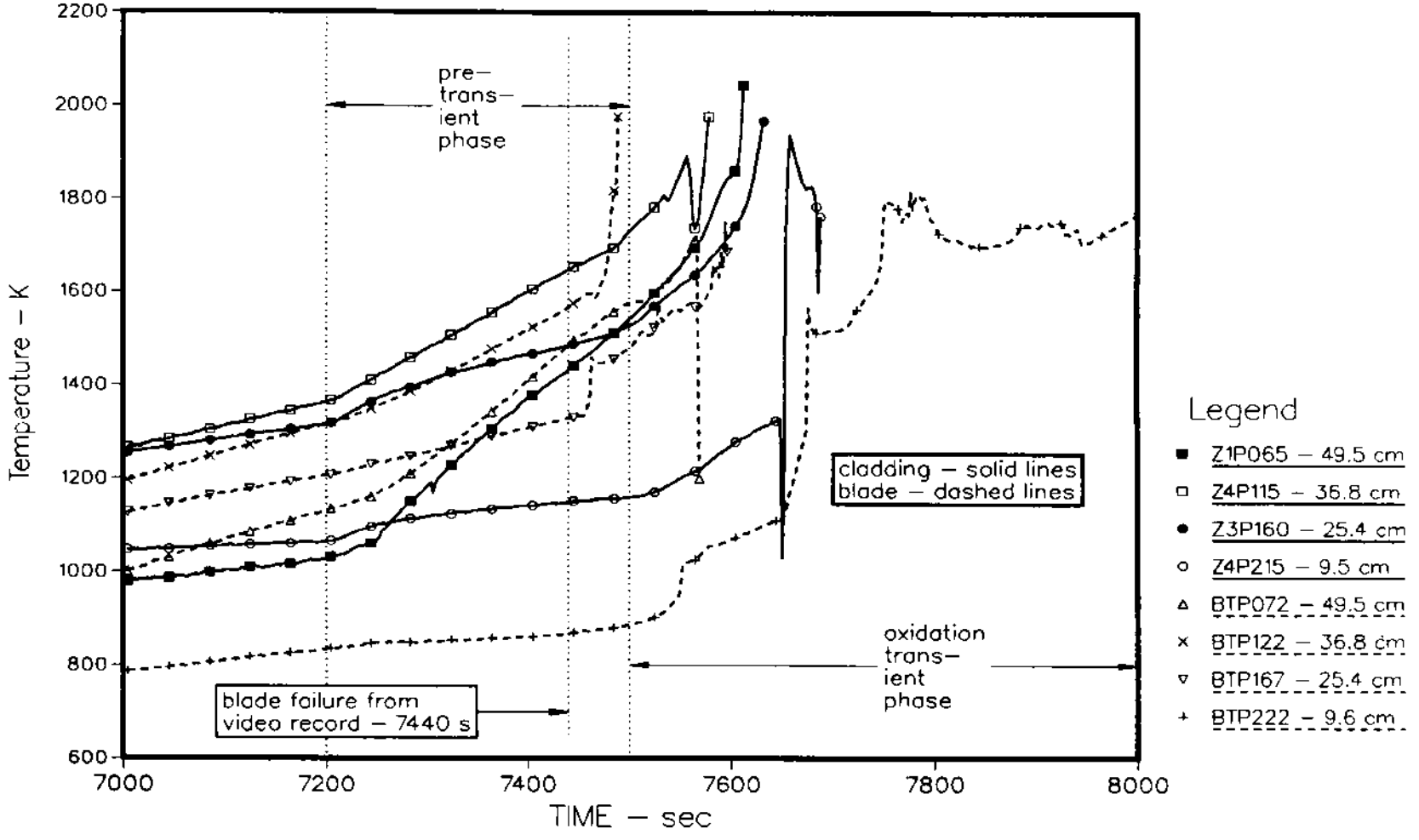

Figure 3-13: Response of type S thermocouples on the fuel cladding and control blade during the oxidation pre-transient and transient phases. Junction failures occur at peak temperature values.

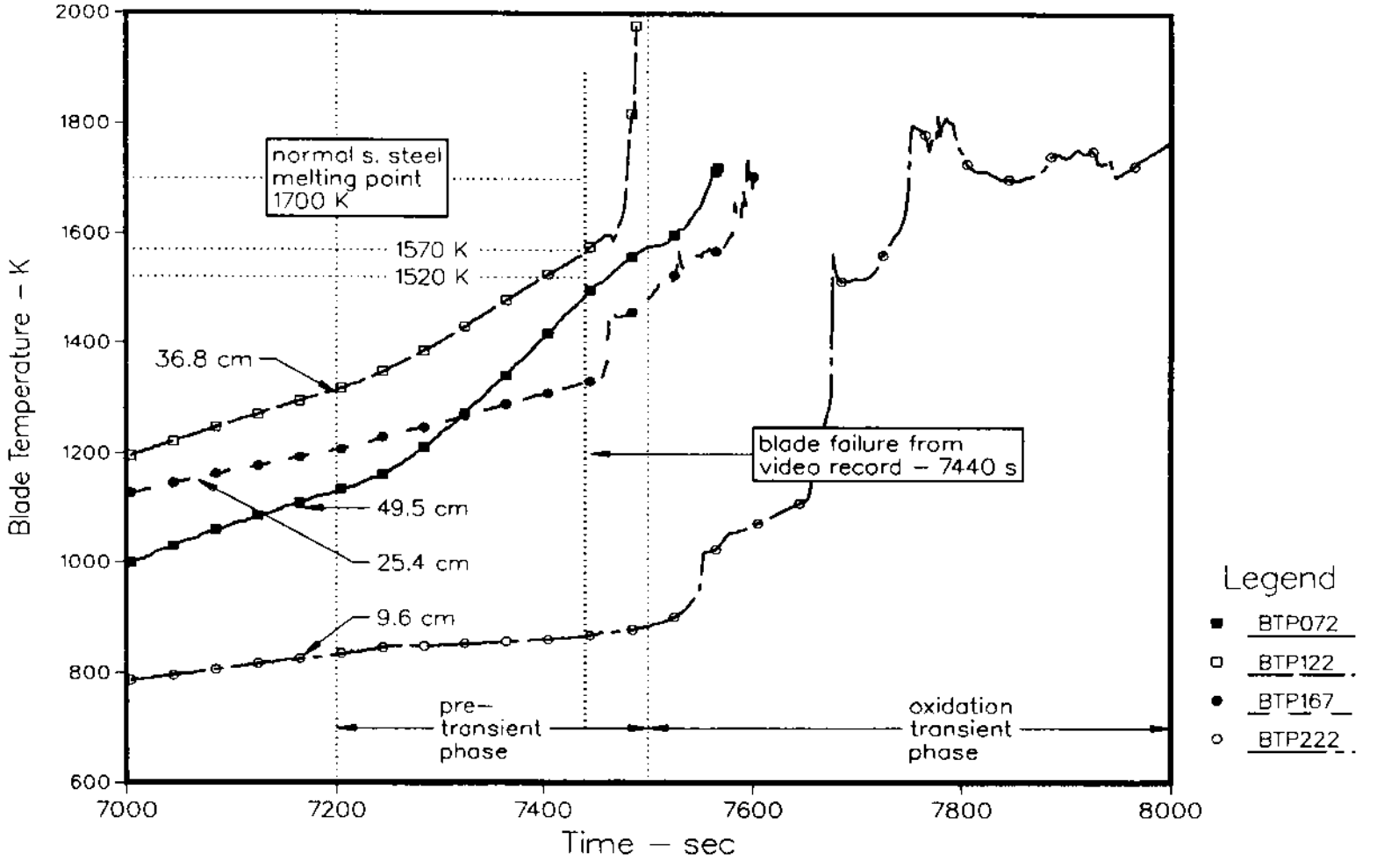

Figure 3-14: Response of the control blade "tip region" type S thermocouples during the fuel damage phase. (See Figure 2-4 for thermocouple location).

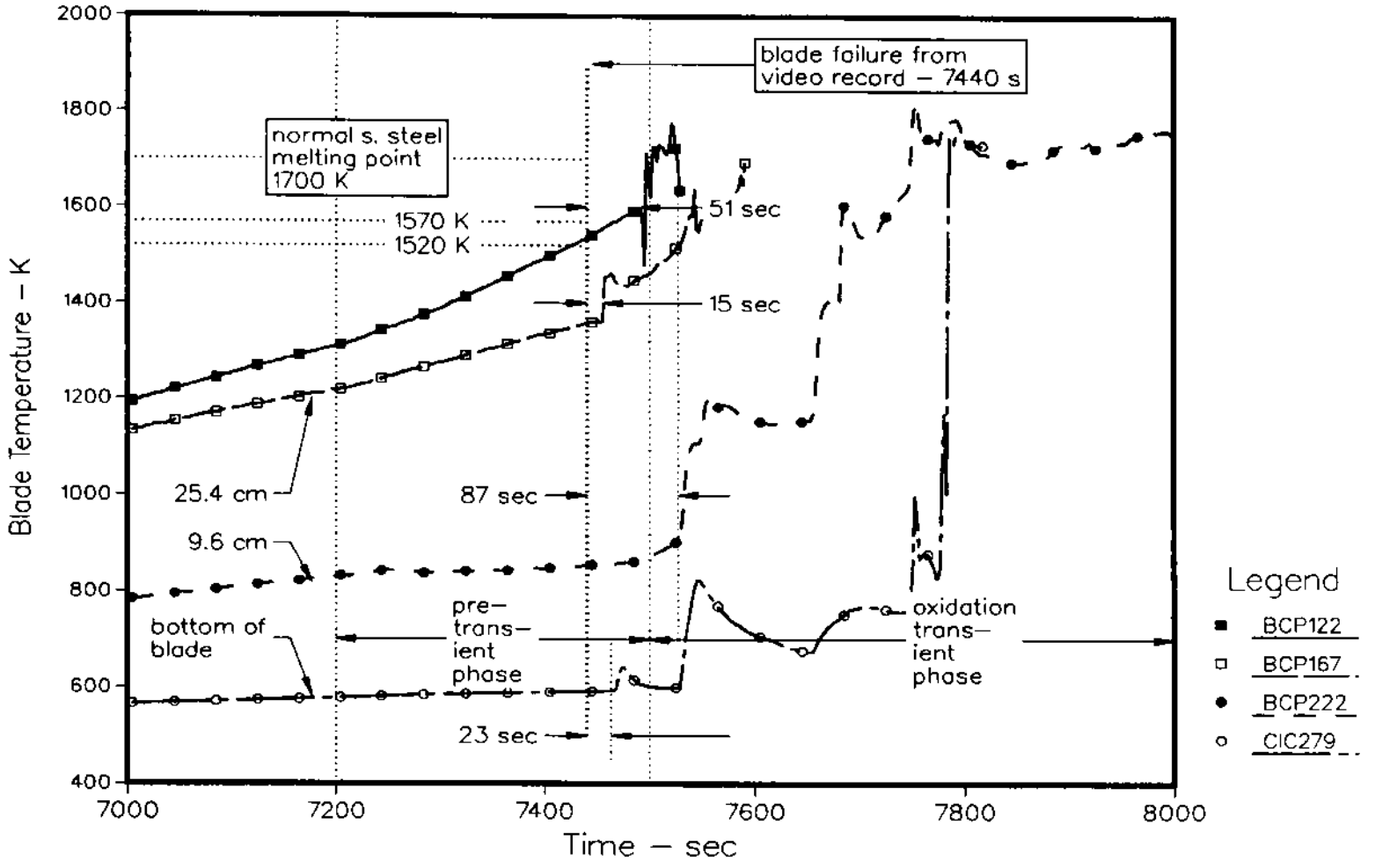

Figure 3-15: Response of the control blade "side region" type S thermocouples during the fuel damage phase. (See Figure 2-5 for thermocouple locations).

droplets were observed in the video record to be spilling out of the control blade was ~7440 s. At this time, the maximum measured blade temperature was between 1520 K and 1570 K at the 36.8 cm bundle elevation (approximately 70% high in the fissile length). Within 15 s after the observed blade failure, the thermocouples at the 25.4 cm elevation (48% high in the fissile length) indicated a large sudden temperature increase, presumably due to liquefied control blade materials relocating downward from the initial failure region between the 25.4 cm (48%) and 36.8 cm (70%) axial locations. Roughly 23 s after the visual blade failure time, the arrival of a small amount of molten material (perhaps only a few molten drops) was indicated at the base of the blade region by a small but sudden increase in temperature there (Figure 3-15, thermocouple CIC279). At about one minute (51 s) after the observed blade failure, the blade instrumentation at the 36.8 cm location failed suddenly, suggesting that the failure region had propagated upwards to this zone from below. The temperature just before failure was 1600 K, about 100 K below the melting point of stainless steel (1700 K). Just after failure of the original junction, a new junction subsequently formed with an indicated temperature of ~1700 K.

The blade failure appears to be quite extensive by 87 s after the visual blade failure time, as evidenced by the simultaneous large temperature increases at both the 9.6 cm plane and at the base of the blade which is about 6.6 cm below the bottom of the fissile length. The behavior of these thermocouples after this time (~7550 s) becomes difficult to interpret since the location of the thermocouple junction is no longer certain. It is interesting to note that late in time, at around 7800 seconds, several of the thermocouples which were located at 9.6 cm or below indicate a temperature of ~1700 K. This may be due to the presence of stainless steel arrested at its melting point of ~1700 K, however as was noted, the location of the sensing junction at this time is not known. (The junction could lie anywhere between 9.6 cm and the base of the blade.)

3.3.3.2 Fuel Rod Cladding Thermal Response

The fuel rod cladding thermal response during the pretransient and transient oxidation phase is shown in Figure 3-16. The temperature rise rate during the pre-transient period ranged from 0.63 K/s to 1.8 K/s, varying with axial location, however, the heatup rate for the axial zone that was the first region to encounter the zircaloy oxidation transient was ~1.2 K/s. The Pt/Rh intrinsic junction thermocouples all experienced junction failure very shortly after indicating the increase in heatup rate which identifies the oxidation transient phase. Based on the thermocouple responses just prior to junction failure, the heatup rate at the start of the oxidation transient would appear to be ~12 K/s.

The first instrumented zone to enter the oxidation transient was at the 36.8 cm axial plane (70% elevation), which did so at ~7540 s. The temperature at this time was between 1750 K and 1800 K. About 65 s later, the thermocouples at the next higher and lower instrumented locations [49.5 cm (95% elevation) and 25.4 cm (48% elevation)] responded similarly. One interpretation of these trends is that a vigorous zircaloy oxidation began near the 36.8 cm location and subsequently migrated both up and down to the 49.5 cm and 25.4 cm locations.

The cladding thermocouples located at the 9.6 cm axial position did not respond as the thermocouples higher in the bundle did. The heatup at this location was much slower during the pretransient period, being only about 0.1 K/s. The thermocouples here

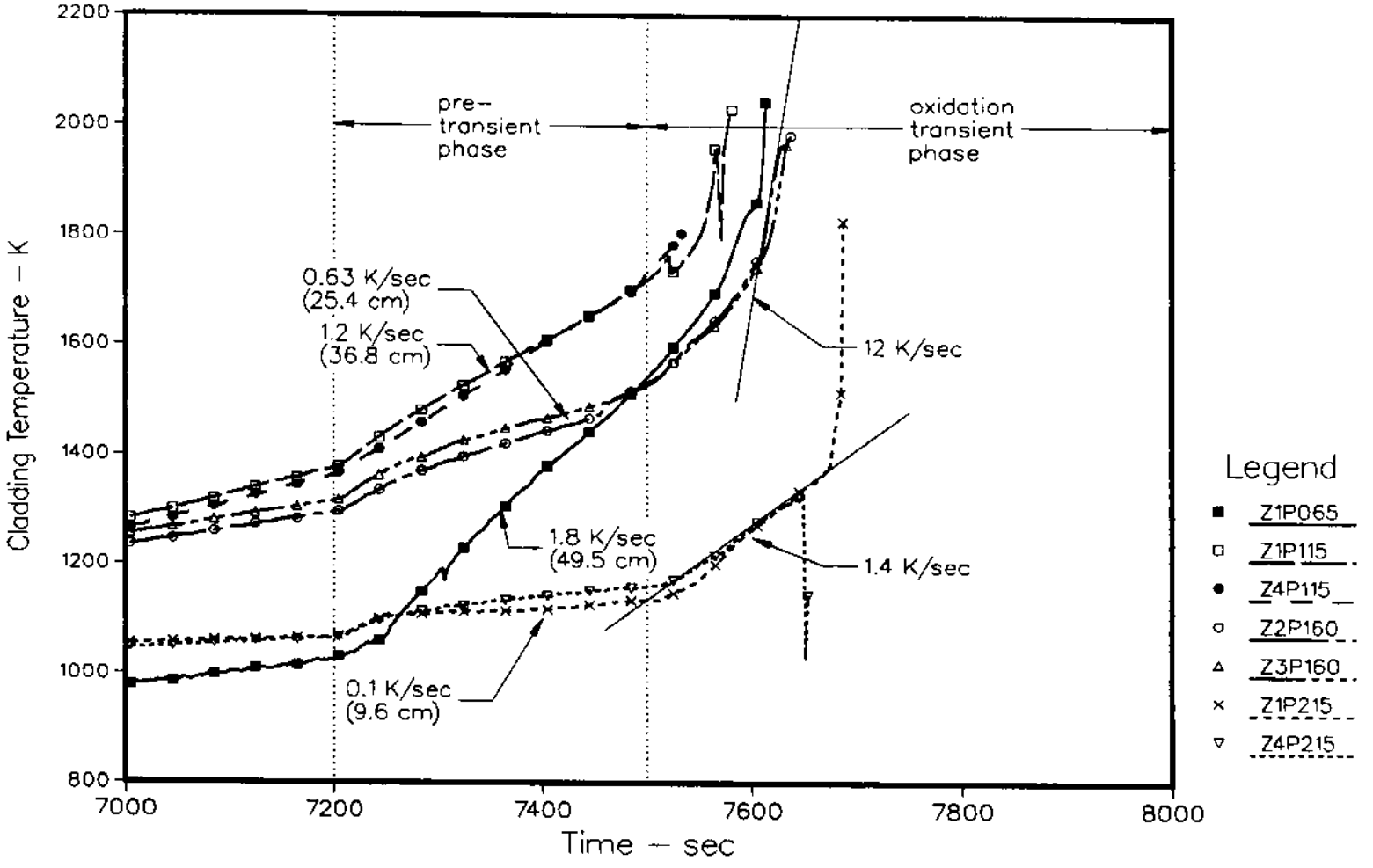

Figure 3-16: Response of the fuel cladding intrinsic junction type S thermocouples during the fuel damage phase (oxidation pre-transient and transient phases).

showed a step change in heatup rate, from .1 K/s to 1.4 K/s, at 7533 s, probably responding in part to an increase in ACRR power which occurred at 7510 seconds (660 kW to 880 kW), but possibly also from thermal radiation from the upper bundle region where the oxidation transient was initiating. Later, at about 7680 s, the temperatures at the 9.6 cm location increased suddenly. This increase is assumed to be due to the arrival of molten zircaloy and liquefied fuel from regions higher up in the bundle.

The fuel cladding thermal response was also measured by W/Re thermocouples which were specially sheathed within a helium filled, ceramic zirconia, closed end tube, as described in Section 2.1.6.1. The locations of the W/Re assemblies were prescribed in Section 2.1.6.2 via Figure 2-4. It should be pointed out that the W/Re assemblies monitored the clad temperature of the outer "guard" rods which faced the low density zirconia fiber insulating shroud, whereas the intrinsic junction Pt/Rh thermocouples monitored the inner "hot" fuel rods which were adjacent to the channel box.

As discussed earlier, the design and installation of the W/Re thermocouple assemblies, while allowing temperature measurement effectively throughout the high temperature transient period of the test, also introduces unavoidable errors in measurement. The errors are a result of the fact that the junction is thermally "insulated" from the fuel cladding by the protective sheath, and for this reason, may lag the actual clad temperature by several hundred degrees K. This may be seen by comparing the measurements obtained from the W/Re and Pt/Rh thermocouples at the same axial elevation, as shown in Figure 3-17. Two axial elevations are represented in Figure 3-17, and in both cases the W/Re assembly lags the intrinsic Pt/Rh thermocouple response significantly. In Chapter 4, the observed differences between the Pt/Rh thermocouple response (assumed to represent the true cladding temperature) and the W/Re behavior will be used to "calibrate" a thermal model of the W/Re assembly called WRET.

The W/Re thermocouples were used to instrument the fuel rods at the four principal axial locations. These data are shown in Figure 3-18. The general behaviors indicated by these thermocouples are very similar to those indicated by the Pt/Rh data shown in Figure 3-16, but differences exist in both rate of temperature increase and in the magnitude. For example, for the 36.8 cm axial plane which was the first location to encounter the oxidation transient, the heatup rate just prior to the transient measured by the W/Re instrumentation was 0.8 K/s. This compares to 1.2 K/s measured by the Pt/Rh thermocouples. Similarly, during the oxidation transient, the W/Re heatup rate was 6 K/s compared to ~12 K/s estimated from the Pt/Rh data just before the junction failed. The peak measured junction temperatures for the thermocouples at the 36.8 and 25.4 cm locations were both about 2200 K. Based upon the WRET analysis discussed in Chapter 4, this junction temperature corresponds to an actual cladding temperature of about 2500 K.

As with the "9.6 cm" Pt/Rh thermocouples, the W/Re fuel rod thermocouple at this location behaved differently from the thermocouples located higher up. The W/Re thermocouple at this location also appeared to respond to sudden heating caused by relocating molten material at the same time as the Pt/Rh thermocouples at this elevation (7670 s). The temperature at this location continued to increase, eventually becoming the hottest location in the bundle. The peak temperature measured by the thermocouple was 2400 K. The actual peak temperature estimated for this region based upon the WRET analysis of the thermocouple response is 2620 K.

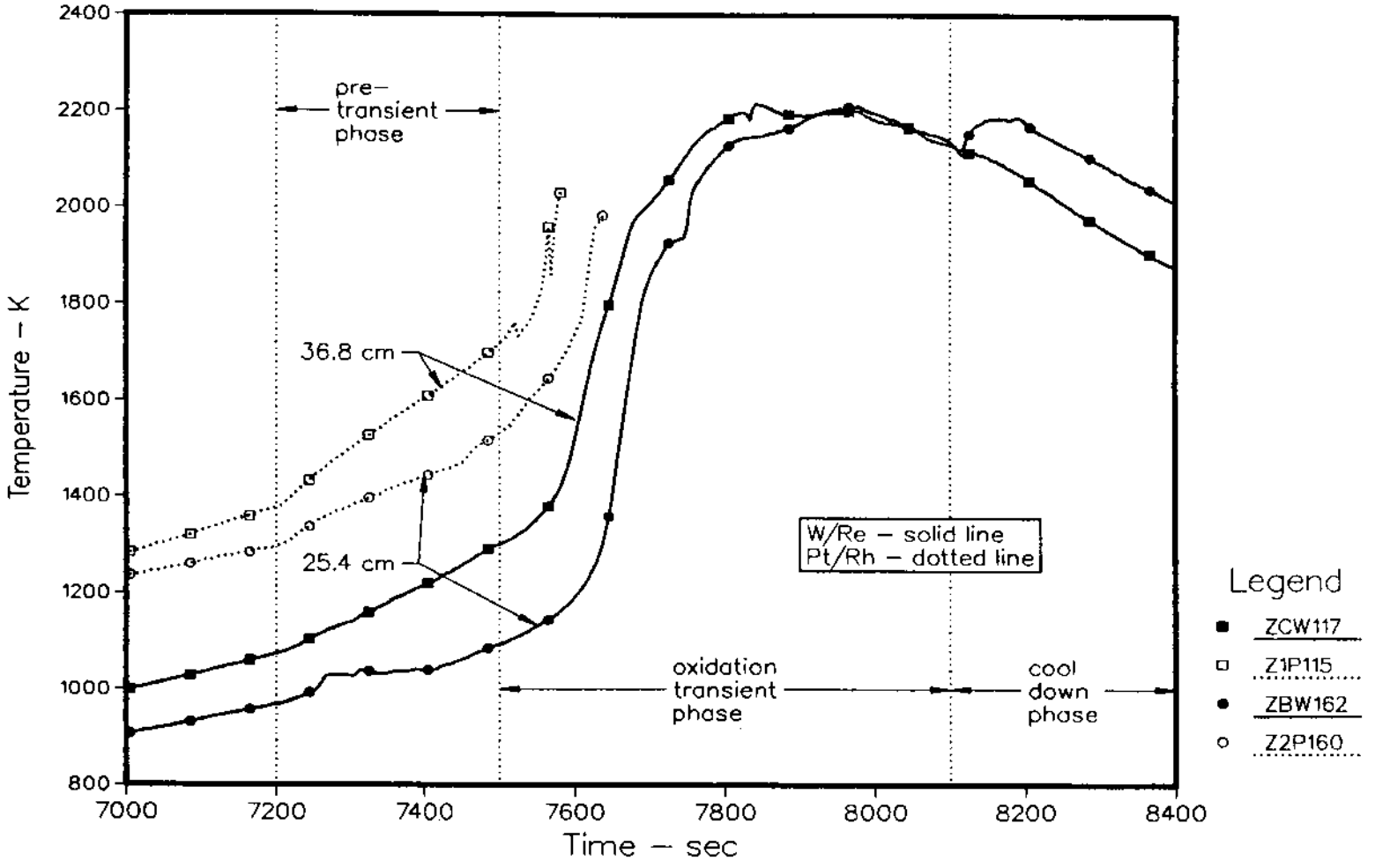

Figure 3-17: Comparison of Pt/Rh intrinsic junction (type S) fuel cladding thermocouple responses to the zirconia sheathed W/Re (type C) thermocouple responses at the 36.8 cm and 25.4 cm axial locations. Notice the temperature lag associated with the W/Re thermocouples.

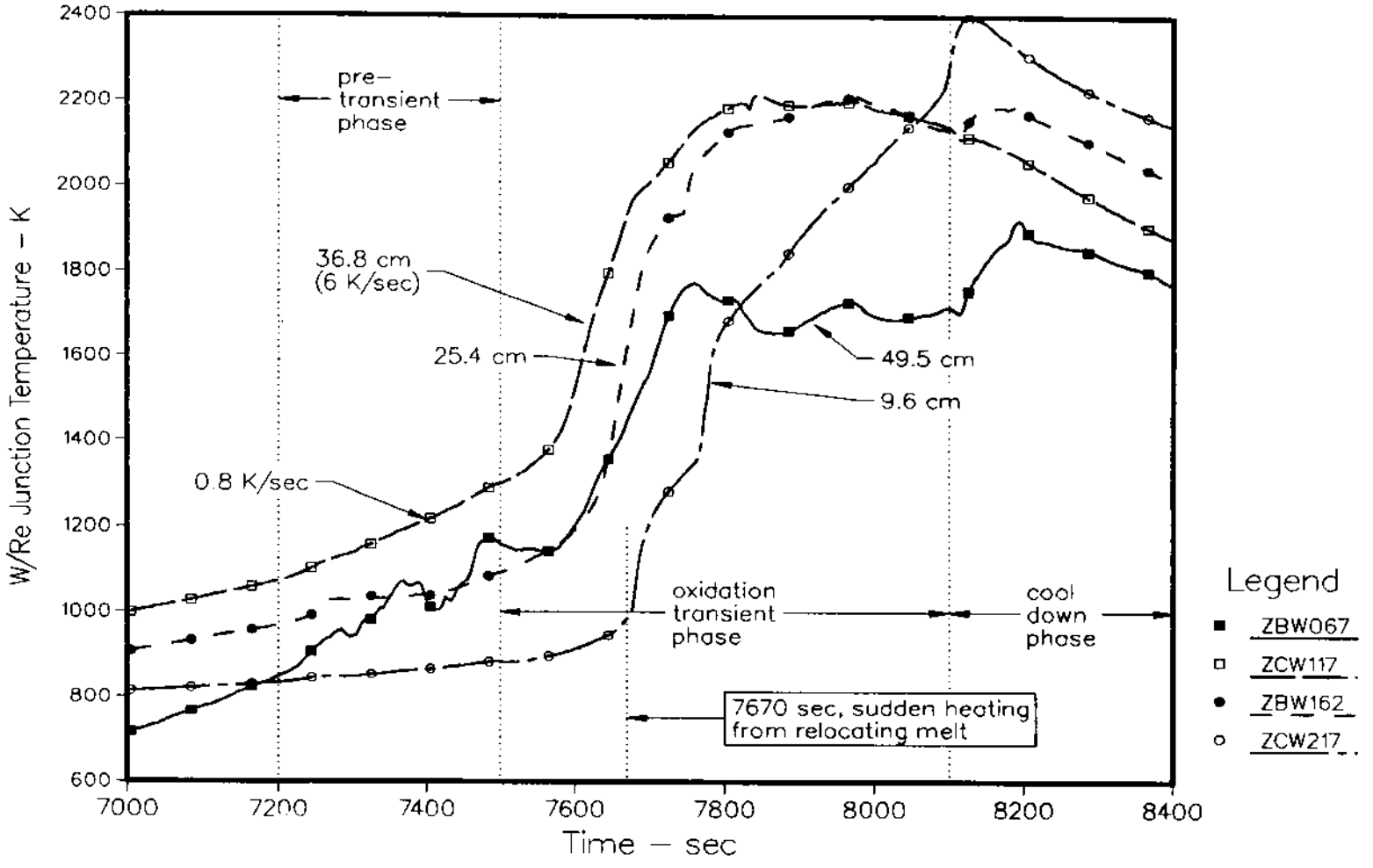

Figure 3-18: Thermal response of the fuel rod cladding as measured by the zirconia sheathed W/Re (type C) thermocouples during the oxidation pre-transient and transient phases.

3.3.3.3 Channel Box Thermal Response

Only the zirconia sheathed W/Re thermocouple assemblies were used to instrument the channel box. As seen in Figure 2-4, these assemblies contacted the zircaloy box only on the corners. This was done because of spatial constraints, and consequently had the disadvantage that the thermocouples contacted the box at a location which might have been colder than at other points. For example, the side of the box opposite the fuel rods numbered 1 and 3 in Figure 2-4 could be hotter than the corner because of its proximity to the heated fuel rods and its ability to oxidize effectively on both sides of the box. In contrast, the side wall of the box faces the colder zirconia fiber insulating shroud, and may not oxidize as readily on the outer surface facing the shroud because of the resistance to steam flow in the small gap there.

In spite of being located in a potential cold spot, the thermal response of the channel box thermocouples was very similar in timing and magnitude with the response of the fuel cladding W/Re thermocouples. These are shown in Figure 3-19. The timing of the "oxidation transient onset" was essentially the same as with the fuel cladding, and the indicated rise rate just before and during the transient was 0.6 K/s followed by about 7 K/s during the transient. Based on the timing of the transient period for each axial location it would appear that the rapid oxidation zone for the channel box was first detected at the 36.8 cm (70%) axial location, and quickly spread downwards to the 25.4 cm (48%) axial location. The top axial station at 49.5 cm (98%) was the next to indicate the transient behavior. The total time elapsed between the first and last zones to indicate the transient behavior was ~75 s, very similar to the fuel rod response. The difference in time response for the two channel box thermocouples at the 25.4 cm location is puzzling. No explanation is given at this time for the difference, since it was expected that CTW162 would lead CBW162 (see Figure 2-4) in response during the oxidation transient because of the richer supply of steam near CTW162 and the additional thermal mass of the control blade near CBW162. As can be seen in Figure 3-19, the observed behavior is just the opposite. In fact, thermocouple CBW162 registered the highest temperature throughout the entire bundle, indicating a sustained high temperature above 2400 K and a peak temperature exceeding 2500 K (uncorrected for thermocouple heat losses).

Similar to the fuel rod thermal response, the channel box instrumentation at the 9.6 cm location (CTW217) responded differently than the thermocouples higher in the bundle. This thermocouple also exhibited a behavior which suggested the sudden arrival of relocating molten material coincident with similar responses in the fuel rod region. This event seems to mark a major relocation of molten material which spread over the entire lateral extent of the bundle near the 9.6 cm axial location, between 7670 and 7700 s. Interestingly, the appearance of a dense aerosol becomes evident in the video record of the test during the same time period; 7640 s aerosol onset - 7650 s very dense aerosol. In earlier DF series experiments (DF-1 and 2) the generation of tin aerosol was observed and was attributed to Sn being released from the zircaloy cladding as the cladding melted. Because of the coincidence in detecting relocating molten material and the release of aerosol, the relocating melt is assumed to be zircaloy, and because of the large lateral extent of the thermal response, it is assumed to be composed in large part of channel box zircaloy. From this, it is inferred that the failure (melting) time for the channel box was no later than 7640 seconds, although it is probable that the earlier failing of the control blade would have caused breaching of the channel box locally by interaction with molten steel before this time.

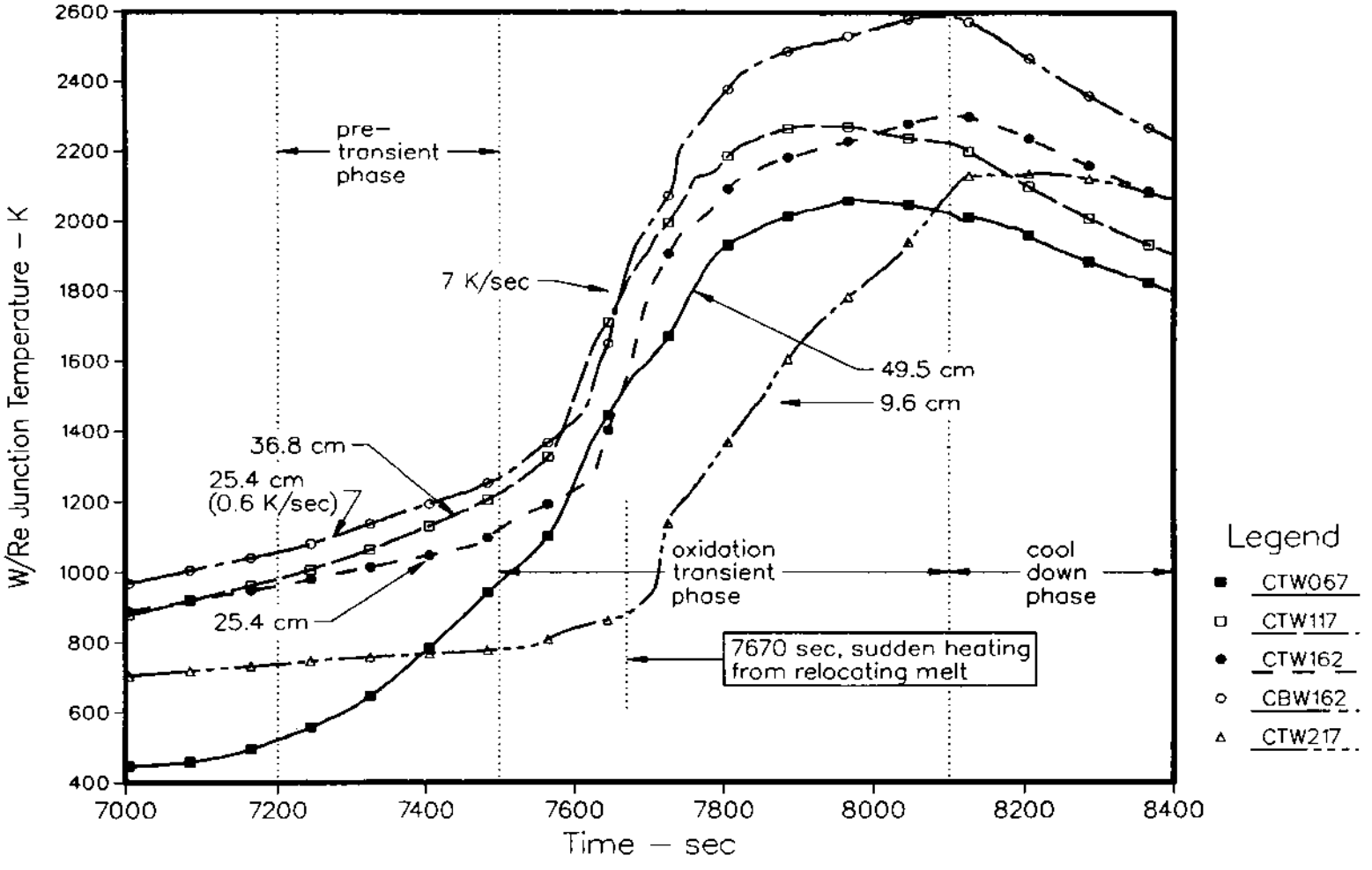

Figure 3-19: Thermal response of the channel box as measured by the zirconia sheathed W/Re (type C) thermocouples during the oxidation pre-transient and transient phases.

3.3.3.4 CuO/H_2 Recombiner Response

The thermal response of the CuO/H_2 recombiner tubes is shown in Figures 3-20 and 3-21 for the two internally instrumented tubes. Recall that each instrumented tube is representative of three other tubes in the two tube banks, shown schematically in the flow circuit of Figure 2-5. Notice the convection cooling effect at ~5500 s caused by steam flow when the exit valves were opened. The inlet steam flow adjustment made during the pre-transient phase is also apparent in the bed thermal behavior.

The major bed response however, was due to the reaction with hydrogen that was generated in the test bundle during the oxidation transient period. This period is shown in an expanded time plot in Figures 3-22 and 3-23. The consecutive response of each thermocouple is clearly seen as the CuO/H_2 reaction front migrated through the bed. Notice that the thermocouples near the entrance of the bed (2.54 cm and 7.62 cm) showed only a moderate response, whereas the thermocouples located deeper into the bed responded much more vigorously. This was due to the prior consumption of the CuO in the bed entrance during the hydrogen calibration phase described earlier in Section 3.2. Because the CuO in the entrance region had already been converted to Cu (although not with 100% efficiency) the hydrogen reacted during this period did so for the most part downstream from the entrance. As the bed was consumed by the CuO/H_2 reaction, the temperature measured by each thermocouple rose and then fell when the reaction front passed by. The total time required to react the ~28 cm of instrumented bed length for recombiner tube 5 was ~640 s. (Additional CuO existed beyond the 27.94 instrumented station, however no internal thermocouples were located above 27.94 inches.)

The thermal behavior of the second bank of recombiners was different from the first as seen from Figure 3-23. In this recombiner bank, represented by instrumented recombiner tube 10, the consumption of the ~28 cm of instrumented bed length took place over only about 300 seconds in comparison to the 640 seconds required for the other tube bank. In addition, the peak temperature indicated in tube 10 was 1124 K compared to 1000 K in tube 5. These trends may be explanable by a difference in flow rate between the two banks of tubes. A higher flow rate in tube 10 could cause higher temperatures and a more rapid bed consumption because of the resulting higher hydrogen flow rate. This will be considered as a possibility when performing the thermal analysis of the CuO reaction.

Note that the inlet steam to the test bundle (which sustains the hydrogen production) was terminated at ~8100 s (Figure 3-9). In view of this, the thermal response measured by the instrumented bank for tube 5 appears to have covered most of the duration of the hydrogen production period of the test. In closing this discussion of the H_2 generation data, it should again be noted that a thorough analysis of the CuO bed thermal measurements will be conducted to derive the actual H_2 generation rate for this test. The results of this analysis will be presented in a subsequent document, currently under preparation.

3.4 Posttest Radiographic Examination

The posttest configuration of the test bundle was examined using radiography. An image of the test section was obtained by exposing x-ray film located near the experiment capsule using a "point" Co^{60} source. The Co^{60} source was located 3.05 m (10 ft.) in front of the experiment test section and the x-ray film, about 15 cm (6 in.)

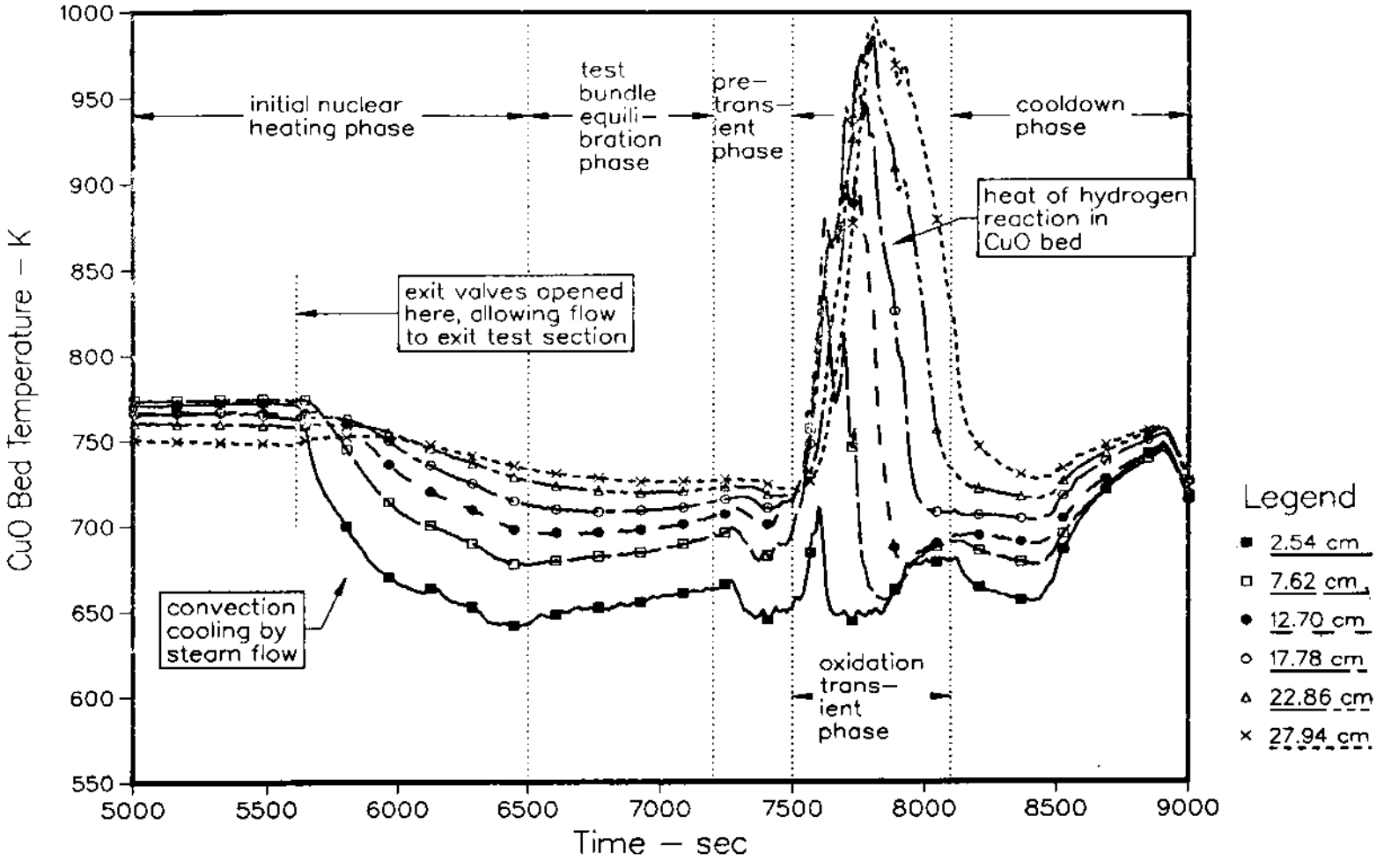

Figure 3-20: Thermal response of CuO recombiner tube 5 measured by the internal bed thermocouples during the fuel damage phase of the experiment. The high temperatures measured during the oxidation transient phase are due to hydrogen reacting in the CuO bed.

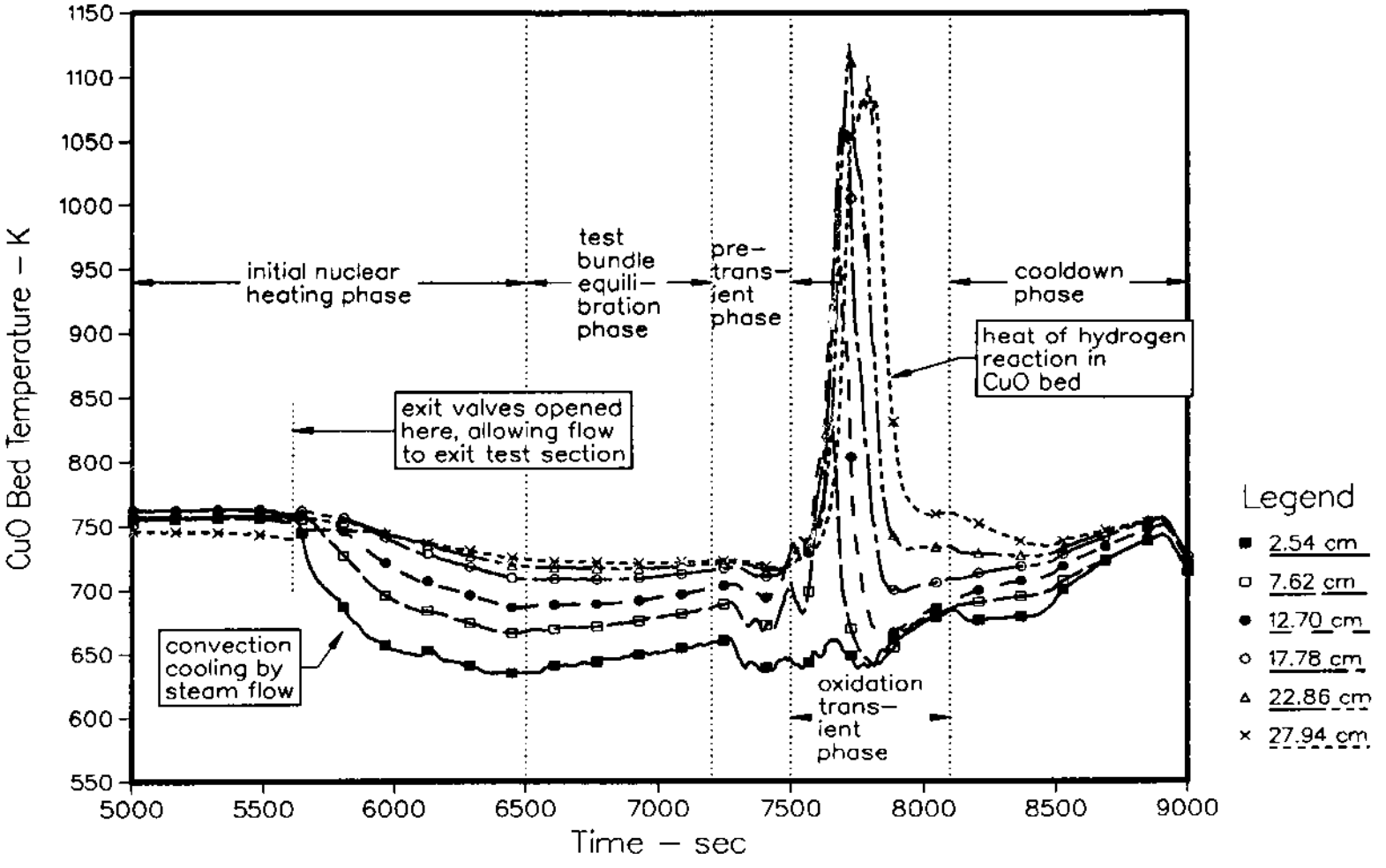

Figure 3-21: Thermal response of CuO recombiner tube 10 measured by the internal bed thermocouples during the fuel damage phase of the experiment. The high temperatures measured during the oxidation transient phase are due to hydrogen reacting in the CuO tube 10.

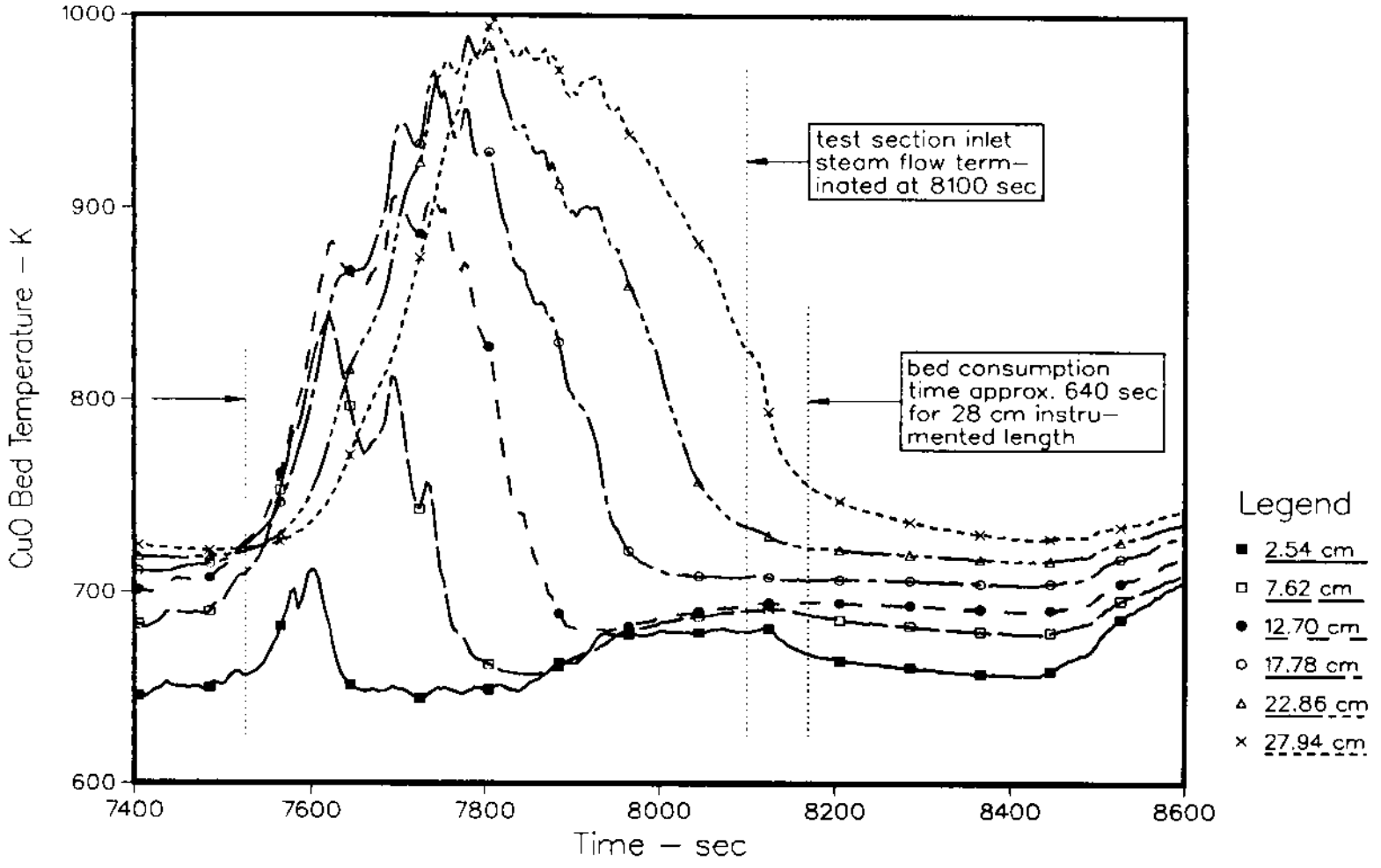

Figure 3-22: Hydrogen induced thermal response in tube 5 during the oxidation transient phase.

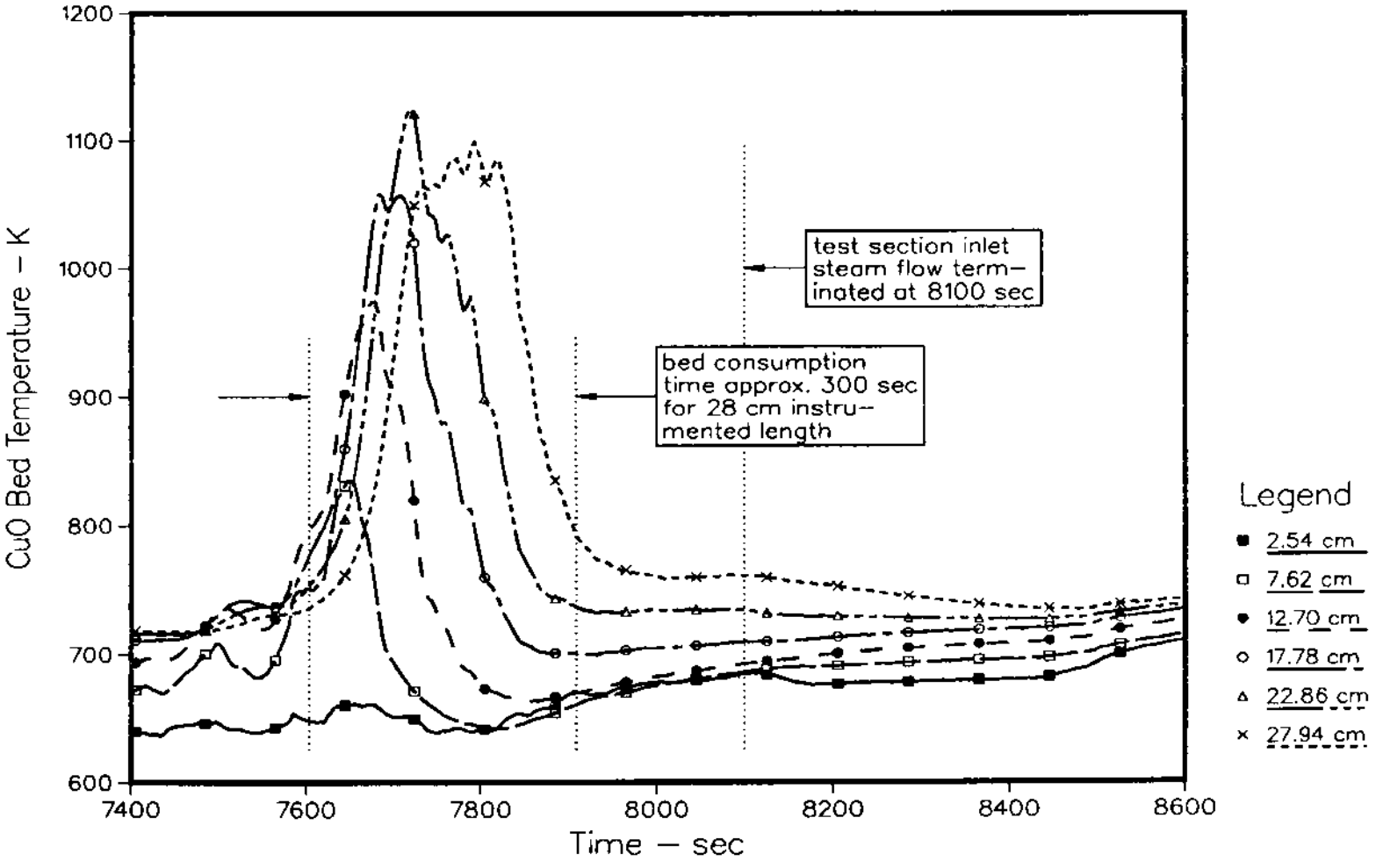

Figure 3-23: Hydrogen induced thermal response in tube 10 during the oxidation transient phase.

behind the test section. This geometry resulted in some amount of parallax distortion but on the whole, gave quite an acceptable image. By careful positioning (azimuthally) of the test section, the channel box, control blade, and fuel rods were aligned to obtain a sharp image. Shown in Figure 3-24 are pre- and posttest images of the DF-4 test section. The viewing angle is indicated on the figure. In the "before" image, the channel box walls and control blade are clearly visible as are the four rows of fuel columns. The axial extent of the fueled region is also identifiable due to the high density of the UO_2 pellets. Other test section features are indicated in this figure, such as pressure and containment boundaries, ceramic ZrO_2 barrier, etc.

The "after" image shows the extent of damage sustained by the test bundle during the course of the experiment. Most notable is the extensive damage to the control blade and channel box structures. The structures appear to have melted and relocated downward from the upper three-fourths to the lower 25% of the test assembly. In the upper half of the bundle, a collapsed fuel column is seen to lie across the region previously occupied by the control blade and channel box. The lower 25% of the bundle is significantly increased in density starting from about 12 to 15 cm above the bottom of the fissile zone and continuing downward to the base of the bundle about 7 cm below the bottom of the fissile length. The blockage zone appears to have largely conformed to the boundaries of the insulating zirconia shroud in the lower 20 cm, but at the top of the blockage (12 to 15 cm above the bottom of the fissile zone), significant intrusion into the surrounding porous shroud is apparent. This suggests that the lower part of the blockage was formed by relocating material that quickly refroze in the relatively cold lower extremities of the bundle, whereas the upper region remained molten long enough to flow into the surrounding ZrO_2 shroud before freezing. The conclusion that material remained molten at the top of the blockage region (12 to 15 cm) for some time is quite consistent with the observed peak W/Re thermocouple temperatures of 2600 K nearby at 9.6 cm. The only trace of the original channel box and control blade is found in the lower 7 cm below the bottom of the fissile length. Consistent with these observations, the overall density in the upper half of the bundle is visibly less than the lower half. Based upon the appearance of the upper half of the bundle, the loss of material is from relocation of both metallic components and dissolved UO_2.

It should be noted that the test section experienced some rough handling during the unloading process from the ACRR. The fractured fuel column visible in the "after" image in Figure 3-24 may be due to the shock received by the test bundle when the experiment capsule unintentionally was bumped against the side wall of the posttest experiment storage tube.

In the following chapter, the thermal behavior of the test bundle is modeled using the MARCON-DF4 computer code. The analysis provides a basis by which the experimental data may be evaluated for general consistency. Although the computer model is not necessarily correct in every detail, the exercise is useful in assessing the measured information and in identifying data which seems inconsistent and therefore "suspect." Another major result described in Chapter 4 is an analysis of the W/Re thermocouple response where the "corrected" fuel cladding temperatures are derived from the W/Re junction measurements.

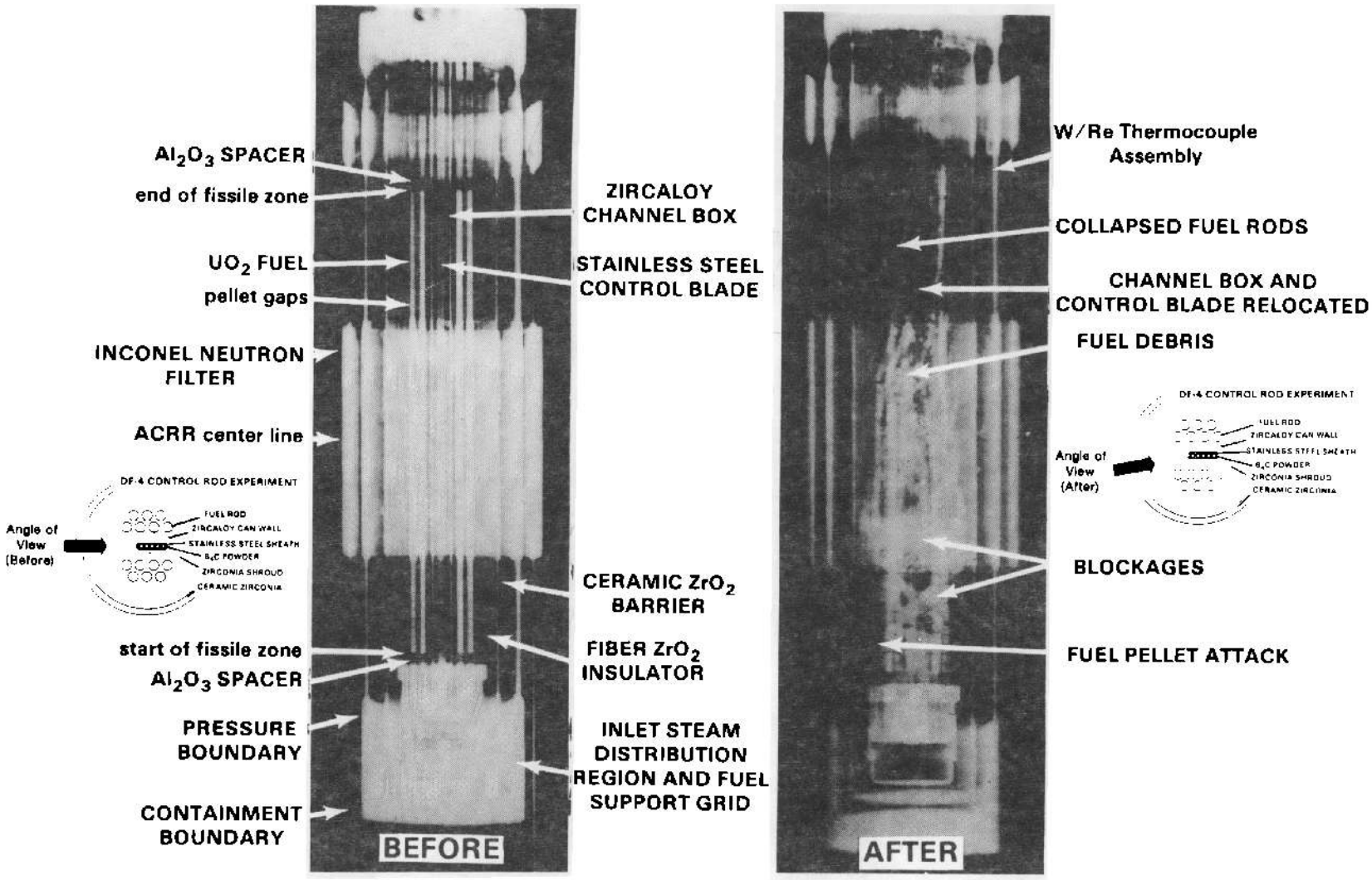

Figure 3-24: Radiographic images of the test section, comparing pretest configuration to the posttest damaged state.

4. EXPERIMENT ANALYSIS

A number of post-experiment analyses which are reported on in this chapter have been carried out for the DF-4 test. The purpose of the analyses presented here is to provide for some evaluation and interpretation of the measured data so that the information may be more easily applied to more sophisticated analyses by state-of-the-art severe reactor accident codes such MELPROG,[4] SCDAP,[7] MELCOR,[5] BWRSAR,[6] etc. For example, one of the analysis in this chapter deals with determining the fission power generated in the test fuel from knowledge of the measured ACRR power history and the response of the test fuel cladding thermocouples. The result of this is a characterization of the fuel rod power and the axial distribution of power, both of which are primary input data for the before mentioned accident analysis codes but neither of which are primary measurements from the experiment.

Also examined are the measured steam injection flow rates which are compared to calculated outflow rates and observed flow system pressurization effects. This comparison demonstrates the consistency of several measured parameters, giving users of the data an increased level of confidence in the accuracy of the measurements.

A major portion of this chapter is given to a presentation of results from a thermal analysis of the test progression performed using the MARCON-DF4 analysis code that contain specific models of the DF-4 geometry. *(This code was assembled at Oak Ridge National Laboratory by L.J. Ott using modules from the MARCON2.1B code.*[6] *Specific heat loss structures unique to the DF-4 experiment were added to allow for heat transfer paths not normally present in a full scale reactor fuel assembly.)* The code was designed to predict the heat transfer rates, chemical reaction rates, and the temperatures in the test section during the experiment. The heat transfer processes include conduction in solid structures, convection in the gas phase and radiation between the interacting surfaces. Metal/water reaction kinetics are modeled to determine the reaction rates of steam with zircaloy in the rods and canister and with steel in the control blade. The metal/water reaction model uses the Urbanic-Heidrich model[27] for solid state oxidation together with models for steam starvation, a representative geometry for the gaseous diffusion oxidation rate, and provision for a laminar or turbulent flow regime. The hydrogen generation rate and the spatial distribution of surface oxide layers are derived from the metal/water reaction calculations. The code is thus able to produce estimates of the temperature history of the test assembly as well as clad oxidation, hydrogen generation, and the extent of melting of assembly components. The primary limitation of the code is that it does not model the relocation of molten materials, and is, therefore, not strictly applicable after significant melting has occurred. The code was initially applied as a predictive tool to characterize the experiment response to the adjustable experimental parameters.

For the posttest analysis, measured information such as the test section inlet steam flow rates and the reactor power were used as input to the MARCON-DF4 code. Again these results are intended to illustrate where possible the general consistency of the various measured quantities and to provide additional insight into the events that occurred in the progression of the test.

Another major focus of Chapter 4 is on the behavior of the W/Re-ZrO_2 shrouded thermocouple assemblies. Results of a thermal analysis of the thermocouple assembly

response are given that provide estimates of the actual fuel cladding temperatures based upon the perturbed W/Re junction temperature history.

4.1 Test Section Inlet and Exit Steam Flow Rates

A check was made to verify the accuracy of the measured steam flow rates by comparing the measured inlet flows to calculated outlet flows. The outlet flows were estimated from a valve flow equation which makes use of measured temperatures and pressures in the vicinity of the outlet valves together with the measured valve orifice position.

The equations used to calculate the exit valve flow rate were forms suggested by the valve manufacturer (Nupro 4B series, Nupro Co., Willoughby, OH, 44094) that relate the valve flow to the pressure drop across the valve and the fractional amount that the valve is opened. The forms used in DF-4 were:

$$\dot{m} = A * C_v(x) * P_1 \qquad [g/s] \text{ for } P_2/P_1 \geq 0.53 \text{ (sonic flow)}$$

or

$$\dot{m} = B * C_v(x) * \sqrt{P_1^2 - P_2^2} \qquad [g/s] \text{ for } P_2/P_1 < 0.53$$

where $C_v(x)$ = valve flow coefficient provided by manufacturer

x = fraction open of valve stem

P_1 = upstream steam pressure (psia)

P_2 = downstream steam pressure (psia)

A = 0.147 and B = 0.169.

The leading coefficients A and B were adjusted to give consistent predictions compared to the measured steam input flow rates to the flow system under steady flow conditions (i.e., stable flow rates and system pressure).

The predicted valve flow rates were integrated over time and compared to the measured total condensate collected in the condensate tank as a second check on the accuracy of the equation. In the application of the equations, the valve flow coefficient was expressed as a polynomial function of x, the valve fraction open. The form used was:

$$C_v(x) = 0.0162637(x^3) - 0.45292(x^2) + 0.64576(x) + 0.62284*10^{-2}$$

The valve fraction open, x, was measured by using potentiometer that was connected to the motorized valve stem so that a voltage measurement could be related to the valve stem position.

The parameters used in the flow equation are shown in Figure 4-1. The sequence of events that determined the test section steam flows can be seen in this figure. The position (percent open) of the outlet valves control the steam flow exiting the test section. The outlet valves were throttled from 100% open to a few percent open at 5200 s. At about 5300 s the inlet valve was opened and steam pressure began to build up in the test section. After the desired pressure (100 psia) was established at 5600 s, the exit valves were opened an additional amount to maintain the required steam flow rate and pressure. A comparison of the integrated inlet and outlet flows is shown in Figure 4-2 and indicates that the steam flows are known quite accurately throughout the experiment.

4.2 Bundle Fission Power

The fission power generated in the test fuel was known approximately prior to execution of the experiment from the results of a neutronic analysis of the test geometry. An more accurate determination of the power generated in the test bundle fuel rods based upon actual measurement of the fission power is a necessary step in the characterization of the experiment before an accurate thermal analysis of the test may be performed. The following analytical technique was developed to determine the test bundle heating characteristics. It is convenient to characterize the test bundle power using a figure of merit relative to the measured ACRR driver core power. This figure of merit will be referred to as the *coupling factor,* f (W/gm/MW-ACRR), that when multiplied by the measured ACRR power (MW) gives the test fuel power in units of W/gm. This quantity is determined at four axial locations in the test bundle using the Pt/Rh intrinsic junction cladding thermocouple data. The method makes use of the observed rate changes in the fuel cladding heatup as the reactor power level was adjusted in step increases or decreases.

The details of the method are as follows:

Assuming that the fuel rod heatup was by fission only and that the heat losses were approximately constant during the step change in reactor power, an energy balance on a small section of fuel rod gives

$$\int MC_p dT = f\int Pdt - L\int dt \qquad (4\text{-}1)$$

where MC_p = heat capacity of the fuel/clad segment (J/gm°K),

T = clad surface temperature (assumed to approximate the temperature of the fuel and cladding,

f = fuel coupling factor W/gm/MW-ACRR,

P = ACRR power, MW and,

L = constant assumed heat loss from fuel/clad segment (W).

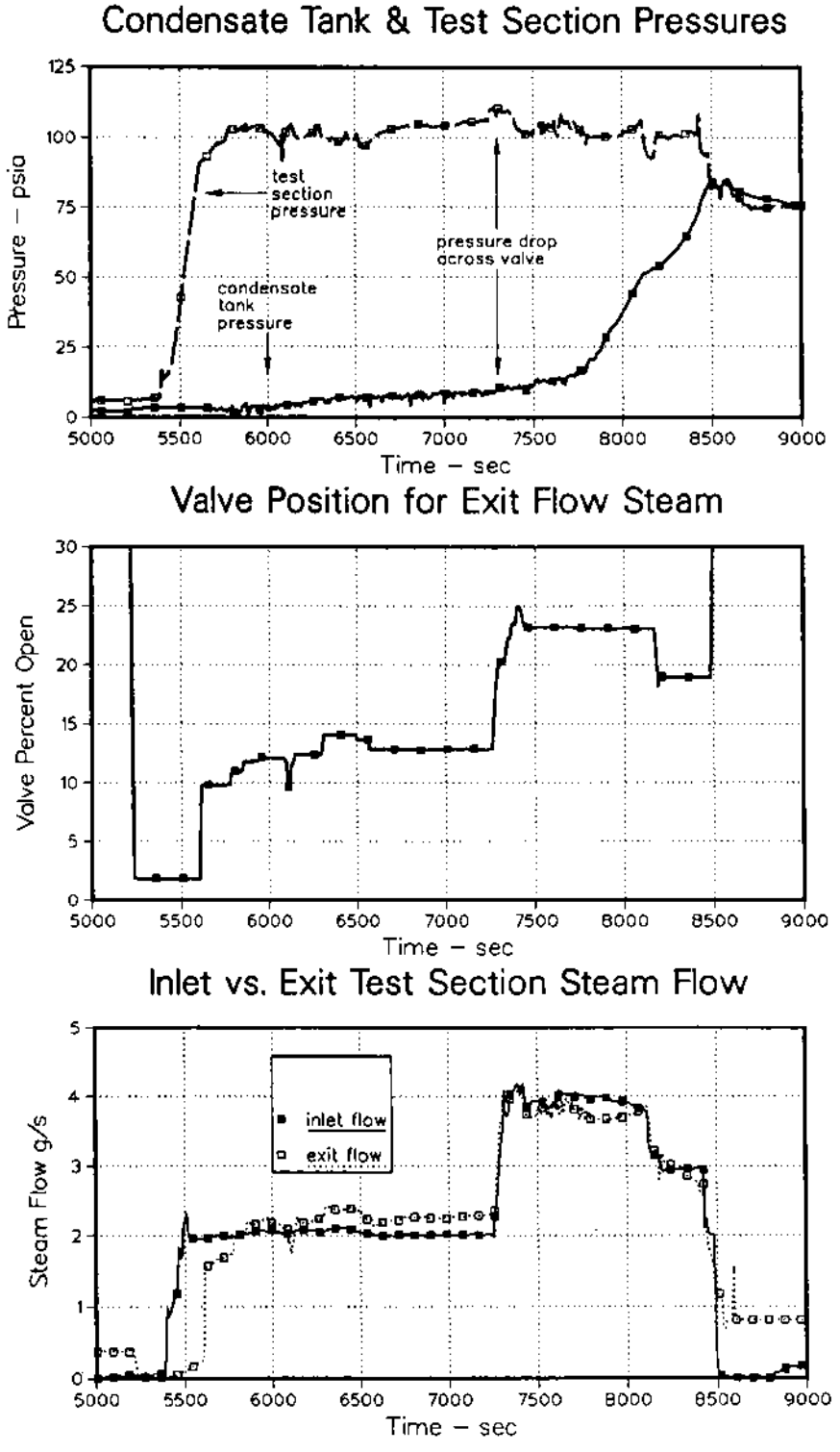

Figure 4-1: DF-4 Steam Flow Parameters.

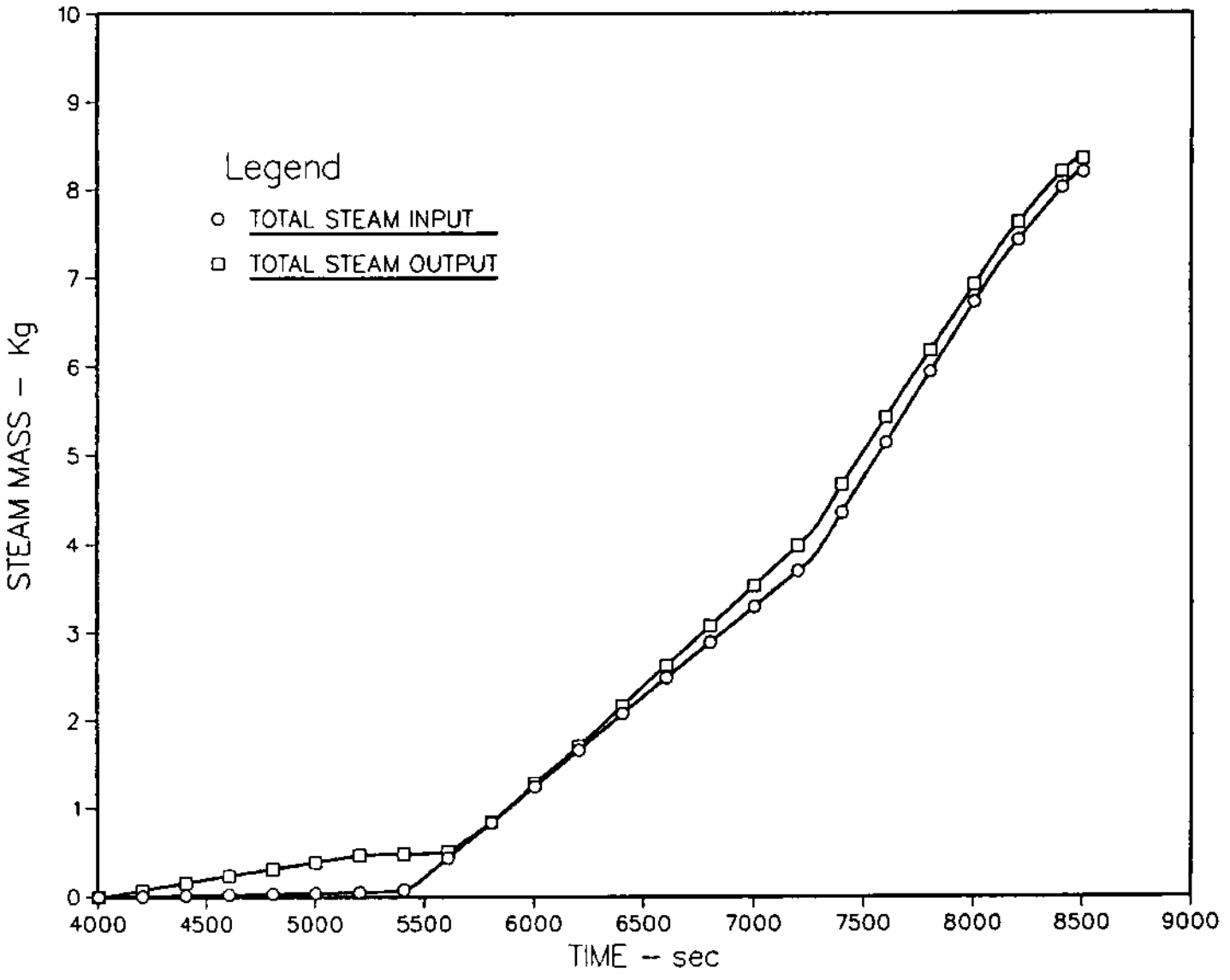

Figure 4-2: DF-4 Integrated Steam Flow

Here, the limits of the integration must be suitably small in order that the loss rate, L, be approximated as a constant (this is felt to be the weakest assumption). Equation 4-1 may be applied as the basis for a bi-variate linear regression applied to the experimentally measured cladding temperatures and ACRR power levels.

The regression was applied to data of the form

$$X_i f + Y_i L = Z_i$$

where
$$X_i = \int_{t_o}^{t_i} P(t)\,dt, \quad Y_i = -\int_{t_o}^{t_i} dt = (t_i - t_o) \tag{4-2}$$

and
$$Z_i = \int_{T(t_o)}^{T(t_i)} (MC_p)\,dT = H(T_i) - H(T_o);$$

where i ranges from 1 to N, the number of measured data values.

In equation 4-2, the integral of $MC_p(T)$ is the enthalpy change $[H(T_i)-H(T_o)]$ of the fuel/clad system over the time interval between data values at $t=t_o$ and $t=t_i$, and the integral of P(t) gives the reactor energy generated over the same interval.

Approximately 40 s of measured thermocouple data, 20 s either side of a step power adjustment (about 20 data points) were used to obtain a least squares regression of equation 4-2 yielding f and L as correlation coefficients. This procedure was performed for each thermocouple and each step power adjustment. Table 4-1 gives the calculated coupling factors and statistical information regarding the errors involved in the regression analysis for the 7 Pt/Rh thermocouples. Data is shown for all five of the power adjustments that were made before significant oxidation had occurred. Of these five power adjustments, two consistently showed the lowest standard errors for both the coupling factor and the overall curve regression. These were the adjustments at 6390 and 6500 s. There are basically three statistical criteria that can be used for selecting the the most reliable coupling factor data: the standard error of estimate, σ_{yx}, of the overall curve fit, the standard error of estimate of the correlation coefficient, σ_f, (in this case the coupling factor itself), and the coefficient of determination, r^2. The standard error of estimate, σ_{yx}, is a measure of the disparity between the estimated and actual values of the dependent variable in the regression. The standard error of the correlation coefficients is an estimate of the variability in the coefficients. The coefficient of determination is a measure of the "explained" variation relative to the total variation in the regression. In general the lower the values of σ_{yx} and σ_f and the higher the value of r^2 (ranges from 0 to 1, where 1 indicates a perfect fit) the better the fit. To facilitate comparisons of the variability in the calculated

coupling factors, a parameter, Π (in Table 4-1), was computed using the three error parameters just discussed,

$$\Pi = \sigma_{yx}\sigma_t/r^2. \tag{4-3}$$

The best data (least variability) is then obtained for the smallest value of Π. Inspection of Table 4-1 reveals that, although the test parameter, Π, for some thermocouples during the first three power adjustments are relatively low, they are generally higher than the adjustments at 6390 and 6500 s. Therefore, the data from the 6390 and 6500 second power adjustments were retained and the data for the other three adjustments were rejected. The resulting coupling factor profile is shown in Figure 4-3. Also shown in this graph are the 95% confidence bands and the coupling factor profile that was used in the MARCON-DF4 code analysis (and which seems to best predict the heatup rate).

The coupling factors obtained from the 6400 and 6500 second power adjustments for the 20%, 48%, and 70% (9.6 cm, 25.4 cm, and 36.8 cm) locations have a sample size of 4 (these locations each have two redundant thermocouples). The 95% location with only *1* thermocouple has a sample size of *2*. The small sample size together with a systematic bias between the 6400 second and 6500 second coupling factors (discussed below) result in a large uncertainty (95% confidence band is ± 1.68 W/gm/MW) in this location. The other three locations have 95% confidence bands of ± 0.35, ± 0.55, and ± 0.58 W.gm/MW for the 20%, 48%, and 70% locations respectively. It is clear from a comparison between the standard errors of estimate for the individual coupling factors seen in Table 4-1 and the 95% confidence bands displayed in Figure 4-3 that the individual regressions appear to have significantly less variation within the sample space than occurs between samples. For example, the standard error estimate for the coupling factor on T/C Z2P162 at the 6400 second power adjustment was 0.0358 W/gm/MW, which for the data sample size used for its calculation yields a 95% confidence band of ± 0.073 W/gm/MW. This is a factor of 7.5 times smaller than the confidence band established by the variability between the four samples used to obtain the mean coupling factor at this location. This indicates that, although the variability in the measured data for a given power adjustment is small, there is a much larger variation associated with repeatability between the coupling factor estimates for the various power adjustments.

Examination of the coupling factors for each thermocouple in Table 4-1 reveals a systematic bias between the factors for the 6400 and 6500 second power adjustments, the latter being consistently larger than the former by amounts varying between 13% and 32%. The small standard deviation of the individual regression coefficients together with the large deviation between the sample means indicate that the two samples cannot be considered as random variability in a single population, but must be viewed as separate populations with different means. This suggests that, either there is an error in the method employed in determining the coupling factor, or the coupling factor or losses are not constants with respect to time even at a given location in the bundle.

As a check on the calculational method, an alternate method was developed. It was noted from the digitized data output that there was a small delay (4 to 6 s) between the time that a power adjustment was initiated and when the thermocouples

Table 4-1
DF-4 Coupling Factors

T/C	ELEV	TIME	f	σ_{yx}	σ_f	r^2	Π
		sec	W/gm/MW	J	W/gm/MW		
Z1P215	.204	6100	1.237	.226	.0534	.9939	.0121
		6170	1.524	.254	.0687	.9984	.0175
		6250	1.048	.273	.0795	.9994	.0217
		6390	1.343	.254	.0295	.9996	.0075
		6500	1.563	.211	.0241	.9998	.0051
Z4P215	.204	6100	1.359	.373	.0883	.9794	.0337
		6170	1.314	.374	.1012	.9969	.0379
		6250	1.312	.412	.1199	.9985	.0494
		6390	1.262	.348	.0404	.9993	.0141
		6500	1.423	.443	.0506	.9988	.0224
Z2P160	.480	6100	1.396	.340	.0803	.9988	.0276
		6170	1.501	.406	.1100	.9978	.0448
		6250	1.348	.275	.0800	.9999	.0220
		6390	1.487	.308	.0358	.9996	.0110
		6500	1.684	.325	.0318	.9995	.0121
Z3P160	.480	6100	1.340	.362	.0857	.9903	.0313
		6170	1.831	.240	.0649	.9990	.0156
		6250	1.316	.234	.0681	.9997	.0159
		6390	1.460	.225	.0261	.9998	.0059
		6500	1.888	.312	.0357	.9996	.0111
Z1P115	.707	6100	1.614	.315	.0743	.9946	.0235
		6170	1.770	.273	.0739	.9990	.0202
		6250	1.228	.246	.0715	.9997	.0176
		6390	1.437	.320	.0372	.9997	.0119
		6500	1.903	.327	.0374	.9996	.0122
Z4P115	.707	6100	1.559	.498	.1177	.9843	.0595
		6170	1.549	.432	.1166	.9974	.0503
		6250	1.400	.335	.0977	.9994	.0328
		6390	1.488	.383	.0446	.9994	.0171
		6500	1.645	.311	.0355	.9995	.0110
Z1P065	.953	6100	1.470	.583	.1380	.9066	.0888
		6170	1.256	.502	.1358	.9968	.0684
		6250	1.561	.327	.0952	.9994	.0311
		6390	1.373	.460	.0534	.9990	.0246
		6500	1.638	.490	.0560	.9949	.0276

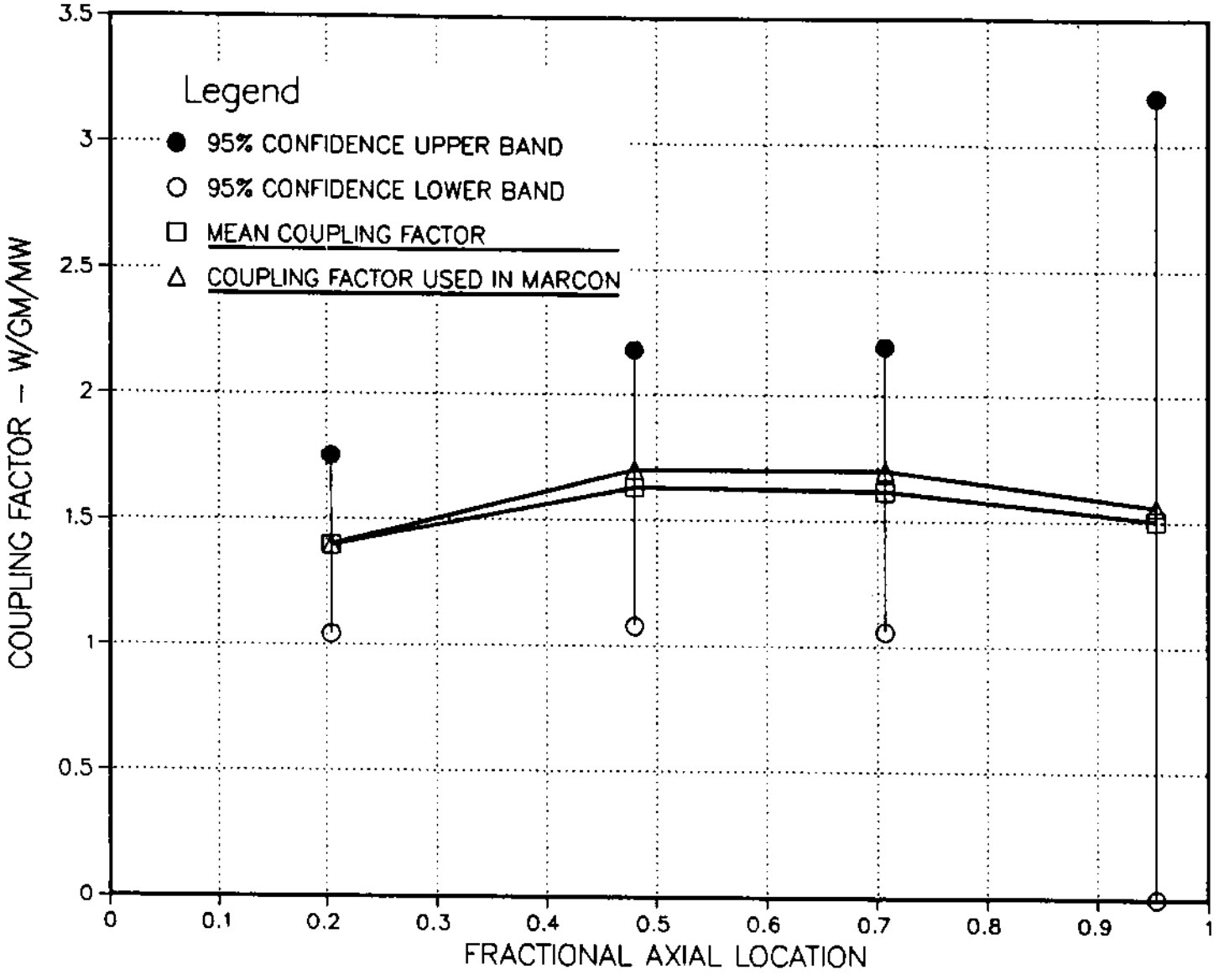

Figure 4-3: DF-4 Coupling Factors

responded by showing a change in the heatup rate. A method was developed whereby the heatup rates before and after the power adjustments could be compared while the data in the delayed period was eliminated. When an array of fuel rod enthalpies are calculated for the thermocouple temperature measurement array on either side of a power adjustment, and separate linear regressions of these enthalpies with respect to time are calculated, the result is

$$H_1 = A_1 t + B_1 \tag{4-4}$$

and

$$H_2 = A_2 t + B_2 , \tag{4-5}$$

where H_1 and H_2 are the time dependent total fuel rod enthalpies before and after the power adjustment. If the constant power levels before and after the adjustment (with the transient removed) are P_1 and P_2 then equation 4-2 reduces to:

$$\frac{dH_1}{dt} = fP_1 - L \tag{4-6}$$

$$\frac{dH_2}{dt} = fP_2 - L \tag{4-7}$$

Differentiating 4-4 and 4-5 and substituting into 4-6 and 4-7 yields two algebraic equations in f and L:

$$A_1 = fP_1 - L \tag{4-8}$$

$$A_2 = fP_2 - L \tag{4-9}$$

Solving for the coupling factor, gives the result

$$f = \frac{A_1 - A_2}{P_1 - P_2} \tag{4-10}$$

The mean coupling factors obtained by using the above described method are similar in magnitude to those found previously (see Figure 4-4). The variability at the 95% location was greatly reduced by good agreement between the two samples, and the average bias between the two power adjustments was reduced from 19% to 12%, mostly due to improvements at the 20% and 95% locations. However the sample-to-sample variability was not significantly reduced for the thermocouples at the 48% and 70% locations which is due to the aforementioned bias between the two samples. The methodology, having been thus investigated, reveals no systematic error of the magnitude observed here (~12% average, 19% maximum).

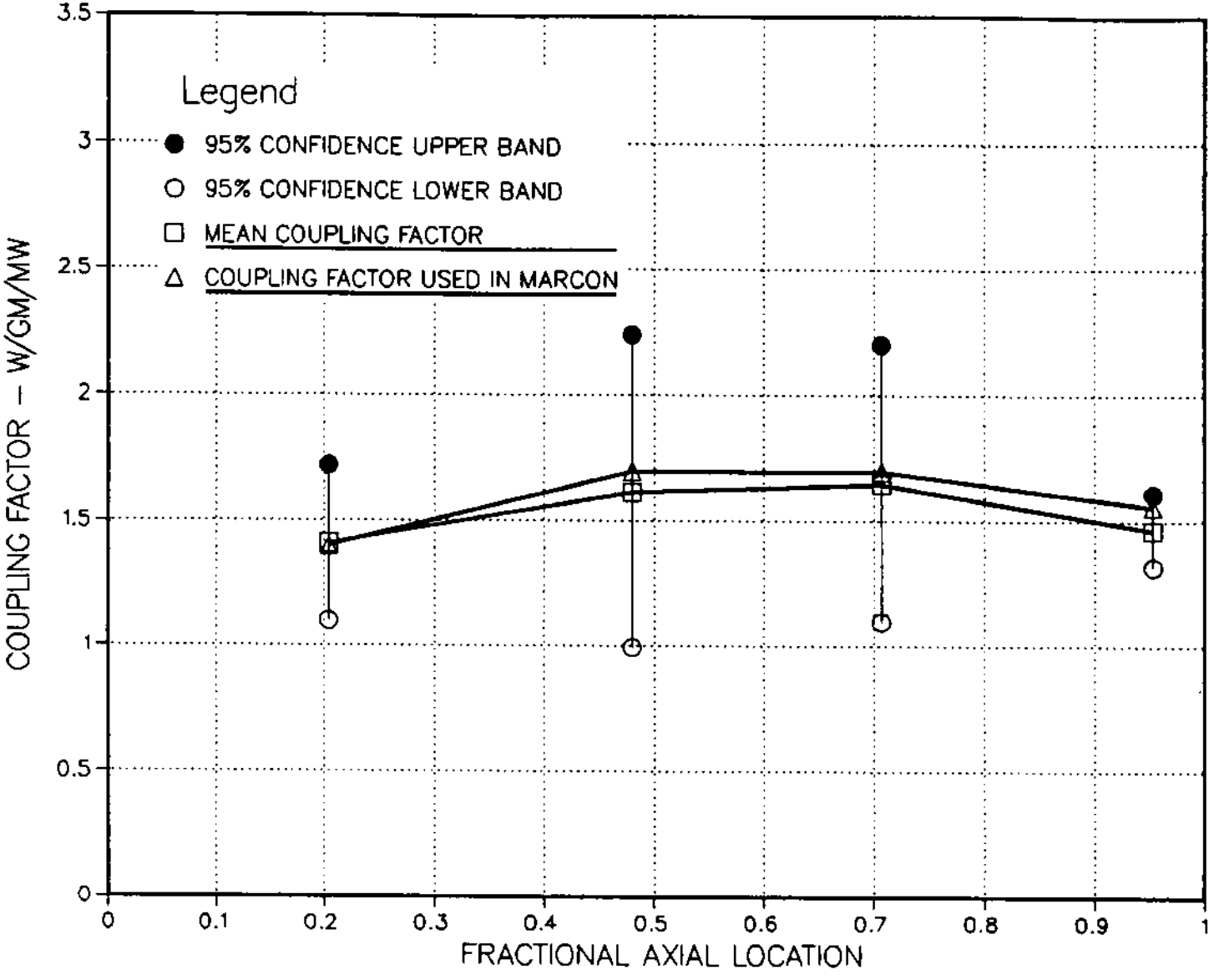

Figure 4-4: DF-4 Coupling Factors with Thermal Delay Removed.

It does not seem fruitful to speculate on what differences in experiment procedure resulted in significantly less uncertainty in one or two of the data sets, but it does appear that a series of power adjustments made in small steps spaced close together do not yield as "clean" a set of data as those obtained for single large power adjustments with sufficient time for transient effects to damp out. The power adjustments at 6400 and 6500 s, for example, represent step power changes of about 0.5 MW, while those at the earlier times were about 0.15 MW.

The spatial variation of the coupling factor determined from the above analysis may be described by a *chopped* sinusoidal shape (away from the axial boundaries of the fissile zone) of the form:

$$f = 1.3 + 0.4\sin[\pi(x-0.2)/\lambda]\,, \qquad (4\text{-}11)$$

where, λ, is the axial length of the fissile zone (50.5 cm), and x is the axial location relative to the bottom of the fissile zone (cm). This correlation skews the power slightly higher toward the upper half of the test section, but reflects the general trend observed in the thermocouple responses.

4.3 Comparison of MARCON-DF4 Calculations with Measured Temperatures

The calculated test fuel power characteristics and experimentally measured test section steam flow rates were used as input parameters for the MARCON-DF4 computer code. In this section the results of the MARCON-DF4 calculations are compared to observed trends of the experiment. One indicator of the accuracy of the modeling, and our understanding of the key processes (heat transfer, chemical kinetics), is the codes ability to predict the temperature histories of the modeled structures in the assembly. To assess this capability, code-predicted temperatures have been compared with Pt/Rh thermocouple measurements at various locations in the test section. Figures 4-5 through 4-8 show the results of these comparisons for locations on the inner bundle fuel rods adjacent to the canister at axial positions of 20% (9.6 cm), 48% (25.4 cm), 70% (36.8 cm), and 95% (49.5 cm), respectively, from the bottom of the fissile zone.

For the three thermocouples, Z1P215, Z2P160, Z1P115 (Figures 4-5 to 4-7), the agreement between measured and calculated temperatures was excellent until about 7700 s, when failure of the junctions occurred. For these three locations the calculated rod temperatures were nearly identical with the thermocouple measurements, indicating that the rod heatup rates governed by fission power, chemically generated power, and heat losses were accurately modeled in the code.

The calculations for the highest thermocouple location (95.3% elevation, Figure 4-8) show good agreement up to the point at which a power reduction was made from 1 MW to 0.4 MW at about 6500 s. From this time until the power was boosted again at about 7200 s (the equilibration period), the code calculated a more rapid heatup rate than was indicated by the thermocouple measurements. When the assumed power shape was altered to reduce the fission power at this location (a rationalization based upon its proximity to the boundary of the fissile zone), the heatup rate during this period was better simulated, but this caused an under-prediction of the initial heatup rate prior to this period. This treatment was probably not appropriate since the

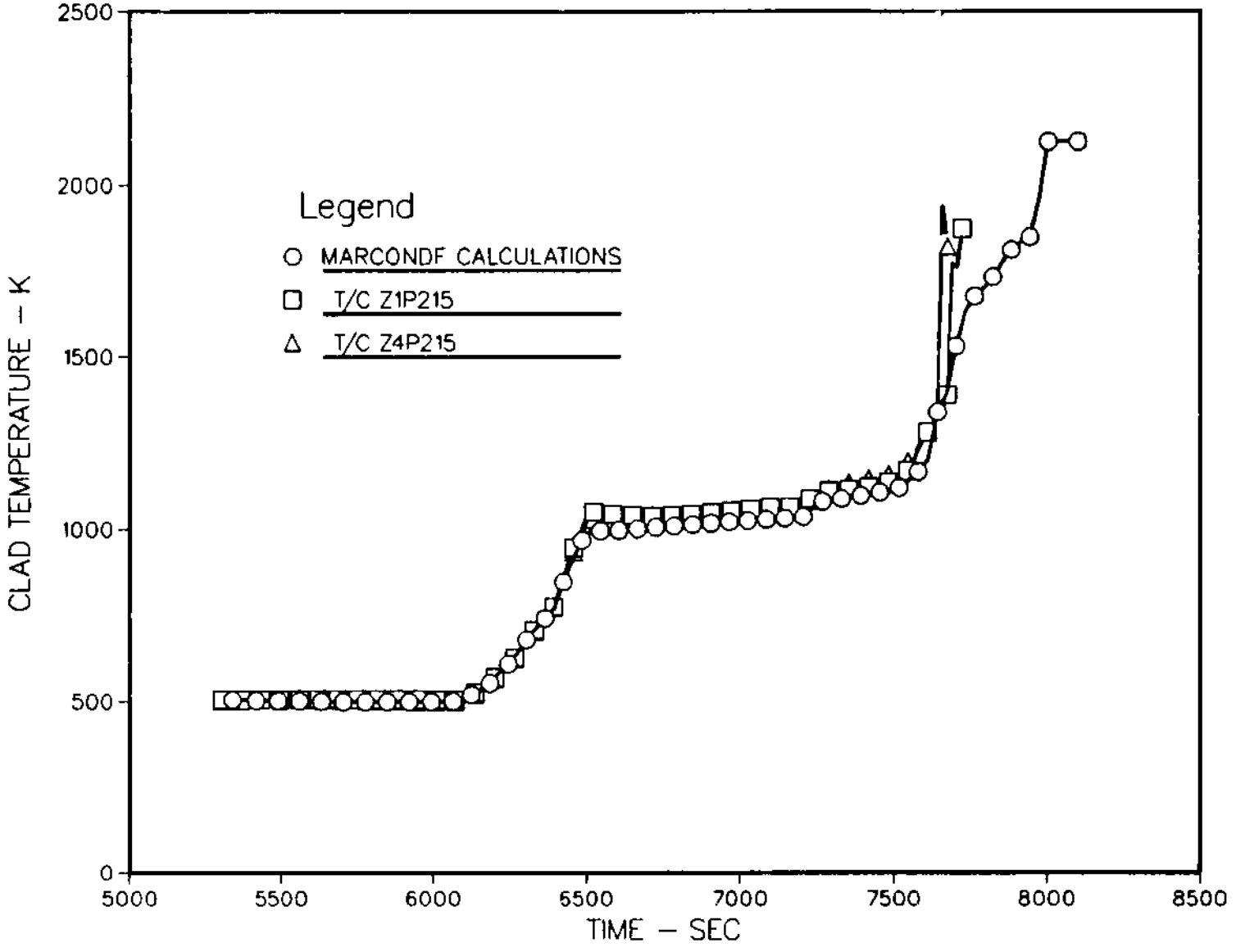

Figure 4-5: Comparison of Measured and Calculated Clad Temperatures at 20% Elevation (9.6 cm)

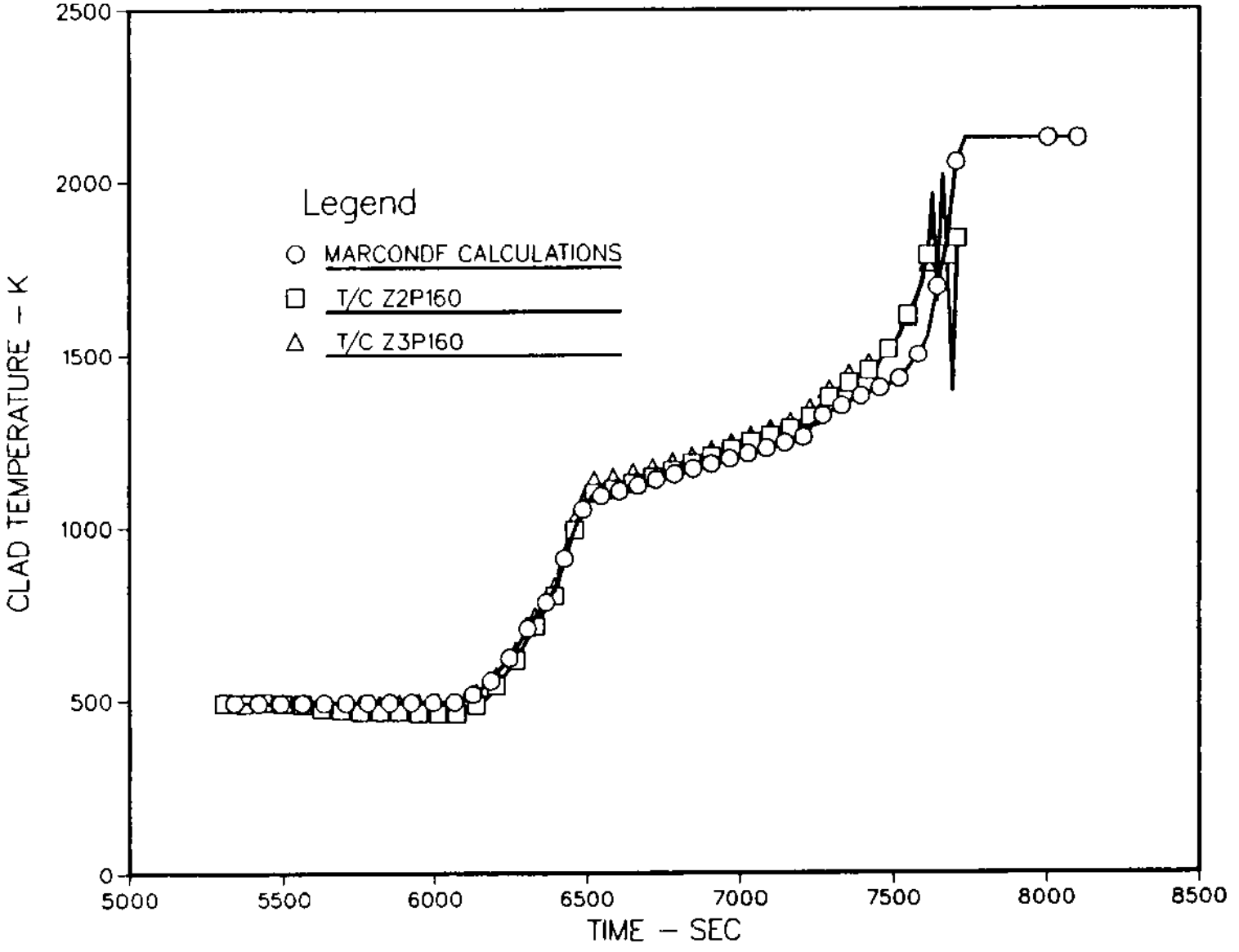

Figure 4-6: Comparison of Measured and Calculated Clad Temperatures at 48% Elevation (25.4 cm)

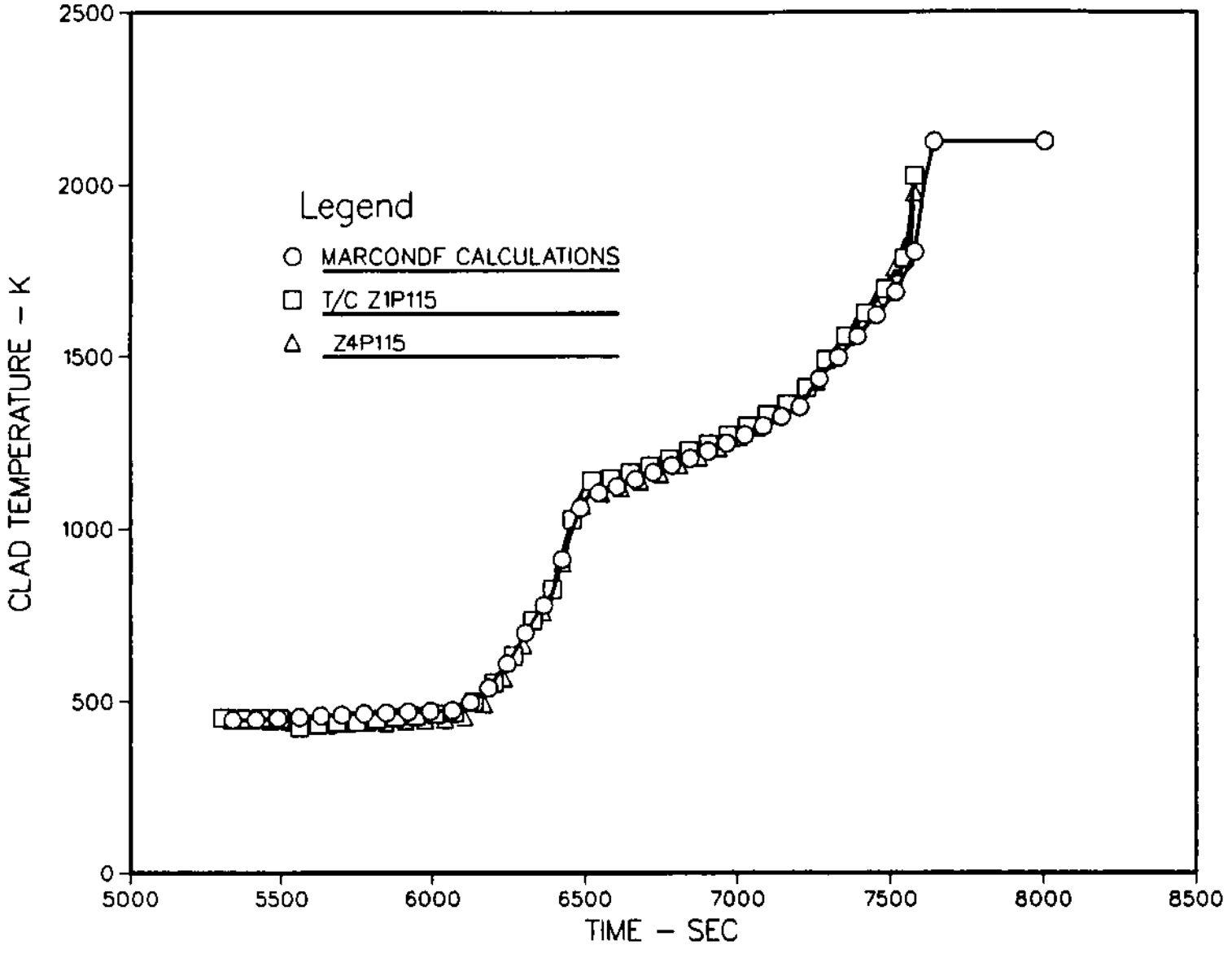

Figure 4-7: Comparison of Measured and Calculated Clad Temperatures at 70% Elevation (36.8 cm)

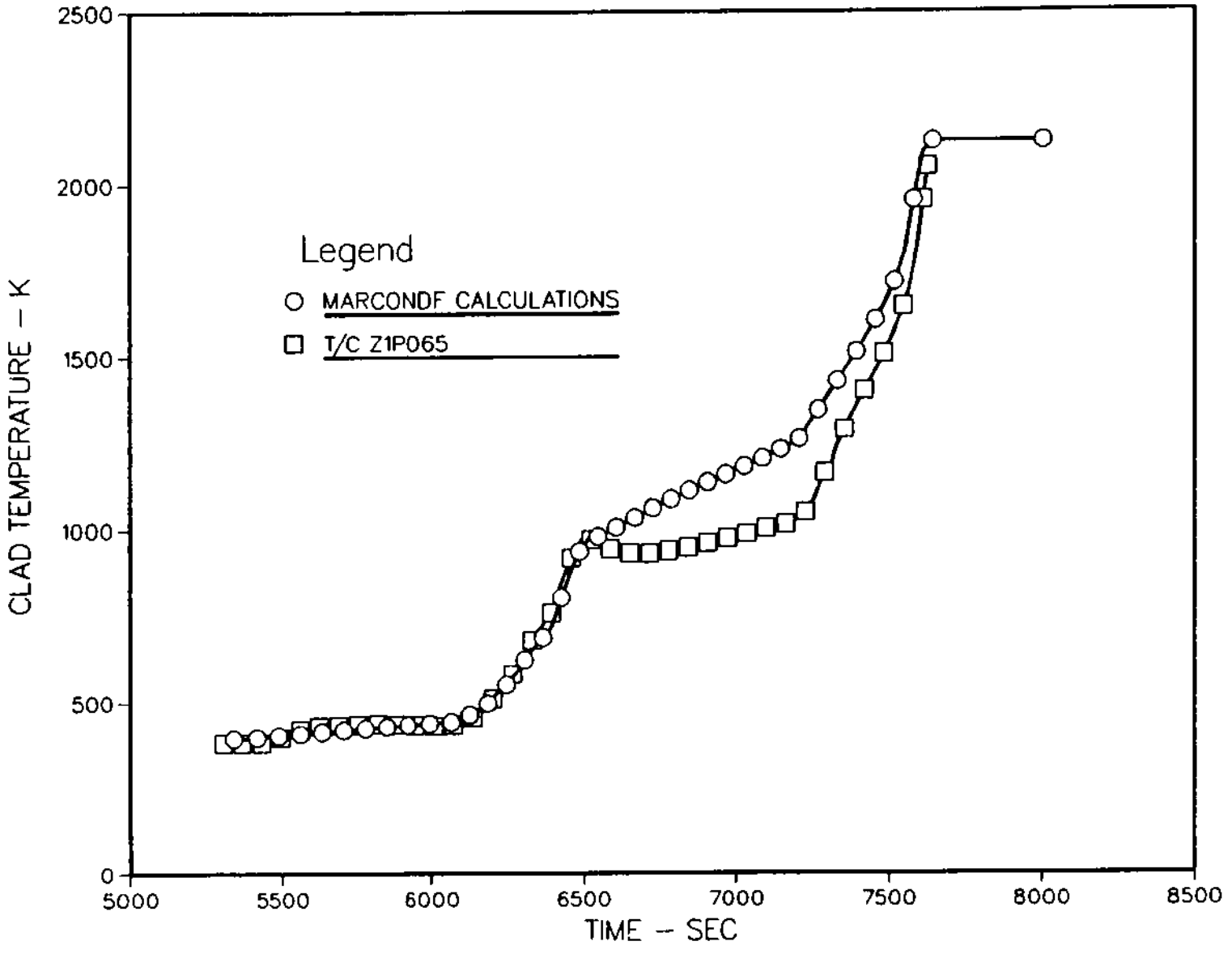

Figure 4-8: Comparison of Measured and Calculated Clad Temperatures at 95% Elevation (49.5 cm)

coupling factor for this location was obtained from the same thermocouple data and should reflect the relative local power level. It is considered more likely that heat losses by radiation from the top of the heated rod zone to the cooler structures above the active region, which is not modeled in the MARCON-DF4 code, was responsible for the over-predicted heatup rate.

The sudden rise in temperature at the bottom of the assembly (thermocouples Z1P215 and Z4P215, Figure 4-5) at about 7700 s is presumed to be due to the arrival of molten material from locations higher up in the assembly.

4.3.1 Predictions for Oxidation and Hydrogen Generation

A maximum hydrogen generation rate of about 0.1 gm/s was predicted by MARCON-DF4 to occur soon after the final power boost (to 1.4 MW). This subsequently dropped to about 0.06 gm/s and continued at that level until steam flow to the assembly was terminated at 8100 s. Figure 4-9 shows the predicted total hydrogen generated during the experiment. The code estimated that about 43 gms of hydrogen were generated during the course of the experiment. Although an analysis of the CuO/H_2 recombiner data as of yet has not been completed, it is not out of line with rough estimates made for the amount of copper oxide known to have reacted in the hydrogen getter tubes. Since the MARCON-DF4 code does not model material relocation after melting, the 43 gm estimate may be an upper bound for the following reason. Relocation of molten material to colder regions would tend to reduce the rate of hydrogen generation. On the other hand, specific models in the MARCON-DF4 code may tend towards under-predicting hydrogen production. Although the code option that extends zircaloy oxidation subsequent to melting was exercised, other modeling contingencies result in what may be a premature termination of oxidation on the channel box. This effect will be discussed below. Without an analysis of the CuO/H_2 recombiner measurements, yielding the actual DF-4 hydrogen production rate, it is not certain which, if either, of these two competing effects might be predominating in the codes estimates of hydrogen generation.

During the "oxidation transient" phase of the experiment (from 7500 s) the calculated power generated by oxidation of the fuel rod cladding and the channel box were each comparable to fission power (channel box oxidation in the code terminates due to melting at about 7800 s). The relative contributions to the energy input to the assembly are shown in Figure 4-10. It is seen from Figure 4-10 that significant metal/water reaction was predicted soon after the power boost at 7200 s, and the total oxidation power actually exceeded the fission power by about 7500 s.

The zone of vigorous oxidation was predicted by the code to begin in the upper half of the bundle (see Figure 4-11) and to gradually migrate downward. The spatial distribution of the predicted oxide growth at 7600 s is clearly skewed toward the top half of the bundle, while the distribution at 7800 s shows a flatter profile. By 8000 s the oxidation front was predicted to have moved to the lower half of the bundle and, in fact, a larger fraction of the cladding had been oxidized in that location. This effect was also predicted for the oxidation of the channel box as illustrated in Figure 4-12. Here the effect was even more pronounced. Note that the oxidation of the channel box was terminated some time after 7800 s, whereas oxidation of the rod cladding was not terminated (Figure 4-13) until steam flow to the bundle was terminated. There

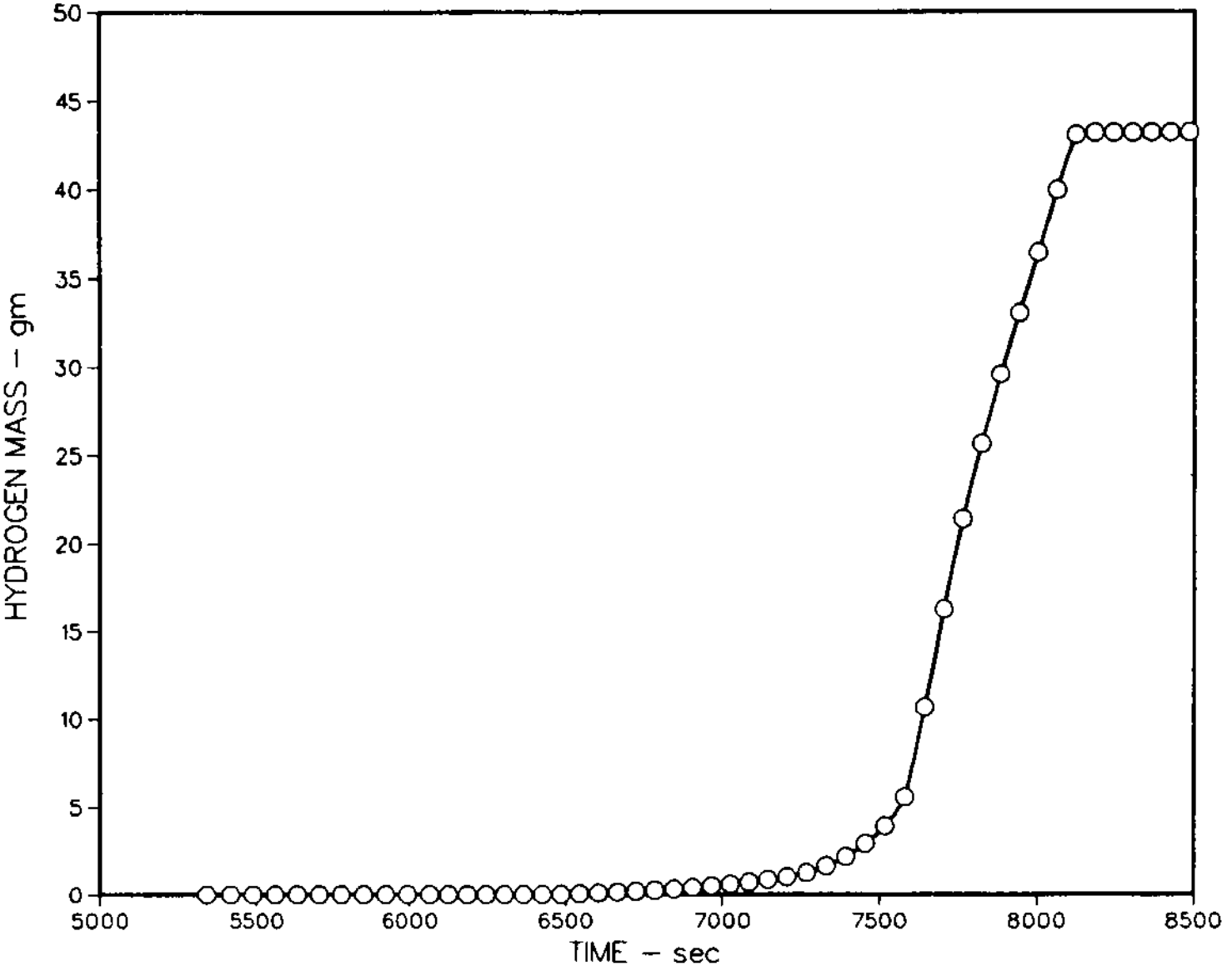

Figure 4-9: DF-4 Total Hydrogen Produced

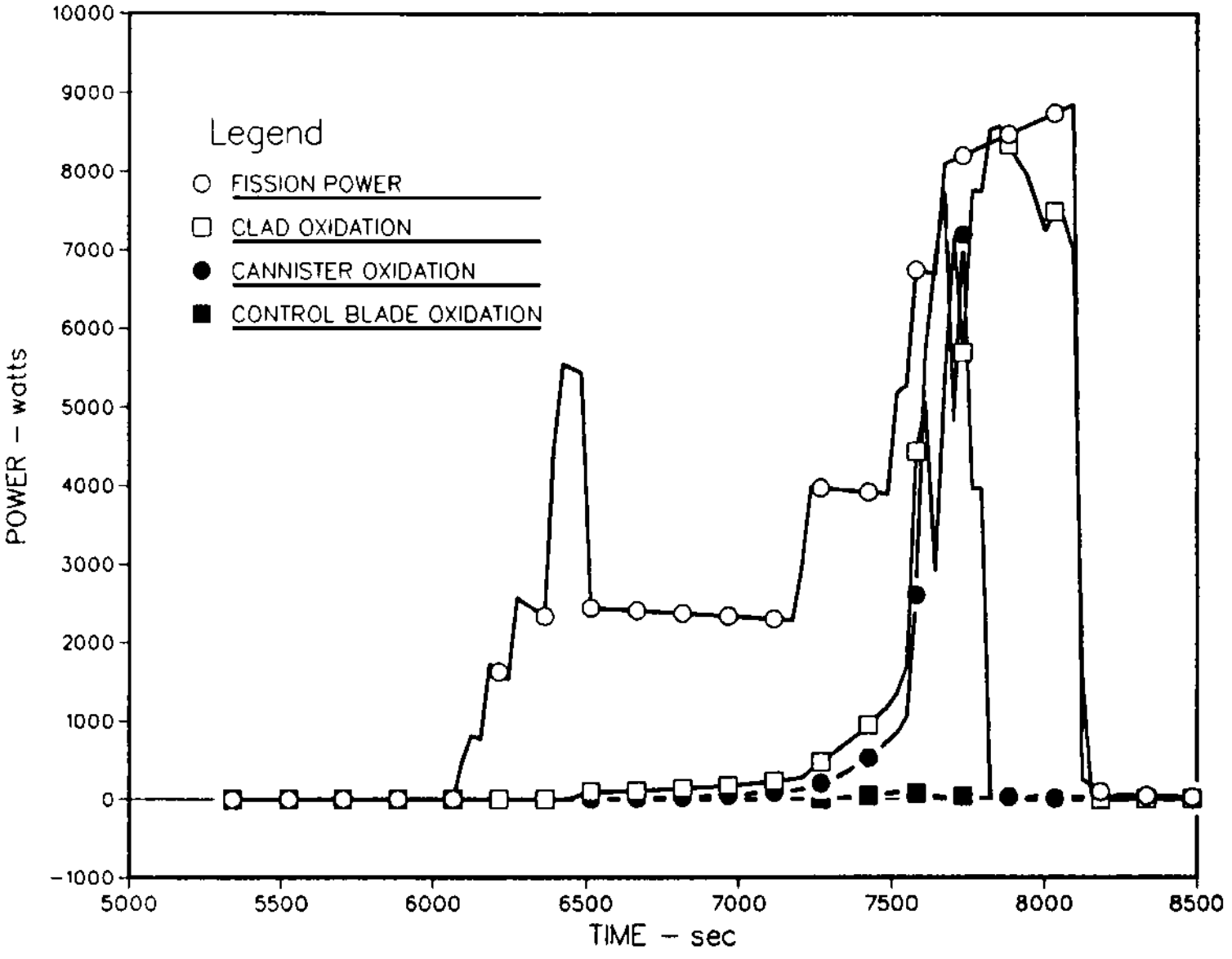

Figure 4-10: DF-4 Bundle Power Generation

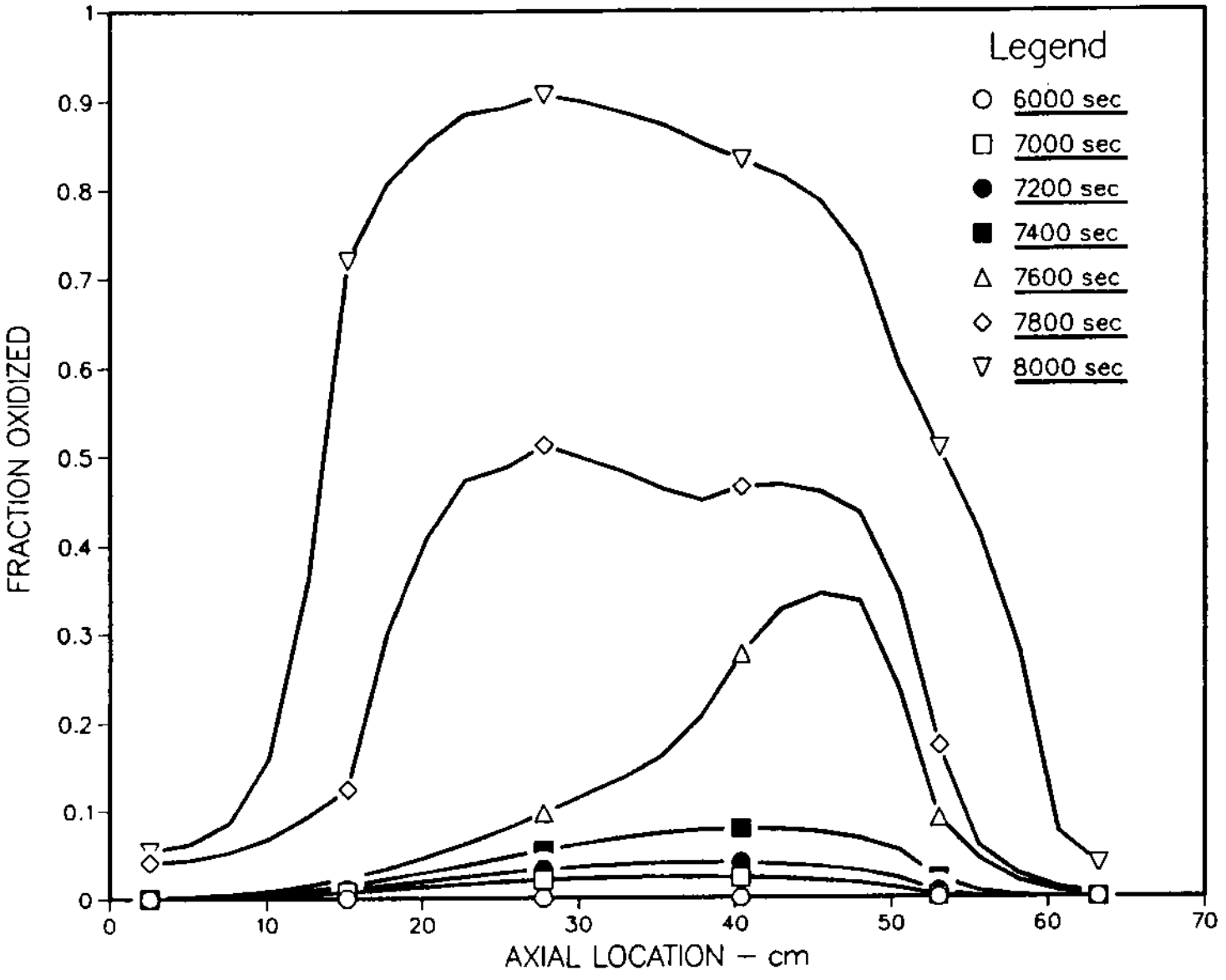

Figure 4-11: DF-4 Fraction of Clad Oxidized - Hot Rod

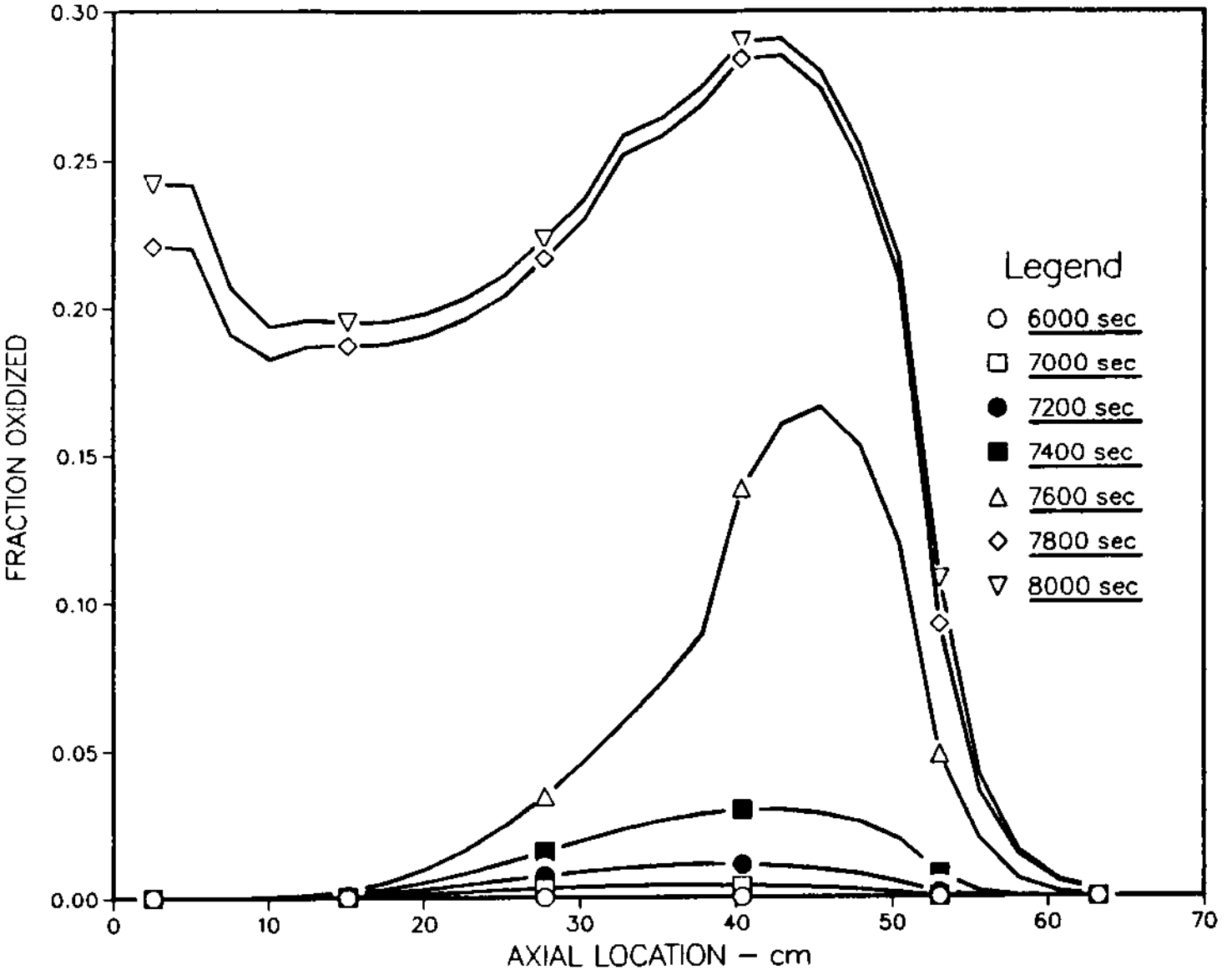

Figure 4-12: DF-4 Fraction of Channel Box Oxidized

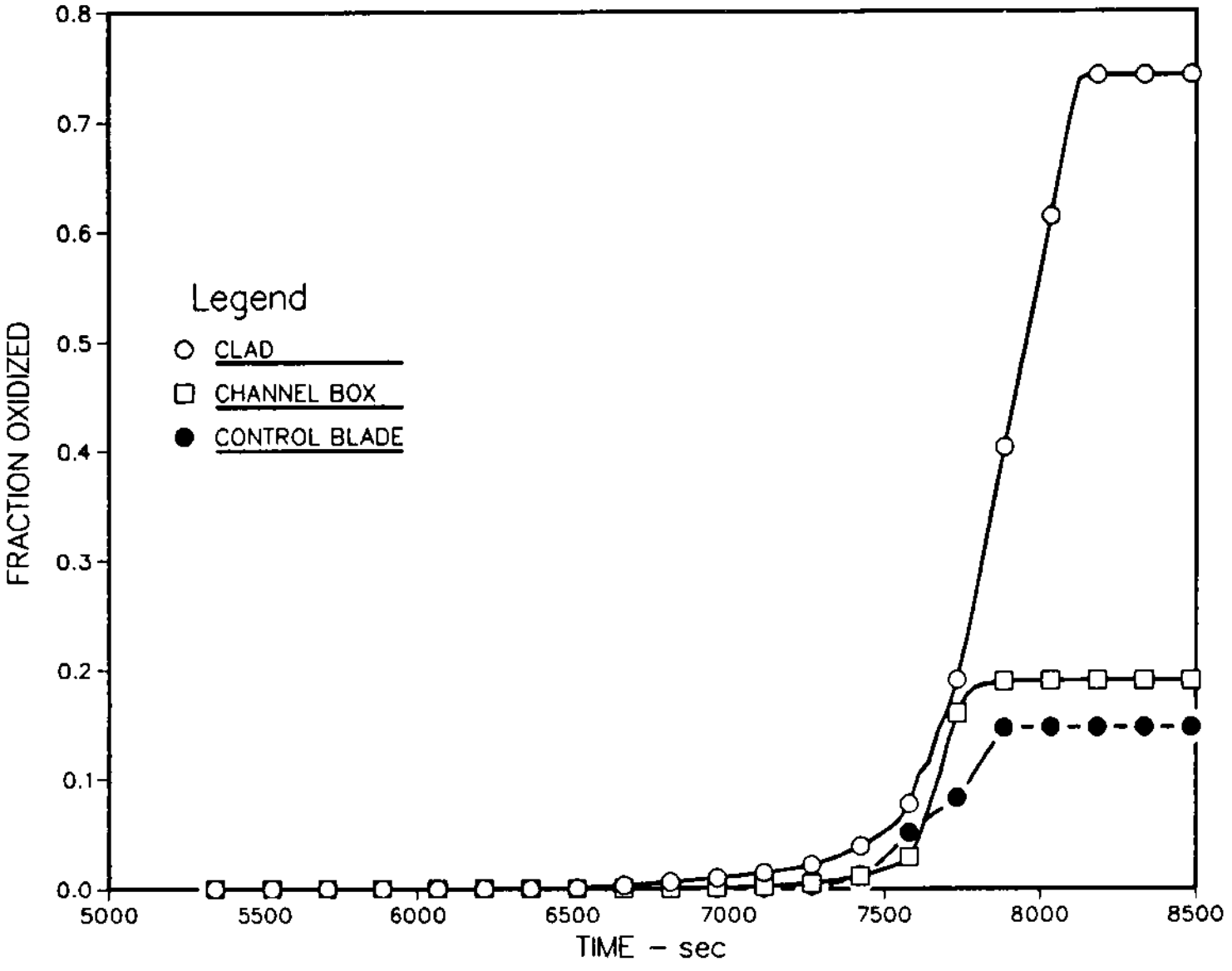

Figure 4-13: DF-4 Fraction of Structures Oxidized

are two code models which are responsible for this behavior. An option that allows continued oxidation subsequent to node melting was used for the rods, the canister, and the blade. However, the option continues to allow oxidation only until the bottom node in that particular radial region (fuel, channel box, etc.) melts, at which time oxidation reactions are discontinued for that structure. The energy balance model in the code is set up such that the energy that is generated or distributed to an already melted node is redistributed downward to unmelted nodes. The net effect is that channel box melting rapidly propagates downward because of the lower heat capacity of the channel box compared to the fuel cladding which is strongly coupled to the fuel pellet. As a result the code predicted that the channel box melt front reached the bottom node and oxidation was "switched off." The fuel rods, on the other hand, had sufficient heat capacity due to the thermal inertia of the fuel pellets so that the melt front never progressed to the bottom of the assembly and oxidation was not terminated in the rod cladding. Figure 4-13 shows this effect graphically. Although about 75% of the fuel rod cladding has been reacted, only about 20% of the channel box and 15% of the blade were predicted to oxidize.

4.3.2 Predicted Structural Melting

The MARCON-DF4 predicted fractions of structures melted during the experiment are indicated in Figure 4-14. The code calculated peak melt fractions of 98% for the control blade, 87% for the channel box, and about 70% for the fuel cladding. Clearly, since the code does not model the relocation of melted material, the axial distribution of energy sources from metal/water reactions may not be accurately tracked after about 7600 s. Gradual cooling of the assembly after the reactor power and steam flows were turned off (about 8150 s) accounts for the re-solidification of rod cladding seen in Figure 4-14. The extremely high calculated melt fractions would imply quite massive relocation of clad, canister, and control blade materials. These implications are consistent with sudden temperature excursions in the lower sections of the assembly measured by thermocouples there, which most likely imply the ingress of molten materials from higher up in the assembly.

Figure 4-14 shows that the control blade was predicted to melt about 100 s before the channel box and rod cladding started to melt. The blade and channel box melt fronts propagated from the original melt front location in the upper half of the bundle down to the bottom by about 7800 s. Additional melting of these structures probably occurred from material located above the original melt front location.

From the experimental evidence it seems likely that melting and slumping of the control blade took place before significant melting in the fuel rods, and that the B_4C and molten steel from the blade relocated to the lower regions of the assembly without appreciable interaction with the fuel. There may have been interactions between B_4C, steel, and zircaloy from the channel box during the period when the blade was melting, but there was no experimental indication of a reaction between the B_4C and steam either during the period when the blade was melting or subsequently.

4.3.3 Peak Temperatures Calculated by MARCON-DF4

The predicted thermal response of the test assembly is illustrated in Figures 4-15 and 4-16. Figure 4-15 gives the axial temperature profile for the inner rods adjacent to the channel box at various times during the experiment. It is notable that the fuel temperature predicted by MARCON-DF4 approaches the $UO_2/\alpha Zr(O)$ monotectic

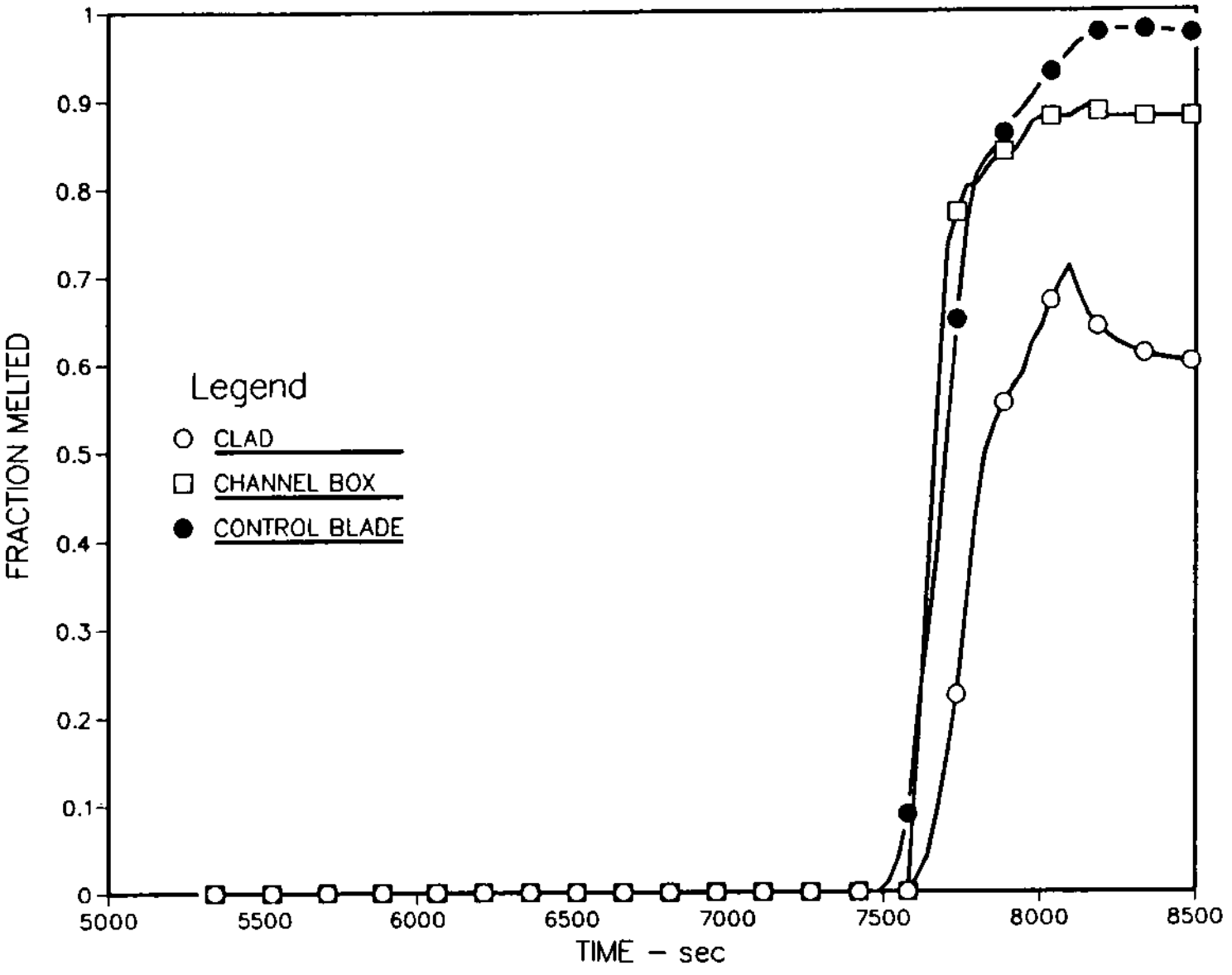

Figure 4-14: Fractions of Structures Melted

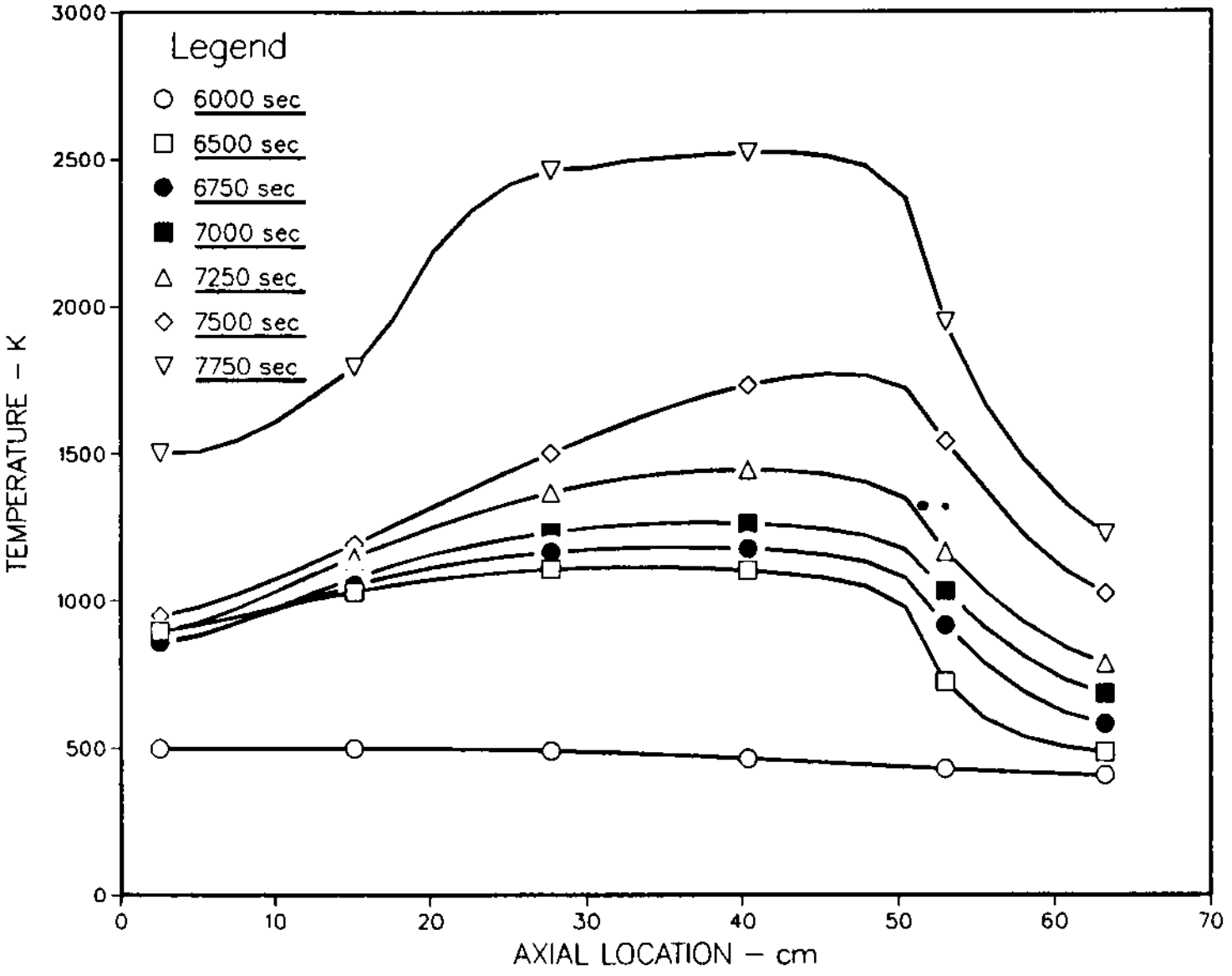

Figure 4-15: Hot Rod Fuel Temperatures

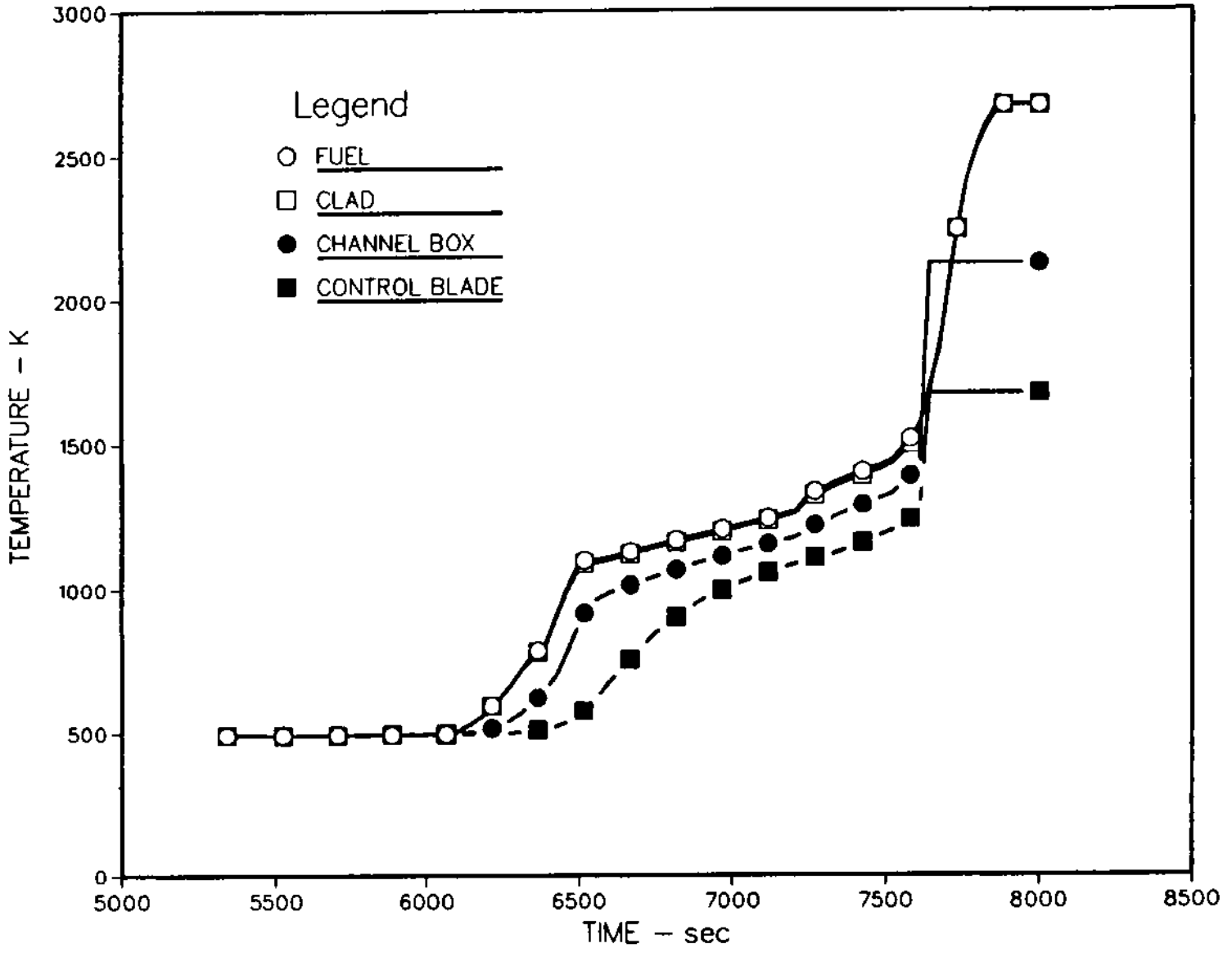

Figure 4-16: DF-4 Radial Temperature Profile at 48% Elevation (25.4 cm)

temperature (2673 K) at 7750 s, which could be an indication of significant fuel dissolution in molten cladding. However, a significant fraction of the energy heating the fuel rods was due to the oxidation of the cladding, and since the cladding would have been molten at these temperatures, it may not be realistic for the code to hold the clad in place while it continues oxidizing adjacent to the fuel. This situation may be supplying too much energy to the fuel and over-predicting the local rod heatup rate. The fuel heatup rate as calculated by the code between 7500 and 7750 s ranges from 3.0 to about 3.6 K/s. The W/Re thermocouples indicate heatup rates in the range of 3.1 to about 3.3 in this axial region, which do not appear to be out of line with the code prediction. In addition, peak temperatures measured by the W/Re thermocouples did not exceed about 2400 K. Given that these thermocouples lag the actual local temperature by perhaps 200 to 350 K (see section 4.4), the actual peak temperature could have been in the range of 2600 to 2750 K. This is comparable to the temperatures reached in the MARCON-DF4 calculations.

A comparison of the calculated temperatures for the fuel, cladding, channel box, and control blade are shown in Figure 4-16. There existed a distinctly negative temperature gradient from the fuel to the control blade until about 7600 s. At that time vigorous oxidation on the channel box caused its temperature to exceed the fuel cladding temperature. After oxidation was terminated for the channel box, the primary energy source again became the fission heating in the fuel and clad and the fuel temperature again exceeded the channel box temperature.

The thermal analysis of the DF4 experiment was performed with the intent of establishing the general characteristics of the test, and the MARCON-DF4 code proved to be an excellent vehicle for the task. The code performed well in terms of the thermal response despite the limitation inherent in its inability to relocate melted materials. The preliminary analysis has laid the groundwork for a more rigorous analysis which will utilize the MELPROG code as the appropriate BWR models become available in that code. The MELPROG code contains a sophisticated set of models for tracking the movement and re-solidification of molten materials, and therefore, does not suffer from the same limitations as the MARCON-DF4 code.

4.4 Analysis of High Temperature (W/Re) Thermocouples

The analysis of the high temperature W/Re thermocouple data was approached in two ways, both of which are presented in this section. The first approach involved using the MARCON-DF4 code to provide estimated cladding temperatures which would be used as a boundary condition for a detailed thermal model of the thermocouple assembly. The result of this is a predicted junction temperature which could be compared to the actual observed junction temperature. This approach suffers from the fact that the correct cladding temperature must be predicted by the MARCON-DF4 code in order for the predicted and measured T/C junction temperatures to agree. To overcome this problem another approach was taken. The second approach involved solving in effect an inverse heat conduction problem where the observed thermocouple junction response was used to estimate the cladding temperature. Both techniques are discussed in the following sections.

4.4.1 Predictions Based on MARCON-DF4 Results

Tungsten/Rhenium (W/Re) thermocouple data can extend the effective measured temperature range up to about 2700 K, nearly 1000 K, higher than the failure

temperature of the platinum/rhodium (Pt/Rh) thermocouples. However, unlike the Pt/Rh thermocouples, which do not react with steam in the test section, the W/Re thermocouples must be protected from the oxidizing atmosphere by enclosing them in a specially designed housing. The necessity of isolating the thermocouple junction from the test section environment had the unfortunate effect of thermally insulating the temperature sensing junction from the structure that was being monitored. Thus, a bias between the actual and measured temperature was introduced as well as a lag in response time. To aid in interpreting the W/Re thermocouple data and to facilitate calibration of these thermocouples a code called WRET (W/Re T/C Temperatures) was developed.

The WRET code employs finite difference techniques to calculate the thermal response of the W/Re thermocouple assembly (thermocouple and housing), given: the rod cladding temperatures predicted by the MARCON-DF4 code at the four thermocouple locations, measured temperatures at the containment boundary (boundary condition), radiation heat transfer rate between the fuel rods and the walls as calculated by MARCON-DF4, and the ACRR power. Appendix C gives a detailed description of the WRET code. The key phenomena modeled include: radiation from fuel rods to the thermocouple tip, convective heat transfer from the flowing steam and hydrogen to the thermocouple, radiation in the gas space between the ZrO_2 housing and the rhenium sheath, axial conduction in the thermocouple housing and in rhenium sheath, and gamma heating in the thermocouple assembly.

An important assumption was made in the WRET code analysis of the W/Re thermocouples and was probably the primary source of uncertainty. The dimensions of the W/Re thermocouple assemblies precluded their being mounted in contact with the inner (hot) fuel rods. They were, in fact, installed in proximity to the guard rods (the outer set of rods adjacent to the wall). The assumption was that the guard rod temperatures were as accurately predicted by the MARCON-DF4 code as the "hot" rod temperatures appear to be (see section 4.3). A modeling deficiency that may affect the results is that the MARCON-DF4 code does not calculate an azimuthal temperature variation in the fuel rods. This probably does not introduce a significant error for the inner group of "hot" rods which do not "see" much of the cold boundary wall, but it may be a factor for the outer "guard" rods which face the hot rod temperatures on one side and the colder shroud wall on the other side. It is likely that the guard rods had a considerable temperature gradient from the hot side to the cooler side. The single temperature associated with a radial node that represents a guard rod structure may not accurately describe the guard rod temperature (in the code) as it would "appear" to a thermocouple that contacted the rod from the cold wall side. In addition, posttest examination of the test section reveals some displacement of the fuel rods during the test, possibly due to bowing caused by the azimuthal temperature variation on the fuel rods, particularly the guard rods. There is some uncertainty, therefore, regarding the interpretation of the W/Re data with respect to the location of the thermocouples relative to the fuel rods.

In general the WRET code analysis of the W/Re thermocouple assemblies was able to produce predicted results that compared overall favorably with the measured temperatures obtained from the thermocouples. Figures 4-17 through 4-20 show the results of the calculations for the 4 guard rod thermocouples. These graphs compare the MARCON-DF4 code predicted guard rod temperature histories, the WRET code predicted thermocouple junction temperatures and the actual measured W/Re

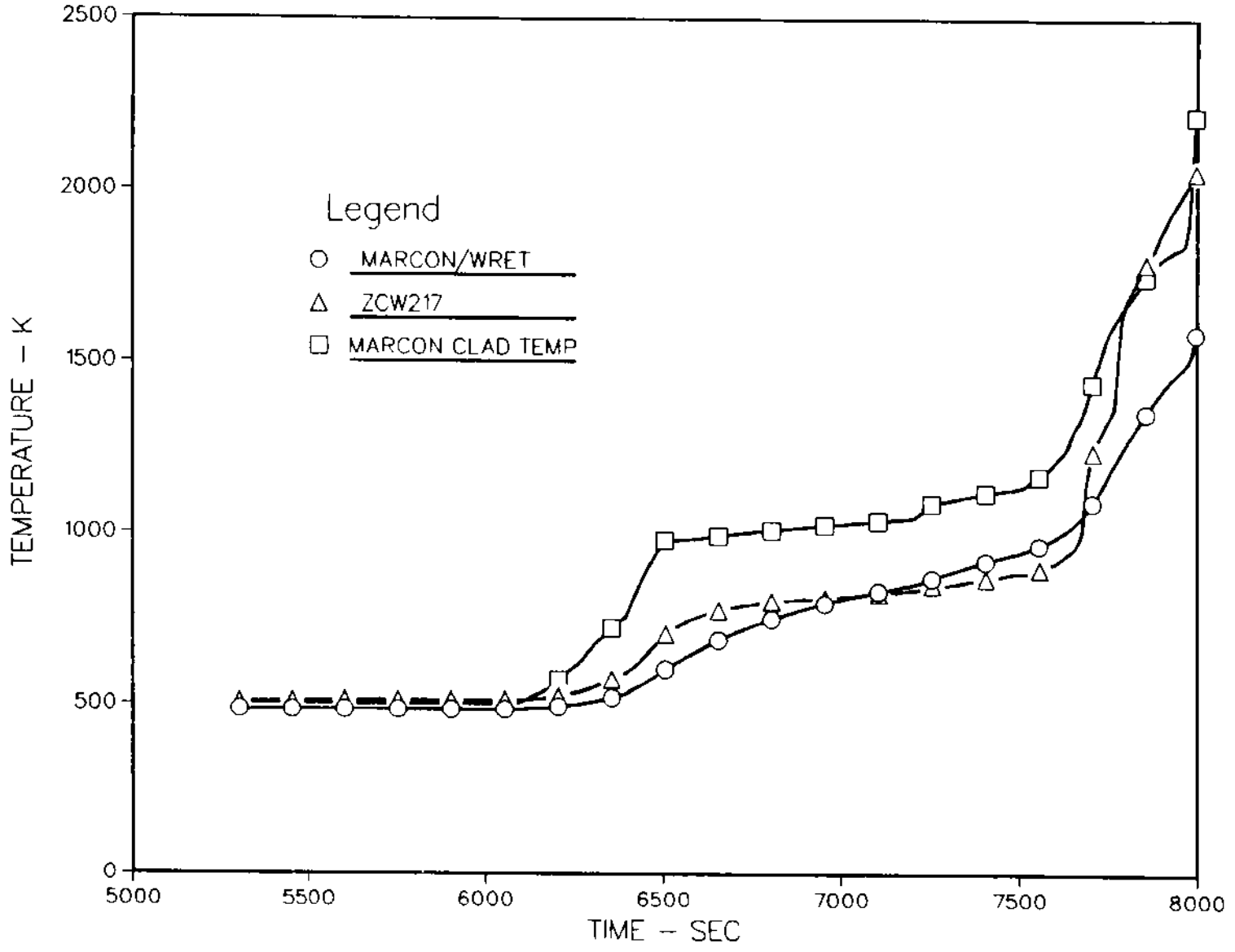

Figure 4-17: Comparison of Measured with Calculated Junction Temperatures - 20% Elevation (9.6 cm)

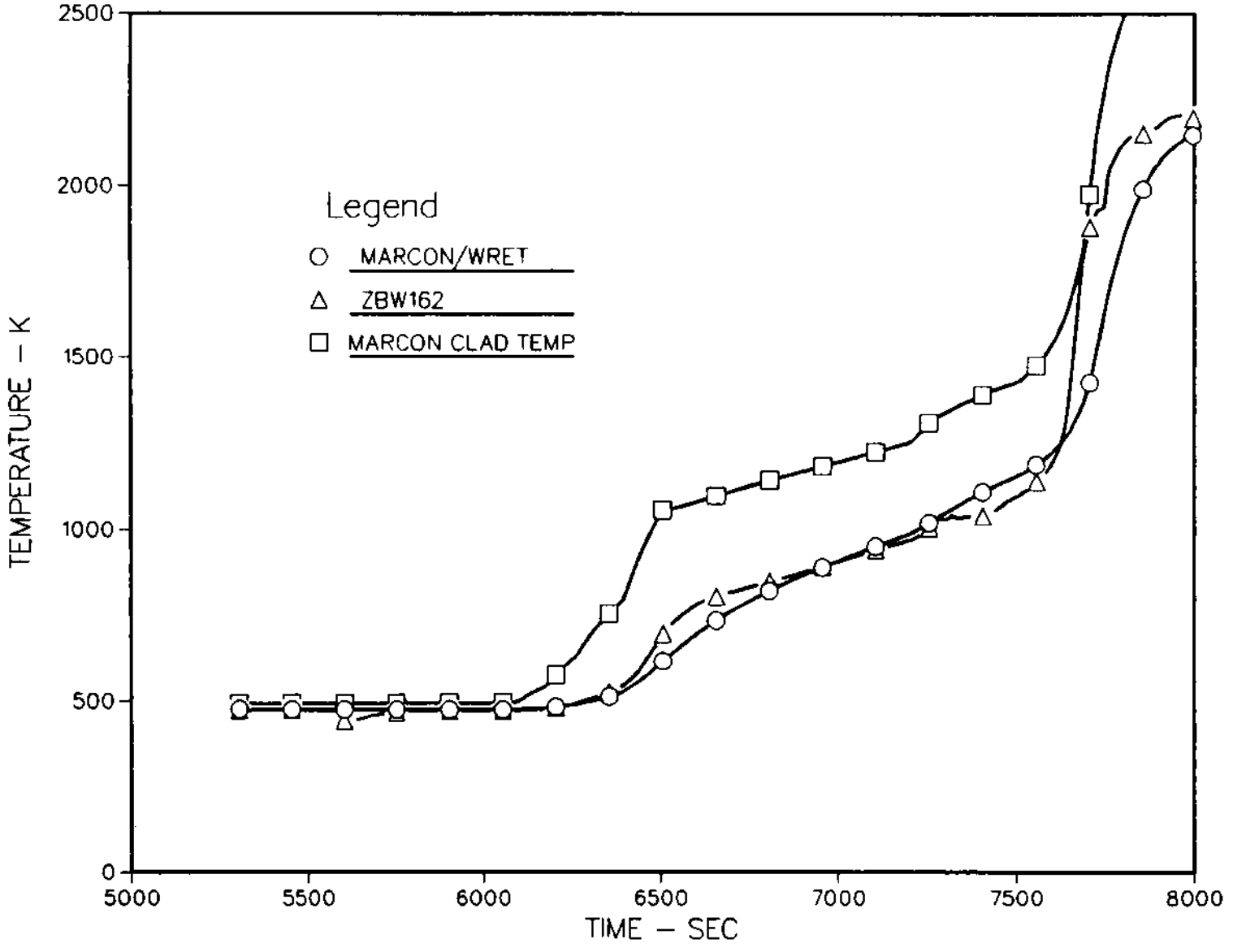

Figure 4-18: Comparison of Measured with Calculated Junction Temperatures - 48% Elevation (25.4cm)

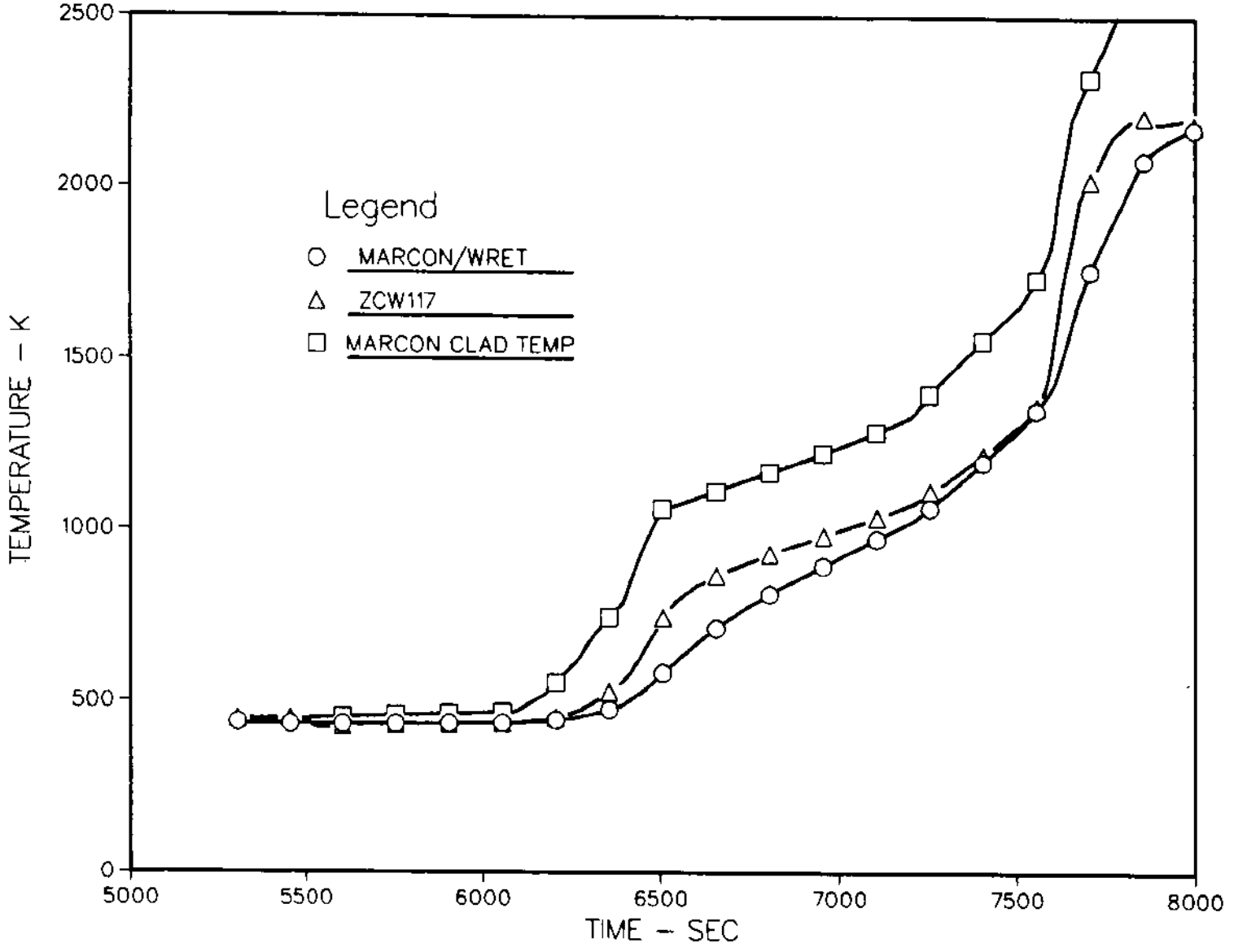

Figure 4-19: Comparison of Measured with Calculated Junction Temperatures - 70% Elevation (36.8cm)

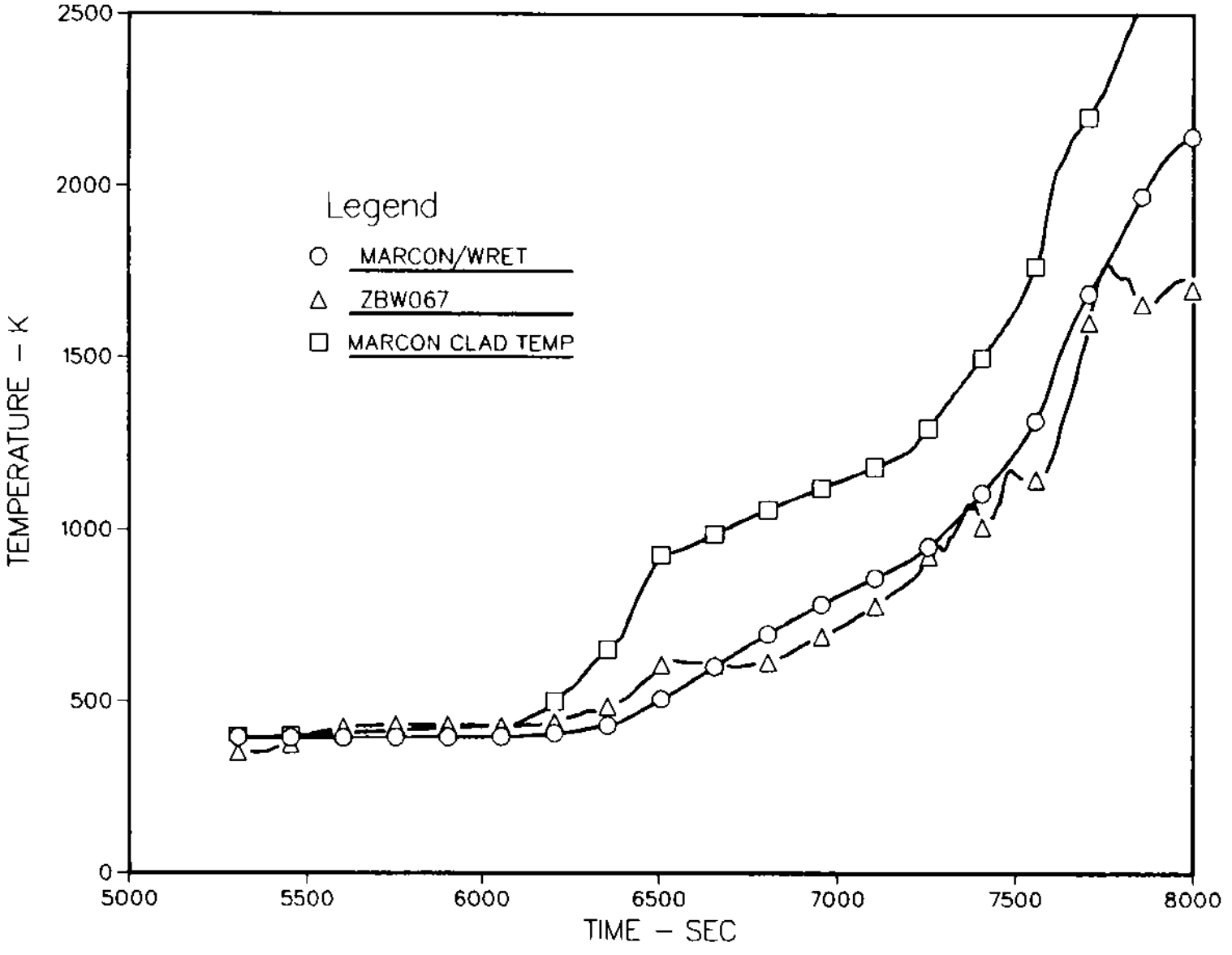

Figure 4-20: Comparison of Measured with Calculated Junction Temperatures - 95% Elevation (49.5 cm)

thermocouple junction temperatures. The mean absolute difference between the measured and the calculated junction temperatures was about 60 K (from 5000 through 7500 s) for all four locations. The agreement was better for the 20% (9.6 cm Fig, 4-17) and 48% (25.4 cm, Fig 4-18) locations (41 and 48 K, respectively).

The WRET code appears to slightly under-predict the heatup rate during the first 350 s of the transient (6150 to 6500 s) and then slightly over-predict the heatup rate until the metal/water reaction begins to predominate at about 7700 s. This characteristic was seen for all four thermocouples, but was most pronounced for the lowest thermocouple (20% elevation - ZCW217). The thermocouple at the 20% (9.6 cm, Fig 4-17) location also exhibited an extremely fast heatup rate, diverging from the predicted junction temperature and actually approaching the predicted rod temperature at about 7750 s. These anomalously high measurements may be due to contact of the thermocouple with molten materials relocated from above, and possibly from a failure of the protective ZrO_2 shroud surrounding the Re thermocouple sheath.

A number of parametric calculations were performed in which material properties such as thermal heat capacities, and thermal conductivities were varied as well as heat transfer coefficients and gamma heating rates to determine which parameters might be responsible for the differences in heatup rate between measured and calculated results. No parameter variation was identified that could precisely reproduce the measured heatup characteristics observed in the thermocouple responses. A variation in temperature between measured and predicted of ±60 K is, however, probably within the uncertainty band associated with thermophysical properties of the materials and other system parameters.

The thermal resistances associated with the W/Re thermocouple assemblies can be seen in terms of the node temperatures traversing from the rod to the shroud tip, the rhenium sheath tip, and finally to the thermocouple junction. Figure 4-21 shows the temperature histories for these four locations for the mid-plane thermocouple (48% elev, 25.4 cm-ZBW162). The maximum temperature drop from the rod surface to the tip of the thermocouple ZrO_2 shroud was on the order of 100 K while the drop from the shroud tip to the rhenium sheath was at times over 300 K. The primary thermal resistance, therefore, was due to the conduction pathway through the thickness of the shroud body. The shroud was about 0.67mm thick and had a relatively low thermal conductivity. The rhenium sheath which was ~0.3 mm in thickness with a thermal conductivity 20 times higher presented a relatively small thermal resistance. The result, as indicated in Figure 4-21, was a negligible temperature drop from the rhenium sheath to the thermocouple junction.

A by-product of the tungsten/rhenium thermocouple analysis was a more detailed knowledge of the thermal response of the structures surrounding the test section. The MARCON-DF4 code modeled these structures in a less detailed fashion using only 2 or 3 nodes. The thermocouples and their housings penetrated most of the way through the heat shielding structures that enclosed the test section. For this reason it was necessary to calculate the temperature profile through these structures as a function of time and radial position at each thermocouple location in order to characterize the thermocouple environment along its axial length (radial direction relative to the test section). A description of the shielding structure is given in section 2.1.4 (also see Figure 2-1). A typical temperature profile in the test assembly thermal shielding is illustrated in Figure 4-22. The location shown is at the 48% (25.4 cm) elevation level (location of T/C ZBW162). The graph shows the temperatures of the heat shielding

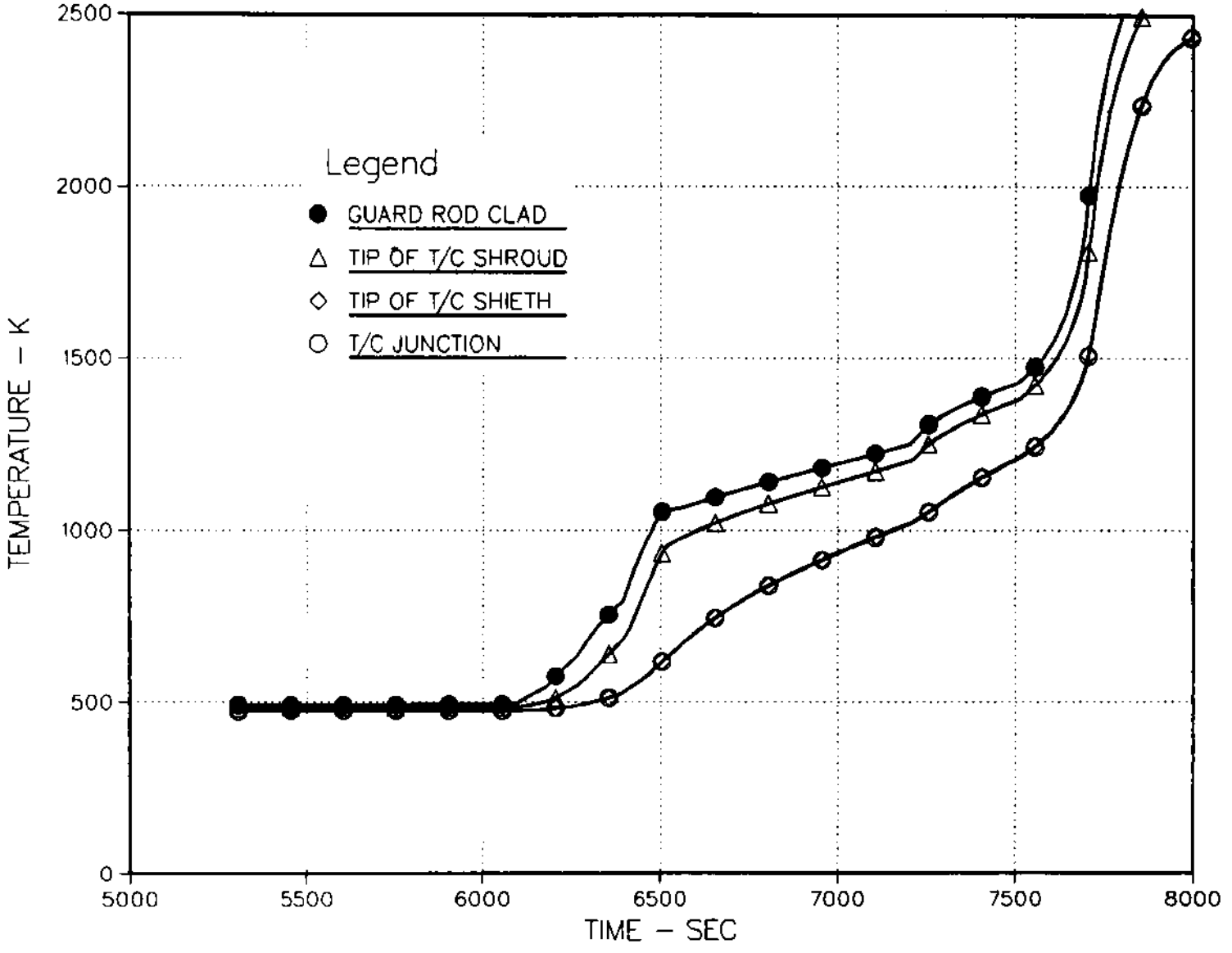

Figure 4-21: Calculated Thermocouple Assembly Temperatures at 48% Elevation (25.4 cm)

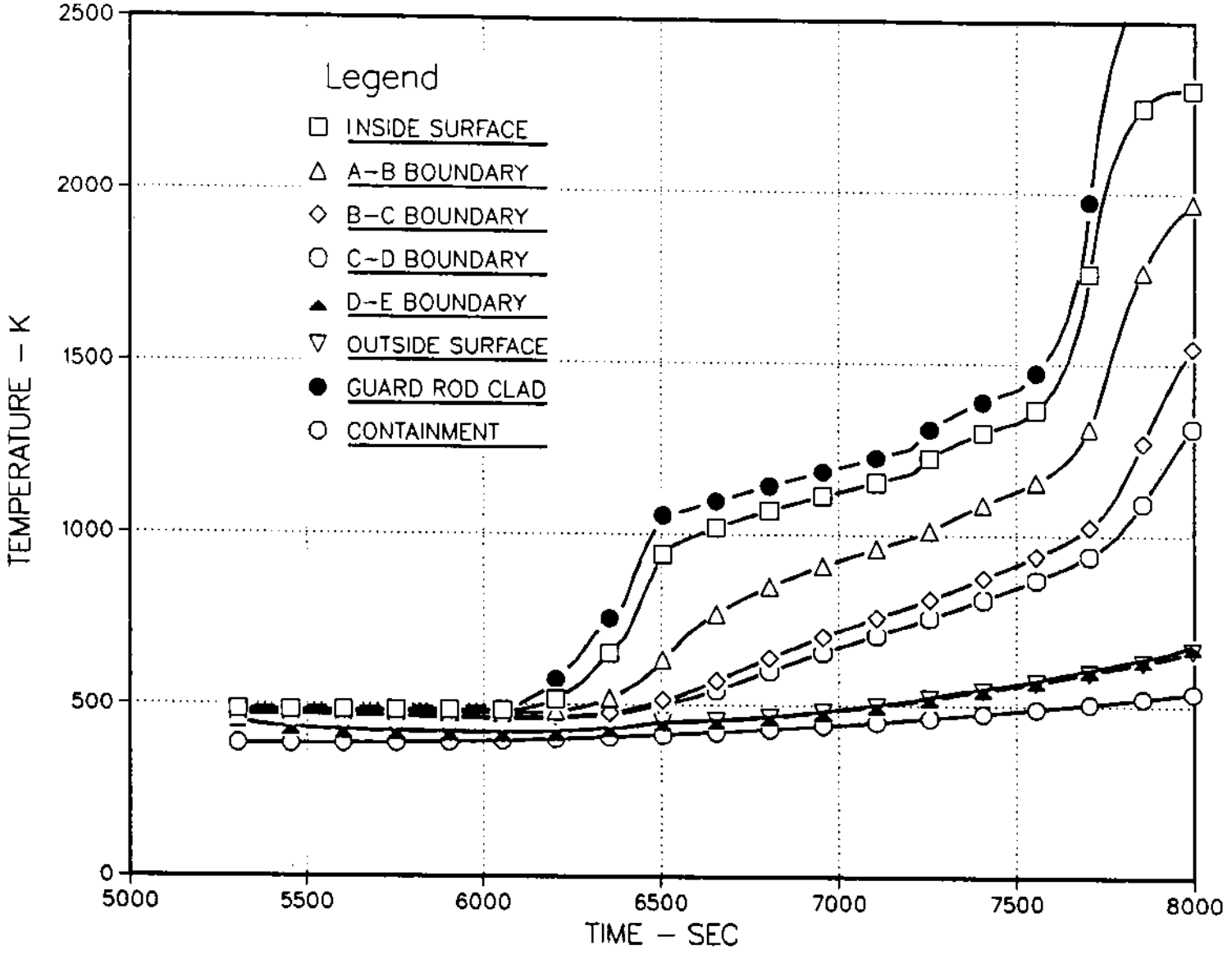

Figure 4-22: Calculated Shroud Temperatures at 48% Elevation (25.4)

shroud at various radial locations starting at the inside surface of the assembly (facing the guard rods) and ending at the cool containment structure wall. The guard rod temperature is also shown. There are essentially 4 material boundary interfaces in the shroud; these include the inside surface which faces the fuel rods, the interface between the inside layer of zirconia fiber and the ceramic zirconia layer (B-C boundary), the interface between the outside of the ceramic zirconia layer and the outside zirconia fiber (C-D boundary), and the interface between the outside zirconia fiber layer and the steel test section jacket (D-E boundary). The containment temperature and the guard rod temperature were the bounding conditions on the thermal calculation and were input to the WRET code. The graph shows that the extremely low thermal conductivity of the ZrO_2 fiber yields a large drop across these layers, i.e., between the inside surface and the B-C boundary, and between the C-D boundary and the D-E boundary (the A-B boundary is a intermediate location within the inner fiber layer). For example, the temperature drop from the inside surface to the ceramic zirconia shell was about 410 K at 6500 s. Near the end of the test (at 8000 s) the test section jacket temperature at the 48% (25.4 cm) location had risen to somewhat over 660 K while the inside surface temperature was in excess of 2300 K. Comparisons with thermocouple (SHC210) data at the C-D boundary (outside of the ceramic zirconia shell) agree well (maximum difference is less than 100 K) with the temperatures calculated by the code at this location (~25% elevation).

4.4.2 The Inverse Heat Conduction Method

The primary purpose for instrumenting the test package with shrouded W/Re thermocouples was, of course, to obtain data beyond the range at which the Pt/Rh thermocouples failed, with the intent of estimating the peak test section temperatures during the experiment. It was desired, therefore, to use the measured W/Re thermocouple data after the Pt/Rh thermocouples had failed and after the point in time when the MARCON-DF4 code-predicted-temperatures became suspect (these occur at nearly the same time since material relocation begins about the time of Pt/Rh thermocouple failure).

In order to directly utilize the W/Re thermocouple measurements to estimate the guard rod temperatures it was necessary to solve an inverse heat conduction problem (IHCP). Inverse problems are a subset of a larger class of problems that have been referred to as "ill-posed" problems.[28] In the standard heat conduction problem the boundary conditions are specified and the internal thermal response of the body is calculated. The procedure is reversed for the IHCP, that is, the thermal history at one or more points interior to the body is known and it is necessary to calculate the boundary conditions (i.e., surface temperature or heat flux). This type of problem is commonly encountered in the analysis of experiments including heat transport and structural analysis.

The larger class of problems is referred to as "ill-posed" in the sense that the solutions may not satisfy the classical requirements for uniqueness, existence, and stability that are necessary for a "well-posed" problem. For example, small changes or noise in the data may lead to large differences or large magnitude oscillations in the solution (unstable solution). For most IHCPs, however, adequate solutions can be obtained. The tendency of the solutions to be unstable can be handled in several ways. For the IHCP treated here it was necessary that the time step be sufficiently large compared to the thermal relaxation time of the system such that variations in the boundary

conditions were adequately sensed in the thermocouple junction during the time step. Since small variations in the response function can result in large changes in the solution, high frequency oscillation in the measured thermocouple data may need to be removed by filtering or curve fitting of the raw temperature data. For some situations it is not possible to entirely remove all traces of oscillatory behavior in the solution, but the magnitude can be reasonably limited and the solution generally appears to fall along the mean of the peaks and troughs in the oscillation.

In addition to the problems noted above, there may exist sets of physical conditions that inherently resist a solution to the inverse problem. For example, if the heatup rate as measured by a thermocouple is so rapid that a time step comparable in size to the duration of the rapid transient phase is necessary, the loss of definition in the solution may introduce an unacceptable uncertainty in the answer. Also, great care must be taken to assure that the conditions at the point of switch-over from the forward conduction problem to the inverse conduction problem are as continuous as possible, that is, that the calculated thermocouple junction temperature equals the measured junction temperature and the time derivative of the temperature is continuous at the transition point.

The approach taken for the analysis of the W/Re thermocouples in the DF-4 experiment was to use the WRET code (developed for this analysis) which generates an estimate of the actual cladding temperature history that will lead to the observed junction temperatures, accounting for heat transfer and thermal inertia in the thermocouple assembly. In essence, the method depends upon projecting future cladding temperatures based upon current trends in the junction temperatures. Successive guesses within an iterative *guess and correct* algorithm are involved and numerical stability problems further require the use of suitably large time steps between successive temperature estimates. Time steps are on the order of the thermal response time of the thermocouple assembly and can limit the estimated temperature rise rate when the actual cladding response is faster than the characteristic response of the thermocouple.

In the calculational procedure a relatively large time step (30 to 100 s - major time step) was set for the inverse calculation and a fuel temperature was guessed. The heat transfer from the fuel to the junction based upon this guess was calculated using a small time step during the larger time interval under analysis, and the predicted junction temperature was then compared to the measured junction temperature. Based upon the error in calculated and measured junction temperatures, a Newton's method approach was used to predict a corrected fuel temperature estimate for the next iteration. The convergence criteria used in the procedure requires that the calculated junction temperature differ from the known junction temperature by less than 0.2 K. Convergence on an acceptible solution for the large time interval was usually obtained within 3 or 4 iterations.

For two of the four W/Re thermocouples mounted on the guard rods a satisfactory solution was obtained without recourse to filtering or curve fitting the thermocouple data. These were the thermocouples at the 20% and 70% locations (9.6 cm, and 36.8 cm). The uppermost thermocouple (95% location - 49.5 cm) displayed anomalous behavior from about 7750 s until after the ACRR power was terminated so that reliable data was lost from this thermocouple during most of the oxidation transient phase of the experiment. No attempt was made to analyze the data from this

thermocouple. The thermocouple data for the 48% location (25.4 cm) *resisted* the inverse heat conduction analysis because of a high frequency noise component in the data and required least squares curve fitting of the thermocouple data to achieve a reasonably stable solution for the estimated fuel rod clad temperature at this location. (In applying inverse heat transfer methods, small fluctuations in the assumed boundary temperatures, in this case the projected cladding temperature, are translated into large fluctuations in the temperature predicted internally, here, the junction temperature. Therefore, data smoothing is sometimes required to avoid numerical instabilities associated with this method.)

Results for the analysis of the thermocouple located at the 20% position (9.6 cm - ZCW217) are shown in Figure 4-23. Note that the curve corresponding to the results of the IHCP analysis for all three thermocouples discussed below are labeled 'WRET CLAD TEMP' in the figures (diamond symbols). It has been noted previously that the response of this thermocouple showed strong evidence of contact with molten material relocated from above. This is further evidenced by the extremely rapid heatup rate at about 7750 s which may have occasioned the passing of a molten mass past the thermocouple junction. The transition from the forward heat conduction calculation to the inverse calculation was made at 7680 s when the forward calculation of the junction temperature exactly equaled the measured junction temperature. Some loss of resolution was evident in the solution to the inverse conduction calculation due to the large time step required for convergence. This was most noticeable for the first three time steps after transition to the IHCP. It is clear that the decrease in temperature during the 2nd and 3rd time steps are part of a moderate oscillation that resulted from a somewhat over-predicted fuel rod temperature on the first time step. The severe temperature rise rate during the first time step had a duration that was comparable to the major time step (60 s) and probably strained the capability of the code to resolve the fuel temperature in that period. The oscillation was damped out in the next few time steps and the solution was reasonably well behaved during the remainder of the oxidation transient phase and mirrored very well the turnover in the temperature at the transition to the cool-down phase. The calculated peak temperature at the 20% location was 2644 K. Due to the unavoidable loss of resolution, a lot of detail is missing between the 60 s major time steps, and it is, therefore, difficult to estimate the error in the predicted peak temperature. However, it is not expected that the error is much in excess of ±50 K.

The thermocouple at the mid-plane (48% elevation - ZBW162) was the most difficult to analyze in terms of achieving a stable solution. In fact, a solution could not be obtained using the unsmoothed thermocouple data. Evidently the combination of high frequency noise in the data together with the extreme heatup rate during the early oxidation transient phase overtaxed the capabilities of the code numerics and precluded a stable solution. To overcome these problems a cubic spline least squares technique was used to obtain a smooth curve fit of the thermocouple data. The cubic spline technique provides a 3rd order polynomial fit over a selected number of intervals such that the knot points (where the individual curve fits intersect) are continuous in value, 1st derivative, and 2nd derivative. Modifications were made in the WRET code to obtain the junction temperature from the curve fits (rather than from a table) which effectively eliminated the high frequency oscillations in the data and also any variations due to interpolation between discete data points.

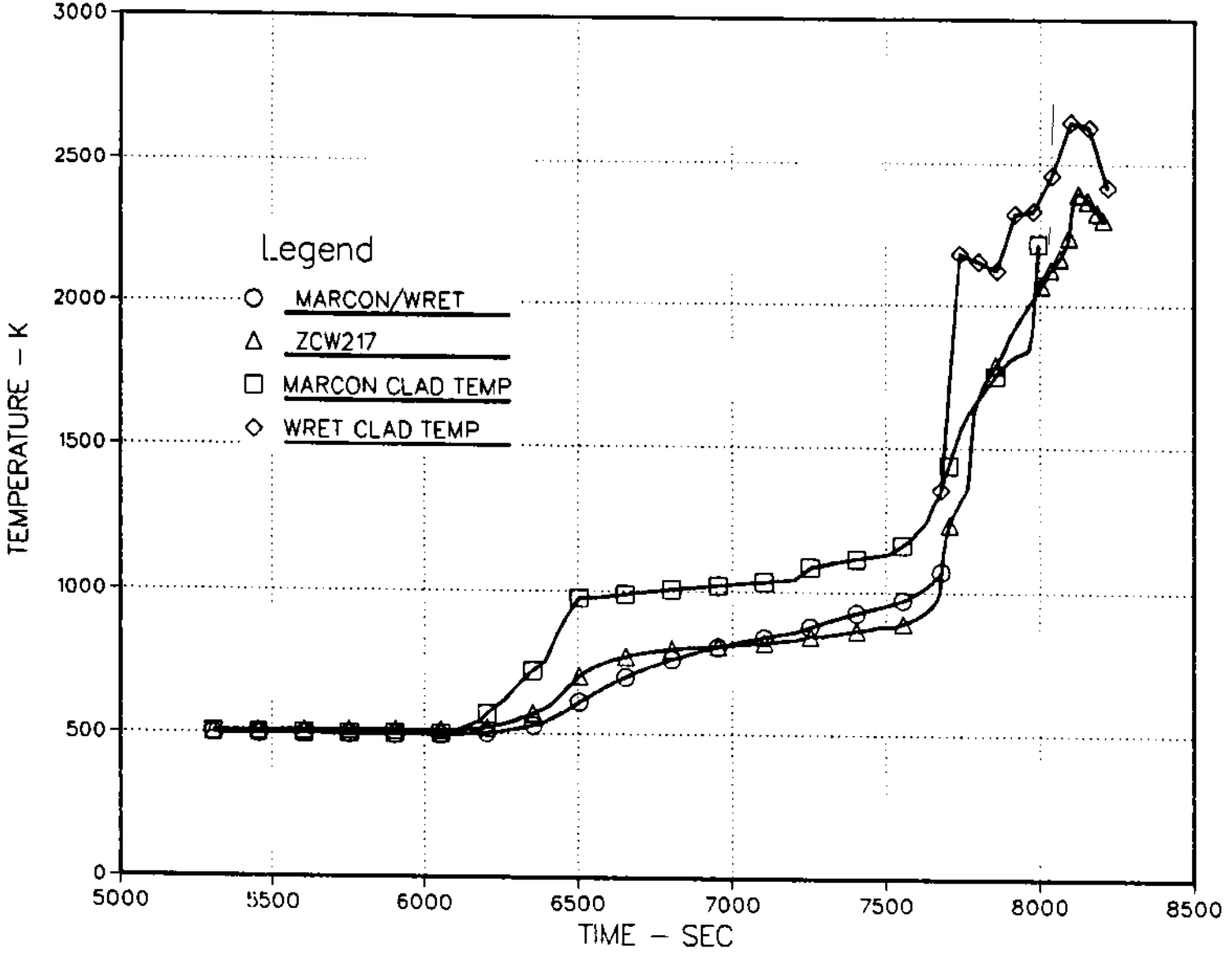

Figure 4-23: Estimated Guard Rod Clad Temperatures in the High Temperature Phase - 20% Elevation (9.6 cm)

Despite the effort taken to eliminate high frequency oscillations in the data it was necessary to use a 100 second time step in the 1st 7 time steps after transition to the IHCP. Upon entering the oxidation transient phase a 60 second time step appeared to give the most stable solution. The results of the analysis for this thermocouple are shown in Figure 4-24. The transition point was taken at 6820 s when the forward calculation and the measured thermocouple data coincided. There was an oscillation in the solution until about 7400 s just before the beginning of the oxidation transient phase, and the peaks of the oscillation appear to correspond well with the MARCON-DF4 predicted rod temperatures. The peak temperature obtained using a 60 second time step during the oxidation transient phase was 2583 K while a temperature of 2574 K was obtained for a time step size of 50 s. The 50 second time step, however, resulted in a considerably higher magnitude in the early oscillations. When a time step of 100 s was employed for the entire calculation the peak temperature was calculated to be 2719 K. This result would seem to indicate that the heatup rate together with the large time step strained the code numerics, and the peak temperature using this large of a time step may have been somewhat over-predicted in the IHCP calculation. The curve shown in Figure 4-24 represents the case run with a 100 second major time step through the entire IHCP calculation. There was a momentary oscillation in the solution coming out of the rapid heatup phase (between 7750 and 7800 s), but it was quickly damped and the solution was stable thereafter.

The most successful IHCP calculation was obtained for the thermocouple (ZCW117) at the 70% location (36.8 cm above the bottom of the fissile zone). Convergence was achieved with acceptable oscillation using a 30 second time step and no data smoothing. The ease of solution for this thermocouple was probably due to the relatively smooth behavior of the data and the more moderate heatup rate. Both of these characteristics are most likely due to an absence of molten material from a hotter region contacting or migrating past the thermocouple location and perturbing the temperature history as was undoubtedly the case for the two lower thermocouples previously discussed. The calculated fuel rod clad temperature history for this thermocouple is shown in Figure 4-25. Transition to the IHCP calculation was accomplished at 7240 s so that the entire pre-transient phase as well as the oxidation transient phase were covered by the calculations. It is interesting to note that the IHCP calculation in the pre-transient phase (~7200 to 7500 s) provides a good check on the accuracy of the method. During this phase the WRET code forward heat transfer calculations of the thermocouple junction temperature (circle symbol in Figure 4-25) which are based on the MARCON-DF4 predicted clad temperatures (square symbol) average about 40K higher than the actual thermocouple measured temperatures (triangular symbol). The MARCON-DF4 predicted clad temperatures in the same interval average about 58K higher than the solution for the clad temperature as obtained from the IHCP calculations. Thus, the bias between the clad temperature estimates is nearly the same as the bias in the junction temperatures. This good agreement indicates that the code produces nearly the same functional relationship between the fuel temperature and the thermocouple junction temperature in the inverse calculation as it produces in the forward calculation, which provides a quantitative verification of the methodology.

At the point where the temperature history emerged from the steep part of the transient (~7700 s) there was a minor oscillation in the WRET predicted clad temperature, but the oscillation was rapidly damped and the solution was well behaved

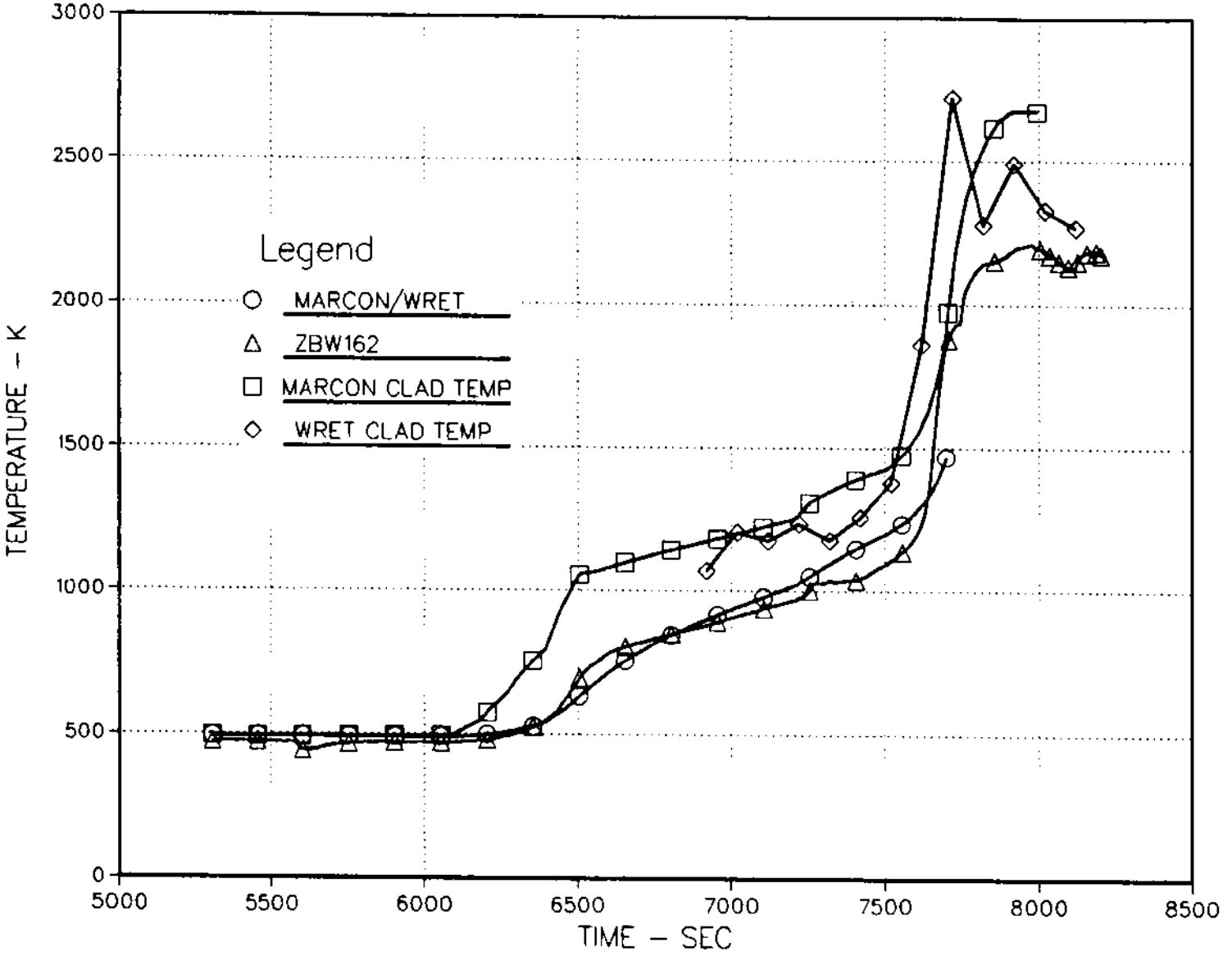

Figure 4-24: Estimated Guard Rod Clad Temperatures in the High Temperature Phase - 48% Elevation (25.4 cm)

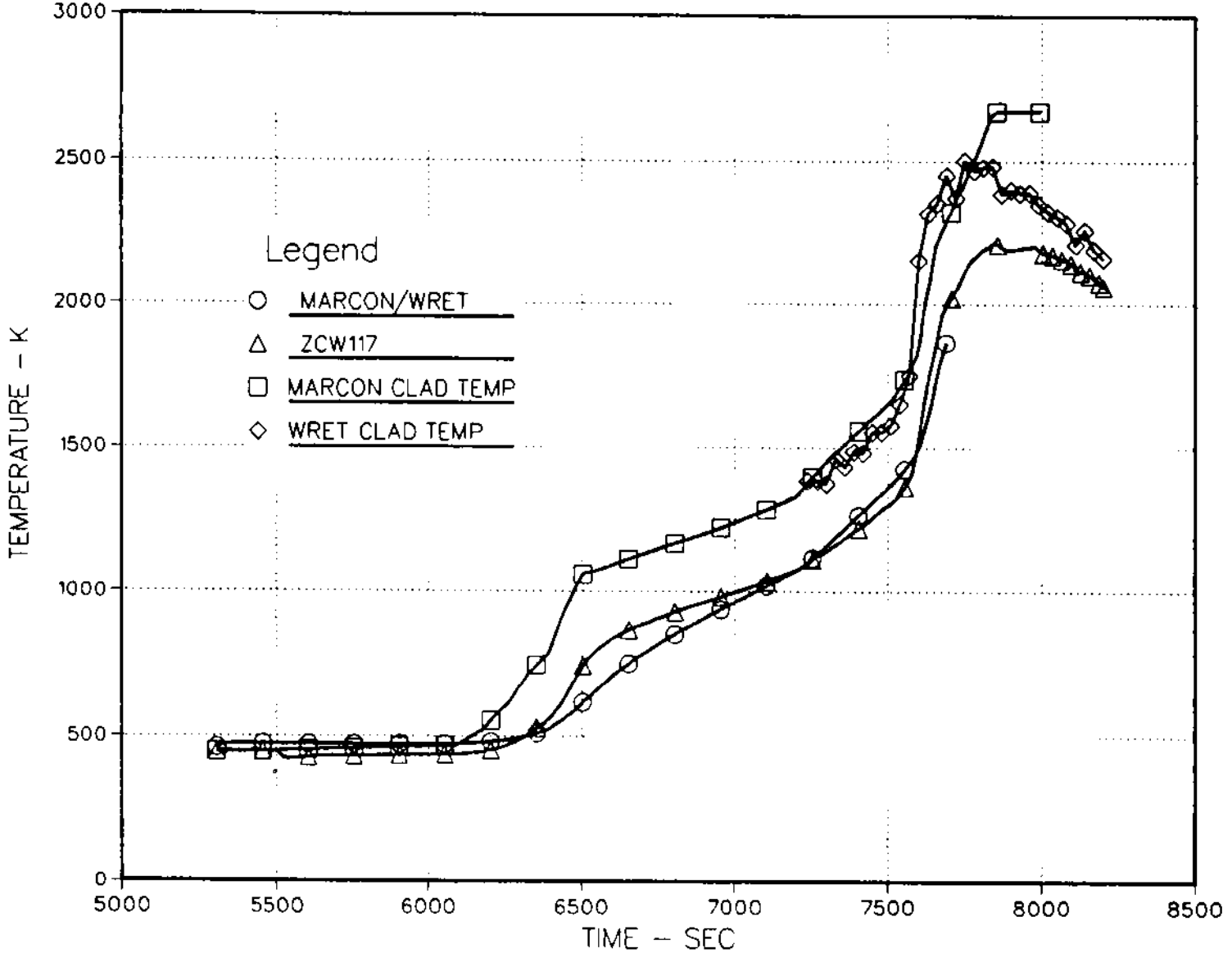

Figure 4-25: Estimated Guard Rod Clad Temperatures in the High Temperature Phase - 70% Elevation (36.8 cm)

during the remainder of the oxidation transient and cool down phases. The peak temperature for the thermocouple was 2502 K which is significantly less than the MARCON-DF4 prediction which shows the temperature increasing up to the α-Zr(O)/UO_2 monotectic (2673 K). The peak calculated fuel clad temperature occurred at about 7750 s, whereas the peak in the measured junction temperature did not occur until about 7850 s. Thus, a full 100 second delay appears to exist between the time that the fuel clad temperature peaked and the time at which the maximum effect was "seen" in the thermocouple junction. The delay between the clad and the thermocouple junction in terms of the time necessary for a change in the fuel temperature to be "perceived" at the thermocouple junction is, of course, considerably smaller, but it is precisely this effect that renders the inverse problem a difficult one.

A peak fuel clad temperature of 2500 K at the 70% location does not seem consistent with the considerable quantity of material relocated from the upper half of the bundle or with the extent of UO_2 eroded from the rods in this region. In fact, the quantity of UO_2 eroded from this region (a detailed discussion of the postirradiation examination, PIE, will be included in a subsequent report) implies that the temperature must have reached at minimum the α-Zr(O)/UO_2 monotectic temperature (2673 K). This is reinforced by the fact that the temperature at the mid-plane thermocouple may have exceeded 2700 K and the peak temperature of the lowest thermocouple (2644 K) appears to be recording the monotectic temperature. The thermocouples in the 48% and 20% locations are almost certainly recording the arrival or passage of molten material at or above the monotectic temperature which must have been relocated from the upper half of the bundle. There are several additional reasons to believe that the fuel temperature at the 70% elevation did, in fact, reach the monotectic temperature. First, the reaction zone wherein oxygen reacts with zircaloy is internal to the cladding structure at this phase of the transient, and there exists a layer of ZrO_2 that separates the thermocouple housing tip from the actual location of the reaction zone (and, therefore the highest temperatures). Second, there is indication that the fuel rods moved relative to the thermocouple tips during the experiment, so that the assumed close proximity of the thermocouple and the rod may be somewhat compromised. And finally, material that reached the monotectic temperature may have flowed away from its original location so rapidly that it could not be "sensed" by the thermocouple junction. It should also be noted that the W/Re thermocouples were located on the cool side of the guard rods which themselves ran somewhat cooler than the interior "hot rods." The temperature on the "hot rods" could be appreciably higher. The thermocouples in the upper half of the bundle, being located in a region that was a source of molten material, may well show a lower thermocouple junction temperature, for the above stated reasons, than thermocouples lower down in the bundle which recorded temperatures that are characteristic of molten U/Zr/O mixtures. Thermal contact between flowing molten material in the lower half of the bundle would also be more efficient than heat transfer processes in the upper half where it is likely that the thermocouple tip was not in direct contact with molten material.

There are three primary sources of error in the thermocouple temperature measurements. The first error is associated with the composition of the thermocouple wire as compared to the standard. The type "C" thermocouple wires used in the DF-4 experiment meet the ASTM standard that requires ±1% accuracy above 400°C. The second error source involves the instrumentation uncertainty in the voltage measurements. Tests were performed on the voltmeters used in the experiment and

were found to compare to within ±.07 to ±.09 mv of the standard EMF source depending on the instrumentation channel and the temperature. The third error source is generated in using a polynomial curve fit to convert voltage measurements into temperature estimates. The polynomial fit used in the DF-4 data reduction is a 6th order regression. This regression was compared to the ASTM standard tables and found to agree within ±1.86 K (95% confidence band). An error, ΔV, in the voltage measurement when propagated through the 6th order polynomial,

$$T = C_0 + C_1V + C_2V^2 + C_3V^3 + C_4V^4 + C_5V^5 + C_6V^6, \qquad (4\text{-}11)$$

will yield an error in the resulting temperature estimate of:

$$\Delta T = \Delta V \sum_{n=1}^{6} nC_nV^{n-1} \qquad (4\text{-}12)$$

The error in temperature due to instrumentation error is in the range of ±7 to ±10 K.

A summary of the four errors discussed above as applied at the peak estimated temperatures is given in Table 4-2. In this table the first three errors, ϵ_1, ϵ_2, and ϵ_3, are the errors associated with the thermocouple alloy composition, the instrumentation error, and the error in the curve fit of the standard thermocouple data respectively. The fourth error, ϵ_4, is the estimated error in the IHCP calculation. The total error (and excluding ZBW-067) is probably in the range of ± 100K for the estimated peak temperatures.

4.5 Summary of Experiment Analysis

The principal goal of the analyses presented in this chapter has been to characterize and qualify the experimental data. Fuel cladding thermocouple measurements were analyzed to determine the time varying test bundle power and axial power shape. The measured and calculated system steam flow rates were examined to evaluate the overall flow behavior and found to be very self consistent. These derived results were used as input parameters to the MARCON-DF4 thermal analysis code so that the calculated test behavior could be used as a basis for evaluating the actual measured quantities.

A thermal analysis of the DF-4 experiment was completed and excellent agreement was obtained between code predicted thermal responses and data taken from test instrumentation. Although calculated reactor-to-test section coupling factors displayed considerable sample-to-sample variability, the mean coupling factor produced an accurate code simulation of the test assembly thermal history.

The MARCON-DF4 code was used as the primary tool for the thermal analysis. The code estimates of fuel rod cladding temperature agreed very well with measured clad temperatures in three of the four instrumented locations until near the end of the

Table 4-2
Summary of Estimated Peak Temperatures
and Estimated Errors

T/C #	T_p	ε_1	ε_2	ε_3	ε_4	ε_{tot}
ZCW217	2644	±19.8	±6.8	±1.9	±50	±80
ZBW162	2719	±22.8	±8.2	±1.9	±50	±80
ZCW117	2502	±24.8	±9.2	±1.9	±50	±90
ZBW067	--	±23.2	±10.7	±1.9	---	---

T_p - estimated peak cladding temperature
ε_1 - Thermocouple Composition Error
ε_2 - Instrumentation Error
ε_3 - Standard T/C Data Curve Fit Error
ε_4 - Error in Regression of Temperature Difference

oxidation transient phase of the experiment when significant melting and material relocation had occurred. The only deviation between measured and calculated temperature responses occurred for the instrumented location at the top of the fissile zone (within a few centimeters of the top) when axial heat losses by radiation (not modeled in MARCON-DF4) became significant for locations near the fissile zone boundary. Deviation from predicted temperatures were measured late in the oxidation transient phase on the middle and lower thermocouples (20% and 48% from the bottom of the fissile zone). These deviations are believed due to the increase of molten materials relocated from the middle and upper half of the bundle. The MARCON-DF4 code does not model the relocation of molten material and is not strictly applicable after incipient melting or liquefaction.

The MARCON-DF4 code predicted the expected clad and canister oxidation profile wherein rapid metal/water reactions were incipient first in the upper half of the bundle and then moved downward as the rapid oxidation transient phase progressed. A peak hydrogen production rate of about 0.1 gm/s was predicted with an average rate of about 0.05 gm/s during the oxidation phase. The total hydrogen produced was estimated by the code to be on the order of 40 gm. Analysis of the CuO hydrogen getter data is ongoing, but initial indications are that 40 gms is not inconsistent with the getter thermal responses.

The analysis indicated a very large fraction of the fuel cladding was oxidized (75%) while relatively smaller fractions of the channel box (20%) and control blade (15%) were oxidized. Melt fractions for the cladding, channel box, and control blade were estimated at about 70%, 90%, and 98% respectively. The coupled effects of melting,

liquefaction, material relocation, and oxidation rates are not treated rigorously in the code, so that the magnitude of the metal/water reaction as predicted by the code subsequent to incipient melting is subject to considerable uncertainty. Final estimates of the end condition with respect to oxidation, melting, and relocation await completion of the destructive test bundle examination.

Analysis of the W/Re thermocouple data using a code developed specifically for the DF-4 thermocouple configuration (WRET Code) was able to predict the measured thermocouple junction temperatures using the cladding temperatures measured by the Pt/Rh thermocouples which were welded directly to the cladding. With these calculations as a baseline, the code was used in the inverse heat conduction calculational mode to estimate the fuel cladding temperatures during the oxidation-transient phase after the Pt/Rh thermocouples had failed. These calculations indicated that the W/Re thermocouple in the lower half of the assembly (20% and 48%) "saw" temperatures in the range of 2650 to 2700 K. These temperatures strongly suggest the passage of molten materials near or across the thermocouple housing tips. The calculated temperatures are in the range of the α - $Zr(O)/UO_2$ monotectic temperature (2673 K) and imply that significant liquefaction involving UO_2 occurred.

5. SUMMARY AND DISCUSSION

The DF-4 experiment is the fourth test in a series of severe fuel damage experiments carried out in the Annular Core Research Reactor (ACRR) at Sandia National Laboratories, and the first in-pile experiment to examine the behavior of boiling water reactor (BWR) structural and control elements (fuel canisters and control blade) under severe accident conditions. Examined in the test was a .5m long test bundle, which included 14 zircaloy clad UO_2 fuel rods, a zircaloy-4 channel box (fuel canister), and a stainless steel control blade containing B_4C powder. The test bundle was fission heated in the ACRR, with flowing steam introduced to the bottom of the test bundle (both inside the channel box and around the fuel rods) to simulate fission product decay heating of a local region of an uncovered BWR core. In addition to monitoring the thermal response of the test bundle using thermocouple instrumentation, the damage progression was visually observed from an end on view provided by a quartz window located in the experiment capsule.

The purpose of the experiment was to obtain both phenomenological insight and quantitative information concerning the initial severe damage processes that would occur in an uncovered and overheated BWR core. The information obtained in the test is to be used in the development and assessment of computer models of severe core damage progression. Insight into the important phenomena is first necessary in order to develop physical models that treat the observed behaviors. For example, in DF-4 it is concluded that molten control blade material pooled into the lower confines of the channel box and alloyed with the zircaloy box walls, creating a side wall breach in the otherwise intact channel box. This observation informs the developers of mechanistic core damage computer codes that a model which allows for this behavior should be included in the code if the phenomena are judged to be important. The quantative information from the experiment allows for the accurate assessment and calibration of the models that are numerically coupled together in an analysis code.

Since the test bundle in the experiment was a little under 0.5 m in length, the information gained from the test corresponds most closely to the damage processes that would take place in a localized region of a BWR core where the severe damage might initiate. The effects of scale, such as length, must be assessed when applying the observations from the experiment to the behavior of the whole core.

5.1 Summary of the Test Progression

The initial fission heating of the test bundle caused the fuel temperatures to increase at approximately 1.2 K/s. Because of efficient radiative coupling, the unheated channel box and control blade lagged the fuel temperature by only about 50 K when bundle temperatures exceeded 1000 K. When the control blade temperature reached between 1520 and 1570 K, blade failure occurred. This was apparent from the thermocouple instrumentation on the blade, some of which failed suddenly and from the video record of the damage progression. In the video record, molten drops of blade material can be seen spilling out of the blade in the small gap between the blade and the zircaloy channel box. The effective melting point of the stainless steel is believed to have been lowered due to an interaction between Fe and B_4C, which has been found in tests conducted at Kernforschungszentrum Karlsruhe (KfK Germany) to cause melting in B_4C filled steel tubes at temperatures as low as 1520 K, or roughly

210 K below the 1700 K melting point of stainless steel. The liquefied blade quickly relocated to the base of the bundle, freezing largely within the confines of the channel box geometry, forming a tight blockage in this region. It is known from metallurgical examination (not presented in this document - to be presented in a subsequent document currently under preparation) that the control blade steel intereacted with the Zr channel box wall near the bottom of the bundle where the molten steel pooled up within the confines of the channel box. This interaction is thought to have resulted in failure of the channel box wall by eutectic reaction between Fe and Zr, causing liquefaction of the Zr well below the normal Zr melting point.[39] This may be very important from a modelling perspective since potentially large amount of Zr metal may be liquefied and relocated by molten steel which would lead to failure of the hydraulic integrity of the channel box flow channel as well as flooding of the lower fuel canisters with the molten alloy.

Although fission heating in the 10% enriched fuel rods provided the initial heating of the test bundle, the exothermic zircaloy/steam oxidation reaction eventually became the dominant heating source within the test bundle. At about 1800 K, fuel temperature rise rates were observed to increase from the 1.2 K/s value provided by fission heating, to approximately 10 K/s, driven by the rapidly accelerating oxidation kinetics. The channel box heatup, which had no direct fission heating component, followed this autocatalytic behavior also. It is possible that the channel box temperatures actually exceeded the fuel cladding temperatures based upon the thermocouple behavior during the oxidation transient period. During this time, sustained hydrogen generation from the metal/steam oxidation reaction was detected in the H_2 measurement diagnostics. (Quantitative estimates of H_2 production will be reported in a subsequent document, currently under preparation.) Relocation of molten zircaloy from the fuel cladding and the channel box occurred about 100 seconds after the initiation of the oxidation transient, resulting in the accumulation of a large blockage region in the relatively cold lower portion of the test bundle. Radiographic and destructive post test examination of the test bundle revealed that all but the coldest lower 10% of the channel box had melted during the test, leaving only slight traces of any oxide channel box remnants in the upper 90% of the bundle length. The fuel rods were largely intact, although some rod fracturing and a considerable amount of lateral rod distortion was evident.

5.2 Discussion of the Observed Phenomena

5.2.1 Control Blade Failure

In DF-4, the control blade failed at a fairly low temperature (~1550K) and relocated to the base of the bundle. The post test destructive examination revealed that the inner confines of the channel box were completely filled with refrozen blade material, although the material apparently froze out just prior to hitting the base - a slight gap on the order of 0.5 cm was found between the lower extent of the refrozen blade material and the actual base of the channel box. (The details of the destructive post test examination of the bundle will be presented in a subsequent report.) From the video record of the blade failure, the blade components were observed to spill downward and spread laterally to the walls of the channel box. As the blade failure became more complete, the field of view within the channel box inner boundaries became very bright, initially an orange color that gradually became whitish orange. Thermocouple instrumentation that had been routed up through this region to

instrument the lower half of the control blade showed evidence of having been shunted by the relocated blade materials, as the indicated temperatures for these thermocouples was approximately 1700 K. This evidence together with the whitish orange luminescence of the relocated blade materials suggests that at least the upper extent of the steel blockage remained molten, or very nearly so, after coming to rest in the bottom of the channel box. In view of this, it would appear very likely that the molten steel would have quickly breached the zircaloy wall by alloying with the Zr. Additional evidence from the destructive examination will be presented in a future report which verifies this conclusion, however, at this point it is known that the amount of material found in the steel blockage inside the channel box accounts for only about 2/3's of the original blade volume. The balance of this material is suspected to be outside the channel box at the bottom of the blockage region and distributed along the axial length of the original blade region as a foamy material attached to the slight channel box oxide remnants.

In the BWR core, if the control blade were to become molten and slump to the lower open spaces between the channel boxes, the height of the compacted blade material could be as great as 1.5 meters. The upper extent of this column of material would very likely be molten so that vigorous attack of the fuel canister walls would be expected. The attack and failure of the zircaloy channel box wall is a significant phenomena because it provides a means for the steam that is produced inside the BWR fuel canister to pass into the interstitial regions where the steam production rate is lower. This effect would expose more zircaloy to higher steam mass fluxes and also allow flow bypass around blockages that might have formed within the fuel canister, thus potentially affecting hydrogen production.

The failure of the control blades in a BWR core damage accident may have another impact on the progression of the accident. In DF-4, the control blade was observed to fail at about 150 K below the steel melting point, presumably due to interaction between the boron in the B_4C and the iron in the stainless steel. It appears possible then, that under certain conditions, the control blades in local regions of the BWR core could be destroyed well before severe oxidation damage and failure of the zircaloy components had occurred. This might be more likely if the heatup rate of the blades in the vicinity of 1550 K were very slow, allowing time for the alloying reaction to take place. This prospect may be an important consideration from the standpoint of possible reactor recriticality when attempting to reflood a damaged core.

5.2.2 Channel Box Failure

One of the major observations from this test was the nearly complete failure of the zircaloy channel box. Although significant amounts of channel Zr may have been dissolved by molten control blade material, evidence from DF-4 also suggests that significant amounts of Zr later relocated when Zr melting temperatures were attained. This is known from the large thermal responses due to molten material relocating to the blockage region as Zr melting temperatures were exceeded. Any oxide layers that might have formed during the heatup and oxidation of the channel box were not sufficiently robust to remain standing after the unoxidized material melted, since only the smallest oxide remnant was found in the original channel box location. (Again, note that the results of the destructive examination will be presented in a subsequent document - these results are mentioned here to provide a clearer picture of the

phenomena discussed in this report.) The slight remnant appears to be a thin portion of one of the corners of the box that in many cases appears to be stabilized by a frothy substance that was internal to the box. The frothy material is likely to be of control blade origin, however this will be verified when the results of the metallurgical analysis become available.

The melting behavior of the channel box is significant because the loss of the box geometry in the BWR effectively opens up the fuel rod lattice to something that more closely resembles the PWR geometry. This is of course providing that the fuel rods remain standing. The fuel rods may remain standing when the channel box and fuel cladding melt, if the fuel cladding oxide layer could stabilize the fuel stack. This effect was observed in DF-4 (which used fresh UO_2 pellets) and was further assisted by a tendency for the molten cladding to wet the fuel pellet interfaces and effectively fuse individual pellets together by forming a high melting point U/Zr/O compound between individual pellets. The behavior of irradiated fuel pellets under similar conditions may be different in that the fuel rods may have a greater tendency to collapse when denuded of cladding due to cracks and internal stresses from trapped fission gases. The large amount of channel box zircaloy that relocates on melting also may interact with the standing fuel rods and affect their stability through erosion when molten or by stresses induced on the rod lattice if or when freezing occurs.

Some perspective on the amounts of relocating metallic components may be gained by considering the height that the material would occupy if collected on the lower core plate. If 50% of the fuel cladding relocated as molten metal, and 90% of the channel box zircaloy did likewise together with 100% of the control blade materials, the total height of this mixture collected around the fuel rods in the bottom of the core would be about 1 meter, or a little under 1/3 of the core height.

The behavior of this huge quantity of metallic material in the lower portion of the core is extremely important in the understanding of the subsequent core degradation behavior. One proposed behavior has been that the molten metallic components of the core cause failures in the lower core plate that allow a path into the lower reactor head for the subsequently failing fuel rods.[6] This is proposed to result in solid fuel pellets falling into the lower water filled plenum as the supportive cladding oxide for the fuel rods fail. Another possibility, however, could be that the metallic core materials would freeze in the lower 1/3 of the core where the axial thermal gradient is large and where water may yet exist. In this case, the fuel pellets may collapse and fall upon a robust metallic blockage where a molten pool of fuel material may collect.

The two events just described would imply dramatically differing initial conditions for the entry of fuel material into the lower reactor head; one in which solid debris falls into the water of the lower head, and the other in which fuel may become molten before it relocates to the lower head. These differences in assumed core melt progression behavior may have a large impact upon the failure mode of the BWR lower head and upon the initial conditions for ex-vessel molten core phenomena such as core concrete interactions and containment liner attack (Mark-1). The substantial differences in these two scenarios emphasizes the necessity to better understand the behavior of the relocating metallic components as they approach the lower core plate and lower plenum regions.

5.2.3 Onset of Rapid Oxidation

Many separate effects studies of high temperature zircaloy oxidation have noted a sudden increase in the rate of oxidation at a temperature of ~1800K.[30,31] This abrupt increase in oxidation rate has been attributed to an increase in gas diffusion through the forming ZrO_2 layer due to the phase change from the tetragonal to the more open cubic lattice at 1840 K.[32] The effect of this change in oxidation kinetics appears to be evident in the DF-4 test for the first axial location to reach about 1800 K. This occurred at the 36.9 cm elevation relative to the bottom of the fissile length (Figure 3-16). At this location the intrinsic fuel cladding thermocouples are seen to exhibit a sudden change in heatup rate from about 1.2 K/s to something on the order of 12 K/s. Although the reactor power was also increased slightly before this, the increase in power of roughly 15% was not sufficient to account for the factor of ten increase in fuel cladding heatup rate. Subsequently thermocouples at other axial locations were observed to suddenly increase in heatup rate starting from temperatures lower than 1800 K, however, it is believed that these thermocouples were responding to axial heat transport from the much hotter approaching oxidation front. By observing the timing difference between the rapid temperature transients for the cladding thermocouples at 36.8 cm and 25.4 cm, the mean downward propagation velocity of the rapid oxidation front may be estimated. The value from this estimation is 11.4 cm in about 54 seconds, or roughly 0.2 cm/s.

A crude estimation of the width of the rapid oxidation zone may be derived from the transient response of the W/Re instrumentation on the fuel rods shown in Figure 3-18. The thermocouple records for the 36.8 cm and 25.4 cm elevations indicated a sudden increase in heatup rate when the oxidation front reached the thermocouple elevation. Both thermocouples also indicated a break in the heatup rate between 60 and 100 seconds after the initiation of the transient. If the break in rapid heatup was due to the passing of the oxidation front, then this information together with the apparent front velocity gives an estimate of the front width. These values suggest an oxidation zone width on the order of 10 to 20 cm. One must admit that this estimate is crude and depends strongly on the speculative interpretation of the W/Re thermocouple trends.

5.2.4 SRV Steaming Effects

An effect not addressable directly from the DF-4 test is the impact of SRV related core steaming transients associated with high pressure BWR accidents. The SRV actuations are the principal source of steam production in the interstitial region when the accident occurs without vessel depressurization. The oxidation behavior in both the control blade region and within the fuel canisters is expected to be very transient also. In that these conditions were not implemented in DF-4, and the effect then can only be calculated via model extrapolation, additional experimental examination of the transient phenomena may be necessary.

5.3 Discussion of the Analyses

While this document is principally a data report for the DF-4 experiment, it was recognized that a simple presentation of the raw and uninterpreted experimental data was not a suitable form for computer code verification purposes (i.e., MELPROG, etc.). In order to make the application of this information more straightforward for

code assessment exercises, a number of separate analyses were performed. The steam flows into and out of the experiment test section were analyzed for storage and pressurization effects and found to be well characterized. The fission heating history for the test bundle was evaluated by correlating the change in the observed fuel cladding heatup rate with changes in the reactor power. A least squares regression technique was used to estimate the mean fuel rod power coupling to the ACRR and was determined to be approximately 1.7 W/gm/MW-ACRR to within about 10%. From this information, the axial power distribution in the test fuel was also determined. (Note that neutronic analyses conducted early in the design phase of the experiment concluded that the failure of the centrally located control blade had no appreciable effect on the power generation in the fuel rods because of the low neutronic worth of the B_4C in that location in the bundle.)

The overall thermal behavior of the bundle was investigated using the MARCON-DF4 experiment analysis code. This code was developed specially for the DF-4 geometry and provided a convenient and easy to implement tool for evaluating the basic experiment trends. The code performed remarkably well in tracking the observed bundle heatup behavior prior to the time when structural melting and relocation occurred. One early observation from the code results indicated that axial radiation out of the top of the test bundle was likely responsible for the codes tendency to overestimate the temperatures in this location. The heatup rate for most of the bundle closely matched the observed rates and the degree of structural melting predicted by the code was consistent with the observed end state damage condition of the test bundle.

A model was developed to analyze the response of the high temperature W/Re thermocouples. This was necessary to account for the large heat losses and delays in response that are characteristic of these thermocouples. The results of the analysis are estimates of the test bundle temperature history throughout the duration oxidation transient phase. Peak temperatures estimated from this analysis range from 2600 K to 2700 K. Temperatures of this magnitude are sufficiently high to lead one to expect a large amount of fuel attack and liquefaction due to the high solubility of UO_2 in molten cladding in this temperature range. For example, the solubility of UO_2 in molten $\alpha Zr(O)$ has been reported to be about 80 atom percent, i.e. 0.8 parts $U_{.33}O_{.66}$ dissolved in 0.2 parts $Zr_{.7}O_{.3}$, which is the monotectic composition for this quasi-binary system.[33]

It is hoped that the results of these calculations and analyses will facilitate the application of the experimental results to further modeling assessment exercises by providing a good characterization of the test and an illustration of the application of the basic data to a simple thermal analysis.

The appendixes of this document contain among other things, a microfiche packet that contains each of the on-line measured quantities for the independent evaluation of the reader. The data are also listed with a brief description given to identify the measured quantities in Appendix A. As was mentioned in the preface to this document, several follow-on documents for this experiment will be forthcoming. These documents will report on, among other things, the results of the hydrogen generation for the test and the metallurgical characterizations of the destructive test bundle examination.

REFERENCES

1. U.S. Nuclear Regulatory Commission, "Nuclear Power Plant Severe Accident Research Plan," NUREG-0900, 1983. Available for purchase from National Technical Information Service, Springfield, VA 22161.

2. U.S. Nuclear Regulatory Commission, "Nuclear Power Plant Severe Accident Research Plan," NUREG-0900, 1986. Available for purchase from National Technical Information Service, Springfield, VA 22161.

3. M. Silberberg, et al., "Reassessment of the Technical Basis for Estimating Source Terms," NUREG-0956, 1986. Available for purchase from National Technical Information Service, Springfield, VA 22161.

4. W. J. Camp, et al.,"MELPROG-PWR/MOD0: A Mechanistic Code for Analysis of Reactor Core Melt Progression and Vessel Attack Under Severe Accident Conditions," NUREG/CR-4909, SAND85-0237, 1987. Available for purchase from National Technical Information Service, Springfield, VA 22161.

5. F. E. Haskin, et al.,"Development and Status of MELCOR," *Proceedings of the U.S. Nuclear Regulatory Commission Fourteenth Water Reactor Safety Information Meeting*, Gaithersburg, MD., October 27-31, 1986, NUREG/CP-0082, Vol.1, February 1987.

6. L. J. Ott, "Advanced Severe Accident Response Models for BWR Application," *Proceedings of the USNRC 15th Water Reactor Safety Research Information Meeting*, October 1987, NUREG/CP-0090. Available for purchase from National Technical Information Service, Springfield, VA 22161.

7. C. M. Allison, et al.,"SCDAP: A Computer Code for Analyzing Light Water Reactor Severe Core Damage," *Proceedings of the International Meeting on Light Water Reactor Severe Accident Evaluation*, Cambridge, Massachusetts, August 28-September 1, 1983.

8. R. O. Gauntt, et al., "Results of the ACRR-DFR Experiments," *Proceedings of the International ANS/ENS Topical Meeting on Thermal Reactor Safety*, San Diego, CA, February 2-6, 1986.

9. S. Hagen and P. Hofmann, "LWR Fuel Rod Behavior during Severe Accidents," *Nuclear Engineering and Design*, 103(1), pp. 85, 1987.

10. P. E. McDonald, et al.,"PBF Severe Fuel Damage Program: Results and Comparisons to Analysis," *Proceedings of the International Meeting on Light Water Reactor Accident Evaluation*, Cambridge, Massachusetts, August 28-September 1, 1983.

11. "Coolant Boilaway and Damage Progression Testing Program," Quarterly Report, NUREG/CR-4318, Vol. 2, October 1985. Available for purchase from National Technical Information Service, Springfield, VA 22161.

12. "World List of Nuclear Power Plants," *Nuclear News Vol. 30(10)*, pp. 83-102, 1987.

13. S. H. Kim, et al., "An Analysis of Core Meltdown Accidents for BWR's," *Fifth ANS/ENS International Meeting on Thermal Nuclear Reactor Safety, Vol 2*, pp.958, Karlsruhe, FRG. September 9-13, 1984.

14. S. R. Greene, "Realistic Simulation of Severe Accidents in BWR's - Computer Modelling Requirements," NUREG/CR-2940, ORNL/TM-8517, 1984. Available for purchase from National Technical Information Service, Springfield, VA 22161.

15. Anthony Ness, *A Guidebook to Nuclear Reactors*, Univ. Calif. Press, 1975.

16. R. T. Lahey and F. J. Moody, *The Thermal Hydraulics of a Boiling Water Nuclear Reactor*, ANS Monograph Series on Nuclear Science and Technology, 1977.

17. L. E. Anderson et al., "In-Vessel Core Melt Progression Phenomena," IDCOR T15.1B, Vol.3, pp.1-7, 1983.

18. L. J. Ott and R. M. Harrington, "The Effect of Small Capacity High Pressure Injection Systems on TQUV Sequences at Browns Ferry Unit One," NUREG/CR-3179, ORNL/TM-8635, 1983. Available for purchase from National Technical Information Service, Springfield, VA 22161.

19. M. Z. Podowski, R. P. Taleyarkham, and R. T. Lahey Jr., "Mechanistic Core-Wide Meltdown and Relocation Modeling for BWR Applications," NUREG/CR-3525, December 1983. Available for purchase from National Technical Information Service, Springfield, VA 22161.

20. R. O. Wooten and H. I. Avci, "MARCH Code Description and Users Manual," NUREG/CR-1711, 1980. Available for purchase from National Technical Information Service, Springfield, VA 22161.

21. L. E. Anderson et al., "In-Vessel Core Melt Progression Phenomena," IDCOR T15.1A, 1983.

22. J. A. Gieseke, et al., "Radionuclide Release Under Specific LWR Accident Conditions, Volume II, BWR MARK-1 Design," BMI-2104, 1984. Available for purchase from National Technical Information Service, Springfield, VA 22161.

23. S. E. Dingman, et al., "Analysis of Peach Bottom Station Blackout with MELCOR," *Fourteenth Water Reactor Safety Research Information Meeting*, NUREG/CP-0082, Vol. 1, p. 353, Gaithersburg, MD, October 27-31, 1987. Available for purchase from National Technical Information Service, Springfield, VA 22161.

24. S. R. Greene, "The Role of BWR MK-I Secondary Containments in Severe Accident Mitigation," *Fourteenth Water Reactor Safety Research Information Meeting*, NUREG/CP-0082, Vol. 1, p. 27, Gaithersburg, MD, October 27-31, 1986. Available for purchase from National Technical Information Service, Springfield, VA 22161.

25. D. R. Bradley and Ann W. Shiver, "Uncertainty in the Ex-Vessel Source Term Caused by Uncertainty in In-Vessel Models," *Proceedings of the International ANS/ENS Topical Meeting on Thermal Reactor Safety*, San Diego, CA, February 1986.

26. D. A. Powers, "Combustible Gas Generation During the Interactions of Core Debris with Concrete," *Reactor Safety Research Semiannual Report, July-December 1986*, NUREG/CR-4805 (2 of 2), p. 18, 1987. Available for purchase from National Technical Information Service, Springfield, VA 22161.

27. V. F. Urbanic and T. R. Heidrick, "High Temperature Oxidation of Zircaloy-2 and Zircaloy-4 in Steam," *J. Nucl. Mat.* 75:251-261, 1978.

28. A. N. Tikhonov and V. Y. Arsenin, *Solution of Ill-Posed Problems*, Winston/Wiley: New York, 1977.

29. M. Hansen, *Constitution of Binary Alloys*, Metallurgy and Metallurgical Engineering Series, McGraw-Hill Book Company, 1958, pp. 741-743.

30. L. Baker Jr., "An Assessment of Existing Data on Zirconium Oxidation Under Hypothetical Accident Conditions in Light Water Reactors," ANL/LWR/SAF 83-3, 1983. Available for purchase from National Technical Information Service, Springfield, VA 22161.

31. J. T. Prater and E. L. Courtright, "High Temperature Oxidation of Zircaloy-4 in Steam and Steam-Hydrogen Environments," NUREG/CR-4476, PNL-5558, 1986. Available for purchase from National Technical Information Service, Springfield, VA 22161.

32. D. L. Hagrman, "Zircaloy-UO_2-Steam Interactions," Report No. SE-RSTD-85-010, EG&G, Idaho Falls, ID, September 1985.

33. A. Skokan, "High Temperature Phase Relations in the U-Zr-O System," Fifth International Meeting on Thermal Nuclear Reactor Safety, KfK 3880, Vol. 2, P. 1035, Karlsruhe, FRG, 1984.

Appendix A: Listing of On-Line Data

NUMBER OF VARIABLES IS: 216

1	TMMAIN	MAIN TIME	TIME
2	AUCOIN	INSIDE AUXILLARY COOLANT WATER INLET LINE	
3	AUFMHI	AUXILLARY COOLANT FLOW METER	TURBINE
4	AUFMLO	AUXILLARY COOLANT FLOW METER	TURBINE
5	AUFMPT	AUXILLARY COOLING WATER PRESSURE (FOR FM)	
6	AUFMTC	AUXILLARY COOLING WATER TEMP (FOR FM)	
7	BCP122	CONTROL BLADE (180 DEG), 12.2 " < FUEL SUPPORT GRID	
8	BCP167	CONTROL BLADE (0 DEG), 16.7" < FUEL SUPPORT GRID	
9	BCP222	CONTROL BLADE (180 DEG), 22.2" < FUEL SUPPORT GRID	
10	BOILPT	BOILER PRESSURE	
11	BOILTC	INSIDE BOILER EXIT STEAM LINE	
12	BTP072	CONTROL BLADE TIP (180 DEG), 7.2" < FUEL SUPPORT	
13	BTP122	CONTROL BLADE TIP (180 DEG), 12.2" < FUEL SUPPORT GRID	
14	BTP167	CONTROL BLADE TIP (0 DEG), 16.7" < FUEL SUPPORT GRID	
15	BTP222	CONTROL BLADE TIP (180 DEG), 22.2 < FUEL SUPPORT GRID	
16	CBORSL	CONTAINMENT BULKHEAD RING SEAL	
17	CBOU01	CONTAINMENT BULKHEAD TOP	
18	CBOU02	CONTAINMENT BULKHEAD TOP	
19	CBW117	W/RE OUTSIDE CHANNEL BOX @ 270 DEG, 11.7"< FUEL SUPPORT GRID	
20	CBW162	W/RE OUTSIDE CHANNEL BOX @ 270 DEG, 16.2"< FUEL SUPPORT GRID	
21	CBWNSL	CONT. BULKHEAD/WINDOW EXTENSION TUBE SEAL	
22	CCSFT4	INSIDE TUBE 6 OF THE 0 DEG HALF OF THE DOME	
23	CCSFT8	INSIDE TUBE 3 OF THE 0 DEG HALF OF THE DOME	
24	CIC279	INSIDE CHANNEL BOX, BOTTOM SURFACE, 27.9"< FUEL SUPPORT GRID	
25	CLDH2O	INSIDE COLD WATER LINE	
26	CNCOIN	INSIDE CONDENSER COOLANT INLET LINE	
27	CNCOOU	INSIDE COOLANT WATER OUTLET LINE	
28	CNFMHI	CONDENSER COOLANT FLOW METER 0-10 GPM RANGE	TURBINE
29	CNFMLO	CONDENSER COOLANT FLOW METER 0-2 GPM RANGE	TURBINE
30	CNFMPT	CONDENSER COOLING WATER PRESSURE (FOR FM)	
31	CNFMTC	CONDENSER COOLING WATER TEMP (FOR FM)	
32	CNISL1	INSIDE CONDENSER ON STEAM SIDE WALL	
33	CNISL2	INSIDE CONDENSER ON STEAM SIDE WALL	
34	CNLI01	INSIDE CONDENSATE LINE AT CONDENSER OUTLET	
35	CNWI01	CONDENSER INNER WALL 6" < TOP	
36	CNWO01	CONDENSER OUTER WALL 6" > BOTTOM	
37	CONENV	CONTAINMENT ENVIRONMENT	
38	CONPR1	CONTAINMENT TUBE PRESSURE	

39	CONPR2	CONTAINMENT TUBE PRESSURE	
40	CONTB1	CONTAINMENT TUBE WALL JUST BELOW n-FILTER	
41	CONTB2	CONTAINMENT TUBE -- CENTER OF n-FILTER	
42	CONTB3	CONTAINMENT TUBE WALL JUST ABOVE n-FILTER	
43	COOUOB	COOLANT OUTLET ABOVE BULKHEAD (INSIDE)	
44	CSASHT	HEATER DUTY CYCLE FOR COOL STEAM INLET LINE AT BULKHEAD	
45	CSDPPT	COOL STEAM CHECK VALVE DELTA-P	
46	CSFMLO	COOL STEAM FLOW METER	
47	CSFMPT	COOL STEAM PRESSURE (FOR FM)	
48	CSFMTC	COOL STEAM TEMP (FOR FM)	
49	CSIN01	INSIDE COOL STEAM PORT AT 90 DEGREES	
50	CSINOB	INSIDE COOL STEAM LINE, TOP OF ACCESS TUBE	
51	CSLASP	COOL STEAM LINE WALL ABOVE SHIELD PLUG	
52	CSLLS2	COOL STEAM LINE WALL, LOWER SHIELD PLUG	
53	CSLUS2	COOL STEAM LINE WALL UPPER SHIELD PLUG	
54	CTCOIN	CONDENSATE TANK COOLANT INLET (INSIDE)	
55	CTIN01	INSIDE CONDENSATE TANK AT BOTTOM	
56	CTKPR1	CONDENSATE TANK PRESSURE	
57	CTKPR2	CONDENSATE TANK PRESSURE	
58	CTLEVP	CONDENSATE TANK LEVEL MONITOR (DEL. P)	
59	CTLVDT	CONDENSATE TANK LEVEL DETECTOR HEATER	
60	CTW067	W/RE OUTSIDE CHANNEL BOX @ 90 DEG, 6.5" < FUEL SUPPORT GRID	
61	CTW117	W/RE OUTSIDE CHANNEL BOX @ 90 DEG, 11.7" < FUEL SUPPORT GRID	
62	CTW162	W/RE OUTSIDE CHANNEL BOX @ 90 DEG, 16.2" < FUEL SUPPORT GRID	
63	CTW217	W/RE OUTSIDE CHANNEL BIX @ 90 DEG, 21.7" < FUEL SUPPORT GRID	
64	CTWL01	CONDENSATE TANK OUTER WALL 8" < TOP	
65	FILT01	FILTER WHEEL POSITION AT START OF CYCLE	FILTER
66	FILT02	FILTER WHEEL POSITION AT MID CYCLE	FILTER
67	FNB&W1	FRAME NUMBER FOR B & W CAMERA AT START OF CYCLE	FRAME #
68	FNB&W2	FRAME NUMBER FOR BLACK & WHITE CAMERA AT MID CYCLE	FRAME #
69	FNCOL1	FRAME NUMBER FOR COLOR CAMERA AT START OF CYCLE	FRAME #
70	FNCOL2	FRAME NUMBER FOR COLOR CAMERA AT 1/4 CYCLE	FRAME #
71	FNCOL3	FRAME NUMBER FOR COLOR CAMERA AT MID CYCLE	FRAME #
72	FNCOL4	FRAME NUMBER FOR COLOR CAMERA AT 3/4 CYCLE	FRAME #

73	GLC284	STEAM CUP MANIFOLD TOP PIN SUPPORT,>1&7<, 28.4" < FUEL SUPPORT GRID	
74	GUC004	TOP SURFACE FUJ SUPPORT GRID @ 270 DEG	K
75	H2FLOW	HYDROGEN FLOW METER OUTPUT	
76	H2OMPT	MAIN WATER PRESSURE	
77	HEFLOW	HELIUM FLOW METER OUTPUT	
78	HG02H6	H2 GETTER TUBE 2, HEATER LOCATION,6" > BOTTOM	
79	HG02M0	H2 GETTER TUBE 2, MIXING TUBE SIDE, 0" > BOTTOM	
80	HG03H6	H2 GETTER TUBE 3, HEATER LOCATION,6" > BOTTOM	
81	HG03M2	H2 GETTER TUBE 3, MIXING TUBE SIDE, 2" > BOTTOM	
82	HG04C4	H2 GETTER TUBE 4, CONDENSER SIDE, 4" > BOTTOM	
83	HG04H6	H2 GETTER TUBE 4, HEATER LOCATION,6" > BOTTOM	
84	HG05H6	H2 GETTER TUBE 5, HEATER LOCATION,6" > BOTTOM	
85	HG05I1	H2 GETTER TUBE 5, INTERNAL, 1" > BOTTOM	
86	HG05I2	H2 GETTER TUBE 5, INTERNAL, 2" > BOTTOM	
87	HG05I3	H2 GETTER TUBE 5, INTERNAL, 3" > BOTTOM	
88	HG05I4	H2 GETTER TUBE 5, INTERNAL, 4" > BOTTOM	
89	HG05I5	H2 GETTER TUBE 5, INTERNAL, 5" > BOTTOM	
90	HG05I6	H2 GETTER TUBE 5, INTERNAL, 6" > BOTTOM	
91	HG05I7	H2 GETTER TUBE 5, INTERNAL, 7" > BOTTOM	
92	HG05I8	H2 GETTER TUBE 5, INTERNAL, 8" > BOTTOM	
93	HG05I9	H2 GETTER TUBE 5, INTERNAL, 9" > BOTTOM	
94	HG07H6	H2 GETTER TUBE 7, HEATER LOCATION,6" > BOTTOM	
95	HG07M8	H2 GETTER TUBE 7, MIXING TUBE SIDE, 8" > BOTTOM	
96	HG08H6	H2 GETTER TUBE 8, HEATER LOCATION,6" > BOTTOM	
97	HG09H6	H2 GETTER TUBE 9, HEATER LOCATION,6" > BOTTOM	
98	HG0I10	H2 GETTER TUBE, INTERNAL, 10" > BOTTOM	
99	HG0I11	H2 GETTER TUBE, INTERNAL, 11" > BOTTOM	
100	HG10H6	H2 GETTER TUBE 10, HEATER LOCATION, 6" > BOTTOM	
101	HG10I1	H2 GETTER TUBE 10, INTERNAL, 1" > BOTTOM	
102	HG10I2	H2 GETTER TUBE 10, INTERNAL, 2" > BOTTOM	
103	HG10I3	H2 GETTER TUBE 10, INTERNAL, 3" > BOTTOM	
104	HG10I4	H2 GETTER TUBE 10, INTERNAL, 4" > BOTTOM	
105	HG10I5	H2 GETTER TUBE 10, INTERNAL, 5" > BOTTOM	
106	HG10I6	H2 GETTER TUBE 10, INTERNAL, 6" > BOTTOM	
107	HG10I7	H2 GETTER TUBE 10, INTERNAL, 7" > BOTTOM	
108	HG10I8	H2 GETTER TUBE 10, INTERNAL, 8" > BOTTOM	
109	HG10I9	H2 GETTER TUBE 10, INTERNAL, 9" > BOTTOM	
110	HG5I10	H2 GETTER TUBE 5, INTERNAL, 10" > BOTTOM	
111	HG5I11	H2 GETTER TUBE 5, INTERNAL, 11" > BOTTOM	
112	HG8M10	H2 GETTER TUBE 8, MIXING TUBE SIDE, 10" > BOTTOM	
113	HG9C12	H2 GETTER TUBE 9, CONDENSER SIDE, 12" > BOTTOM	
114	HGHT20	HEATER DUTY CYCLE FOR CUO TUBES 2 AND 10	
115	HGHT34	HEATER DUTY CYCLE FOR CUO TUBES 3 AND 4	
116	HGHT57	HEATER DUTY CYCLE FOR CUO TUBES 5 AND 7	
117	HGHT89	HEATER DUTY CYCLE FOR CUO TUBES 8 AND 9	
118	HOTH2O	INSIDE HOT WATER LINE	

119	ISABPT	INLET STEAM PRESSURE (ACCESS TUBE REGION)
120	ISASHT	HEATER DUTY CYCLE FOR INLET STEAM LINE NEAR BULKHEAD
121	ISDPPT	INLET STEAM CHECK VALVE DELTA-P
122	ISFMLO	INLET STEAM FLOW METER
123	ISFMPT	INLET STEAM PRESSURE (FOR FM)
124	ISFMTC	INLET STEAM TEMP (FOR FM)
125	ISIN01	INSIDE INLET STEAM LINE, AT STEAM CUP ELBOW
126	ISINOB	INSIDE INLET STEAM LINE, TOP OF ACCESS TUBE
127	ISLASP	INLET STEAM LINE WALL ABOVE SHIELD PLUG
128	ISLLS2	INLET STEAM LINE WALL, LOWER SHIELD PLUG
129	ISLUS2	INLET STEAM LINE WALL UPPER SHIELD PLUG
130	JKHTRB	HEATER DUTY CYCLE FOR JACKET HEATER (BOTTOM)
131	JKHTRL	HEATER DUTY CYCLE FOR JACKET HEATER (LEFT HALF)
132	JKHTRR	HEATER DUTY CYCLE FOR JACKET HEATER (RIGHT HALF)
133	LLC294	INSIDE STEAM CAP < STEAM CUP MANIFOLD, 29.4" < FUEL SUPPORT
134	MTHTL	HEATER DUTY CYCLE FOR MIXING TUBE (LOWER)
135	MTHTU1	HEATER DUTY CYCLE FOR MIXING TUBE (UPPER 1)
136	MTLO01	MIXING TUBE LOWER OUTER WALL NEAR BULKHEAD
137	MTLO02	MIXING TUBE LOWER OUTER WALL 9" > BULKHEAD
138	MTLO03	MIXING TUBE LOWER OUTER WALL 6" < PLENUM
139	MTPHTR	HEATER DUTY CYCLE FOR MIXING TUBE PLENUM
140	MTPLI1	MIXING TUBE PLENUM INSIDE
141	MTPLO1	MIXING TUBE PLENUM OUTSIDE
142	MTPLO2	MIXING TUBE PLENUM OUTSIDE
143	MTUO01	MIXING TUBE UPPER OUTSIDE 12" > PLENUM
144	MTUO02	MIXING TUBE UPPER OUTSIDE 24" > PLENUM
145	MTUO03	MIXING TUBE UPPER OUTSIDE 36" > PLENUM
146	MTUO04	MIXING TUBE UPPER OUTSIDE 1" > CONDENSER
147	MVBODY	MOTOR VALVE BODY
148	MVJK01	MOTOR VALVE JACKET
149	MVJK02	MOTOR VALVE JACKET
150	NCDW01	NON CONDENSIBLE DOME OUTER WALL
151	NCDW02	NON CONDENSIBLE DOME OUTER WALL
152	PSMONA	POWER SUPPLY MONITOR
153	PSMONB	POWER SUPPLY MONITOR
154	RADTMP	COMPUTED TEMPERATURE FROM SPOT RADIOMETER
155	REAPOW	REACTOR POWER CONSOLE POWER ON 2 MW SCALE
156	S3P115	SHROUD 0.3" INSIDE WALL, 11.5" < FUEL SUPPORT GRID
157	S3P160	SHROUD 0.3" INSIDE WALL, 16.0" < FUEL SUPPORT GRID
158	S3P215	SHROUD 0.3" INSIDE WALL, 21.5" < FUEL SUPPORT GRID
159	SHBBT3	INSIDE TUBE 3 OF THE 180 DEG HALF OF THE DOME
160	SHBBT6	INSIDE TUBE 6 OF THE 180 DEG HALF OF THE DOME
161	SHC110	SHROUD HEATER L90 DEG, 11" < FUEL SUPPORT GRID
162	SHC210	SHROUD HEATER @ 180 DEG, 21" < FUEL SUPPORT GRID
163	SHRHTR	HEATER DUTY CYCLE FOR THE ZRO2 SHROUF HEATERS

164	SMC153	FLOW CHANNEL, H8" INSIDE LMTIS #2, 15.3" > FUEL SUPPOI GRID	
165	STATB1	STATUS BOARD OUTPUT WORD 1 BITS 0-15	STATBD
166	STATB2	STATUS BOARD OUTPUT WORD 2 BITS 15-25	STATBD
167	STTLHT		
168	STTLOS	STEAM LINES AT TOP OF LOS TUBE	
169	TAC110	NEAR TLMA @ 0 DEG, 11" < FUEL SUPPORT GRID	
170	TBC210	NEAR TLMB @ 90 DEG, 21" < FUEL SUPPORT GRID	
171	TCMB01	THERMOCOUPLE MOUNTING BLOCK WALL	
172	TCMB02	THERMOCOUPLE MOUNTING BLOCK WALL	
173	TIME02	TIME FOR COLOR CAMERA AT 1/4 CYCLE	TIME
174	TIME03	TIME FOR CAMERAS AT MID CYCLE	TIME
175	TIME04	TIME FOR COLOR CAMERAS AT 3/4 CYCLE	TIME
176	TLMCON	THERMAL LIMIT MONITOR CONTINUITY	TLM
177	TMOFST	TIME OFFSET - OFFSET TIME FOR SEQUENCING OF DATA SETS	
178	TRISE1	COMPUTED MAXIMUM TEMPERATURE RISE FOR CLAD TC'S	
179	TRISE2	COMPUTED MAXIMUM TEMPERATURE RISE FROM W/RE TC'S	
180	TRISE3	COMPUTED MAXIMUM TEMPERATURE RISE FROM H2 GETTERS	(INTERNAL)
181	TSBU01	TEST SECTION BULKHEAD BETWEEN FITTINGS 1&2	
182	TSBU02	TEST SECTION BULKHEAD BETWEEN FITTINGS 8&9	
183	TSJK05	TEST SECTION JACKET 5" < TOP	
184	TSJK10	TEST SECTION JACKET 10" < TOP	
185	TSJK15	TEST SECTION JACKET 15" < TOP	
186	TSJK20	TEST SECTION JACKET 20" < TOP	
187	TSJK24	TEST SECTION JACKET 24" < TOP	
188	TSJK26	TEST SECTION JACKET (BOTTOM) 26" < TOP	
189	TVLLPO	POSITION OF TV LIGHT LEVEL CONTROL WHEEL	
190	VALMON	ISOLATION VALVE MONITOR TREATED AS CONTINUIT	
191	VOVPOA	MOTOR DRIVEN VALVE POSITION	
192	VOVPOB	MOTOR DRIVEN VALVE POSITION	
193	WIINSL	INNER WALL AT INTERNAL WINDOW SEAL	
194	WIINWN	INNER WALL AT INTERNAL WINDOW	
195	WIOU01	OUTER WALL OF WINDOW EXTENSION TUBE AT WINDOW	
196	WSABPT	WINDOW STEAM PRESSURE (ACCESS TUBE REGION)	
197	WSASHT	HEATER DUTY CYCLE FOR THE WINDOW STEAM TUBE (BULKHEAD)	
198	WSDPPT	WINDOW STEAM CHECK VALVE DELTA-P	
199	WSFMLO	WINDOW STEAM FLOW METER	
200	WSFMPT	WINDOW STEAM PRESSURE (FOR FM)	
201	WSFMTC	WINDOW STEAM TEMP (FOR FM)	
202	WSINOB	INSIDE WINDOW STEAM LINE, TOP OF ACCESS TUBE	
203	WSLASP	WINDOW STEAM LINE WALL ABOVE SHIELD PLUG	
204	WSLLS2	WINDOW STEAM LINE WALL, LOWER SHIELD PLUG	
205	WSLUS2	WINDOW STEAM LINE WALL UPPER SHIELD PLUG	
206	Z1P065	ZIRC CLAD ROD #1, PT/RH 6.7" < FUEL SUPPORT GRID	
207	Z1P115	ZIRC CLAD ROD #1, PT/RH 11.5" < FUEL SUPPORT GRID	
208	Z1P215	ZIRC CLAD ROD #1, PT/RH 21.5" < FUEL SUPPORT GRID	

209	Z2P160	ZIRC CLAD ROD #2, PT/RH 16.0" < FUEL SUPPORT GRID
210	Z3P160	ZIRC CLAD ROD #3, PT/RH 16.0" < FUEL SUPPORT GRID
211	Z4P115	ZIRC CLAD ROD #4, PT/RH 11.5" < FUEL SUPPORT GRID
212	Z4P215	ZIRC CLAD ROD #4, PT/RH 21.5" < FUEL SUPPORT GRID
213	ZBW067	ZIRC CLAD ROD #11 W/RE 6.7" < FUEL SUPPORT GRID
214	ZBW162	ZIRC CLAD ROD #11 W/RE 16.2" < FUEL SUPPORT GRID
215	ZCW117	ZIRC CLAD ROD #12 W/RE 11.7" < FUEL SUPPORT GRID
216	ZCW217	ZIRC CLAD ROD # 12 W/RE 21.7" < FUEL SUPPORT GRID

Appendix B

A Description of the COPOX Code and Its Application to Hydrogen Analysis in the DF Experiments

This appendix is a report prepared by Ken Muramatsu of the Japan Atomic Energy Research Institute while on assignment at Sandia National Laboratories. Originally prepared as an informal JAERI report, it has been reproduced here in its original form.

A Method for Estimating Hydrogen Generation Rate in ACRR Debris Formation (DF) Experiments

Ken MURAMATSU

Chemical Engineering Safety Laboratory

Department of Fuel Safety Research

Tokai Research Establishemt, JAERI

(Received December, 1986)

A method of measuring hydrogen generation was developed for use in the Debris Formation (DF) experiments being conducted using the Annular Core Research Reactor (ACRR) at Sandia National Laboratories. The hydrogen generation was estimated, in the present method, from reaction-tube temperature profiles which were produced by the exothermic reaction of copper oxide with hydrogen.

The present method was successfully applied to DF-1 and DF-2 experiments and hydrogen generation for both experiments were reasonably estimated.

CONTENTS

1. INTRODUCTION

The TMI-2 accident has drawn a considerable attention to hydrogen behavior in a containment since hydrogen burn occurred and resulted in a sharp pressure rise in the containment[1]. Even though the containment remained intact during and after the hydrogen burn, the hydrogen issue has become one of the important items on reactor safety. Considerable amount of experiment data have been accumulated especially at Sandia National Laboraotries (SNL) in the past years[2].

One of the important issues, however, is to predict hydrogen generation in a damaged core due to Zircaloy-steam reaction. It is essential to experimentally verify models to predict hydrogen generation rate in severely damaged core in order to accurately estimate the amount of hydrogen which would be released into a containment. Therefore United States Nuclear Regulatory Commission (USNRC) has been conducting several integral experiments, such as the Power Burst Facility (PBF) Severe Fuel Damage (SFD) experiments at Idaho National Engineering Laboratory (INEL)[3] and Annular Core Research Reactor (ACRR) Debris Formation (DF) experiments[4],[5] at Sandia National Laboratories (SNL).

The author stayed one-half years at at SNL based on the USNRC-JAERI research agreement on the Severe Fuel Damage and Fission Product Source Term Research Program and participated in the DF experiment program in which, in cooperation with staffs of the program, the author developed a method for estimating hydrogen generation during the ACRR DF experiments. The hydrogen generation was estimated in this method from the reaction-tube temperature profiles which were produced by the exothermic reaction of copper oxide with hydrogen.

The present method was successfully applied to DF-1 and DF-2 experiments and hydrogen generation rates for both experiments were reasonably calculated.

The measurement technique, the analytical method, and the results from an application to the DF-1 experiment are described in the present report.

2. METHOD OF MEASUREMENT

2.1 Principle of Measurement

The basic principle of measurement is to utilize temperature rise

due to CuO-H_2 reaction in a reaction tube where copper oxide bed is placed. When hydrogen reacts with copper oxide in the reaction tube, chemical reaction generates heat of 45.3 kJ/g of hydrogen which is transferred to the surface of the reaction tube. The change of temperature of the reaction tube can be related to CuO-H_2 reaction and consequently to hydrogen generation rate. Principle of the present method is then to first measure the surface temperature of a reaction tube and to correlate the temperature change to hydrogen generation rate.

2.2 Reaction Tube Design and Configuration

A reaction tube containing a copper oxide bed is illustrated in Figure 1. The bed is composed of thin copper oxide wires, which are contained in a stainless-steel tube. Three layers of steel fiber, which serve as filters, are placed upstream of the bed to moderate the temperature of the incoming gas and to trap any aerosols that might interfere with the reaction. Pertinent dimensions for the bed are given in Table 1.

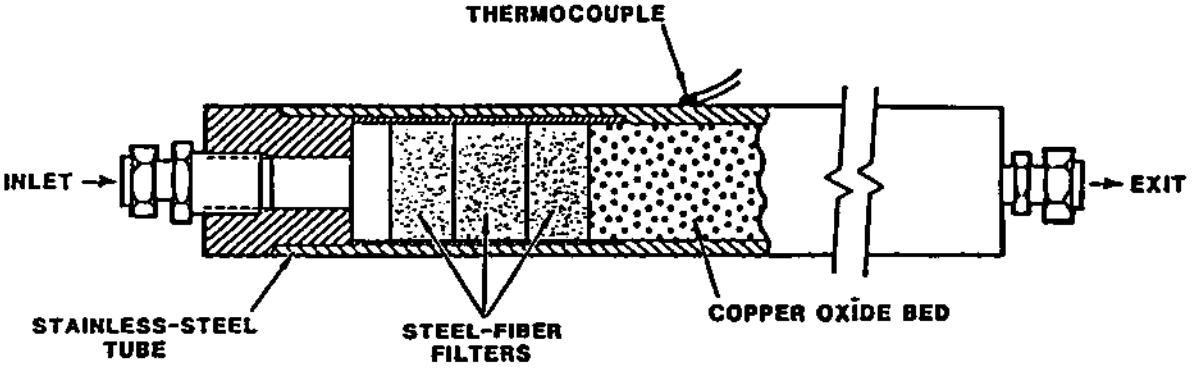

Fig. 1 CuO-H_2 Reaction Tube.

Table 1 Bed Dimensions

CuO wire diameter	0.2 mm
CuO wire length	3.0 - 5.0 mm
Tube diameter (ID)	25.4 mm
Tube thickness	3.2 mm
Bed void fraction*	0.6
Bed length	500.0 mm

* Based on weight to volume ratio

The configulation of the experiment capcule used for the in-reactor fuel damage experiment at ACRR is illustrated in Figure 2.

Ten reaction tube were arraged around the upper portion of the window steam tube to form a circular array of parallel, vertical tubes as shown in this figure. The gases flowing from the test section were mixed with the bypass cooling steam and the window steam and then introduced into the CuO bed.

The temperatures of the beds were monitored with 20 Cr/Al thermocouples (TCs) welded to the outer steel surfaces of the tubes. Ten of the TCs were placed at the same standard axial position on each tube (6 inches from the bed bottom) to detect differences in tube-to-tube behavior. The other ten TCs were placed, one to a tube, at positions (elevations) that varied (at 1-inch axial intervals) from one tube to another. Of the TCs placed at different elevations, six were placed on tube surfaces (inner surfaces) facing the window tube, and the other four were placed on tube surfaces (outer surfaces) facing the condenser. The positions of the TCs are indicated in Figure 3. (In this figure, bed bottom is defined not at the filter/bed interface, but at a plane 1 cm higher than this interface.)

The reaction tubes were heated (up to 300 W available per tube) to provide a thermodynamically and kinetically favourable temperature (between 400°C and 500°C) for the reaction between copper oxide and hydrogen. The heat of this reaction at 500°C is -45.3 kJ/g of hydrogen. This energy, produced locally within the CuO bed and then transported to the tube surfaces, is registered by the TCs as an increase in temperature over that of the initial heater-induced steady-state temperature.

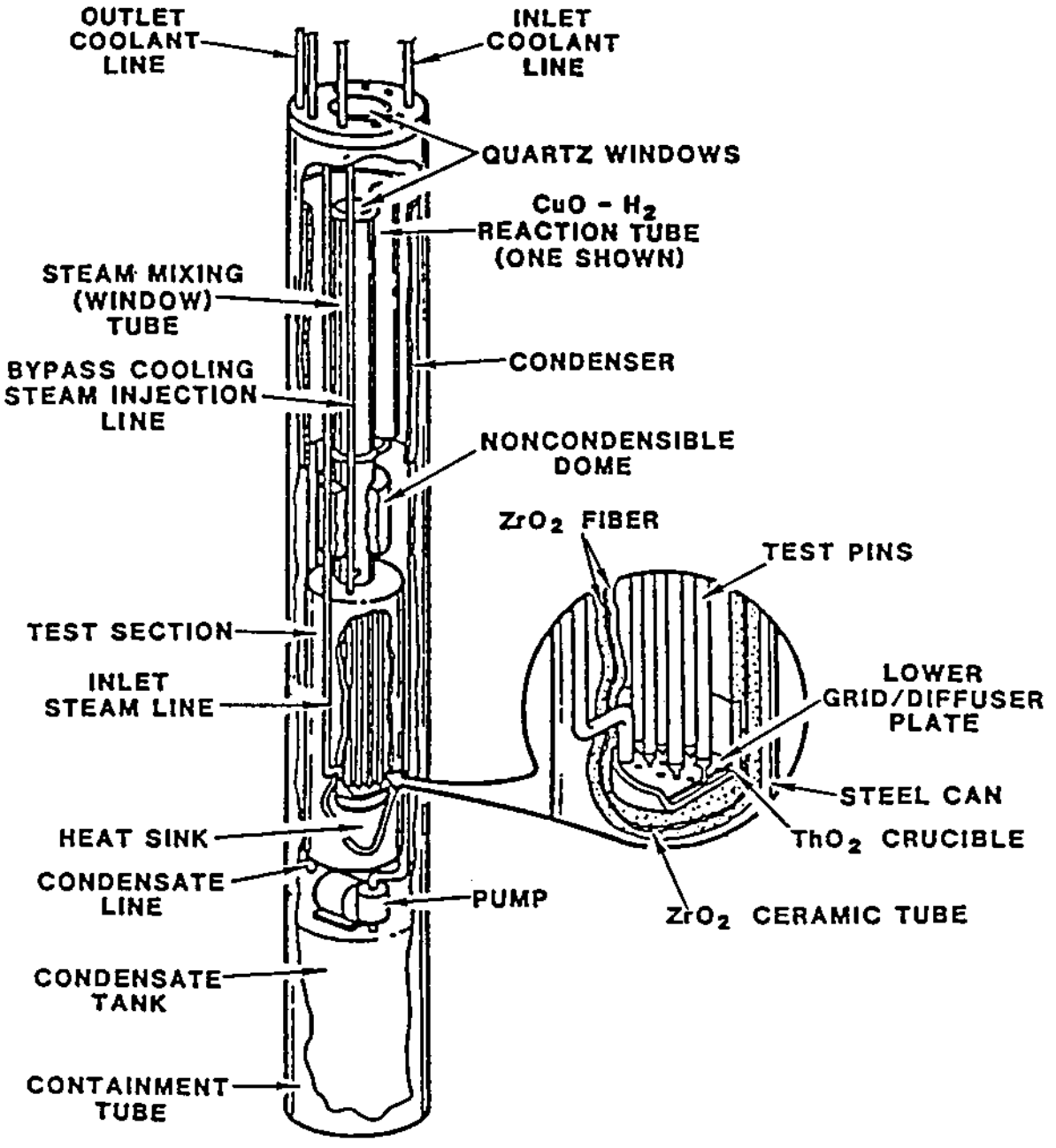

Fig. 2 DF-1 Experiment Capsule.

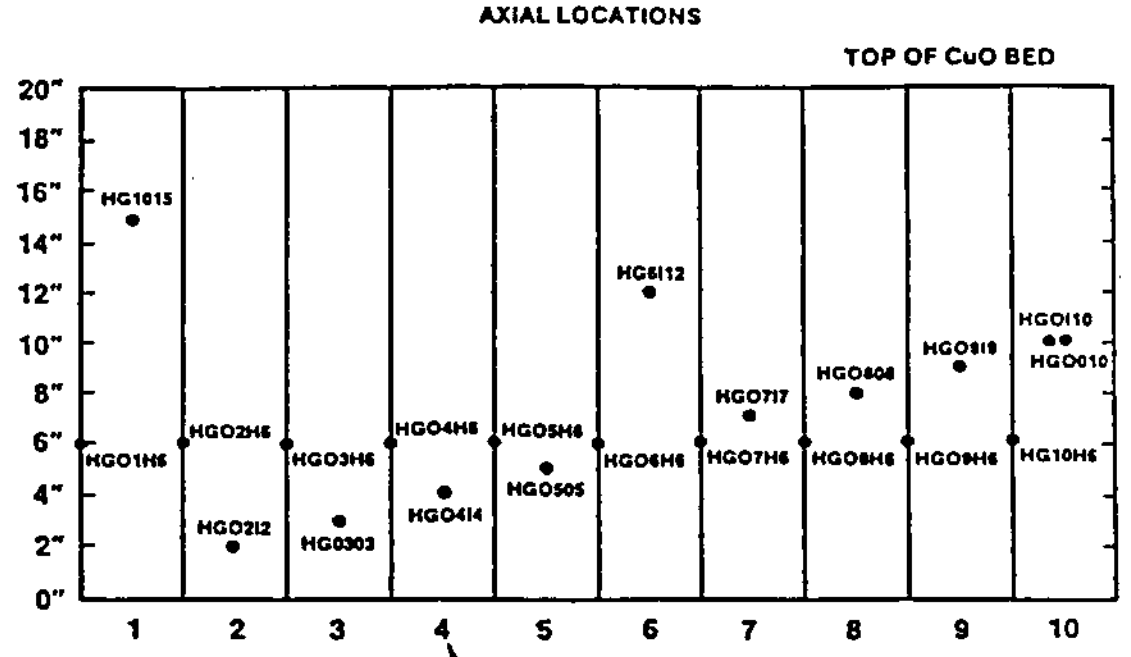

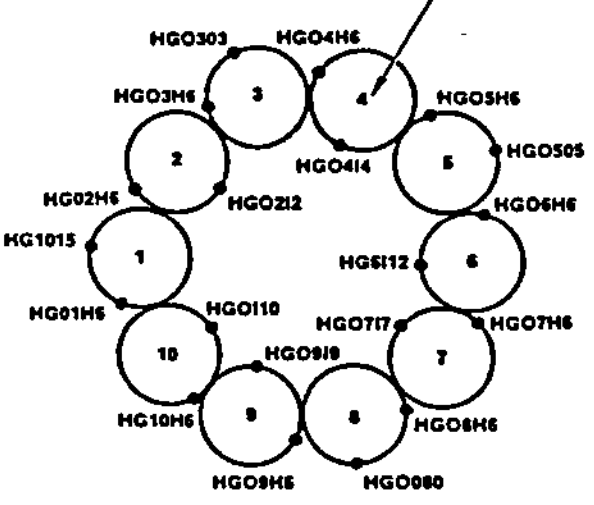

ID.	TUBE NO.	POSITION	
		AXIAL	RADIAL
HGO1H6	1	6"	HEATER
HGO2H6	2	6"	HEATER
HGO3H6	3	6"	HEATER
HGO4H6	4	6"	HEATER
HGO5H6	5	6"	HEATER
HGO6H6	6	6"	HEATER
HGO7H6	7	6"	HEATER
HGO8H6	8	6"	HEATER
HGO9H6	9	6"	HEATER
HG10H6	10	6"	HEATER
HGO2I2	2	2"	INNER
HGO4I4	4	4"	INNER
HGO6I12	6	12"	INNER
HGO7I7	7	7"	INNER
HGO9I9	9	9"	INNER
HGOI10	10	10"	INNER
HG1015	1	15"	OUTER
HGO303	3	3"	OUTER
HGO505	5	5"	OUTER
HGO808	8	8"	OUTER
HGO010	10	10"	OUTER

Fig. 3 Locations of Thermocouples on CuO-H_2 Reaction Tubes.

2.3 Temperature Measurement

The temperature histories recorded at different axial positions from tube to tube show the progress of the reaction front and the total extent of the reaction zone for a composite reaction tube, i.e., the tube that would be formed by combining the instrumented interval, or section, from each of the (presumably equivalent) tubes used. The temperature histories recorded by the standard-positioned TCs allow tube-to-tube comparisons and thus an estimate of the magnitudes of tube-to-tube departures from equivalence.

Figure 4 shows the temperatures measured at various elevations on the tube surfaces. These temperatures were taken at different locations on different tubes, and large differences exist, even among the initial steady-state temperatures. The inner TCs facing the window tube (those at 2, 4, and 7 inches from the bed bottom) register higher initial temperatures than the outer TCs facing the condenser (those at 5 and 8 inches from the bed bottom). During the test, the temperature of the wall of the window tube was about 200°C at its top, and the temperature of the wall of the condenser was about 100°C. The initial temperature at one of the standard TCs (6-inch elevation) falls between the values registered by the inner and outer TCs. This behavior is not unexpected, because the standard TCs lie on a radius that falls between the inner- and outer-TC radii as shown in Figure 3.

Figure 5 shows the variation in the temperature histories recorded at the standard TCs. Differences may arise because of (a) variations in the packing density of the CuO wires, (b) variations in the flow rates to and through the tubes, and (c) variations in the effectiveness of the insulating material around the tubes.

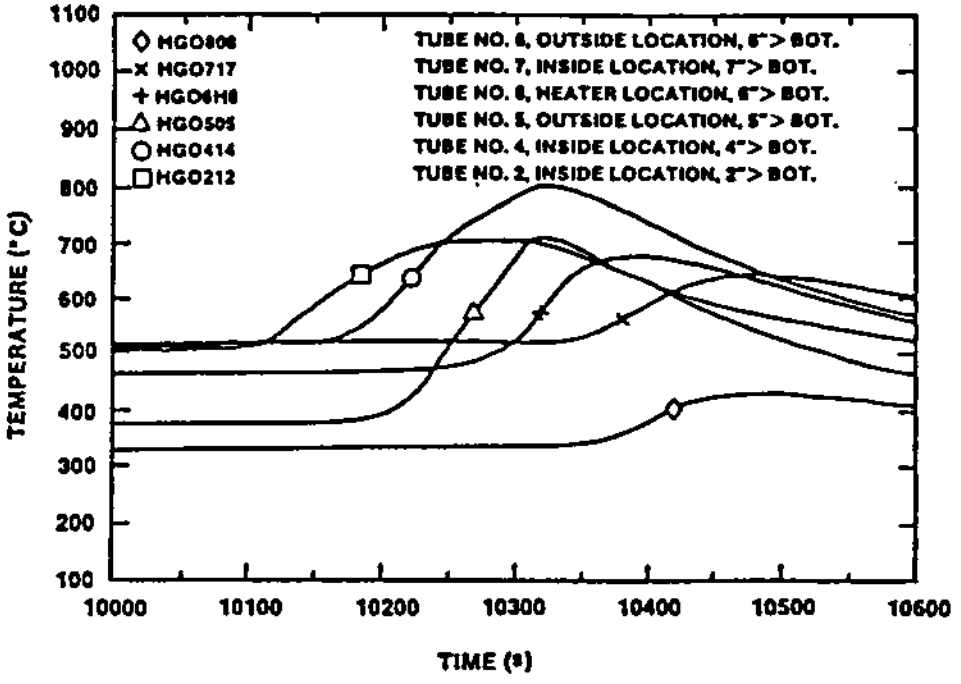

Fig. 4 Temperature Profiles Measured at Various Elevations Along the Surfaces of Six CuO-H_2 Reaction Tubes.

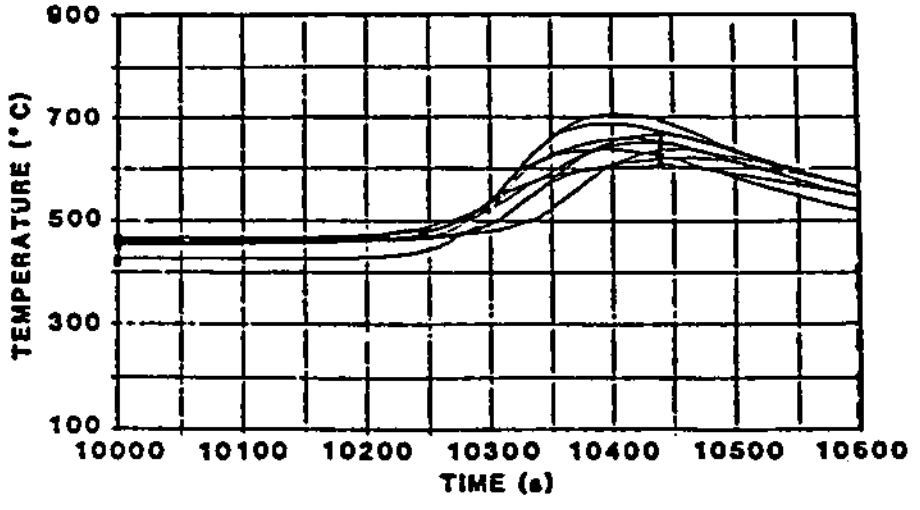

Fig. 5 Temperature Profiles Measured at the Same (6-inch Elevation) Position on the Surfaces of Nine CuO-H_2 Reaction Tubes.

3. METHOD OF ANALYSIS

3.1 Outline of Method

The present method uses observed temperature profiles and takes into account the convective and conductive heat-transfer processes in a representative (i.e., the composite) reaction tube and in the structures immediately surrounding it using the temperature profiles, certain boundary conditions (such as the steam flow rate and the electric power to the heaters), and suitable values for heat-transfer areas and coefficients. The modeling procedure unfolds the local bed-temeprature profiles (i.e., reaction-site profiles) from the input profiles using a heat balance that, accounting for losses, determines the quantity of heat that must be supplied locally by the $CuO-H_2$ reaction in order to produce the local temperature profiles. This quantity of heat, in turn, fixes the amounts of reactants needed, and therefore, the hydrogen generation rate.

3.2 Heat Transfer Model

The heat-transfer model used in the present method is shown schematically in Figure 6. The temperature-monitored portion of the representative reaction tube is divided into 9 control volumes corresponding to 9 TC locations. Each control volume is represented by a computational node. Because the steel wall of the composite tube sees essentially two different heat-transfer surroundings, the wall is divided into two halves for modeling purposes. One half faces the window tube, and the other half faces the condenser.

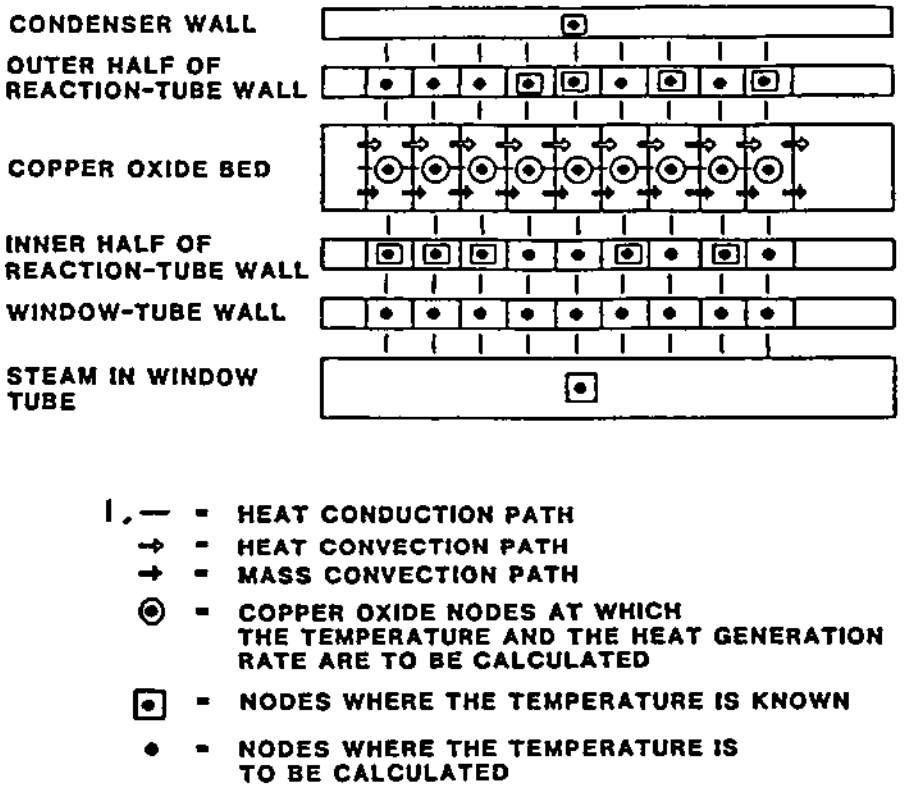

Fig. 6 Heat-Transfer Model Used for the Determination of the Hydrogen Reaction Rate in the Composite (Representative) Reaction Tube.

3.3 Governing Equations

(1) Heat Balance Equation

The heat-balance equation for each control volume is

(heat generated) = (heat stored)
+ (heat lost by convection by steam)
+ (heat lost by conduction to the tube wall)
+ (heat lost by conduction in the axial direction). (1)

Assuming that the temperatures of the copper oxide bed and the convecting gas are equal and uniform within each control volume, then the terms in Equation (1) can be approximated as follows:

$$Q_r S_i = (C_{pCuO} M_{CuO,i} + C_{pCu} M_{Cu,i}) \frac{dT_{c,i}}{dt} + W_g C_{pg} (T_{c,i} - T_{c,i-1}) + h_{c-s} A_{c-s} (T_{c,i} - T_{sI,i}) + h_{c-s} A_{c-s} (T_{c,i} - T_{sO,i}) + \frac{(k_c A)}{\Delta x} [(T_{c,i} - T_{c,i-1}) + (T_{c,i} - T_{c,i+1})]. \quad (2)$$

where

Q_r = heat of reaction (4.53×10^4 J/gH_2 at 500°C),
S_i = rate of hydrogen reaction in volume i (g/s),
C_{pCuO}, C_{pCu} = specific heat of CuO and Cu (J/g-°C)
$M_{CuO,i}, M_{Cu,i}$ = specific heat of CuO and Cu in volume i (g),
$T_{c,i}$ = copper oxide temperature in volume i (°C),
W_g = mass flow rate of gas (H_2/H_2O mixture) flowing through the bed (g/s),
C_{pg} = specific heat of this gas (J/g-°C),
h_{c-s} = heat transfer coefficient between copper oxide and steel tube (J/cm^2-s-°C),
A_{c-s} = heat transfer area between copper oxide and steel tube ($\pi R_{Is} \Delta x$ cm^2),
Δx = length of a control volume (2.54 cm),
R_{Is} = inner radius of steel tube (1.27 cm),
$T_{sI,i}$ = temperature of the tube wall for the half that faces the window tube at volume i (°C),

$T_{sO,i}$ = temperature of the tube wall for the half that faces the condenser at volume i (°C),

k_c = effective thermal conductivity of the copper oxide bed (J/cm-s-°C),

A = cross-sectional area of the copper oxide bed (cm^2).

The value of $W_g C_{pg}$ in the convection term of Equation (2) is obtained using the total flow rate, W_g, due to inlet, bypass, and window-tube steam and, because the contribution of hydrogen is small, the heat capacity, C_{pg}, of steam alone.

(2) Other Equations

A number of other equations are needed to account for the effects of the heaters, the condenser, and the steam in the window tube. For the half of the steel tube wall that faces the window tube:

$$C_{ps}M_{s,i}\frac{dT_{sI,i}}{dt} = Q_{h,I,i} + h_{s-wt}A_{s-wt}(T_{wt,i} - T_{sI,i}) + h_{c-s}A_{c-s}(T_{c,i} - T_{sI,i}) , \quad (3)$$

$$C_{pwt}M_{wt,i}\frac{dT_{wt,i}}{dt} = -h_{s-wt}A_{s-wt}(T_{wt,i} - T_{sI,i}) + h_{wt-ws}A_{wt-ws}(T_{ws} - T_{wt,i}) . \quad (4)$$

For the half of the steel tube wall that faces the condenser:

$$C_{ps}M_{s,i}\frac{dT_{sO,i}}{dt} = Q_{h,o,i} + h_{s-con}A_{s-con}(T_{con,i} - T_{sO,i}) + h_{c-s}A_{c-s}(T_{c,i} - T_{sO,i}) , \quad (5)$$

where

C_{ps}, C_{pwt} = specific heat of steel tube and window tube, (J/g-PC),

$M_{s,i}$ = mass of steel tube in volume i (g),

$M_{wt,i}$ = mass of window tube in volume i (g),

$Q_{h,I,i}$ = heater power at the tube wall for the half that faces the window tube at voluem i (W),

$Q_{h,o,i}$ = heater power at the tube wall for the half that faces the condenser at volume i (W),

h_{s-wt}, A_{s-wt} = heat-transfer coefficient and heat-transfer area between the steel tube and the window tube (J/cm^2-s-°C, cm^2),

h_{s-con}, A_{s-con} = heat-transfer coefficient and heat-transfer area between the steel tube and the condenser (J/cm^2-s-°C, cm^2),

h_{wt-ws}, A_{wt-ws} = heat-transfer coefficient and heat-transfer area between the window tube and steam it contains (J/cm^2-s-°C, cm^2),

$T_{wt,i}$ = window tube temperature at voluem i (°C),

T_{ws} = temperature of steam flowing in the window tube (°C),

T_{con} = temperature of condenser wall (°C).

Values for the parameters, $Q_{h,I,i}$, $Q_{h,o,i}$, T_{ws}, and T_{con} are obtained by measurements, and these values are also provided as inputs to a code that solved the equations.

(3) Mass of CuO and Cu

The mass of copper oxide and of reduced copper in a control volume can be calculated as follows

$$\frac{dM_{CuO,i}}{dt} = - \frac{s_i m_{CuO}}{m_{H_2}} \quad , \tag{6}$$

$$M_{Cu} = \frac{(M_{CuO,i,0} - M_{CuO,i}) m_{Cu}}{m_{CuO}} \quad , \tag{7}$$

where

m_{CuO}, m_{Cu}, m_{H_2} = molecular weights of CuO, Cu, and H_2 (g/g-mole),

and

$M_{CuO,i,0}$ = initial mass of CuO in volume i (g).

3.4 Method of Solution

A computer program, COPOX-R, was developed to solve the Equations (2) through (7) with input data of observed temperature and boundary conditions. The numerical method used in the code is basically a simple Euler method with a constant time step specified by the user. A backward difference form was used for the heat conduction terms in Equation (2) through (5) in order to maintain the numerical stability of the calculation.

4. RESULTS AND DISCUSSION OF APPLICATION TO DF-1 EXPERIMENT

4.1 Adjustment and Assumptions

The present method was applied to the DF-1 experiment to estimate hydrogen generation rate. Some adjustments were made to the measured data and some assumptions were invoked in order to apply the present method to the DF-1 experiment:

(1) Heat-transfer parameters

There were no significant design differences between the DF-1 and DF-2 CuO-H_2 reaction systems, but the boundary conditions for DF-2 were better known. Therefore, the heat-transfer coefficients and thermal conductivity (h_{c-s}, h_{s-wt}, h_{s-con}, h_{wt-ws}, and k_c) that were inferred from temperatures measured in and around the reaction tubes during the DF-2 test were used in the COPOX-R analysis of the DF-1 data.

(2) Heater power data

Because data on the electric power delivered to the heaters were not available in the DF-1 test, a simple power history, inferred from the temperature data for the reaction tubes, was used. Power was regarded as constant (and equal to the initial power level used in DF-2) up to 10,300 s, at which time it was assumed to have decreased linearly to zero and remained there from 10,350 s on.

(3) Input temperature profiles

Because a thermocouple placed 3 inches from bed bottom was defective, the 3-inch temperature profile was assumed to be the average of the profiles for the 2-inch and 4-inch locations. No input profile was provided below the 2-inch location because a calibration test performed before the DF-1 test consumed an estimated 4-cm-long initial portion of each CuO bed.

In addition, in order to provide a reasonably consistent set of input temperature profiles for the wall nodes of the representative, or average, reaction tube, the measured tube-surface temperature profiles were shifted by amounts in the range of -50°C to +50°C. These baseline-adjusted input temperature profiles are shown in Figure 7.

The amount of the shift at each elevation equaled the amount needed to compensate for the difference between the observed initial steady-state

temperature and the conduction- and convection-calculated steady-state temperature. The effect of the calculated convection term can be noted in the shifted contours by observing that for locations near the inlet (lower elevations) the initial temperatures are higher than for those more distant.

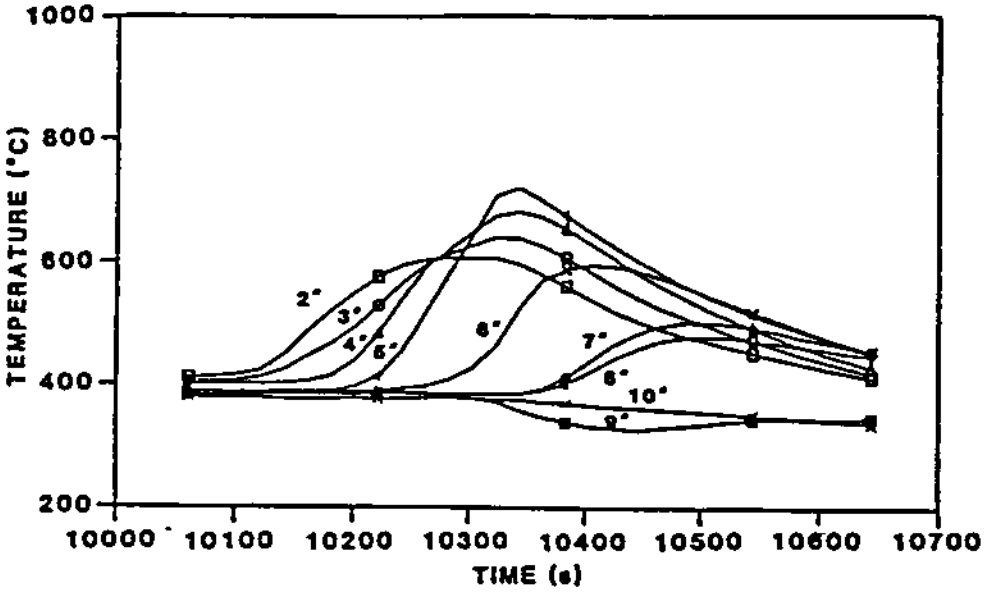

Fig. 7 Baseline-Adjusted Temperature Profiles Used as Input to COPOX-R.

4.2 Results and Discussions

(1) Results

Figure 8 shows the temperature profiles at various elevations along the centerline of the reaction-tube bed. These temperatures are as much as 50% higher than the corresponding baseline-adjusted surface temperatures.

Figure 9 shows the calculated heat generation rates in the CuO bed as a function of distance from the bed bottom. These profiles clearly show the progress and extent of a reaction zone. A typical zone spans a length greater than the length of one control volume. Thus, the suitability of using a 1-inch interval between TCs is confirmed.

Figure 9 also shows some elevations at which the calculated heat

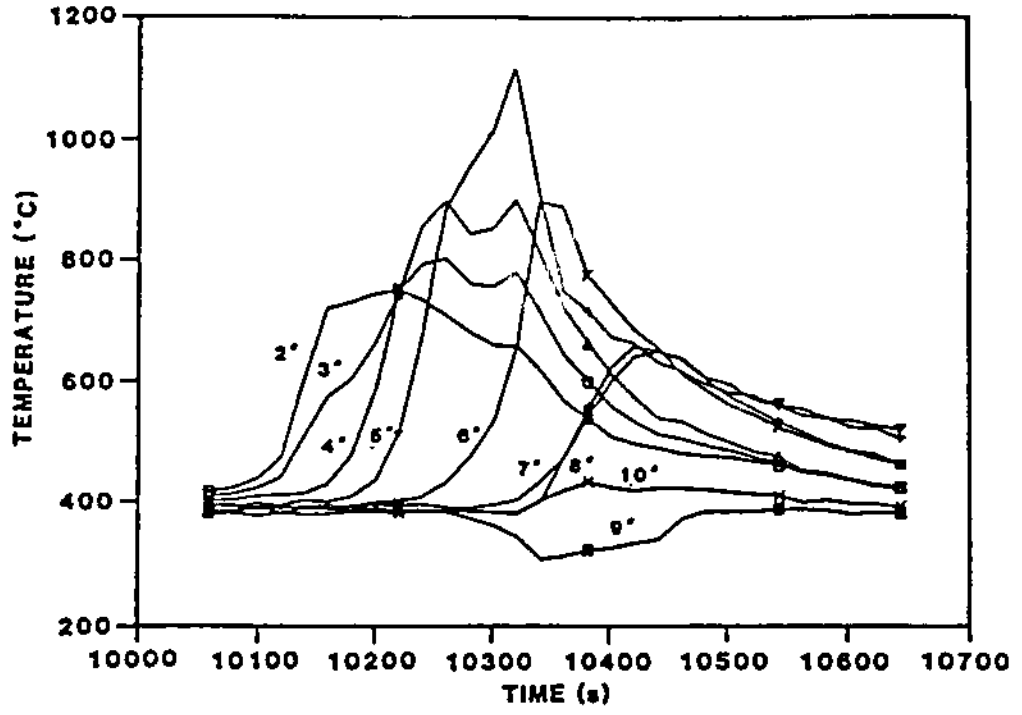

Fig. 8 Temperature Profiles Calculated at Various Elevations Along the Centerline of the Reaction-Tube Bed.

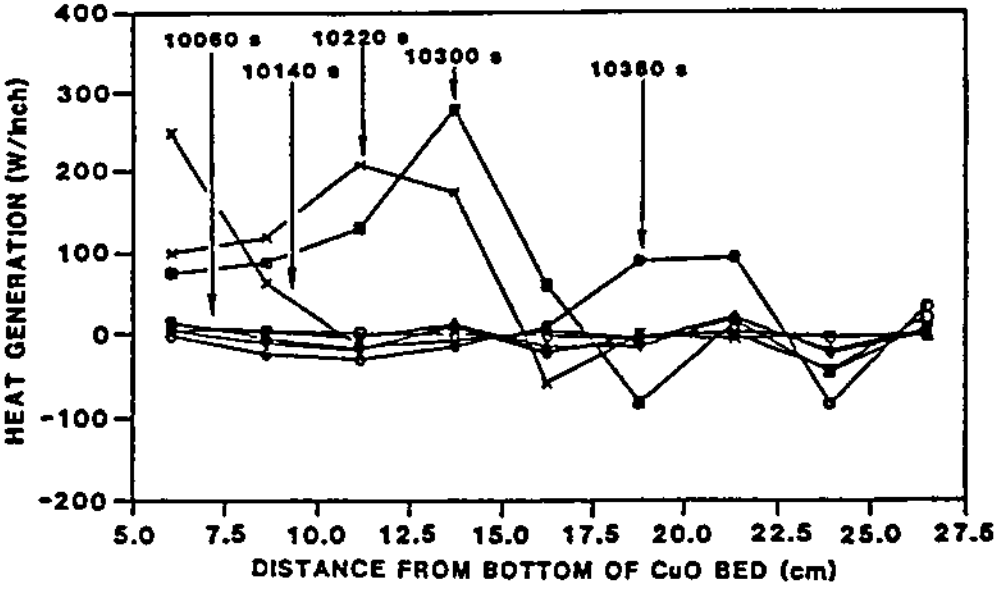

Fig. 9 Heat Generation Rates in the CuO Bed.

generation rates alternate between positive and negative values for the plotted 80-second intervals. This behavior is most pronounced at elevations above 16 cm, but it appears to damp out at late times.

The code's treatment of the convection term may be responsible for calculations of negative heat generation. The assumption of an instantaneous elevation of the local gas temperature to the local bed temperature leads to an overestimate of the loss by convection. This loss can be expected to be relatively more important where and when little or no reduction occurs and when the heater power is zero, i.e., at elevations greater than 15 cm and at times greater than 13,350 s.

Figure 10 shows the calculated fraction of CuO remaining in the bed as a function of position for various times. Incomplete reduction of CuO is indicated, even in the lower portion of the bed where complete reduction is expected. Negative heat generation rates are manifested here (by virtue of Equation (6) and an 80-second delay) as CuO fractions in excess of 1.0 at elevations above 16 cm.

The results shown in Figures 9 and 10 suggest that the uppermost position reached by the reaction front is in the vicinity of 15 cm to 19 cm from bed bottom. This range is consistent with posttest examinations of dissected reaction tubes.

Figure 11 shows the calculated hydrogen production rate and the total amount generated as a function of time. A total of approximately 18 g of hydrogen was produced. Most of this was generated in the interval between 10,100 s and 10,300 s at rates not exceeding 0.12 g/s.

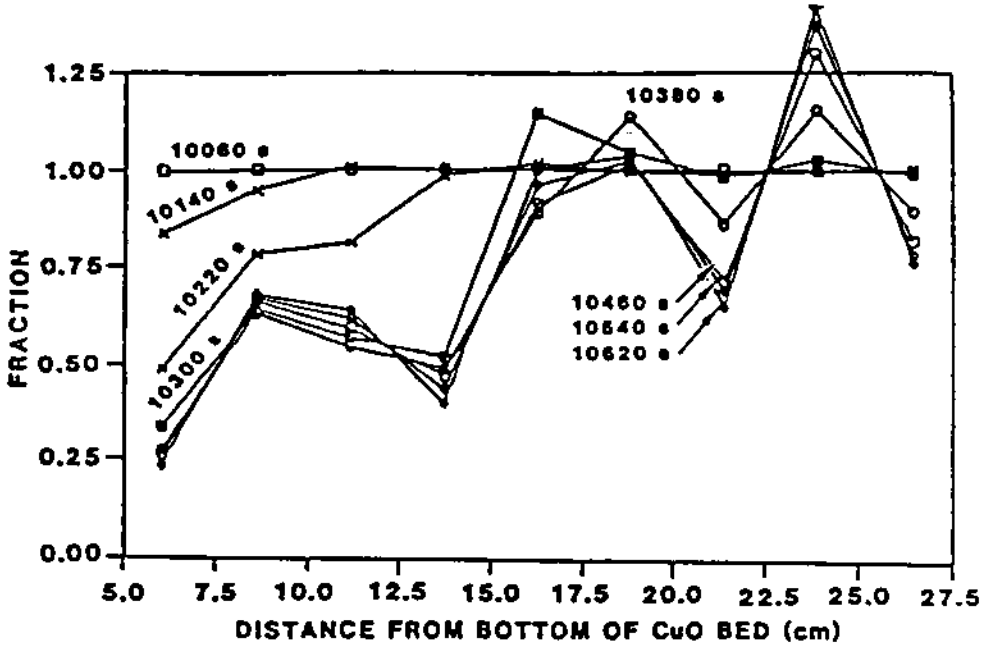

Fig. 10 Fraction of CuO Remaining in the Bed at Various Positions and Times.

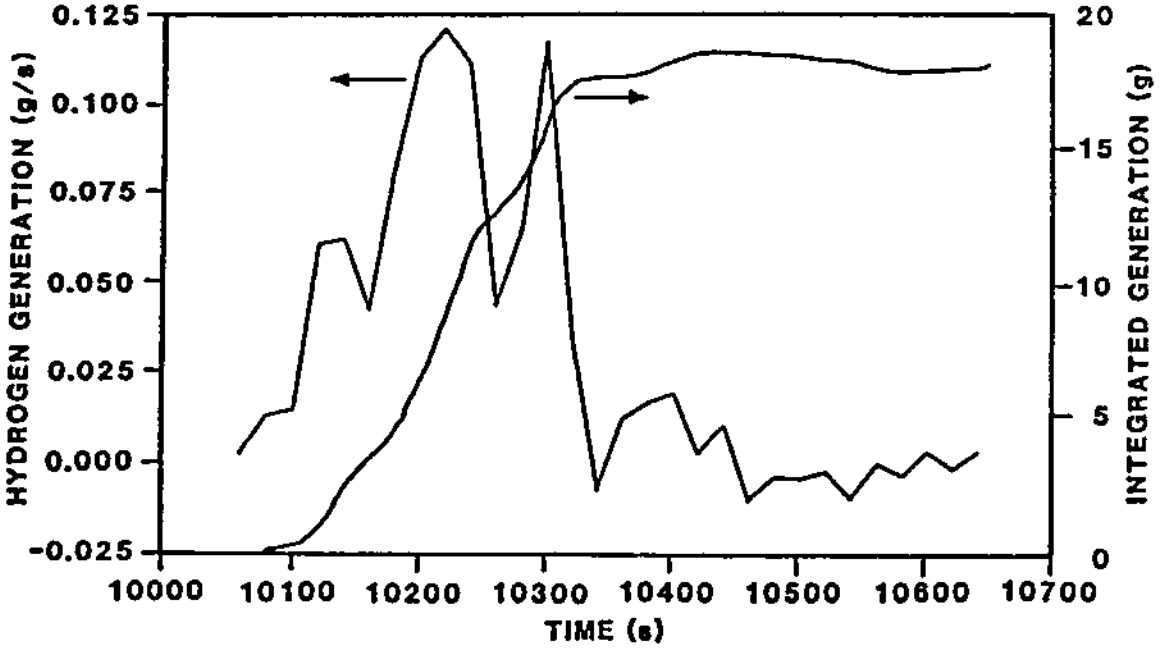

Fig. 11 Hydrogen Generation Rate and Total Amount Generated.

(2) Posttest Examination

Sections 20 cm long were cut from three reaction tubes and then split lengthwise so that the reaction volumes in each could be examined. Figure 12 shows the photographs of these sections. In each case, a boundary can be seen between the dark unreacted portion (CuO) and the light-gray reduced portion (Cu). The parabolic shape of the reaction-front boundary suggests that the reaction may take place earlier at the wall than at the center of the bed.

A large void can also be seen near the bottom of each tube. Both the void and the shape of the reaction-front boundary may be the result of the decrease in molecular volume that occurs when CuO is reduced to Cu (from 12.6 cm^3/mole to 7.65 cm^3/mole). A more homogeneous distribution of the void would seem to be more likely however. The concentrated void may have been created during the posttest handling of the tubes, possibly during the epoxy-injection process.

Assuming that the unreacted portion was not disturbed by volume changes in the reacted portion or by posttest handling, it is possible to estimate the total length, including void, of the reaction volume. From the photographs, this volume appears to be from 15 cm to 20 cm long.

If the average reaction volume is 16 cm in length and completely reduced, then each of the 10 reaction tubes would have seen a total of 5.1 g of hydrogen, including 1.2 g of hydrogen used during the pretest calibration. This corresponds to a total production of 39 g of hydrogen during the DF-1 test. The present analysis indicates, however, that on the average only about 50% of the CuO in the reaction volume was reduced to Cu. If this is indeed the case, then a better estimate of total production is 20 g, which is close to the previous estimate of 18 g.

(3) Modeling Uncertainties

To provide additional information about the uncertainties associated with the present analysis, a number of sensitivity calculations were carried out in which the effects of (a) variations in the size of the timestep, (b) variations in the heater power history, and (c) tube-to-tube variations were explored.

User-specified timesteps of 5 s, 10 s, and 20 s were used in repeated applications of the present method to the DF-1 data. Caclulated hydrogen-production-rate histories showed large oscillations in the rate when

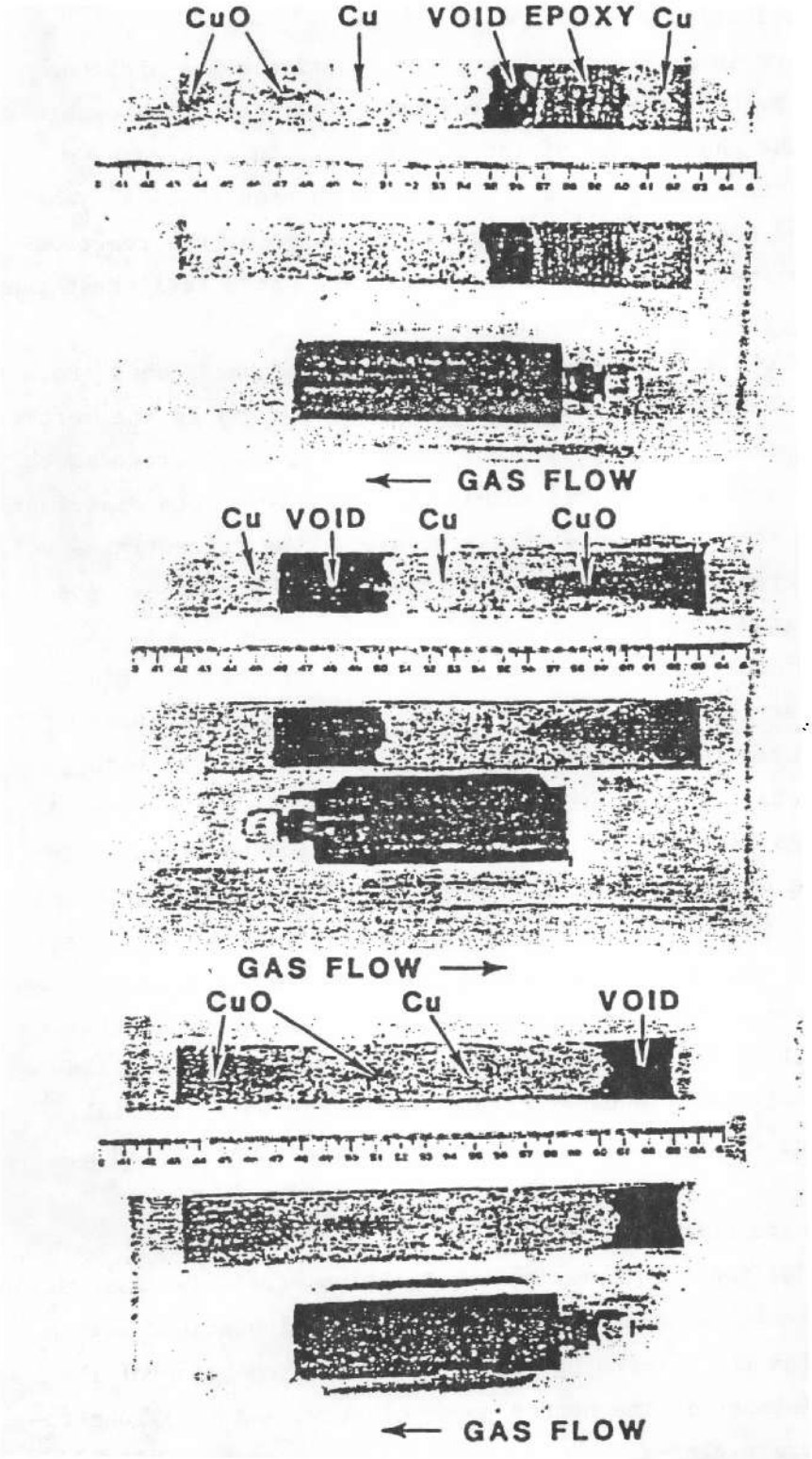

Fig. 12 Posttest Photos of Reaction Volumes of Tubes 2, 4, and 5.

timesteps less than 20 s were used. The integrated production history, by contrast, was only slightly affected by changes in the size of the timestep. Therefore, in applications of the present method to experiments in which centerline bed temperatures must be inferred from the surface-measured temperatures using the inversion procedure, use of a 20-second or greater timestep is recommended. For experiments, such as DF-2, in which the TCs were located within the CuO bed, a smaller timestep can be used. Five-second resolution was obtained in the analysis of the DF-2 data.

The power delivered to the DF-1 heaters was not accurately known, particularly with respect to the timing. Therefore, in addition to the base-case analysis, two other calculations were done. The base-case power-versus-time profile was retained in both calculations; the profile was merely shifted forward by 100 s in one case and backward by 100 s in the other case. Both calculations led to large (compared to the base case) negative rates of hydrogen production at about 10,350 s. Because these results are physically unrealistic, the use of the power history that was assumed for the base-case analysis appears to be justified.

The effects of tube-to-tube variations on the calculated results were examined using each of the 10 temperature (6-inch-elevation) profiles shown in Figure 5. Ten calculations were carried out for a composite reaction tube, which in all other respects was unchanged, except that with each succeeding calculation the profile for the 6-inch elevation was replaced by another. The overall effects of these variations are not great. Total hydrogen production does not vary by more than ±10%.

The uncertainities associated with the general method of hydrogen analysis described here are probably on the order of ±10%. In the specific applications to the DF-1 test, however, the uncertainties are much greater, due principally to the lack of information about thermal boundary conditions and the final compositions of the Cu/CuO beds. As other tests in the DF series are carried out, additional opportunities to quantity the uncertainties will arise. For the present, the estimates of the hydrogen production rate and total hydrogen produced in DF-1 should be regarded as semiquantitative results.

5. CONCLUSION

A method for estimating hydrogen generation based on chemical reaction of copper oxide with hydrogen was developed. The method was applied to ACRR DF experiments and the following conclusions were drawn.

(1) It was estimated that, in DF-1 a total of approximately 18 g of hydrogen was generated and the majority of the hydrogen was generated within 200 s at the rate of not exceeding 0.12 g/s.

(2) The present analysis predicted that the reaction front reached the vicinity of 15 cm to 19 cm from bed bottom in DF-1. The prediction was consistent with posttest examinations of dissected reaction tubes.

(3) Accuracy and time response of the present method depends on response time of heat conduction within a reaction tube.
It was recommended that time step of 20 s or greater be used for the reaction tube employed in DF-1.

(4) Higher time resolusion can be achieved by locating additional thermocouples on the centerline of the copper oxide bed.

(5) It was demonstrated by applying the present method to ACRR DF experiments that the method is simple and valuable tool to measure hydrogen generation rate during experiments involving Zircaloy-water reaction.

ACKNOWLEDGEMENT

The author wishes to express sincere appreciation to the colleagues at SNL, especially to Dr. P.S. Pickard for providing the opportunity to analyze the CuO temperature response, Dr. A.C. Marshall and Dr. K.O. Reil for their valuable comments and encouragements.

The author also acknowledges Dr. M. Hirata, Dr. M. Ishikawa, Kr. K. Hirano, and Mr. A. Kohsaka for their support to participate in the SFD program at SNL. Special thanks go to Kr. K. Soda for his valuable suggestions.

REFERENCES

(1) Nuclear Regulatory Commission Special Inquiry Group," Three Mile Island, A Report to the Commissioners and to the Public, Vol.2, January, 1980.

(2) Berman, M., "A Critical Review of Recent Large-Scale Experiments on Hydrogen-Air Detonations," Nuclear Science and Engineering 93, 321-347, 1986.

(3) Knipe, K.D., Ploger, S.A., and Osetek, D.J., "PBF Severe Fuel Damage Scoping Test-Test Results Report," NUREG/CR-4683, EGG-2413, August, 1986.

(4) Real, K.O., et al., "Results of the ACCR-DFR Experiments," Proceedings of 6-th International Topical Meeting on Thermal Reactor Safety, San Diego, CA, U.S.A., February, 1986.

(5) Sandia National Laboratories, "Reactor Safety Research Semiannual Report, July-December 1985, Volume 34," NUREG/CR-4340 (2 of 2), SAND 85-1606 (2 of 2), July, 1986.

APPENDIX C
Description of the WRET Code

This appendix contains a description of the WRET code. The WRET code was written to analyze the data obtained from the Tungsten/Rhenium (W/Re) thermocouples used in the DF-4 experiment assembly. The code uses an explicit finite difference technique to calculate the W/Re junction temperatures for the DF-4 thermocouple configuration which features a specially designed shroud or housing. The code models a set of 6 heat structures that include the W/Re thermocouple wires surrounded by a HfO_2 insulator, a rhenium sheath, a second insulator composed of ZrO_2 fiber, and finally an outer sheath or housing of dense ZrO_2. The sixth structure consists of the shroud wall that insulates the test section and through which the thermocouples and their housings penetrate.

The code uses the fuel rod and gas temperatures either calculated by the MARCON-DF4 code or estimated by some other means together with measured containment temperatures and estimated gamma heating rates to calculate the temperatures that are expected at the thermocouple junctions. A comparison of the predicted junction temperatures to the measured thermocouple temperatures provides a check and calibration of the W/Re thermocouple data. When coupled to an inverse heat conduction calculation, WRET provides a means of estimating the DF-4 fuel cladding temperature based on the observed W/Re junction temperatures.

Figure C-1 shows both the Pt/Rh and the W/Re thermocouples and how they are situated relative to the fuel rods inside the DF-4 test section. Unlike the Pt/Rh thermocouples, the W/Re thermocouples are not bonded directly to the fuel rod cladding, but are merely in contact with or in close proximity to the rod cladding. In fact, the thermocouple junction is separated from the fuel cladding by the thickness of the zirconia housing which serves to protect it from the oxidizing atmosphere within the test section. A more detailed description of the thermocouple and its housing is shown in Figure C-2.

In order to estimate the thermocouple junction temperature it is necessary to model all the heat transfer pathways in the thermocouple and its immediate environment. The heat transfer processes involved include: (1) radiation from the fuel rod to the shroud and thermocouple tip, (2) convection from the flowing steam/hydrogen mixture to the shroud and thermocouple, (3) axial and radial conduction in the thermocouple and its housing and between the thermocouple and the shroud, (4) radiation across the helium filled gas spaces inside the housing and the rhenium sheath, (5) convection from the outside of the test section jacket to the gas space and the containment structure, and (6) internal heating due to gamma ray absorption.

Because the system to be analyzed involves a number of materials with widely differing thermal properties and significant temperature gradients, it was necessary to calculate both temperature and spatially dependant thermophysical properties. A "soft link" (no feedback) was established between the MARCON-DF4 code and the WRET code in which key parameters were passed to the WRET code. The parameters include the fuel and gas temperatures at the 4 thermocouple locations, the effective radiative heat transfer coefficients between fuel rod and shroud wall, and the convective heat transfer coefficient between the gas and the shroud. The heat transfer

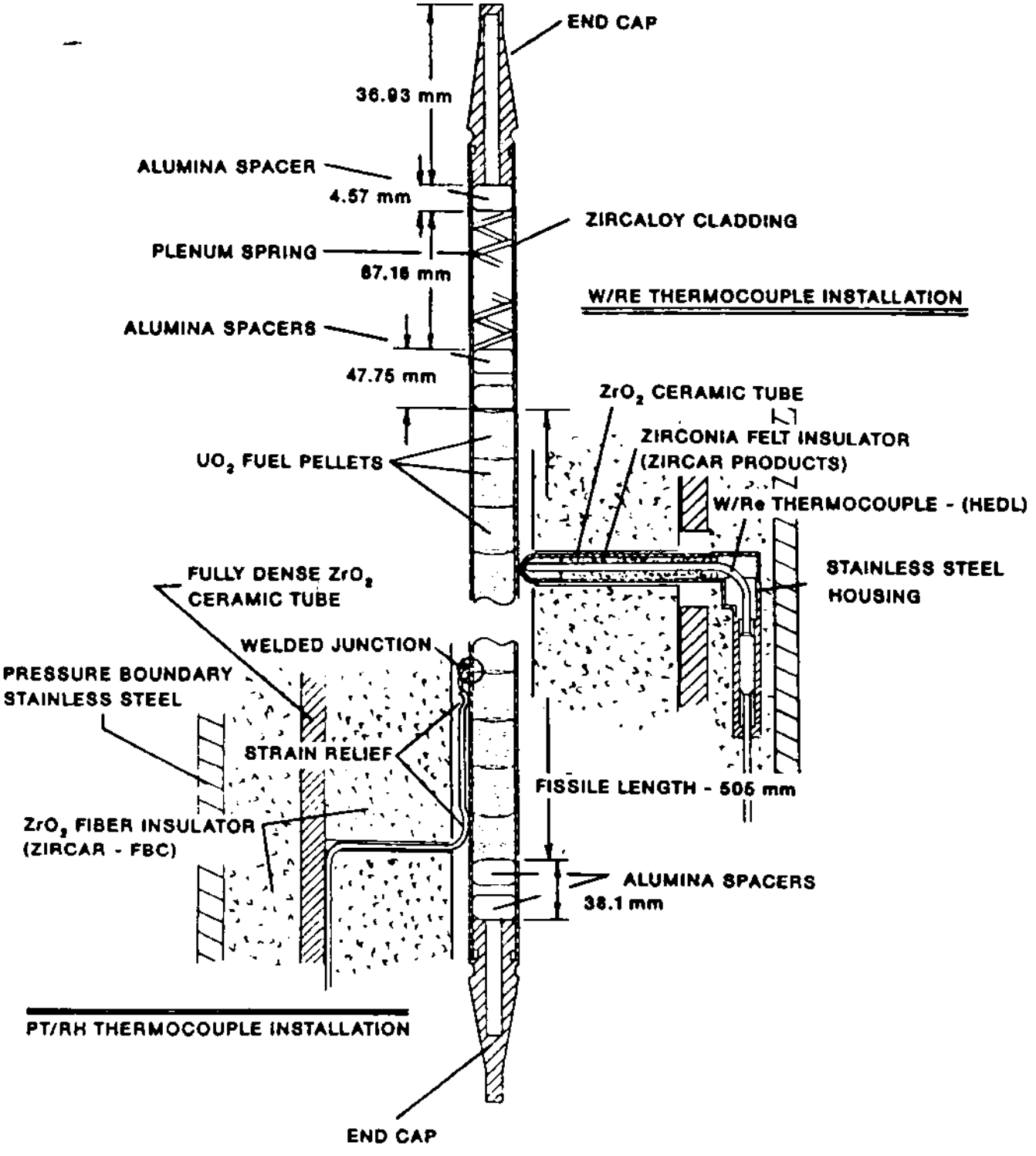

Figure C-1 Diagram of Thermocouple Installation.

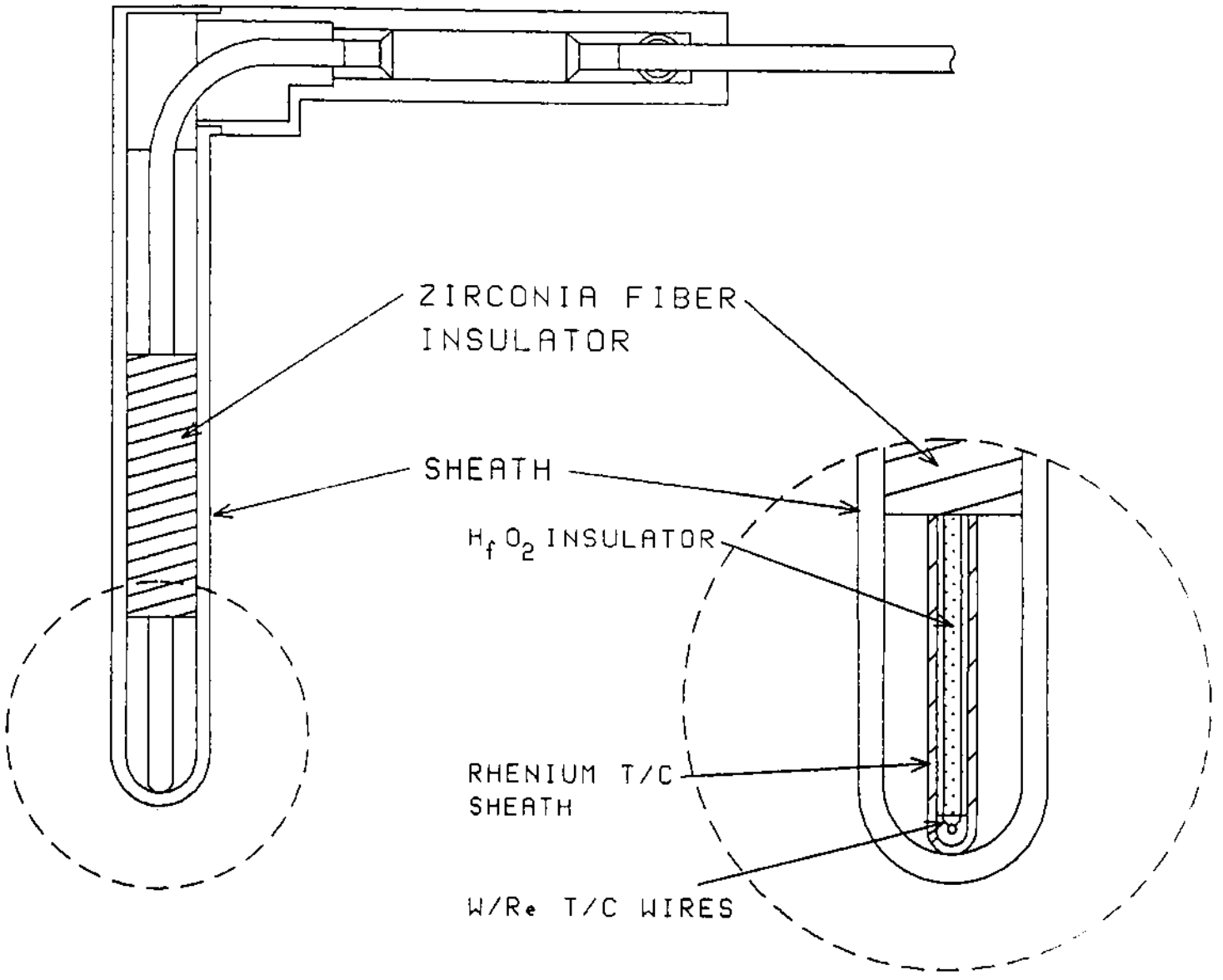

Figure C-2: Diagram of W/Re Thermocouple Assembly.

coefficients between the rod and the thermocouple and between the gas and the thermocouple were assumed to be essentially the same as from those elements to the shroud wall, except that a correction was applied for differences in temperature between the shroud wall and the thermocouple tip (exposed tip of thermocouple housing).

A diagram of the two-dimensional nodalization scheme used for the finite difference calculations in the thermocouple and housing structures is shown in Figure C-3. Figure C-4 describes the one-dimensional finite difference mesh structure for the shroud wall. It was possible to use a one-dimensional nodalization in the shroud by assuming that the presence of the thermocouple perturbs the wall temperature profile only locally. Thus, the wall temperature profile serves as a boundary temperature for each axial node in the zirconia housing and heat transfer is calculated between the housing and the wall across whatever gradients may exist at each nodal location, but heat transfer from the thermocouple is not accounted for in determination of the shroud temperature. The central set of nodes in Figure C-3 labeled 1,1 through 1,21 represent heat structure number 1 and consists of the tungsten/rhenium thermocouple wires. The next structure radially outward, nodes 2,1 through 2,20 is the HfO_2 insulator in which the thermocouple wires are embedded. The structure that is domed at the top and labeled 3,1 through 3,20 is the rhenium metal sheath that encases the thermocouple wire. Outside the rhenium sheath is a second layer of insulation that also acts as a separator between the rhenium sheath and the housing. This layer is composed of ZrO_2 low density fiber and is modeled as structure number 4, nodes 4,1 to 4,15. The thermocouple protective housing or sheath is also domed and labeled 5,1 to 5,20. The uppermost node, (5,1) is the exposed hemispherical tip of the housing that is in direct contact with the fuel rod. The upper node of the rhenium sheath (3,1) is in close proximity or actually in contact with the inside of the tip of the housing (node 5,1). Node 1,1 corresponds to the thermocouple junction and the length of W/Re wire that extends outside of the HfO_2 insulator. The gaps or spaces between nodes 5,1 and 3,1 and between 3,1 and 1,1 are helium filled.

For thermocouple internal nodes writing the energy equation for a node yields:

$$M_{ij} C_{p,ij} \frac{dT_{ij}}{dt} = h_{j-1\to j} A_{j-1\to j} (T_{i,j-1} - T_{i,j}) +$$

$$h_{j\to j+1} A_{j\to j+1} (T_{i,j} - T_{i,j+1}) + h_{i-1\to i} A_{i-1\to i} (T_{i-1,j+m} - T_{i,j})$$

$$+ h_{i\to i+1} A_{i\to i+1} (T_{i,j} - T_{i+1,j+n}) + Q_{\gamma,ij} \quad . \qquad \text{(C-1)}$$

In equation C-1, M_{ij} and $C_{p,ij}$ are the mass and heat capacity of the j-th node in the i-th heat structure. Similarly the temperatures and the gamma heat source strengths at these locations are denoted by T and Q_γ respectively. The effective heat transfer coefficients and areas between adjacent heat structures and nodes are given by $h_{i\to i+1}$ and $A_{i\to i+1}$, which represent the heat transfer coefficient and area between heat

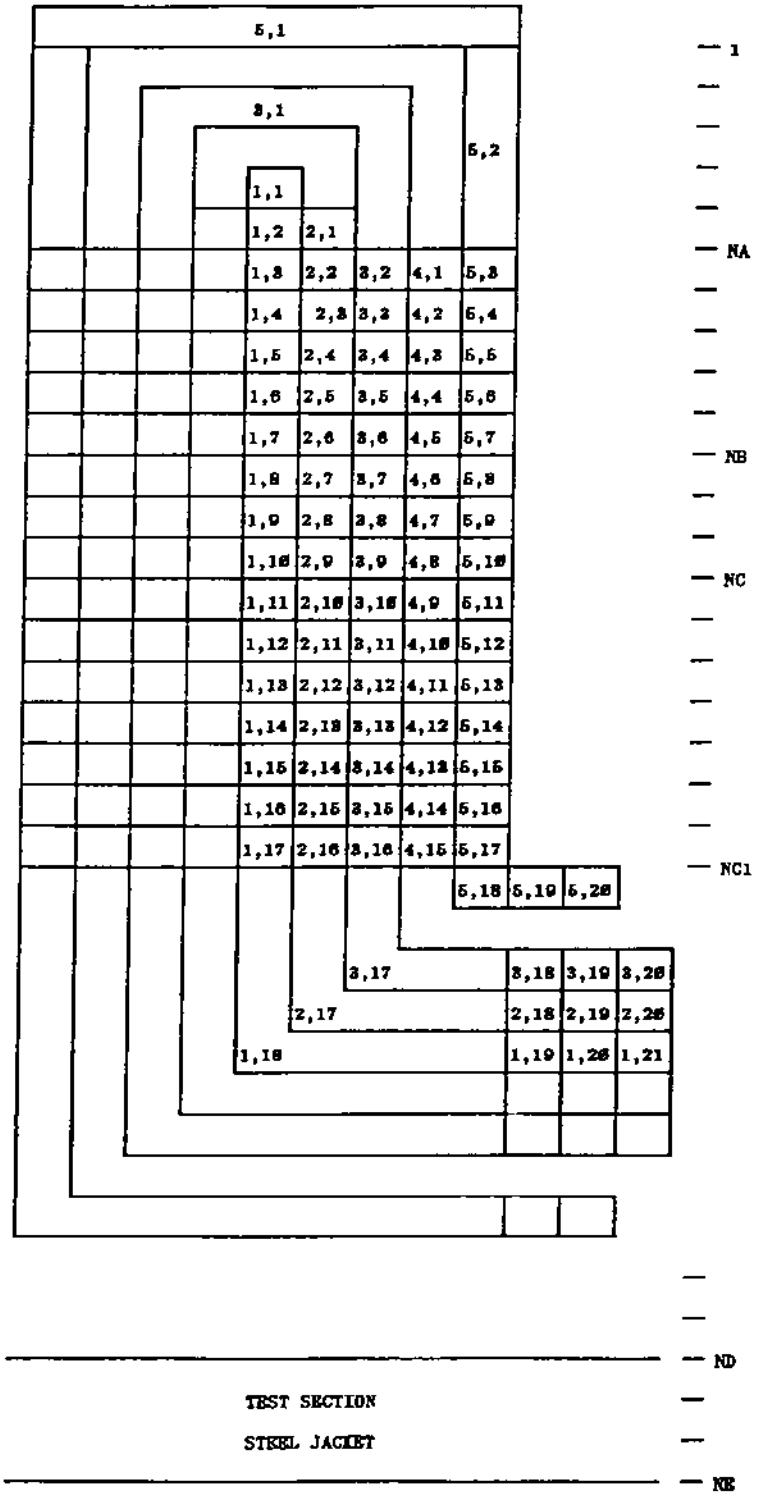

Figure C-3 WRET Thermocouple Nodalization Scheme.

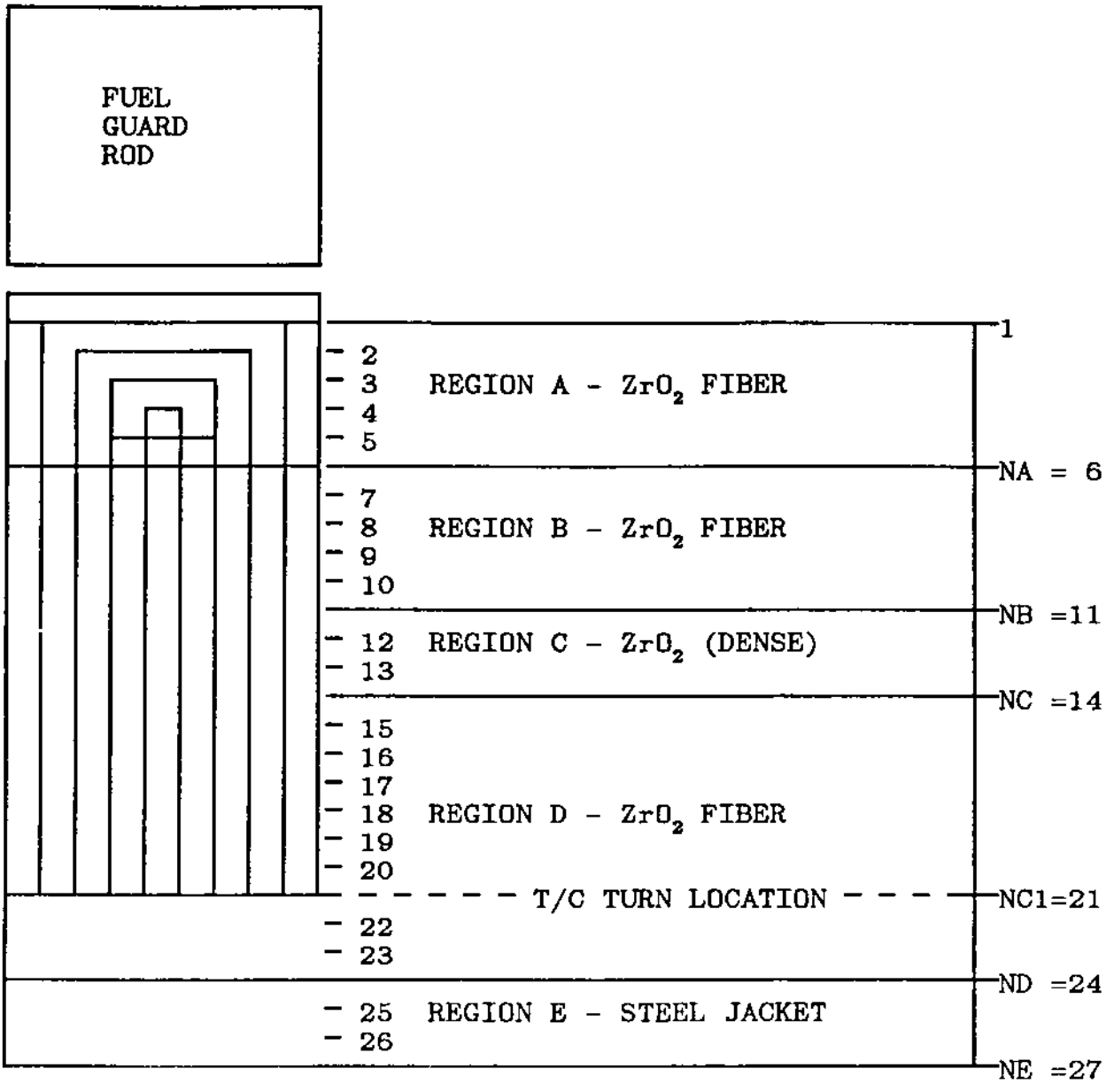

Figure C-4 WRET Shroud Nodalization Scheme.

structure i and heat structure i+1. The constants m and n in the 3rd and 4th terms on the right of equation C-1 account for the fact that the heat structures are not nodalized the same. That is, the jth node in heat structure i does not necessarily lie adjacent to the jth node in heat structure i+1. Clearly the constants m and n can be positive or negative depending on the heat structure interface.

The effective heat transfer coefficients are calculated by using the temperature and material dependent thermal conductivities together with the half/node lengths in the case of axial conduction and the appropriate half/volume characteristic lengths for radial conduction (from one heat structure to the next radially outward or inward). For axial conduction the effective heat transfer coefficient is,

$$h_{j\to j+1} = \frac{1}{\frac{\Delta x_j}{2K_j} + \frac{\Delta x_{j+1}}{2K_{j+1}}} , \qquad \text{(C-2)}$$

while for radial conduction the expression is,

$$h = \frac{1}{\frac{\sqrt{2(r^2-r_1^2)} - r_1}{K_{i,j}} + \frac{\sqrt{2(r_3^2-r_2^2)} - r_2}{K_{i+1,j+m}}} \qquad \text{(C-3)}$$

where r_1, r_2, and r_3 represent the inner radius of the ith structure, the outer radius of the ith structure (and inner radius of the i+1 structure), and the outer radius of the i+1 structure respectively.

For heat structure number 6, the shroud wall, an explicit finite difference scheme with time and spatial dependant thermophysical properties was employed. This structure has five zones in which three different materials are located. For interior nodes that are not located on a material boundary (see Figure C-4) the temperature at node n and time t ,T_n^*, is related to the the temperatures at time t-Δt by:

$$T_n^* = T_n \left[1 - \frac{\Delta t}{\Delta x^2}\left[\alpha_{n-1,n} + \alpha_{n,n+1}\right]\right] + \frac{\Delta t}{\Delta x^2}\left[\alpha_{n-1,n}T_{n-1} \quad \alpha_{n+1,n}T_{n+1}\right]$$

$$+ \frac{Q_{\gamma,n}\Delta t}{[\rho C_p]_n} . \qquad \text{(C-4)}$$

In this equation the thermal diffusivity, $\alpha_{n-1,n}$, for example, is evaluated at $T=(T_{n-1}+T_n)/2$. For nodes that are located on material boundaries not only are the thermal diffusivities different due to different temperatures, but also due to different materials, and the node spacings, Δx, are different. The temperatures at internal boundaries is

given by:

$$T_n^* = T_n \left[1 - \frac{2\Delta t}{[\Delta x_{n+1}\ \Delta x_{n-1}]} \left[\frac{\alpha_{n-1,n}}{\Delta x_{n-1}} + \frac{\alpha_{n,n+1}}{\Delta n_{n+1}} \right] \right]$$

$$+ \frac{2\Delta t}{[\Delta x_{n+1} + \Delta x_{n-1}]} \left[\frac{\alpha_{n-1,n}\ T_{n-1}}{\Delta x_{n-1}} + \frac{\alpha_{n,n+1}\ T_{n+1}}{\Delta x_{n+1}} \right]$$

$$+ \frac{\Delta t}{2} \left[\frac{Q_{\gamma,n-1}}{[\rho C_p]_{n-1}} + \frac{Q_{\gamma,n+1}}{[\rho C_p]_{n+1}} \right] \qquad \text{(C-5)}$$

At the inside surface of the shroud there exists two boundary conditions, a convective one and a radiative one. If the gas temperature is T_g and the convective heat transfer coefficient is h_g, while the fuel temperature is T_f and the effective radiative heat transfer coefficient is h_f, the surface node temperature is given by:

$$T_1^* = T_1 \left[1 - \frac{2\alpha\Delta t}{\Delta x^2} \left[\frac{\Delta x h_g}{K_1} + \frac{\Delta x h_f}{K_1} + 1 \right] \right]$$

$$+ \frac{2\alpha\Delta t}{\Delta x^2} \left[\frac{\Delta x h_g T_g}{K_1} + \frac{\Delta x h_f T_f}{K_1} + T_2 \right] + \frac{Q_{\gamma,1}\Delta t}{[\rho C_p]_1} \qquad \text{(C-6)}$$

Because the numerical technique used here is explicit, the governing convergence criterion is specified by:

$$\Delta t \leq \frac{\Delta x^2}{2\alpha} \left[\frac{1}{1 + \frac{\Delta x}{K} \left[h_f + h_g \right]} \right] \qquad \text{(C-7)}$$

The estimated volumetric heat source, Q_γ, is obtained from irradiation experiments performed in the ACRR for a wide range of materials. The gamma heat source strength for rhenium metal in radial region n, for example, is calculated as follows:

$$Q_{\gamma,Re,n} = \Gamma_{Re} P_{ACRR} A_{f,n} \rho_{Re} \ . \qquad \text{(C-8)}$$

In this ression Γ_{Re} is the unattenuated gamma heating rate for rhenium in the ACRR nits of watts per Kg of rhenium per megawatt of ACRR power, P_{ACRR} is the rea ower level in megawatts, $A_{f,n}$ is the shielding or gamma attenuation factor in radia on n, and ρ_{Re} is the rhenium density (Kg/m²). Table C-1 gives the values of the ia heating rates, Γ, for the various materials in the DF-4 shroud and thermoc assembly. The attenuation factors for each region of the shroud were calculate ng the standard shielding equation together with the thickness of each material n between the ACRR source and the particular region. The calculated values of ttenuation factors for each of the five radial regions in the shroud are given in T C-2.

Referring back to Figures C-3 and C-4 it is seen from these diagrams that the critical heat transfer pathways in the upper (tip) of the thermocouple housing involve both conduction through solid materials and radiation between surfaces inside the housing and inside the sheath in this region. In the temperature regime in which the DF-4 experiment was conducted the primary heat transfer mechanism inside the tip of the housing is radiation. To calculate the heat transfer rates between structures in the tip region it is necessary to estimate the radiation view factors between the four heat structure nodes that enclose the gas space inside the housing (between the housing and the rhenium sheath), and the three nodes that enclose the gas space inside the tip of the rhenium sheath where the thermocouple junction is located.
The four nodes that enclose the gas space inside housing are nodes (5,1), (5,2), (3,1), and (4,1), while those enclosing the inner gas space are nodes (3,1), (1,1), and (2,1). Node (3,1) was not split into two nodes as in the case of C5,1-2) for two reasons. In the case of structure 5, only the tip of that structure receives radiation from the fuel rod, while the 2nd node in that structure receives heat from the 1st node by conduction and by radiation. In the case of the upper node in structure 3, the entire surface above the insulator (structure 4) receives radiation from structure 5, and in addition it is a metallic structure that will not maintain a significant temperature difference between two adjacent nodes in any case.

In general, view factors for these kinds of geometries are difficult to calculate without making some approximations. To render the calculations feasible, a coaxial finite length cylindrical geometry was adapted for both regions. Figure C-5 shows the geometry of the two regions and the general model used to calculated the view factors. The model assumes that the inside and outside surfaces are cylindrical and co-terminus. If the outside cylinder is denoted as surface 2 and the inside cylinder is surface 1 then the two non-zero view factors between these surfaces are given by:

$$F_{12} = \frac{1}{R} - \frac{1}{\pi R}\left[\cos^{-1}\left[\frac{B}{A}\right] - \frac{1}{2L}\left[\sqrt{(A+2)^2 - 4R^2}\,\cos^{-1}\left[\frac{B}{RA}\right] + B\sin^{-1}\left[\frac{1}{R}\right] - \frac{\pi A}{2}\right]\right] \qquad \text{(C-9)}$$

$$F_{22} = 1 - \frac{1}{R} + \frac{2}{\pi R} \tan^{-1}\left[\frac{2\sqrt{R^2 - 1}}{L} \right]$$

$$- \frac{L}{2\pi R} \left[\sqrt{4R^2 + L^2} \sin^{-1}\left[\frac{4(R^2 - 1) + \frac{L^2}{R^2}(R^2 - 2)}{L^2 + 4(R^2 - 1)} \right] \right.$$

$$\left. - \sin^{-1}\left[\frac{R^2 - 2}{R^2} \right] + \frac{\pi}{2} \left[\frac{\sqrt{4R^2 + L^2}}{L} - 1 \right] \right] , \qquad \text{(C-10)}$$

where R, L, A, and B are defined as,

$$R = \frac{r_2}{r_1}$$

$$L = \frac{Z}{r_1}$$

$$A = L^2 + R^2 - 1$$

$$B = L^2 - R^2 + 1 .$$

Making use of the fact that the geometry is completely enclosed, the view factors from any surface to the other surfaces in the enclosure must sum to 1,

$$F_{11} + F_{12} + F_{13} + F_{14} = 1 .$$

In addition, the special geometry selected for the model assumes that the two ends of the cylinder are identical, so that the view factor is the same, for example, from surface 1 to surface 3 as it is from surface 1 to surface 4 (see Figure C-5). Also the view factor F_{11} is identically zero since it cannot "see" itself. Finally, from reciprocity,

$$F_{12}A_1 = F_{21}A_2 ,$$

enough information is available to easily calculate all 16 view factors.

Radiation between surfaces in the enclosed spaces just described is assumed to be of the gray body type, i.e., the surfaces obey the Lambert cosine law and reflect diffusely (in all directions equally). Since radiation transport includes reflected as well as radiated fluxes it is convenient to calculate the radiosities (total radiation leaving a given surface) and then convert these to energy transport rates between surfaces. The appropriate set of four equations that describe radiation transport inside the enclosures in terms of radiosities are as follows:

$$\left[\frac{\epsilon_i}{1-\epsilon_i}\right]\sigma T_i^4 = \sum_{j=1,4} j\left[\delta_{ij}\left[1+\frac{\epsilon_i}{1-\epsilon_i}\right] - F_{i,j}\right] \qquad \text{(C-11)}$$

$$i = 1,4$$

In equation C-11, ϵ_i is the emissivity of the ith surface, J_j is the radiosity of the jth surface, and δ_{ij} is the Kronecker delta. The set of four simultaneous equations expressed by C-11 above can be easily solved for the radiosities, J_j using Cramers rule without the necessity of matrix methods, and the heat transport rate between surface m and n is determined by:

$$q_{mn} = (J_m - J_n)F_{m\to n}A_m\,, \qquad \text{(C-12)}$$

while the effective radiation heat transfer coefficient can be calculated,

$$h_{rad,m\to n} = F_{m\to n}(J_m - J_n)/(T_m - T_n)\,. \qquad \text{(C-13)}$$

If λ_m and λ_n are the characteristic conduction lengths in the heat structure nodes associated with surfaces m and n, and the thermal resistances due to conduction through these structures are incorporated into the heat flow network, the overall effective heat transfer coefficients for the radiative path is given by:

$$h_{m\to n} = \frac{1}{\left[\frac{1}{h_{rad,m\to n}} + \frac{\lambda_m}{K_m} + \frac{\lambda_n}{K_n}\right]} \qquad \text{(C-14)}$$

The input to the code specifies which of the four W/Re thermocouple locations is required, start and stop times, data for the calculation of the containment boundary temperature (outside boundary condition), and a table of time verses ACRR power for calculating the gamma heating effects. From an output file generated by the MARCON-DF4 code the WRET code reads the fuel rod and gas temperatures. The DF-4 experiment was run with a long "equilibration" period before the actual transient was initiated to assure that the system was close to thermal equilibrium. The WRET

code, therefore, assumes an equilibrium condition and calculates the initial node temperatures for a steady-state condition. When the steady-state convergence criteria are satisfied, the code sets a time step based on the minimum time step calculated for the heat structures that have the fastest response times. In general, the convergence criteria are controlled by surface nodes that are connected by heat transfer coefficients to the fuel rods or the atmosphere. The convergence criteria for these nodes are similar to that given by equation C-7. The code writes selected heat structure node temperatures to an output file. A plot program allows plotting of any combination of structure and node temperatures.

Table C-1
Gamma Heating Rates in the ACRR

Material	Γ (W/Kg/MW)
ZrO_2	107.2
Re	145.2
HfO_2	134.4
W/Re	142.3
Steel	107.0

Table C-2
Gamma Heating Attenuation Factors

Region Interface	I/I_ϕ
Test Section-A	.350
A-B	.369
B-C	.391
C-D	.444
D-E	.492
E-Containment	.630
Containment-Shield	.754
Shield-ACRR	1.000

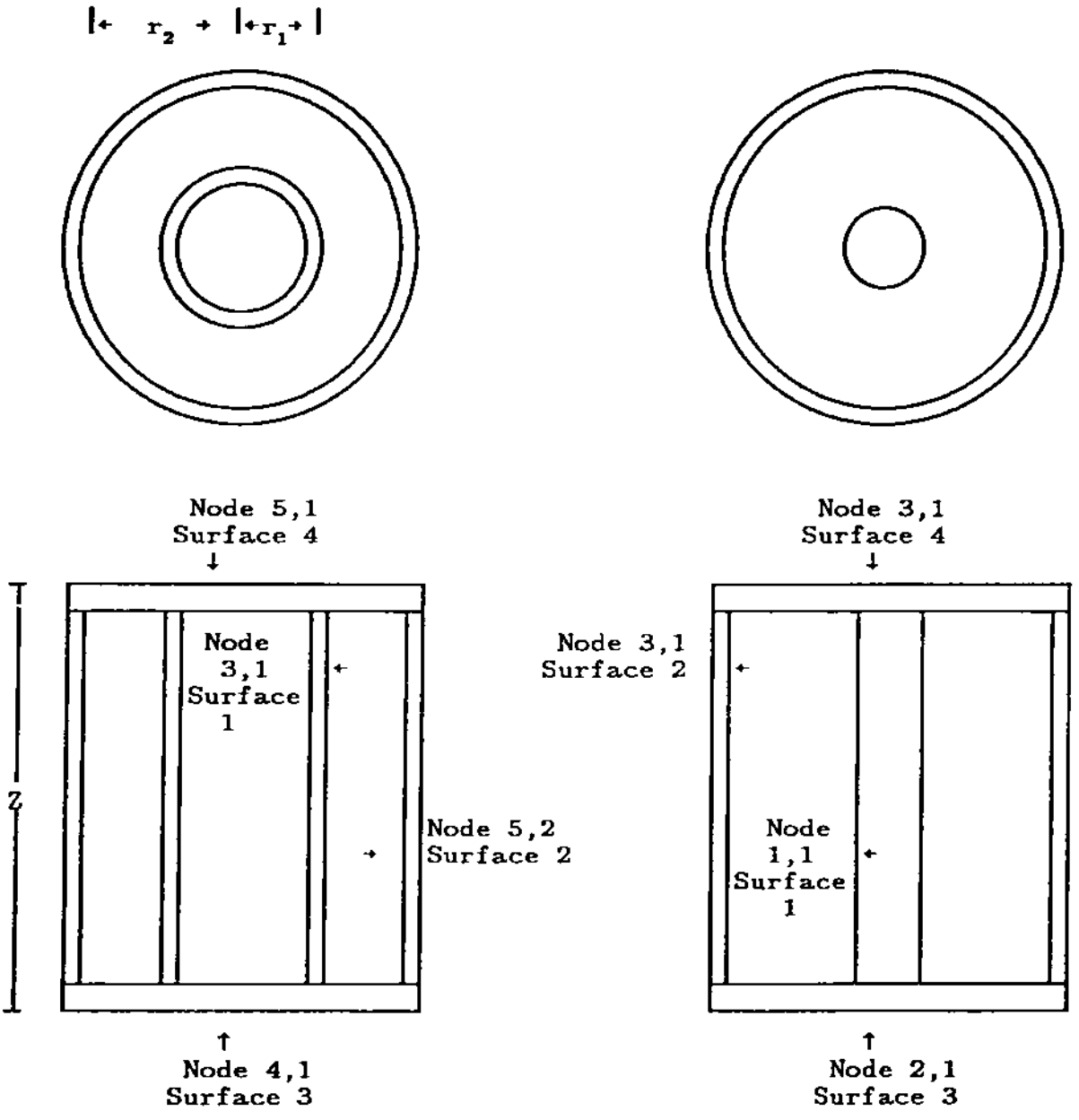

Figure C-5: Radiation View Factor Models for the Thermocouple Housing (left) and Rhenium Sheath (right).

DISTRIBUTION:

U.S. Nuclear Regulatory Commission (11)
Division of Systems Research
Office of Nuclear Regulatory Research
Washington, DC 20555
Attn: B. W. Sheron
J. A. Murphy
F. Costanzi
R. O. Meyer
R. Van Houten
R. W. Wright
F. Eltawila
J. T. Han
T. J. Walker
P. Worthington
M. Cunningham

U. S. Nuclear Regulatory Commission (5)
Advisory Committee on Reactor Safeguards
Washington, DC 20555
Attn: G. Quittschreiber
W. Kerr
M. Corradini
P. Shewmon
D. Houston

M. L. Corradini
University of Wisconsin
Nuclear Engineering Department
1500 Johnson Drive
Madison, WI 53706

U.S. Department of Energy (3)
Albuquerque Operations Office
P.O. Box 5400
Albuquerque, NM 87185
Attn: J. R. Roeder, Director
Transportation Safeguards Div.
J. A. Morley, Director Energy
Research Technology Division
For: C. B. Quinn
R. N. Holton

Argonne National Laboratory (7)
9700 South Cass Avenue
Argonne, IL 60439
Attn: J. Rest
L. Baker
L. Neimark
Dae Cho
R. Anderson
B. Spencer
D. Armstrong

Battelle Columbus Laboratory (4)
505 King Avenue
Columbus, OH 43201
Attn: R. S. Denning
P. Cybulskis
J. Gieseke
C. Alexander

Battelle Pacific Northwest Laboratory (4)
P.O. Box 999
Richland, WA 99352
Attn: M. Freshley
G. R. Bloom
F. Panisko
N. Lombardo

Brookhaven National Laboratory (7)
Upton, NY 11973
Attn: W. Kato
M. Khatib-Rhabar
R. A. Bari
T. Pratt
T. Ginsberg
G. Greene
K. Araj

T. G. Theofanous
University of California
Chemical and Nuclear Engineering Dept.
Santa Barbara, CA 93106

EG&G Idaho (9)
Willow Creek Building, W-3
P.O. Box 1625
Idaho Falls, ID 83415
Attn: Server Sadik
D. Croucher
R. Hobbins
C. Allison
J. Dallman
P. E. McDonald
D. Osetek
D. Petti
L. Siefken

Electric Power Research Institute (5)
3412 Hillview Avenue
Palo Alto, CA 94303
Attn: W. Loewenstein
M. Leverett
B. R. Sehgal
R. Vogel
J. Haugh

Fauske and Associates (3)
16W070 West 83rd St.
Burr Ridge, IL 60521
Attn: R. Henry
M. Plys
M. Kenton

M. I. Temme, Manager
Probabilistic Risk Assessment
General Electric Corporation
Advanced Reactor Systems Department
P.O. Box 3508
Sunnyvale, CA 94088

K. W. Holtzclaw
General Electric Corporation
175 Curtner Avenue
Mail Code N 1C157
San Jose, CA 95125

Henry Piper
Institute of Nuclear Power Operation
Suite 1500
1100 Circle 75 Parkway
Atlanta, GA 30339

Los Alamos National Laboratory (7)
P.O. Box 1663
Los Alamos, NM 87545
Attn: M. Stevenson
R. Henninger
J. Carson Mark
J. Travis
W. R. Bohl
F. Dearing
T. Hirons

N. C. Rasmussen
Massachusetts Institute of Technology
Nuclear Engineering Dept.
Cambridge, MA 02139

Prof. M. Sichel
University of Michigan
Department of Aerospace Engineering
Ann Arbor, MI 47109

University of Michigan
Nuclear Engineering Department
Ann Arbor, MI 48104

S. H. Hobbs
Mississippi Power Light
P.O. Box 1640
Jackson, MS 39205

S. G. Bankoff
Northwestern University
Chemical Engineering Department
Evanston, IL 60201

Oak Ridge National Laboratory (4)
NRC Programs
P.O. Box X, Bldg. 45005
Oak Ridge, TN 37831
Attn: A. P. Malinauskas
T. Kress
S. Hodge
L. Ott

Power Authority State of NY
10 Columbus Circle
New York, NY 10019

Rensselaer Polytechnic Institute (2)
Department of Nuclear Engineering
and Engineering Physics
Troy, NY 12180-3590
Attn: R. T. Lahey Jr.
M. Podowski

Texas A&M University
Nuclear Engineering Dept.
College Station, TX 77843

UCLA
Nuclear Energy Laboratory (2)
405 Hilgaard Avenue
Los Angeles, CA 90024
Attn: I. Catton
D. Okrent

Westinghouse Corporation (3)
P.O. Box 355
Pittsburgh, PA 15230
Attn: N. Liparulo
J. Olhoeft
V. Srinivas

Frances Emert
Westinghouse Electric Corporation
Bettis Atomic Power Lab
P.O. Box 79
West Mifflin, PA 15122-0079

Ian B. Wall
Safety Technology Department
Electric Power Research Institute
P.O. Box 10412
Palo Alto, CA 94303

Paul J. Fehrenbach
Fuel Engineering Branch, RSR Div.
Chalk River Nuclear Laboratories
Chalk River, Ontario
CANADA KOJ 1JO

David J. Wren
High-Temperature Chemistry Branch
Whiteshell Nuclear Res. Establishment
Pinawa, Manitoba
CANADA ROE 1LO

David F. Torgerson
Reactor Safety Research Division
Whiteshell Nuclear Res. Establishment
Pinawa, Manitoba
CANADA ROE 1LO

Erl Kohn
Consequence Analysis Branch
Atomic Energy of Canada Ltd.
Sheridan Park Res. Domm.
Mississauga, Ontario
CANADA L3K 1B2

Sen-I Chang
Institute of Nuclear Energy Research
P.O. Box 3-8
Lung-Tan
TAIWAN 325

Hubert Bairiot
Department of LWR Fuel
Belgonucleaire SA.
25 rue du Champ de Mars
B-1050 Brussels
BELGIUM

B. Tolley
Director Research, Science Education
CEC
Rue De La Loi 200
1049 Brussels
BELGIUM

Battelle Institute E. V. (3)
Am Roemrhof 35
6000 Frankfurt am Main 90
FEDERAL REPUBLIC OF GERMANY
Attn: Dr. Werner Geiger
Dr. Guenter Langer
Dr. Manfred Schildknecht

Institute fur Kernenergetik und
Energiesysteme (2)
University of Stuttgart
Stuttgart
FEDERAL REPUBLIC OF GERMANY
Attn: M. Buerger
H. Unger

Dr. M. Peehs
Kraftwerk Union
Hammerbacher Strasse 12 14
Postfach 3220
D-8520 Erlangen 2
FEDERAL REPUBLIC OF GERMANY

P. Ficara
Department for Thermal Reactors
ENEA CRE Casaccia
Via Anguillarese, 301
00100 Roma Ad.
ITALY

Gianni Petrangeli
Nuclear Health & Safety Protection
ENEA
Via Vitaliano Brancati, 48
00144 Rome
ITALY

M. Carcassi
Departmento Di Costruzioni
Meccaniche E Nucleari
Facolta Di Ingegneria
Via Diotisalvi 2
56100 - ITALY

Japan Atomic Energy Research Institute (4)
Tokai-mura, Naku-gun,
Ibaraki-ken, 319-11
JAPAN
Attn: Dr. Kunihisa Soda
Dr. Toshio. Fujishiro
Mr. Kazuo Sato
Dr. Michio Ichikawa

Dr. Watanabe
Power Reactor Nuclear Fuel Development
Corporation (PNC)
Fast Breeder Reactor Development
Project (FBR)
9-13, 1-Chome, Akasaka
Minato-Ku, Tokyo
JAPAN

H. Jun
Korea Advanced Energy Research Institute
P.O. Box 7
Daeduk Danj i
Chungnam 300-31
KOREA

UKAEA Safety and Reliability Directorate (7)
Wigshaw Lane
Culcheth, Warrington
Cheshire WA3 4NE
UNITED KINGDOM
Attn: A. R. Taig
B. Cowking
S. F. Hall
J. G. Tyror
P. N. Clough
I. H. Dunbar
C. J. Wheatley

K. M. Becker
Royal Institute of Technology
Dept. of Nuclear Reactor Engineering
Stockholm S-10044
SWEDEN

Lennart Hammar
Department of Research
Swedish Nuclear Power Inspectorate
Box 27106
5-102 52 Stockholm
SWEDEN

Kjell D. Johansson
NPS
Studsvik Energiteknik AB
5-611 82 Nykoping
SWEDEN

Wiktor Frid
Dept. of Research
Swedish Nuclear Power Inspectorate
Box 27106
5-102 52 Stockholm
SWEDEN

AERE Harwell (2)
Didcot
Oxfordshire OXll ORA
UNITED KINGDOM
Attn: J. R. Matthews
Theoretical Physics Division
M. R. Hayns, G110/B329

Mr. J. T. Dawson
Severe Accident Studies Section
Central Electricity Generating Board
Berkeley Nuclear Laboratory, Berkeley
Gloucestershire GL13 9PB
ENGLAND

Karl J. Brinkmann
Netherlands Energy Research Foundation
P.O. Box 1
1755 ZG Petten (NH)
THE NETHERLANDS

Juan Bagues
Consejo de Seguridad Nuclear
Sor Angela de la Cruz, 3
Madrid 28020
SPAIN

UKAEA, AEA Winfrith (9)
Dorset DT2 8DH
UNITED KINGDOM
Attn: A. L. Nichols
B. R. Bowsher
A. T. D. Butland
M. Bird
A. J. Wickett
J. N. Lillington
S. R. Kinnersley
P. N. Smith
T. J. Haste

UKAEA, Culham Laboratory (4)
Abingdon
Oxfordshire OX14 3DB
UNITED KINGDOM
Attn: F. Briscoe
D. Fletcher
I. Cook
B. D. Turland

Simon J. Board
Severe Accident Studies Section
Central Electricity Generating Board
Berkeley Nuclear Laboratory, Berkeley
Gloucestershire GL13 9PB
ENGLAND

Nigel E. Buttery
Central Elect. Gen. Board, Booths Hall
Chelford Road, Knutsford
Cheshire WA16 8QG
ENGLAND

K. T. Routledge
NNC Booth's Hall
Chelford Rd. Knutsford
Cheshire WA16 8QG
UNITED KINGDOM

CEGB HSD (3)
Courtenay House
18 Warwick Lane
LONDON
Attn: P. Farmer
E. Beswick
J. P. Longworth

Bernhard Kuczera
LWR Safety Project Group (PRS)
Kernforschungszentrum Karlsruhe
P.O. Box 3640
D-7500 Karlsruhe 1
FEDERAL REPUBLIC OF GERMANY

Jacques Basselier
Nuclear Fuel Dept./Engineering Div.
Belgonucleaire SA.
25 rue du Champ de Mars
B-1050 Brussels
BELGIUM

Sung-Ki Chae
Nuclear Safety Research Division
Korea Advanced Energy Research Institute
P.O. Box 7
Daeduk-Danji
Chungnam 300-31
KOREA

Peter Hofmann
Institute of Matls. & Solid State Research
Kernforschungszentrum Karlsruhe
P.O. Box 3640
D-7500 Karlsruhe 1
FEDERAL REPUBLIC OF GERMANY

Giovanni Banonaro
Regulatory Research Commitment Project
ENEA
Via Vitaliano Brancati, 48
00144 Rome
ITALY

S. Chakraborty
Swiss Federal Nucl. Safety Inspectorate
CH-5303 Wurenlingen
SWITZERLAND

Sigfried Hagen
Kernforschungszentrum Karlsruhe
P.O. Box 3640
D-7500 Karlsruhe 1
FEDERAL REPUBLIC OF GERMANY

G. Caronreso
Dept. for Environmental Protection & Health
ENEA CRE Casaccia
Via Anguillarese, 301
00100 Roma Ad.
ITALY

Jose E. De Carlos
International Relations
Consejo de Seguridad Nuclear
Sor Angela de la Cruz, 3
Madrid 28020
SPAIN

Peter Hosemann
Paul Scherrer Institut
CH-5303 Wurenlingen
SWITZERLAND

Oguz Akalin
Ontario Hydro
700 University Avenue
Toraonto, Ontario
CANADA M5G 1X6

Lasse Mattila
Nuclear Engineering Laboratory
Technical Research Center of Finland
P.O. Box 169
SF-00181 Helsinki
FINLAND

Jorma V. Sandberg
Department of Nuclear Safety
Finnish Center Radiation & Nucl. Safety
P.O. Box 268
SF-00101 Helsinki
FINLAND

Agustin Alonso Santos
Universidad Politecnica de Madrid
J. Gutierrez Abascal, 2
28006 Madrid
SPAIN

SANDIA DISTRIBUTION:

3141 S. A. Landenberger (5)
3151 W. I. Klein
8524 J. A. Wackerly
1131 W. B. Benedick
1510 J. W. Nunziato
Attn: 1512 J. C. Cummings
1530 L. W. Davison
Attn: 1534 J. R. Asay
1541 H. C. Hardee
1415 K. T. Stalker
6400 D. J. McCloskey
6410 D. A. Dahlgren
6412 A. L. Camp
6413 E. D. Gorham-Bergeron
6418 J. E. Kelly
6418 R. M. Summers
6420 W. B. Gauster
6420 D. B. Hente
6422 D. A. Powers
6422 M. D. Allen
6422 M. Pilch
6423 K. O. Reil
6423 R. O. Gauntt (13)
6425 S. S. Dosanjh
6425 R. D. Gasser
6425 A. J. Grimley
6425 A. W. Reed
6425 R. C. Schmidt
6425 R. C. Smith
6425 M. F. Young
6428 J. B. Whitley
6429 K. D. Bergeron
6450 T. R. Schmidt
6500 A. W. Snyder
6510 J. V. Walker
6512 G. G. Weigand
6516 P. S. Pickard
6522 A. C. Marshall

NRC FORM 335 (2-89) NRCM 1102, 3201, 3202

U.S. NUCLEAR REGULATORY COMMISSION

BIBLIOGRAPHIC DATA SHEET

(See instructions on the reverse)

1. REPORT NUMBER (Assigned by NRC, Add Vol., Supp., Rev. and Addendum Numbers, if any.)

NUREG/CR-4671
SAND86-1443

2. TITLE AND SUBTITLE

The DF-4 Fuel Damage Experiment in ACRR with a BWR Control Blade and Channel Box

3. DATE REPORT PUBLISHED

MONTH: November
YEAR: 1989

4. FIN OR GRANT NUMBER

A1355

5. AUTHOR(S)

R. O. Gauntt, R. D. Gasser, L. J. Ott*

*Oak Ridge National Laboratory

6. TYPE OF REPORT

Formal

7. PERIOD COVERED (Inclusive Dates)

8. PERFORMING ORGANIZATION – NAME AND ADDRESS (If NRC, provide Division, Office or Region, U.S. Nuclear Regulatory Commission, and mailing address; if contractor, provide name and mailing address.)

Sandia National Laboratories
Albuquerque, NM 87185

9. SPONSORING ORGANIZATION – NAME AND ADDRESS (If NRC, type "Same as above"; if contractor, provide NRC Division, Office or Region, U.S. Nuclear Regulatory Commission and mailing address.)

Division of Systems Research
Office of Nuclear Regulatory Research
U.S. Nuclear Regulatory Commission
Washington, DC 20555

10. SUPPLEMENTARY NOTES

11. ABSTRACT (200 words or less)

The DF-4 test was an experimental investigation into the melt progression behavior of boiling water reactor (BWR) core components under high temperature severe core damage conditions. In this study 14 zircaloy clad UO_2 fuel rods, and representations of the zircaloy fuel canister and stainless steel/B_4C control blade were assembled into a 0.5 m long test bundle. The test bundle was fission heated in a flowing steam environment, using the Annular Core Research Reactor at Sandia Laboratories, simulating the environmental conditions of an uncovered BWR core experiencing high temperature damage as a result residual fission product decay heating. The experimental results provide information on the thermal response of the test bundle components, the rapid exothermic oxidation of the zircaloy fuel cladding and canister, the production of hydrogen from metal-steam oxidation, and the failure behavior of the progressively melting bundle components. This information is provided in the form of thermocouple data, steam and hydrogen flow rate data, test bundle fission power data and visual observation of the damage progression.

In addition to BWR background information, this document contains a description of the experimental hardware with details on how the experiment was instrumented and diagnosed, a description of the test progression, and a presentation of the on-line measurements. Also in this report are the results of a thermal analysis of the fueled test section of the experiment demonstrating an overall consistency in the measurable quantities from the test. A discussion of the results is provided.

12. KEY WORDS/DESCRIPTORS (List words or phrases that will assist researchers in locating the report.)

Severe fuel damage experiments, melt progression, BWR, boiling water reactors, in-pile experimental study, oxidation, and hydrogen production, Annular Core Research Reactor (ACRR)

13. AVAILABILITY STATEMENT

Unlimited

14. SECURITY CLASSIFICATION

(This Page)
Unclassified

(This Report)
Unclassified

15. NUMBER OF PAGES

16. PRICE

UNITED STATES
NUCLEAR REGULATORY COMMISSION
WASHINGTON, D.C. 20555